Microseismic monitoring of the controls on coastal rock cliff erosion

NORMAN, EMMA,CATHERINE

Microseismic monitoring of the controls on coastal rock cliff erosion

Emma Catherine Norman

Department of Geography

Durham University

Thesis submitted for the degree of Doctor of Philosophy

2012

Declaration

I confirm that no part of the material presented in this thesis has previously been submitted for a degree in this or any other university. In all cases the work of others, where relevant, has been fully acknowledged.

Emma Norman

Abstract

The aim of this thesis has been to improve understanding of the controls on coastal rock cliff erosion, utilising microseismic ground motion. Coastal cliff erosion has remained poorly understood, in part confounded by the challenges associated with monitoring changes to and controls upon steep slopes in the coastal zone. As a result the relative contribution of marine to subaerial and episodic to iterative forcing is based upon models with only limited field validation. For two years, from July 2008 to July 2010, cliff top microseismic ground motions were monitored using a broadband seismometer, installed on top of a 70 m high hard rock cliff of Jurassic mudstone, shale and sandstone, on the North York Moors National Park coast, UK. Concurrently cliff face erosion was monitored using high-resolution 3D terrestrial laser scanning. Regional-scale marine and weather data for the monitoring period and modelled nearshore wave conditions were used to establish the conditions under which cliff microseismic ground motions were generated. Distinct ground motion frequency bands were found to correlate with a range of marine and subaerial processes that transfer energy to the coastline and cliff. Fundamentally, microseismic sources were identified both at the cliff face from, for example, direct wave impact during cliff toe inundation, but also at more distal locations resulting from the transfer of energy from gravity and infragravity waves. Further analysis demonstrates statistically significant correlations between rockfall and cliff ground motion generated by wave impacts and wind at the cliff face, but also surprisingly waves across the nearshore and offshore, implying direct environmental controls on cliff erosion rate. The significance of longer period ground motion, representative of ocean gravity and infragravity waves also identifies an almost constant dynamic loading of the cliff rock mass, highlighting a potential for progressive deterioration of the cliff rock. The analysis demonstrates that cliff top microseismic ground motion provides a valuable proxy for marine and atmospheric forcing at coastal cliffs, overcoming the limitations in quantifying and testing controls on cliff erosion. The findings of this study are used to develop a new conceptual model of the environmental processes and failure mechanisms that control rock cliff erosion.

Acknowledgements

There really are so many people who have helped me over the last few years and who have been instrumental in making this project happen.

First of all I want to thank my supervisors, Nick Rosser and Dave Petley, initially for giving me the opportunity to do such an interesting project and of course for all their help since. Nick has been incredibly supportive and encouraging throughout. He has always been very generous with his time, to help with questions or provide advice, whether on the technical, analysis or writing aspects. Dave has provided focussed and insightful feedback and his big-picture perspective have been of real benefit during the project. Whilst not an official supervisor, Mike Lim has also been instrumental to the project, providing advice and encouragement throughout. He has spent many hours helping with fieldwork, and advising on technical and analysis aspects of the data.

Key to the project have been Cleveland Potash Ltd for providing the funding for this research and continuing to support vital monitoring of this stretch of coastline. They also provided the land in which to install the seismometers. In addition the project would never have taken its current form if not for SEIS-UK. A huge thank you to them, initially for the loan of the seismometers but ever since the first point of contact Alex, David and Victoria have been immensely helpful with problem solving, advice and discussions around how to use the seismic data so unconventionally.

Many thanks to Sam Waugh for help with fieldwork – for always being willing to go out whatever the weather and to help on even the messiest of jobs such as digging seismometers out of a muddy field. Thanks to Matt Brain and John Barlow for discussions around various aspects of the project and beyond, and to Peter Shürch, Rob Parker, Rich Hardy and Patrice Carbonneau for discussions and help with various technical, computer software and maths related issues! I owe a huge thanks to Andreas Vieli for his help with the wave modelling. In addition the workshop and IT staff in the department have always been a great help in helping with kit and technical problem solving.

I would also like to thank Mark Dickson and Marcos Alvarez at the University of Auckland for discussions and sharing ideas around coastal cliff microseismics and Marcos for advice on processing of the seismic data.

Last but by no means least, thanks so much to Nom, Mum, Dad and Ben and my chums for all your support and constant encouragement!

Contents

List of figures

Chapter 2

Chapter 3

Chapter 4

Chapter 5

Chapter 8

List of tables

Chapter 8

List of equations

Chapter 2

Chapter 8

Chapter 1: Introduction

1.1 Context and justification of the thesis

Whilst the application of relatively new techniques, such as Light Detection And Ranging (LiDAR) and terrestrial laser scanning (TLS), to monitor coastal rock cliff erosion has enabled improved understanding of cliff change (e.g. Rosser et al., 2007; Young et al., 2009a; Young et al., 2011a), quantified evidence of environmental controls of cliff erosion remains limited.

This study focuses on hard rock coastal cliffs, where a cliff is defined as a steep sloping surface where the sea meets the elevated land (Hampton et al., 2004), and 'hard' rock cliffs are defined as cliffs developed in bedded, jointed rock of high mechanical strength. These types of cliffs impose a number of limitations to monitoring of both cliff erosion and the environmental conditions that drive erosive processes. Problems associated with accessing steep slopes, confounded by the highly dynamic marine environment, have limited the availability of techniques to accurately monitor cliff erosion (Lim et al., 2005; Rosser et al., 2005) and the corresponding marine and subaerial conditions. Moreover, the range of processes and the complexity of rock characteristics in determining rocky coast erosion, makes establishing controls and drivers challenging (Trenhaile, 2002). With cliff top populations increasing (DEFRA, 2002) and predicted changes in future sea level (Lowe et al., 2009), climate and weather (Murphy et al., 2009), the need to understand rock cliff responses to present and future environmental conditions and processes is of growing importance.

This project is based upon a large body of previous research, examining the nature of hard rock cliff erosion on the North Yorkshire coast, UK (e.g. Rosser et al., 2007; Lim et al., 2010a; Lim et al., 2011). The adoption and adaption of terrestrial laser scanning (TLS) has been fundamental to the previous research, as a technique that overcomes the physical limitations associated with monitoring cliff change in this environment. Using these techniques, a five-year dataset of rockfall volumes has been collected and analysed by previous studies, the results of which have challenged established perceptions of hard rock cliff erosion (Rosser et al., 2007; Lim et al., 2010a). The studies have observed rockfall activity to occur across the whole cliff face, and with an absence of wave notch development at the cliff toe and resulting cantilever failure. These studies found poor correlations between rockfall activity and regional-scale environmental monitoring datasets, resulting in uncertainty over the role of environmental controls in short- and long-term cliff erosion, and therefore also of the underlying failure mechanisms (Rosser et al., 2007; Lim et al., 2010a). The results of these studies suggest that controls of cliff erosion are more diverse than predominantly wave erosion of the toe, and raise a number of questions

regarding the marine and subaerial drivers of hard rock cliff erosion across the cliff face. However, questions also arise regarding how best to test cliff environmental controls, and what representative datasets to use. Indeed these first need addressing to allow the controls of cliff erosion to be examined.

Microseismic ground motion has long been known to be generated by various types of ocean waves in both coastal waters and further offshore (e.g. Haubrich et al., 1963; Hedlin and Orcutt, 1989). However, using cliff top seismometers, a number of studies have recently identified that microseismic motion of cliffs is also caused by tides and waves across the intertidal zone (Adams et al., 2002; Adams et al., 2005; Lim et al., 2011; Young et al., 2011b). These studies have identified that: wave energy delivery to a coastal cliff is modulated by energy dissipation due to wave shoaling and refraction through decreasing coastal water depths (Adams et al., 2002); that wave impacts at the cliff toe produce a high-frequency shaking of the cliff, and wave loading of the foreshore produces cliff swaying at the same periods of incoming waves (Adams et al., 2005); and local infragravity waves cause larger, long-period displacements of the cliff (Young et al., 2011b). It is possible that the loading of the cliff demonstrated by these ground motions may in itself have implications for cliff erosion. Based upon their observed cliff displacements, Adams et al. (2005) proposed that the cyclical wave loading of the cliff could result in strain build up and micro-cracking within the cliff rock mass, degrading cliff rock mass strength, thus making the cliff more vulnerable to erosive processes. Adams et al. (2005) however did not monitor erosion of the study cliff and therefore questions remain regarding the effects of wave loading on cliff rock strength and erosion.

Cliff microseismic ground motion has therefore been shown to provide a good proxy of marine conditions both at and near the cliff. It is anticipated that monitoring of the cliff microseismic ground motion has significant potential to explore and quantify the range of environmental forces acting on coastal cliffs, both marine and atmospheric, and is a technique that overcomes the limitations outlined above. It may therefore provide a valuable tool in exploring environmental conditions at coastal cliffs and controls of cliff erosion. The term ‘environmental conditions’ is used throughout the thesis and refers to the marine and atmospheric forces e.g. winds, tides, waves, and their combined effects e.g. storms, that occur near the cliff and drive the processes that transfer energy to the cliff.

1.2 A new approach to explore environmental controls on coastal cliff erosion

In order to explore controls on coastal cliff erosion, morphological change through time and the environmental conditions acting upon the cliff need to be simultaneously monitored. This study uses high resolution monitoring, and the collation and modelling of regional-scale environmental datasets over a two-year period. The study site sits within the coast of the North Yorkshire Moors National Park, composed of high (approximately 70 m), hard rock cliffs, which have been monitored since 2002, as reported by Rosser et al. (2007) and Lim et al. (2010a).

An array of cliff top seismometers has been installed to monitor coastal cliff ground motions. The measured microseisms are employed as a proxy of both marine and atmospheric conditions acting on the cliff, allowing the quantification of their relative timing, frequency and magnitude. Based upon the findings of previous studies, this dataset was anticipated to provide a new and innovative insight into the conditions at the coastal cliff site. It was anticipated that this data will be capable of quantifying the marine influence on cliffs, widely believed to be so important in driving cliff erosion, which have previously been derived from indirect measurements of wave and tide heights. The ground motion frequencies generated by, and therefore that represent, the range of environmental forces and processes are explored. Regional tide, offshore wave and weather datasets have also been collected. The transformation of offshore wave conditions are modelled into shallow water in front of the cliff, to obtain estimates of at-site wave characteristics, breaking locations and resulting energy flux. This data has been used to consider energy transfer occurring directly at the cliff, and the efficacy of processes that this energy delivery may drive. To monitor cliff change this study uses TLS and the successive monthly monitoring and processing approach developed by Lim et al. (2005), Rosser et al. (2005) and Lim (2006) to produce a dataset of rockfall volumes. Regression analysis has been used to quantify the relationships between the environmental variables, the microseismic response and the resulting cliff rockfall. The analysis tests the environmental controls upon monitored cliff erosion, and compares the microseismic and regional-scale environmental datasets as drivers of this change.

1.3 Research aim and objectives

The overarching aim of this research is to explore the environmental forcing acting on a coastal cliff and to improve understanding of the environmental controls of hard rock coastal cliff erosion. The research objectives are:

Research objectives:

- To quantify environmental forces acting on a coastal rock cliff, using microseismic ground motions;
- To quantify cliff erosion using high resolution terrestrial laser scanning;
- To examine the control of marine and atmospheric conditions and processes on rockfall activity;
- To establish the viability of using microseismic ground motions as a proxy for environmental conditions and processes acting on coastal rock cliffs, and to explore controls on cliff erosion;
- To develop a new conceptual model of the environmental processes and failure mechanisms that control coastal cliff erosion.

1.4 Organisation of the thesis

The thesis is split into eight chapters (2 – 9) following this one. The content of these chapters is described as follows:

Chapter 2 provides a review of the recent literature that underpins current understanding of coastal cliff erosion, and the environmental and material controls.

Chapter 3 explains the data collection methodology, processing and analysis, and outlines the geology, geomorphology and setting at the study site. Emphasis is placed on the collation of the microseismic dataset, including examination of the data quality, as the focus of this research.

Chapter 4 provides an initial qualitative examination of the microseismic dataset collected. The microseismic ground motion time series is largely examined in the frequency domain, considering the variation in power across the frequency spectrum. Frequency power is compared to corresponding time series of environmental conditions to explore the generation of different ground motion signals, and the characteristics of the resulting ground motion. Four frequency bands are identified as a focus of this analysis that closely reflect the forcing mechanisms that are hypothesized to generate them.

Chapter 5 explores the marine and wind conditions in close proximity to the study site over the two-year monitoring period. Offshore wave conditions, monitored at a wave buoy approximately 22 km north of the study site, have been modelled across the nearshore to the foreshore and cliff toe. The model estimates of wave and set-up heights, energy flux and dissipation flux are presented.

Chapter 6 presents a detailed, quantitative exploration of combinations of marine and atmospheric variables which drive a selected range of ground motion frequencies. The frequencies that have been selected are representative of the four frequency bands identified in Chapter 4, that represent the dominant environmental forces acting upon the cliff. Regression analysis is used to identify where within the 1,000 m zone of the nearshore adjacent to the cliff each of the frequency band signals are generated. The processes and mechanisms which these combinations of environmental conditions represent, and which generate the microseismic waves that produce the cliff ground motions are considered. In the regression analyses the signal power is used, however in the last section of the chapter the relative amount of net energy recorded at the seismometer for each of the frequencies are examined.

Chapter 7 presents the two-year rockfall dataset and explores the rockfall characteristics across the cliff face, from which a rockfall magnitude-frequency distribution, and a time series of spatial and temporal distributions of rockfall are generated. The chapter then examines the environmental controls of the observed rockfall characteristics, using relationships obtained from regression analysis between the rockfall data and the ground motion frequencies identified in Chapter 4. Both the microseismic frequency power and energy are used in the regression analysis to explore the interactions between the environmental variables and cliff material that these different measures best represent. The regional-scale and modelled environmental datasets are also compared to the occurrence of rockfall, to ascertain the usefulness of microseismic proxies compared with regional monitored conditions in examining controls upon cliff erosion. Conditions are considered both in the inundation zone at the toe of the cliff, and the dry non-inundation zone of the cliff face above.

Chapter 8 brings together the findings in a discussion of the environmental forces found to transfer energy to coastal cliffs, the observed nature of cliff erosion and environmental and material controls of cliff change. The value of microseismic ground motions in identifying and quantifying the temporal variation in environmental conditions at coastal cliffs, and in exploring environmental controls of cliff erosion is considered. The control on cliff erosion of environmental processes and the microseismic ground motion they generate is explored. And the assumed relative effectiveness of the observed environmental forces acting on coastal cliffs,

as failure triggers and in preparing rock material for failure, is presented. Finally, a new qualitative conceptual model of the environmental and material conditions that determine cliff change and need to be considered by future studies is suggested.

Chapter 9 summarises briefly what the thesis set out to achieve and how, followed by the thesis' principal findings, focussed around the research aims. The extensions to previous studies and original contribution to knowledge are discussed and recommendations for further research are made.

Chapter 2: Review of recent coastal cliff literature

2.1 Introduction to cliffed coasts

Coastal cliffs are defined here as steep, sloping surfaces where the sea meets the elevated land (Hampton et al., 2004). The range of materials that coastal cliffs can be formed in, and varying climatic and marine conditions that cliffs are exposed to, means that cliff characteristics and behaviour vary significantly. A classification of cliff behaviour units (CBUs) has been developed to provide a general description of different types of cliff failure mechanisms, used for cliff management in England and Wales (DEFRA, 2002). These units incorporate the foreshore / beach and the processes which link them with the cliff, which have some control on cliff failure (DEFRA, 2002). This classification provides a useful overview of different types of cliff behaviour (Figure 2.1).

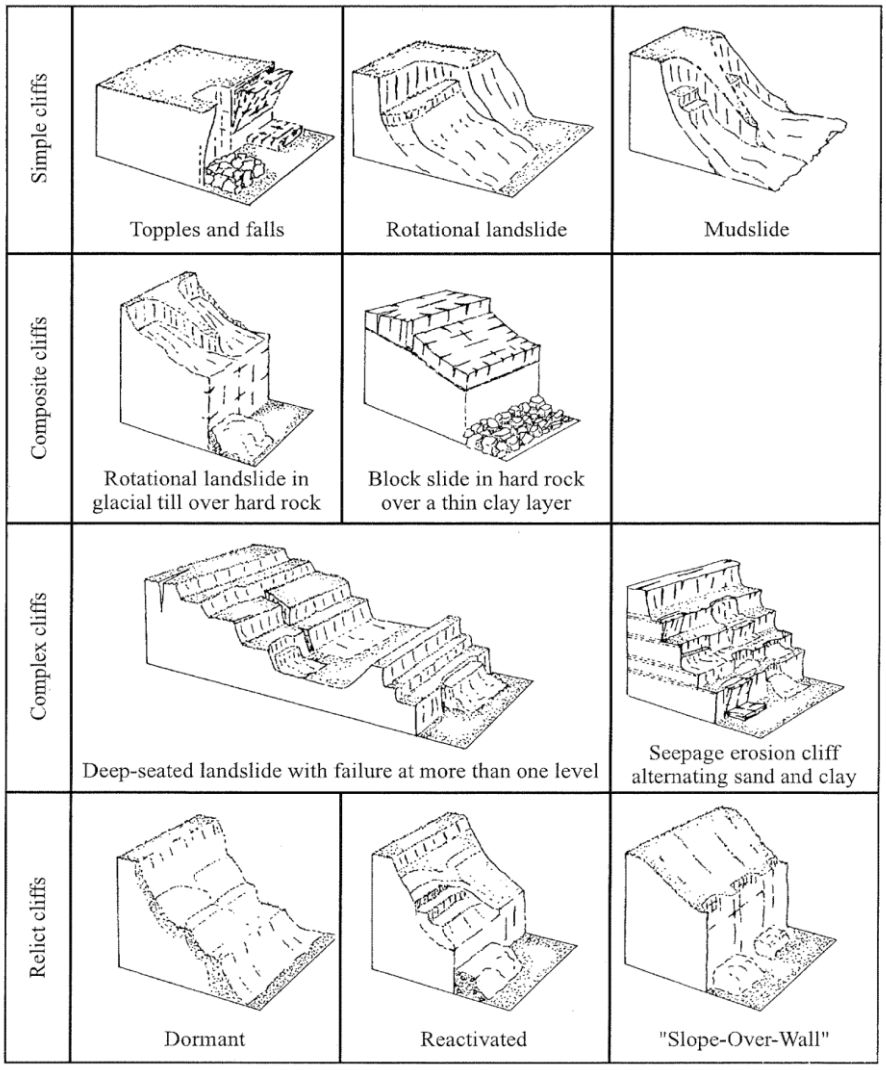

Figure 2.1: The main cliff behaviour unit (CBU) types. From: DEFRA, 2002.

The different cliff failure types are summarised below:

- Simple cliffs: Termed simple because their failure mechanisms are relatively straightforward, with detachment as individual falls, topples or slides, and minimal storage on the cliff face. Formed in either hard, soft or superficial materials (DEFRA, 2002).
- Composite cliffs: Cliffs formed in a contrasting mix of materials e.g. hard rock overlain by deep layer of softer material, that fail via separate mechanisms (DEFRA, 2002).
- Complex cliffs: The cliff slope consists of a number of interlinked sections which fail independently however simultaneously influence surrounding sections via, for example, the transfer of material down-slope or decreased stability of nearby sections. There are complex feedback mechanisms between the sections of the unit (DEFRA, 2002).
- Relict cliffs: Previously active sections of coastal slopes that have stabilised, however changes in more exposed sections of cliff result in de-stabilisation of the relict sections. Sequences of slopes that are at varying stages of activity can form (DEFRA, 2002).

The complexity of cliff behaviour is however determined by the specific composition of material types and strength, the range and variability of environmental processes, the exposure duration of the cliff face to strength degrading processes, and the resulting stability throughout the cliff profile (DEFRA, 2002). In light of the variability of lithological conditions and active processes over time, cliff failure behaviour is therefore temporally and spatially variable over short-, medium- and long-term timescales (DEFRA, 2002).

Coastal cliffs are typically referred to as ‘hard’ and ‘soft’, as determined by their relative strength, most commonly expressed in terms of uniaxial compressive strength. Hard and soft form a continuum and it is common for cliffs to be built in various combinations of both. Examples from which are as follows: soft cliffs such as weakly lithified sand bluffs, examples found along the Californian coast (e.g. Collins and Sitar, 2008), and poorly consolidated sands and clays of the East Anglian coast (e.g. Lee, 2008); medium strength cliffs such as the chalk cliffs that border either side of the English Channel (e.g. Duperret et al., 2005); and hard rock cliffs such as the Jurassic mudstone and sandstones of the North Yorkshire coast (e.g. Rosser et al., 2007).

Cliff material strength is commonly used as a measure of the cliff response to the subaerial and marine processes the cliff is exposed to (Emery and Kuhn, 1982). This however commonly overlooks the effects of the heterogeneity / homogeneity throughout the cliff profile, and the role of rock mass structures such as jointing, faulting or exfoliation. The processes acting on a

cliff are in turn determined by the wider setting, such as the planform geometry of the coast, which has conventionally received little attention (Limber and Murray, 2011). The geology and geomorphology of a cliff determine the cliff morphology and the processes which act upon it, producing a diverse range of cliff features, which vary both around the globe, but also within close proximity (Hampton et al., 2004).

From the afore-mentioned continuum of cliff material strengths, hard rock cliffs have received the least attention and there is little quantitative data on the behaviour of cliff settings such as these. This is anticipated to be due to the slower responses to environmental forcing, the complexity of the varying geology and environmental conditions and processes, in addition to greater difficulties of monitoring high, steep, hard rock cliffs' change using traditional techniques (Lim et al., 2005; Rosser et al., 2005). Hard rock cliffs' interactions with environmental processes, failure mechanisms and resulting patterns of erosion are therefore poorly understood. Considerable work is thus needed focussed specifically on such cliffs.

This study is focussed on 'simple' hard rock cliffs, as defined above. Recent developments in techniques that enable high-resolution monitoring of high, steep cliffs have overcome the long-term limitations to monitoring erosion across entire cliff faces (e.g. Collins and Sitar, 2008; Young et al., 2011a), and have produced results that contradict current conceptual models of hard rock cliff behaviour and raise questions over what is driving the observed behaviour (e.g. Rosser et al., 2007; Lim et al., 2010a). This study has set out to address the questions raised by these studies, by continuing monitoring of hard rock cliff erosion using high-resolution techniques and focussing on developing an approach to monitor and explore the environmental controls of the concurrent cliff erosion. This chapter therefore is focussed upon recent and key cliff studies that have applied new or novel approaches to monitoring cliff erosion and examining the environmental conditions and processes that control this.

The paucity of hard rock cliff research means however that there are few studies to develop on and therefore research based on softer rock cliffs plays a key role in understanding hard rock cliffs' behaviour and in developing approaches to monitor and explore them. This review therefore covers a number of recent studies that have focussed on a range of cliff settings, but the techniques used or the studies' findings, are important to developing our understanding of hard rock cliff erosion and the environmental controls.

2.2 Rocky cliffed coasts

Historically rocky cliffed coasts, defined here as erosional coasts cut into hard rock, have received less attention than cliffs in soft materials, such as clay and sand, and depositional coastal landforms and features such as beaches and wetlands, demonstrated in a review by Naylor et al. (2010). Naylor et al. (2010) identify that this has been partially due to the comparatively slow response of rock coasts to forcing mechanisms such as storms and waves, relative to the more immediate responses of coasts in soft materials. Low rates of change also mean that monitoring rock coast erosion is more problematic as techniques capable of capturing data at finer resolutions are needed. In addition, Naylor et al. (2010) identify that the relative economic and social importance assigned to beaches, and the ecological importance of wetlands, is higher compared to that perceived of apparently static rocky coasts.

Within rocky coast research there has been a greater focus upon foreshore dynamics and evolution, with foreshores providing a much more accessible environment in which to explore the relative controls of subaerial to marine processes and variations in geological controls. This is reflected in the number of recent reviews of foreshore research, including Stephenson (2000), Trenhaile (2002) and Dasgupta (2011), relative to the absence of equivalent reviews for coastal cliffs. More widely, studies of rocky coasts arguably lag behind the recent progress made in other areas of geomorphology. Notably there have been low numbers of studies directly monitoring processes, a lack of wider regional- or global-scale comparative studies, and a lack of uptake of progress from other areas of geomorphology, both in terms of techniques, concepts and resulting wider academic interest.

Traditionally foreshores and cliffs are researched as separate entities. Studies that do consider both typically focus on the evolution of the whole landscape relative to changing sea level and exploring whether the coasts are contemporary or inherited features (e.g. Trenhaile, 2000; Trenhaile, 2001).

The two features are however inextricably linked, as wave transformation over the foreshore determines wave characteristics and energy at the cliff face, and cliff elevation relative to the intertidal zone determines the water depth across the foreshore and therefore exposure to and duration of various marine processes. This distinction is made more surprising when compared to the numerous studies that focus on beach-fronted cliffs, where beach topography is a fundamental consideration in calculating wave energy dissipation and cliff erosion (e.g. Benumof et al., 2000; Ruggiero et al., 2001; Lee, 2008; Limber and Murray, 2011).

A number of factors have contributed to making rock cliffs challenging to research: the physical constraints to monitoring cliff erosion, such as high, steep slopes and restricted viewing angles; the limited access resulting from highly changeable marine environments; the range of scales of change to be monitored (Lim et al., 2005; Rosser et al., 2005); and also the combination of subaerial and marine processes and cliff rock characteristics that control cliff erosion (Trenhaile, 2002).

2.2.1 Definitions of terms

Throughout the thesis a number of definitions are used which delimit the coastal zone to describe the location of marine processes and interactions between the seabed and waves (Figure 2.2).

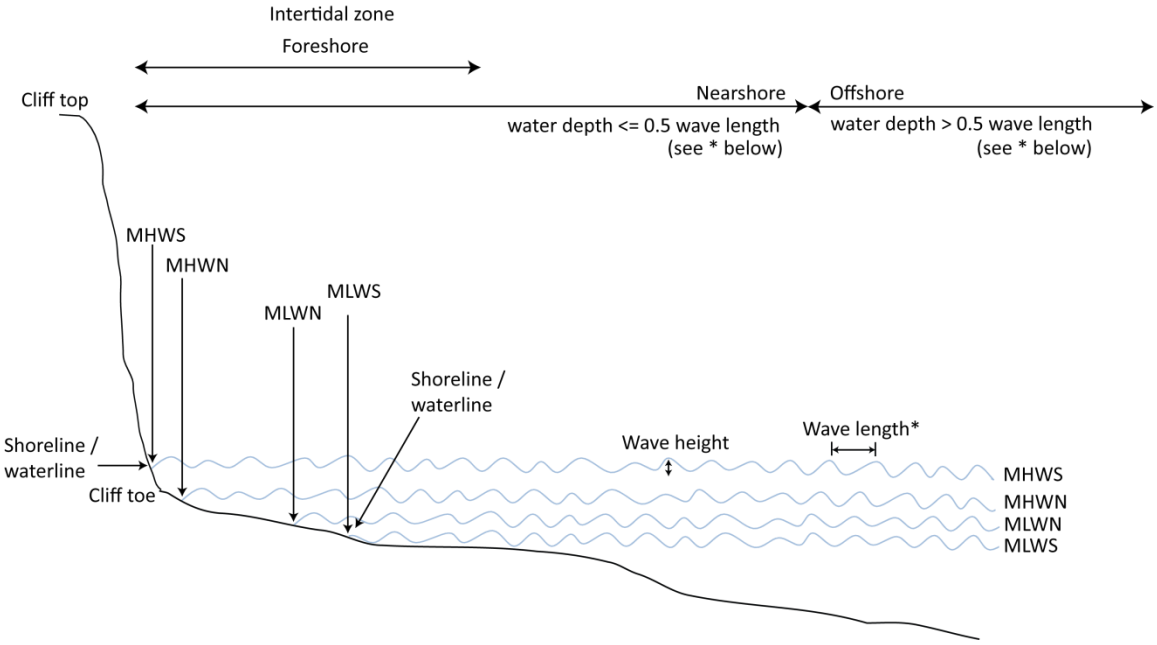

Figure 2.2: Coastal zone definitions and locations used within the thesis. MHWS = mean high water spring tide level; MHWN = mean high water neap tide level; MLWN = mean low water neap tide level; MLWS = mean low water spring tide level.

2.3 Spatial and temporal patterns of rock cliff erosion

Until recently erosion of the whole cliff face was not measured directly, but has been inferred from individual features of the cliff, such as the cliff top or toe. Problems accessing steep cliff faces have resulted in the heavy reliance on aerial methods of monitoring cliff change

behaviour. Most commonly studies have used planimetric changes in the cliff top and toe positions and other distinguishing features such as landslide back scarps to calculate rates of cliff retreat using historical maps and aerial photography (e.g. Agar, 1960; Bray and Hooke, 1997; Budetta et al., 2000; Andriani and Walsh, 2007; Dornbusch et al., 2008). Measurements of cliff position change using these techniques have been used to calculate rates of retreat, averaged over long time periods and large areas, assumed to be representative of the whole cliff. See Crowell et al. (1991) and Moore (2000) for detailed reviews of these techniques.

Ground based approaches that have focussed on erosion rather than retreat have traditionally either been qualitative e.g. photos of change (e.g. Texeira, 2006) or quantitative but only able to monitor changes in small accessible sections of the cliff, for example: using erosion pins (Greenwood and Orford, 2008) or micro-erosion meters (Robinson, 1977) to monitor change at the cliff toe; or measuring of morphological features such as cliff toe notches (e.g. Russell, 1963; Robinson, 1977); or monitoring of the cliff top using stakes (Bernatchez and Dubois, 2008), or photogrammetry and electro-magnetic distance measuring (EDM) (Andriani and Walsh, 2007). Whilst these higher resolution quantitative techniques provide a more accurate estimation of rates of change, they are only capable of representing a small section of the cliff.

With both aerial calculations of retreat rates, and monitored erosion of specific cliff features, there is a widely used assumption that the cliff top and / or toe represent change across the whole cliff face. This does not take into account the variations in environmental processes acting on different parts of the cliff nor the variations in rock characteristics through the profile.

Using relatively new monitoring techniques such as Light Detection And Ranging (LiDAR) and terrestrial laser scanning (TLS), a number of recent studies have been able to examine how cliffs erode, in significantly higher resolution, notably upon the cliff face, than was capable with traditional aerial planform approaches of low resolution aerial photography and maps. These techniques are able to monitor erosion across the cliff face, overcoming the limitations of previous ground based techniques of measuring erosion.

Rosser et al. (2007) and Lim et al. (2010a) used TLS to monitor rockfall activity from high (approximately 70 m), steep near-vertical, hard rock cliffs of mudstone, shale, siltstone and sandstone on the North Yorkshire coast, UK. The high-resolution, monthly monitoring undertaken by both studies has provided significant insight into the failure behaviour of hard rock cliffs, which traditionally have received less attention than softer material cliffs, which erode more visibly. Rosser et al. (2007) and Lim et al. (2010a) observed rockfalls to be distributed across the whole cliff face (Figure 2.3), with similar rates of erosion of the lower cliff

compared to higher parts of the cliff face that are not affected directly by the sea. These results contradict the widely adopted conceptual model of cliff erosion driven by erosion of the toe by wave attack, which may develop a notch at the toe and failure of the above material via cantilever collapse (e.g. Sunamura, 1977; Trenhaile, 1987; Sunamura, 1992). The cliff toe model has traditionally perhaps most commonly been used to explain hard rock cliff erosion, due to the physical modelling work undertaken on hard rock cliffs by Sunamura (1982; 1992). Notably a lack of studies of the whole cliff face has prevented validation of the model. Rosser et al. (2007) and Lim et al. (2010a) identified strong geological controls on the observed rockfall characteristics, with the different rock types producing varying rockfall geometries, clearly determined by structural characteristics. The rock layers also produced varying rates of erosion, identified to be representative of the varying structure and relative rock strength (Rosser et al., 2007). The majority of observed rockfalls were small, with 75% of observed rockfalls of volumes <= 0.001 m^3, and < 5% of rockfalls of volumes > 0.1 m^3 (Rosser et al., 2007).

The findings of Rosser et al. (2007) and Lim et al. (2010a) demonstrated significant influences of rock strength and structure as key controls of rockfall characteristics. With variability of these across the cliff face resulting in variability in the nature of rockfalls. However, the studies struggled to explain environmental controls of the observed rockfall spatial distributions and timing, with no significant seasonality in rockfall volumes or frequency. Poor correlations were found between regional-scale tide and weather data and the rockfall data, although both studies found statistically significant relationships between the mudstone volumes (which feature at the cliff toe) and tide level.

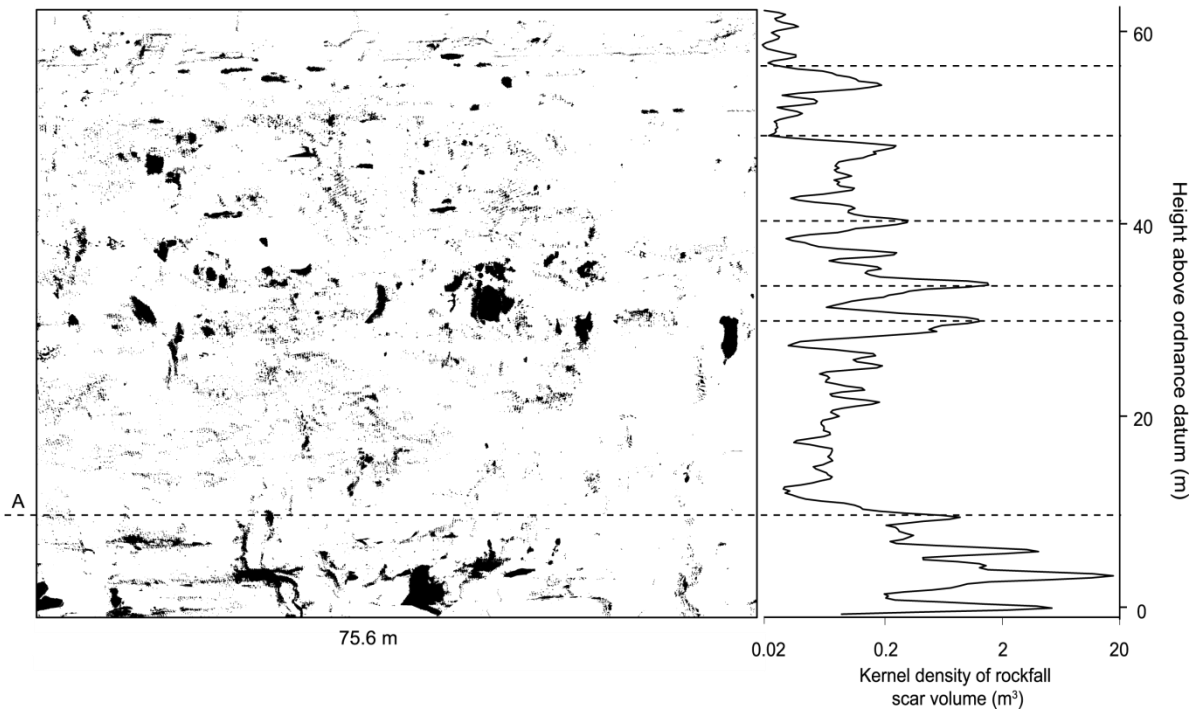

Figure 2.3: Example of rockfall distribution, showing changes across the cliff face for the monitoring period September 2002 – April 2005, obtained using TLS. The rock face is approximately 75 m wide and 70 m high, displayed as a view looking onto the cliff face. (Left) Black areas indicate rockfall scars, with line A representing the highest level of wave inundation at this site; (Right) Kernel density estimate (Epanechnikov kernel, half width = 0.25 m) of rockfall activity up the cliff profile for all sites, with major lithological boundaries marked by dashed horizontal lines. From: Rosser et al. (2007).

The results of these studies indicate that hard rock coastal cliff erosion is significantly more complex than that suggested by Sunamura's (1977) widely cited cliff toe model. Whilst over the long-term the rate of retreat must tend towards that of toe erosion, over short- to medium-term scales, behaviour is more complex. Critically this scale is that at which management decisions are made (DEFRA, 2002). Whilst a variety of rock mass strength controls determining failure behaviour across the cliff face have been observed, Rosser et al.'s (2007) and Lim et al.'s (2010a) findings raise questions regarding the environmental controls of the observed rockfall distributions. Whilst the sea appears to have some influence over erosion of the mudstone at the cliff toe, the extent and relative importance of this upon the wider cliff rock mass above remains unclear. This raises questions regarding the relative balance of marine, subaerial and their combined resulting conditions in controlling erosion of the cliff, and the resulting failure mechanisms.

High-resolution studies of softer cliffs have observed a range of failure types, and due to more rapid rates of change, have been better able to identify significant environmental and material characteristics which control the observed behaviour (e.g. Collins and Sitar, 2008; Young et al., 2009b; Quinn et al., 2010). Collins and Sitar (2008) explored the failure mechanisms driving erosion of weakly lithified sand coastal bluffs, south of San Francisco, California, over five winters using TLS. They used measures of maximum daily total sea water level and 48-hour cumulative rainfall compared to the seasonal averages to represent the magnitude of environmental conditions during the winters being monitored, and found them to correlate well with the occurrence of failure events. Different types of failures and triggers were noted between weakly and moderately cemented sand cliffs. In the weakly cemented sands, wave erosion at the bluff toe was the main mechanism of failure (Collins and Sitar, 2008). Failures were not observed during all storm seasons, due to the presence of fallen material at the bluff toe that provided protection from wave erosion. Collins and Sitar (2008) did not observe notching and instead found that wave erosion of the weakly cemented bluffs resulted in a steepening of the cliff toe followed by wedge failure of the toe before any undercutting occurred due to the material weakness (Figure 2.4).

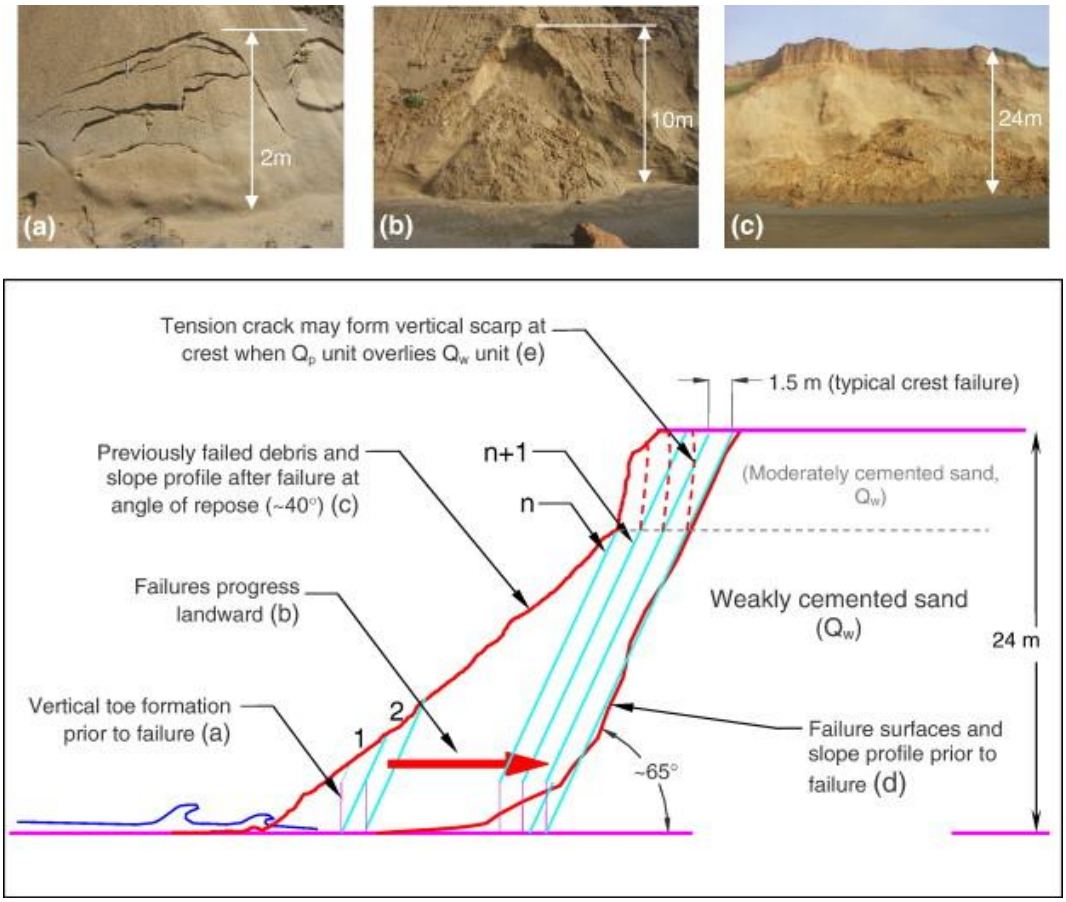

Figure 2.4: Geomorphic model of wave action-induced bluff failure with typical profiles from LiDAR data shown. Waves acting only on previously failed debris results in small, slab failures less than 2 m high (a). Shear failures increase in height (1, 2, *n*) (b), but without crest retreat, as waves erode into either previously failed debris or into unfailed, intact material (c). Failure along the entire bluff height occurs at *n* + 1 with resultant crest retreat along parallel shear planes (d). The cycle will start anew as the resulting debris is eroded by wave action. At Pacifica, moderately cemented sand (Q_p) overlies the weakly cemented sand at the crest and forms vertical scarps (e) that fail in response to wave action induced toe erosion occurring beneath. From: Collins and Sitar (2008).

Although wave action was found to be the dominant driver of erosion, the actual nature of failure differs to that of Sunamura's (1992) cliff toe model, suggesting that for this model to occur very specific rock strength conditions are required. Indeed, wave erosion of the moderately cemented sands was not found to be significant due to the greater resistance of the material (Collins and Sitar, 2008). Instead, in the moderately cemented sands they identified groundwater and surface water build-up and seepage, caused by recent precipitation, and stress-relief induced exfoliation on the upper parts of the bluff to be the dominant mechanisms of failure. This decreased the tensile strength, resulting in tensile fracturing and releasing blocks

of material from cliff face (Collins and Sitar, 2008) (Figure 2.5). This mechanism however was not observed in the freely draining weakly cemented sands.

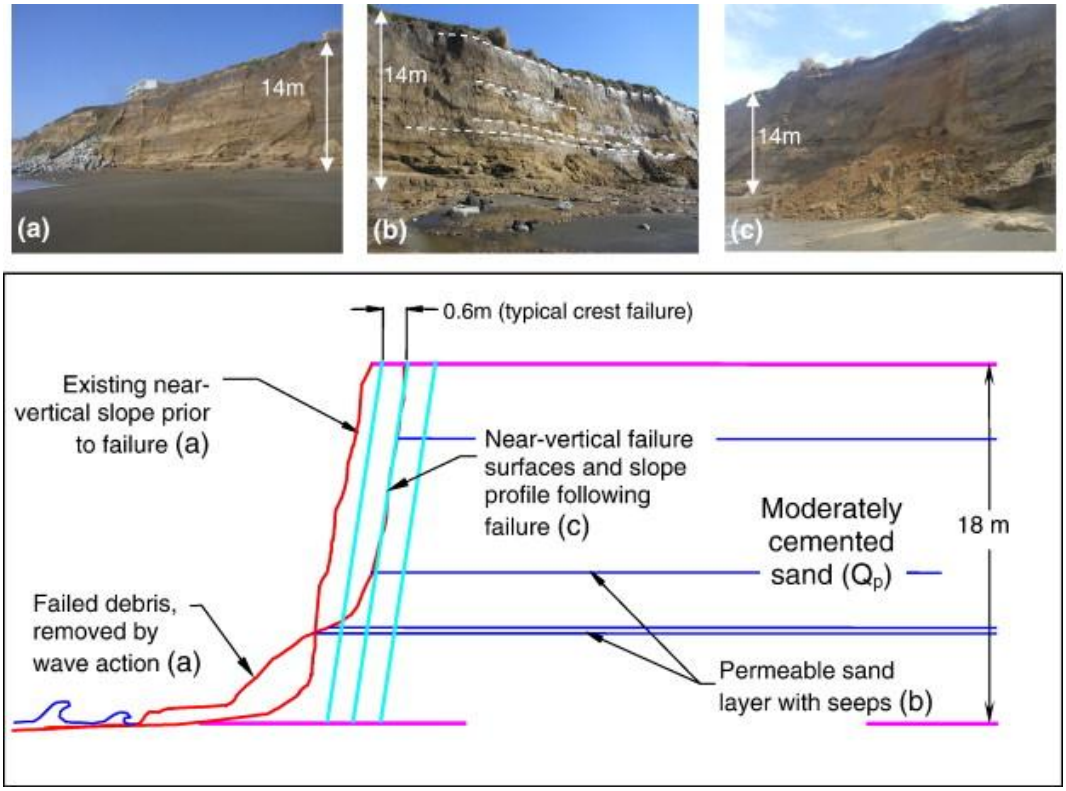

Figure 2.5: Geomorphic model of precipitation-induced seepage bluff failure with typical profiles from LiDAR data shown. The bluff geometry is near-vertical with previously failed debris removed by wave action (a). Water moves downward through the soil profile, ponding on denser layers (b), and visible as seeps in the bluff face. Loss of tensile strength lead to slab failures located above the dense, ponding layers (c). Failed debris may buttress the bluff profile until removed by wave action, however a vertical geometric profile is already established in the upper portions, ready for additional failures. From: Collins and Sitar (2008).

Dewez et al. (in press) monitored rockfall activity of chalk cliffs of alternating layers of soft, medium and hard layers on the Normandy coast, France, over 2.5 years at 3 - 7 month intervals using TLS. During the monitoring period 82,400 m^3 was eroded across an area of 36,000 m^2 of cliff face. The smallest detected failure (limited by scan resolution) was 0.0006 m^3 and largest was 70,950 m^3, demonstrating the chalk to be more actively eroding than the cliffs in North Yorkshire. They found 28% of the monitored cliff face to be active (i.e. measurably eroding), with recurrent erosion occurring in some locations, but not all. Dewez et al. (in press) observed rockfalls to occur most frequently in the lowest 20 m of the cliff, in medium-soft chalk layers. It is not clear if this behaviour generated a consistent cliff geometry, as the authors do not

describe the resulting cliff morphology nor test the environmental controls of this failure behaviour as the emphasis of the study was on the rockfall magnitude-frequency distribution.

Exploration of rockfall magnitude-frequency relationships enables improved predictions of future cliff erosion rates, as compared to that obtained using traditional methods. Advantageously this approach allows the full range of potential failure sizes to be considered in the resulting erosion flux over the modelled time period. Traditionally, historical retreat rates are calculated using low-resolution aerial imagery or historical maps with retreat rates averaged over wide areas and long periods of time (e.g. Agar, 1960; Bray and Hooke, 1997; Andriani and Walsh, 2007), making them potentially highly inaccurate. Rosser et al. (2007), Lim et al. (2010a), Dewez et al. (in press) and Young et al. (2011a) explored the magnitude-frequency distribution of their high resolution cliff rockfall volume datasets, and found the datasets to each produce a negative power law relationship, as identified for non-coastal rockfalls (e.g. Dussauge-Peisser et al., 2002) and wider mass movement datasets (Brardinoni and Church, 2004; Guthrie and Evans, 2004; Malamud et al., 2004). The high-resolution of TLS enables capture of smaller rockfalls and a more accurate distribution and relationship is obtainable (Lim et al., 2010a; Young et al., 2011a). Barlow et al. (2012) examined the effect of temporal resolution of monitoring on magnitude-frequency distributions and demonstrated that more frequent monitoring using TLS improves relationship accuracy as the smaller magnitudes are better represented, as fewer events are obscured by superposition. Both the temporal and spatial issues are demonstrated by comparing the magnitude-frequency distributions of Lim et al. (2010a) to those of Young et al. (2011a), and in particular the 'roll-over' feature at the small rockfall magnitude events in Young et al.'s (2011a) lower temporal and spatial resolution LiDAR dataset, implying an insufficient resolution to represent this part of the rockfall size distribution.

Using the power law of observed data, Barlow et al. (2012) modelled the erosion rates for the North Yorkshire coast, and compared results for different rock types monitored. They found the presence of large failures to result in misleading net long-term estimates of erosion, and therefore recommended longer monitoring periods are required to more accurately represent the frequency of large events. In addition Barlow et al. (2012) explored the magnitude-frequency distributions over monthly and seasonal timescales. Analysing the scaling parameters of the power-law relationship they found the greatest variability in power-law form to occur during winter months, indicating a seasonality in fit to the scaling behaviour, indicative of a rockfall response to environmental conditions. This environmental signal was not apparent in earlier analyses of correlations between rockfall volumes and environmental data found by Rosser et al. (2007) and Lim et al. (2010a). Barlow et al. (2012) conclude that improvements in

understanding of the geological and environmental controls over the magnitude-frequency distribution are needed to improve long-term erosion estimates.

LiDAR enables longer stretches of cliffs to be monitored. Young et al. (2011a) used LiDAR to monitor cliff top retreat over 5.5 years of a 7.1 km stretch of slowly eroding cliffs of sandstone and shale bases overlain by softer terrace deposits near Point Loma in San Diego, California. They identified a variety of failure types - rockfalls, block falls and topples. Whilst 84% of the monitored cliff edge didn't change, they observed a number of large failures that occurred across widths of 2 - 68 m of the cliff top. Maximum cliff top retreats ranged from 0.8 - 10 m and the widths and depths of failures were observed to be regulated by cliff morphology and rock structure. Young et al. (2011a) identified 'hot spots' of erosion activity, identifying that small and medium failures occur at the locations of previous similarly sized failures, which they suggested to indicate progressive failure mechanisms, as also identified by Rosser et al. (2007). They also observed that the areas with higher mean retreat had increased failure activity across the range of failure magnitudes. In planform, this suggests that the geometry of the coast may reflect both the type of failures and the net retreat rates, an area explored in more detail by Limber and Murray (2011).

Sallenger et al. (2002) used LiDAR to explore cliff erosion due to changes in beach elevations caused by the 1997-1998 El Nino. They explored the relationships between the run-up elevation and water inundation duration and resultant cliff erosion. They found correlations between duration of inundation by waves and erosion in locations where beach denudation and width reduction exposed more of the cliff toe to waves. The presence of beach material both acts to protect, as cover, but also to promote, as tools, the erosion process (Murray and Limber, 2011). Sallenger et al. (2002) demonstrate the importance of beach characteristics in determining the cliff exposure to marine processes. Sallenger et al. (2002) suggested a pattern of cliff development where subaerial processes eroded the cliff top, and wave erosion of the cliff toe removed cliff toe material and the failed material from the upper slope, with balances between the two sets of processes determining the cliff slope. They stated however that the temporal resolution of the study was unable to quantitatively define the dominant or relative controls of the different processes.

Both of these studies utilising LiDAR to look at long stretches of coastline identify 'hot spots' of erosion, demonstrating alongshore variation in geological and environmental conditions producing varying rockfall behaviour. Similarly, variations in geology vertically up the cliff profiles of Rosser et al. (2007) and Lim et al. (2010a) have produced varying rockfall characteristics and it is anticipated that vertical variations in environmental processes also

contribute. These studies have enabled improved quantification of coastal cliff erosion and failure behaviour, and therefore greater clarification of the nature of cliff change and in some studies also the factors that control this process.

The results of Rosser et al. (2007) and Lim et al. (2010a) raise questions regarding the environmental controls of the observed rockfall and how best to test this: Do regional-scale environmental datasets accurately represent conditions at the cliff?; If not, then what are the marine and subaerial conditions at the coast relevant to erosion?; How can we more accurately measure or estimate these in harsh and inaccessible cliff environments?

The success of Collins and Sitar (2008) and others, that have used proxies for cliff face environmental conditions by transforming regional datasets to better represent conditions at the cliff (e.g. Benumof et al., 2000; Ruggiero et al., 2001), compared to the results of Rosser et al. (2007) and Lim et al. (2010a) that used regional-scale data, suggest that proxies that represent conditions nearer to the cliff are useful in improving understanding of environmental controls of hard rock cliff erosion.

The results of the studies above from a variety of cliff environments, also question the relative efficacy of wave energy at the cliff toe as the dominant driver of cliff erosion. Critically, the relative importance of marine to subaerial conditions needs to be understood. Clearly, further work is now necessary combining high-resolution monitoring of cliff change, with an improved assessment of environmental conditions that drive erosion.

The following sections discuss recent studies of the environmental, both marine and subaerial, and material controls of rock cliff erosion. Firstly the current conceptual model of coastal cliff erosion is considered. Followed by a review of recent studies' approaches to quantifying marine and subaerial conditions at cliffs, interactions between environmental processes and cliff materials, and material controlled failure behaviour

2.4 Linking cause and effect: controls of cliff erosion

It is widely believed that wave energy delivery to the cliff toe is the key driver of coastal cliff erosion (e.g. Trenhaile, 1987; Bray and Hooke; 1997; Anderson et al., 1999; Adams et al., 2005; Walkden and Hall, 2005), based largely on the work of Sunamura (1975; 1976; 1977; 1982; 1992). Sunamura's work has undoubtedly historically dominated rocky cliff research, in a discipline of relatively few researchers, he has produced a large body of work that semi-quantified cliff behaviour focussing on erosion of the cliff toe. Because of the difficulties of

monitoring marine conditions directly at the coast, Sunamura undertook a series of laboratory scale experiments examining the resulting cliff toe erosion rates and notch profiles resulting from varying marine conditions at the cliff. These included, for example, the relative effects of different wave types (e.g. standing, breaking or broken) published in 1975, and the effects of varying presence of sediments, published in 1976. However Sunamura's experiments were undertaken based on the observation that notches were a ubiquitous feature of eroding cliffs, as was the case in many of his validation field sites. Further, Sunamura's experiments were designed in a manner specifically to reproduce this type of behaviour, using analogue material that enabled notches to develop during his simulations (Sunamura, 1975; 1976; 1977). From these laboratory studies he postulated that the rate of cliff toe erosion was determined by the relative forces of the rock resistance and the assailing force of waves (Equation 2.1) (Sunamura, 1977; 1992):

Equation 2.1: $$x = f(F_W, F_R, t)$$

(Sunamura, 1977, 1992)

Where:

x = cliff toe erosion;

F_W = assailing force of waves;

F_R = resisting force of cliffs;

t = time

In the absence of techniques to quantify rates of hard rock cliff erosion, and in particular that above the toe across the whole cliff, and the difficulties of monitoring marine and subaerial conditions, Sunamura's model provided a logical, qualitative explanation for cliff behaviour, and hence has been widely adopted. Sunamura's (1977; 1992) equation (Equation 2.1) underpins a number of models of cliff erosion (e.g. Budetta et al., 2000; Walkden and Hall, 2005), and his work is a key contributor to rocky cliff research, notably because of the consideration of cliff material properties.

The findings of studies using the new high-resolution monitoring techniques discussed above, capable of monitoring change across the whole face, however indicate that the controls, and resulting distribution of cliff erosion are much more complex than suggested by Sunamura's (1977; 1992) model.

2.4.1 Marine controls of cliff erosion

2.4.1.1 Tidal inundation models

In addition to the height and therefore force of waves, the frequency of impacts of waves at the cliff face is fundamental in determining the rate of wave erosion (Sunamura, 1982). Tidal inundation duration models imply that the elevation of maximum wave energy delivery, is a function of the time spent by the tide at or above any given height up the cliff face (Trenhaile and Layzell, 1981; Carr and Graff, 1982; Trenhaile, 2000). The tidal inundation duration is defined as the fraction of the year that the tide spends at any given height (Trenhaile and Layzell, 1981) (Figure 2.6). Erosion is understood to be concentrated at an elevation just above peak tidal duration, resulting from the elevated influence of wave impacts, wherein the combination of air and water enable hydraulic impact pressures and the mechanical attrition and abrasion and then removal of cliff material (Trenhaile, 2000). Tidal duration models have been adopted within numerical models of cliff erosion, to predict where wave erosive processes are concentrated and how cliff erosion relates to absolute sea level (e.g. Walkden and Hall (2005); Walkden and Dickson (2008); Ashton et al. (2011)). Whilst studies that have compared tidal data with observed rockfall data have found some statistically significant relationships between tide heights and rockfall volumes (Rosser et al., 2007; Lim et al., 2010a), the relationships have been weak. This suggests that either other factors are involved, such as wave heights, or that tides monitored at some distance from the cliff may not be representative at the site of interest. As yet, the distribution of energy delivery to the cliff resulting from tidal inundation, both through time and space, have not been quantified to test how well these models represent the erosive efficacy of wave energy at the cliff toe.

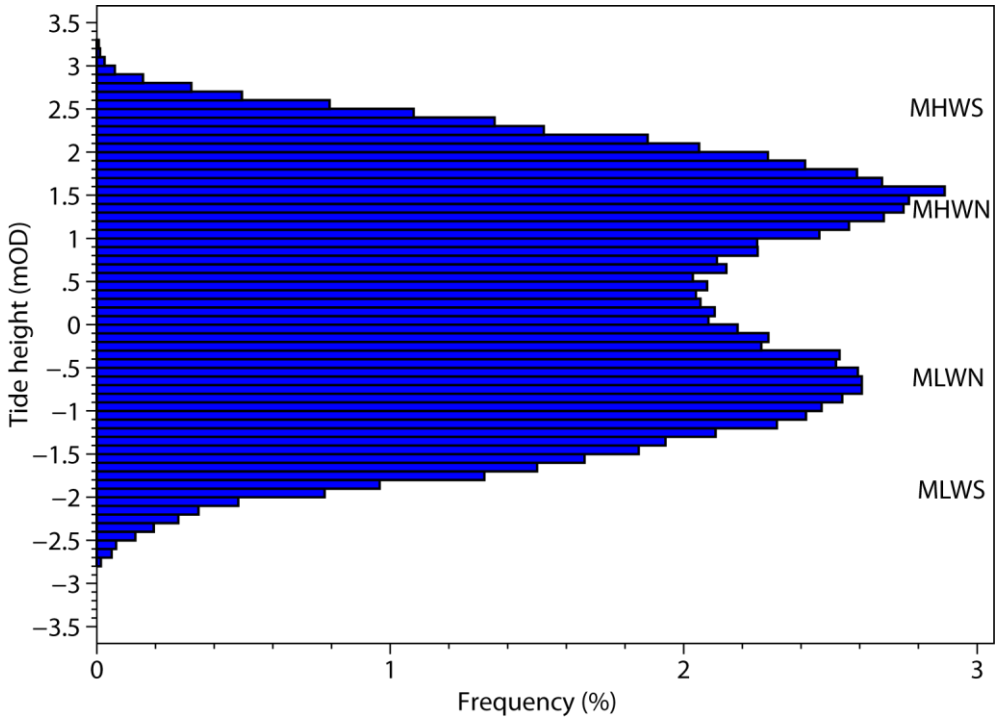

Figure 2.6: Tidal inundation model for Boulby, North Yorkshire. MHWS = mean high water spring, MHWN = mean high water neap, MLWN = mean low water neap, MLWS = mean low water spring. The water level remains still for the longest periods around neap high and low tide levels, whereas the maximum rate of water level change occurs around mid-tide level which results in the trough of low frequencies of this tidal duration even though the water level passes this point in all stages of the tidal cycle. The maximum wave energy delivery is believed to occur at the high and low tidal peaks and the lowest at the mid-tide level (Carr and Graff, 1982). The amount of time the still water level spends at MHWN and MLWN tide levels is greatest because they are occupied at some point throughout all stages of the tidal cycle whereas more extreme levels are either exposed or submerged for longer periods of time than neap tide levels.

2.4.1.2 Monitoring / modelling wave conditions across the foreshore

Wave characteristics change as waves enter increasingly shallow water at the coast, under which conditions the orbital motions of water within the wave start to interact with the seafloor. This occurs when the water depth is <= 0.5 of the wave length (Davidson-Arnott, 2010). As the orbital motions become increasingly elliptical, driven by bottom friction from the seabed, the free water surface generates waves, which steepen resulting from height increases and decreases in length. During this transformation the velocity at the front of the wave crest increases until it exceeds the wave velocity itself and the elliptical orbital motion can no longer be completed, resulting in the breaking of the wave (Davidson-Arnott, 2010). This

transformation of waves within shallow water is termed 'shoaling'. These effects are further complicated by coastline morphology and bathymetry, diffracting and refracting waves, changing the incidence angle relative to the coast (Davidson-Arnott, 2010). There has been a large body of theoretical work developing equations to explain wave transformations (see: Komar (1998) and Davidson-Arnott (2010) for discussions of wave theory) and numerical models produced (e.g. Battjes and Stive, 1985; O'Reilly and Guza, 1993; van der Westhuysen, 2010). Water depth is the key control of the character of wave transformation, and is determined by controls on water level, including tides, wave and weather conditions, overlain on topographic controls, such as coastal geometry and foreshore and offshore bathymetry (Komar, 1998). Energy is transferred within waves as potential energy within the elevated wave crest, and as kinetic energy within the orbital motions of the water. When waves break, the potential energy within the crest is converted to kinetic energy or into the incorporation of bubbles into the water, and then is transferred to the surrounding water, forming turbulent surf conditions. Energy can also be transferred to the seabed resulting from bottom friction.

Waves can reform within the surf zone, however in general wave heights decrease, and therefore wave energy decreases (as wave energy is proportional to the square of wave height), with decreasing water depth towards the shoreline. The transfer of wave energy to the seabed via friction continues throughout the surf and swash zones, resulting in reduced amounts of energy carried within waves nearer to the cliff. The net amount of energy delivered by the sea to a cliff is similarly determined by these local characteristics. Trenhaile (2000) highlighted that, although wave equations have been widely applied to sediment transport and beach evolution models there has been a lack of application to rocky coasts. Since then a number of studies have used physics based wave equations to quantify energy delivery to rocky coasts (e.g. Stephenson and Kirk, 2000a; Trenhaile, 2000; Trenhaile and Kanyaya, 2007).

Stephenson and Kirk (2000a) set out to quantify the roles of wave processes on the erosion and development of foreshore platforms at Kaikoura, New Zealand, to determine whether waves were actually breaking on a platform and whether sufficient wave energy was transferred onto the platform and to the cliff to explain the cliff retreat and platform development. They monitored wave conditions across the platform using pressure transducers, to establish the location where waves break, and to derive the transfer of deep-water wave power that reaches the platform. They also calculated the shear stresses at the wave base acting on the platform, and the dynamic force of the waves resulting upon the cliff. These calculations were used to establish if wave energy exceeds the resisting force of the rock, and therefore would result in erosion. Stephenson and Kirk (2000a) concluded that at Kaikoura, the water depth seaward of

the platform caused waves to break before they reached the platform, leaving insufficient wave energy onto or across the platform to result in erosion of the foreshore or cliff.

Trenhaile and Kanyaya (2007) set out to explore the effects of tide and foreshore gradients on the wave characteristics across foreshore platforms and the resulting ability of waves to erode the platforms. They measured tide and wave heights across two platforms with different tidal ranges and foreshore gradients using poles cemented into the platform. Video was used to record sea heights at each pole throughout the tidal cycle. Tide height, mean water depth, wave height and period were calculated from the video footage. These were used to calculate breaking wave heights and locations and the resulting wave power available for erosion. A theoretical consideration of impact pressures was undertaken to assess whether pressures were sufficient to mobilise blocks of rock on the foreshore. Trenhaile and Kanyaya (2007) found that the gradient and morphology of foreshore platforms combined with the tidal range determine whether waves have enough energy to erode the platform and cliff rocks.

Using measured sea-state characteristics and wave theory, both of these studies demonstrate that the physical conditions of tidal range, foreshore width, gradient and topography are key in determining the amount of wave energy delivery to the cliffs at a rocky coast. Although both studies were focussed on the implications to the foreshore, they demonstrate the influence of the foreshore in either dissipating or transforming wave energy before reaching the cliff. Clearly there arises a need to integrate wave transformations over foreshores into cliff studies to estimate wave conditions at the cliff. Neither of these studies monitored change of the foreshore, so were unable to test whether their conclusions about the energy available for erosion were reflected in observable erosion.

2.4.1.3 Monitoring cliff top microseismic ground motions

Ocean waves generate a significant amount of low-frequency seismic motion, termed microseisms, which can be observed both at terrestrial seismometers, and in ocean bottom seismic monitoring stations (Webb, 1998). Ocean waves are the most significant source of seismic ‘noise’ at both station types (Webb, 1998). Microseismic ground motions generated in this manner have been shown to be a valuable resource to both oceanographers and coastal geomorphologists. Microseisms are generated by energy transfer via pressure variations resulting from ocean waves passing over the seabed, widely acknowledged to lie within the frequency band of 1 - 0.05 Hz. Further, microseisms are divided into ‘primary’ and ‘double-frequency’ signals. Primary microseisms are generated when the orbital water particle motions

beneath ocean waves come into contact with the seabed once they enter shallow water, classed as when the water depth is half the wavelength. In this instance, the pressure perturbations associated with the orbital motions create microseismic waves at the seabed of the same frequency and amplitude of the ocean wave (Hedlin and Orcutt, 1989; Friedrich et al., 1998; Bromirski, 2001). Double-frequency (DF) microseisms are generated when waves of the same wavelength travelling from opposite directions meet and superimpose, producing pressure fluctuations that do not attenuate with depth, and so propagate to the seafloor where resonance creates microseismic waves (Longuet-Higgins, 1950). Because the opposing waves have the same wavelength, the frequency of the resulting microseisms is double that of the ocean waves that generated them. The amplitude of the microseism is the square of the ocean wave amplitude (Longuet-Higgins, 1950). Consequently, DF microseisms have larger amplitudes than primary microseisms. Waves travelling from different directions, generating DF microseisms, can be generated either by storm waves heading in different directions, or by the collision of landward waves with those reflected from the coast (Longuet-Higgins, 1950).

Microseismic signals generated by ocean waves have been shown to be representative of wave energy monitored at the coast (Adams et al., 2002; Adams et al., 2005; Young et al., 2011b). Adams et al. (2002) used cliff top monitoring of microseismic ground motions as a proxy for net energy delivered to the coast from the sea. Adams et al. (2002) observed that the occurrence of high tides and deep-water waves resulted in increased ground motion and therefore energy delivery to the coast (Figure 2.7). They tested this observation using larger-scale bathymetry and offshore deep water wave data to calculate incoming wave energy. They identified the energy received at the cliff was heavily affected by shoaling, refraction and frictional energy dissipation over the foreshore, and that therefore tide height was a key influencing factor to energy delivery.

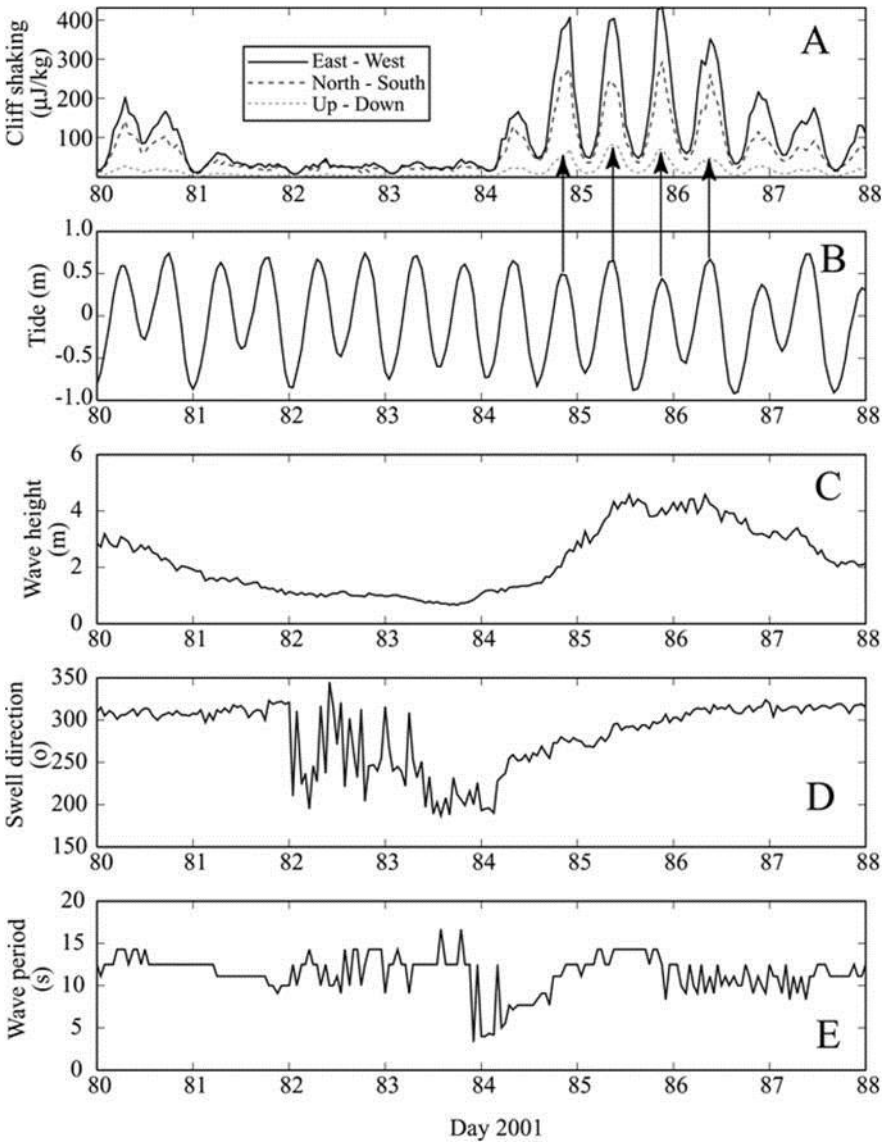

Figure 2.7: Eight-day record of wave conditions and cliff shaking from March 2001. A: Microseismic shaking at cliff edge (three components of ground motion). B: Tidal elevation. C: Offshore significant wave height. D: Swell direction. E: Wave period. Horizontal shaking is considerably stronger than vertical. Note strong correspondence between times of high shaking and times of high tide (shown with arrows) over interval of large wave heights. From: Adams et al. (2002).

Adams et al. (2005) developed the findings of Adams et al. (2002), and used this approach to examine the response of the sea cliff itself to the nearshore wave climate. They focussed on the cliff response to concurrent marine conditions monitored using offshore wave buoy and nearby tide gauge data. Comparing ground motion with marine conditions, Adams et al. (2005) confirmed that increased ground motion velocity and displacement coincides with high tide events with larger waves. The results showed that the dominant direction of cliff motion corresponds to that of the incoming waves, representing wave loading of the foreshore and the

cliff face. Spectral analysis of the data demonstrated that the power spectrum of high tides, regardless of wave height, corresponds well to that of the ground motion, and that the dominant periodicity of cliff motion matches that of nearshore waves. However, during low tides Adams et al. (2005) observed poor links between ground motion and nearshore wave period. The data showed strong relationships between ground motion and tidal height, with greatest cliff motion occurring at tide heights above mean sea level, where waves approached the base of the cliff (Adams et al., 2005). Different frequencies of ground motions linked to various wave conditions at the cliff during high tides were observed, both at the period of incoming waves, and also evident in a high-frequency shaking in response to direct wave impacts at the cliff toe.

Adams et al. (2005) considered the implications of the cyclical loading of the cliff by tides and waves, to cliff material strength, producing a model of progressive stress and strain development. By placing seismometers in a line orthogonal to the cliff edge, Adams et al. (2005) used the difference in displacement monitored between the instruments to estimate the shear strain generated through the cliff over a specified number of loading cycles. They proposed that fatigue of the cliff rock occurs due to micro-fracturing resulting from this cyclical loading, and that this reduces rock strength making the cliff face more vulnerable to erosive processes (Figure 2.8). The model considers a rock parcel within the cliff rock mass. Whilst initially not directly influenced by wave impacts, as the cliff erodes and retreats and the rock parcel is effectively moved closer to the cliff face, the displacement the rock parcel experiences increases, resulting in an increase in the degree of micro-fracturing and corresponding degradation of rock strength. Once the rock parcel is exposed directly to wave impacts, the strength is sufficiently degraded that the rock parcel is more rapidly eroded by the wave erosive processes (Figure 2.8). Direct evidence for this process is however lacking.

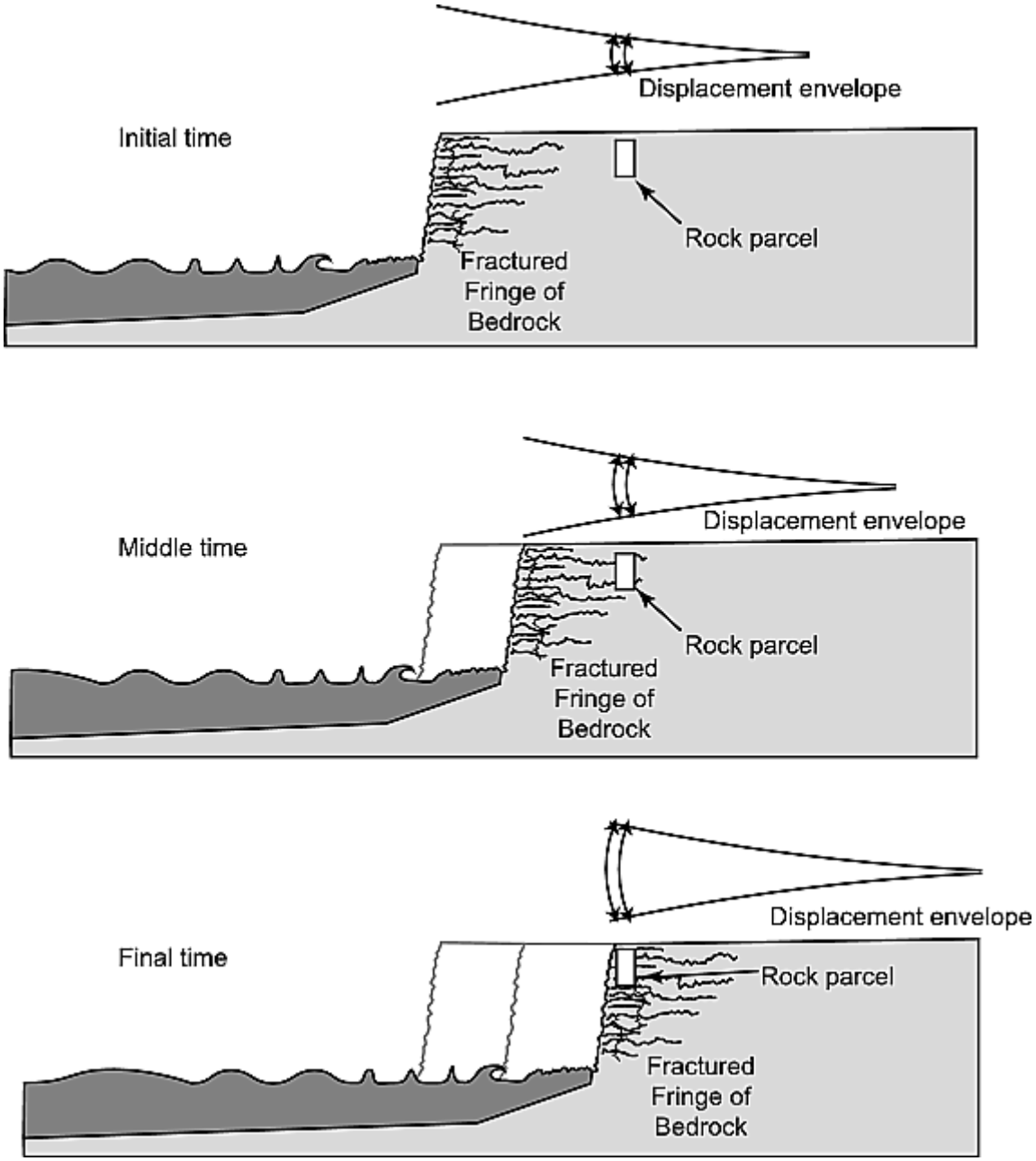

Figure 2.8: Schematic illustrating Adams et al.'s (2005) conceptual model for the displacement and strain history witnessed by a parcel of bedrock within the marine terrace. As sea cliff retreat brings the cliff face progressively closer to the tracked rock parcel, the parcel experiences greater displacements and greater strain until finally becoming exposed to direct wave attack and block removal from the cliff face. From: Adams et al. (2005).

Young et al. (2011b) compared cliff top and inland (10 km from coast) microseismic ground motions with monitored water levels at the cliff toe. In addition to the high-frequency shaking caused by wave impacts at the cliff toe, and swaying of the cliff at frequencies of ocean gravity waves observed by Adams et al. (2005), Young et al. (2011b) identified longer period motions (0.006 – 0.05 Hz) at ocean infragravity wave periods. During high tides Young et al. (2011b)

found the cliff top gravity and infragravity wave ground motions to be more powerful than at the inland seismometer, yet during low tides the difference in spectral power of these two frequencies between the two seismometer locations decreased, notably at the gravity wave periods, suggested to indicate these ground motions were determined by intertidal zone wave conditions. However spectral power levels of the double-frequency microseism ground motions were similar at both seismometers during high and low tides, indicating these ground motions to be generated by distal wave conditions. Via their ability to represent local and distal wave conditions, cliff top microseismic ground motions may provide a valuable tool in measuring environmental forces acting on coastal cliffs.

Lim et al. (2011), based upon the work of Adams et al. (2002) and Adams et al. (2005), explored the number and rate of seismic impacts recorded at a cliff top geophone and examined the relationship with monitored tide heights, wind velocity and rockfall activity, monitored using TLS. 'Seismic impacts' were defined by the count of occurrences that the geophone recorded a shaking value in excess of an arbitrary threshold, per 15 minute period. Lim et al. (2011) identified peaks in number of impact events associated with the tide reaching the level of the toe of the cliff, high-tides and onshore wind speeds. The results of Adams et al. (2002), Adams et al. (2005), Lim et al. (2011) and Young et al. (2011b), suggest that microseismic data collected at coastal cliffs has the potential to generate a useful proxy for environmental conditions at coastal cliffs. Lim et al. (2011) identified no correlation between the monthly total number of seismic events and resultant rockfall volume, however were successful in identifying a positive correlation between monthly number of seismic impacts and the rockfall occurring in the following month. This potentially indicates a lagged effect, between wave energy delivery and rockfall occurrence, although the authors highlighted that this may be a feature of the monitoring interval used. Combining monitoring of microseismic ground motions with TLS monitoring of coastal cliffs enables the quantification of cliff erosion and also a relative measure of marine, and potentially subaerial forcing at the cliff. Constant monitoring using broadband seismometers, as used by Adams et al. (2005) and Young et al. (2011b), may enable improved understanding of links between microseismic ground motions and rockfalls, particularly if individual cliff ground motion signals can be associated with different forcing mechanisms.

2.4.2 Subaerial controls on rock cliff erosion

The emphasis of coastal cliff research upon marine processes of cliff erosion can be demonstrated by the paucity of studies quantifying subaerial controls on cliff erosion. The

difficulties of accessing and instrumenting the coast has meant that studies examining subaerial controls of rocky coast erosion have focussed largely on foreshores. Micro-erosion meters (MEMs) and traversing MEMs (TMEMs) have been important tools in exploring subaerial erosion of foreshores, as they enable millimetre-scale measurements of surface downwearing; scales appropriate to weathering of rock surfaces (Stephenson et al., 2010). Such studies rarely extend up-cliff. A number of studies using MEMs have identified varying rates of erosion across foreshores, attributed to varying exposure to different processes (e.g. Stephenson and Kirk, 1998; Inkpen et al., 2010; Stephenson et al., 2010). Stephenson and Kirk (2000b) developed from their study of marine erosion of Kaikoura Peninsula, NZ, discussed in Section 2.4.1.2 above, to explore the role of subaerial conditions on foreshore erosion. Using a MEM the authors focussed on weathering associated with alternating wetting and drying of the foreshore during the tidal cycle, and found that the area of the foreshore that experienced the greatest number of cycles of wetting and drying, (calculated from tidal cycles, rainfall occurring during low tides, and algae coverage which prevented drying), also experienced the highest erosion rates. Field monitoring and laboratory tests using MEMs to monitor erosion rates of foreshore rocks across the foreshore intertidal range by Porter et al. (2010) identified that the highest rate of erosion occurred between the neap high and low tides, notably the period during which the greatest variability in wetting and drying occurs. These results are anticipated to be applicable to cliff rock surfaces, both at the inundated toe and above.

Studies examining subaerial controls of rock slope erosion have largely been focussed on non-coastal settings. Studies typically take two different approaches: Focus on a specific set of processes, such as frost weathering, and instrument a rock face to specifically monitor these variables directly at the rock face, such as rock temperature or moisture fluctuations (e.g. Anderson, 1998; Sass, 2005; Krautblatter et al., 2010; Gunzburger and Merrien-Soukathchoff, 2011). Some studies that take this approach attempt to simultaneously monitor rock response, such as via crack growth (e.g. Matsuoka, 2008). Alternatively studies adopt a broader scale approach, and collect rockfall inventories and regional-scale data of environmental conditions, such as rainfall or air temperature, to identify triggering thresholds and relate this to the occurrence or rate of rockfall (e.g. Wieczorek and Jager, 1996; Fraysinnes and Hantz, 2006; Krautblatter and Moser, 2009). Results of studies monitoring micro-climate combined with change of the rock surface, have identified mass wasting in response to local-scale subaerial conditions (e.g. Matsuoka et al., 1996; Matsuoka, 2008).

Two recent coastal cliff studies have developed innovative cliff face monitoring approaches to better constrain cliff face subaerial conditions, which are known to drive erosive processes.

Lim et al. (2010b) set out to explore coastal cliff face micro-climate and to make comparisons with regional-scale weather data that had previously shown only poor correlations with rockfall. In doing so, the value of regional datasets in representing local cliff face conditions was assessed. Moreover, the distribution of instruments up the cliff profile was used to attempt to examine the variability in micro-climate up the cliff face. The authors installed sensors to monitor rock moisture and temperature in different rock types in the cliffs at Boulby, in addition to cliff top and cliff face weather stations. Results show significant differences between the cliff top and cliff face conditions, as a result of cliff geometry. The cliff face experiences sheltering from solar radiation, as the north-east facing cliffs experience much less direct sun exposure, and also sheltering from the prevailing south-west wind and rain. However, the wind and rain that the cliff does experience is generally more intense, most likely caused by focussing of onshore winds against the rock face. In addition, the temperature of the three rock types assessed varied, due in part to slope angle and exposure to winds. Additionally, evidence of the combined effects of the multiple variables was apparent, including accelerated drying of the rock face during periods of irradiance. The results demonstrate a high variability in conditions up the cliff profile, due to the characteristic morphology of each of the different cliff layers, combined with their relative position up the cliff. Perhaps more importantly, the results demonstrate the cliff micro-climate to vary significantly from that recorded at the cliff top. By implication the local conditions at the cliff face vary in comparison to regional-scale weather datasets, commonly used in analysis of controls on cliff erosion. This observation may help to explain the relatively poor correlations between regional-scale weather conditions and rockfalls monitored from the site found by previous studies (e.g. Rosser et al., 2007; Lim et al., 2010a). The findings of Lim et al.'s (2010b) study demonstrate the necessity for obtaining measures of environmental conditions locally, ideally at the cliff face itself.

As discussed, correlations between subaerial conditions and rockfall from hard rock cliffs have not been successful. This either arises from differences in the temporal resolution of the datasets used in the analysis, the different locations or scale of the dataset, or ultimately a lack of a direct cause and effect between environmental conditions and erosion. On soft rock coasts, stronger relationships have been found between intense rainfall events and cliff failures, attributed to direct increases in pore pressures, generating a more rapid response to current environmental conditions (e.g. Dupperet et al., 2002; Collins and Sitar, 2008). The temporal scale at which cliff erosion and environmental conditions are monitored and the duration over which data is collected is commonly insufficient to fully capture the cliff response to changing conditions (Bernatchez et al., 2011). Bernatchez et al. (2011) used the thermal regime of rock sub-surface temperatures and air temperatures to examine cliff erosion response to

temperatures ranging between -35 to 30^{o} C, on the Canadian east coast. Bernatchez et al. (2011) tested three systems for monitoring cliff rock temperature, combined with erosion pins and a weather station. The authors recorded rock temperature at 30-minute intervals, and at regular depth intervals within the cliff rock mass in addition to at the cliff surface. Bernatchez et al. (2011) then used the gradient of rock temperature throughout the length of the erosion pins compared to the air temperature measured at the weather station to identify when failure events occurred and to what depth failure reached. This demonstrated that when the temperature recorded matched the air temperature, it was evident that this section of the erosion pin was exposed at the cliff face. The authors found that mild winter temperatures and solar radiation were key controls on the observed rate of erosion due to the reduction in ice cover on the surface. In addition, the melting of ice within the rock during spring accounted for over 70% of the observed retreat and was found to be a much more significant control on erosion compared to frost shattering.

2.4.3 Material controls on coastal cliff erosion

Coastal cliff failure mechanisms are largely controlled by the material properties of the cliff, including: rock structure and strength, and the interactions with environmental conditions both externally upon the cliff face, and internally within the rock mass (Rosser et al., 2007). Rock slope behaviour is widely acknowledged to be a function of intact rock strength, weathering, discontinuities, and also the movement of water in and around the rock material (Hoek and Bray, 1977; Selby, 1993). These parameters are commonly used as proxies for the resistance of the cliff material to environmental forcing, whilst defining the failure types that may occur (Sunamura, 2005). Combined with the nature of environmental forcing acting on the cliff, rock characteristics therefore control the magnitude and frequency of cliff failure behaviour. The stratigraphy of various rock types which compose a cliff profile is also important to determining net cliff change behaviour, and its response to the varying environmental conditions and processes up the profile.

As shown in Equation 2.1, the rate of cliff erosion can be considered as the relative resisting force of cliff rock, as compared to the assailing force of waves acting at the cliff toe (Sunamura, 1977). Different measures of rock strength have been tested to explore the parameter that best represents rock resistance to erosion, including tensile, shear and penetration strength. Compressive strength has been generally adopted as a good representative and comparable measure of intact strength, and with established field testing techniques (Sunamura, 2005).

Coastal cliff studies examining rock strength often tend to use intact rock compressive strength tests at the cliff toe, combined with broadly qualitative observations of discontinuity characteristics at the cliff surface (e.g. Budetta et al., 2000; Dickson et al., 2004; Andriani and Walsh, 2007). Rock mass classifications, such as that proposed by Selby (1980), are also often used in rocky coast geomorphology to assess rock material properties, enabling a semi-quantitative measure for comparison of the relative strengths and erosion rates of cliffs along a stretch of coastline (e.g. Budetta et al., 2000; Andriani and Walsh, 2007). The presence and characteristics of discontinuities at the cliff face exposed to waves, has a significant influence over the effectiveness of hydraulic wave erosion, as the presence of cracks and joints at the surface enable highly effective processes of air compression, shock pressure, water hammer, which via the generation of shear stress, tension or compression promote the removal of cliff material (Sunamura, 1992). In softer cliff rocks the interaction between groundwater and cliff materials is a determinant of the rate of cliff erosion (Collins and Sitar, 2008). Dupperet et al. (2002) observed combined structural and groundwater conditions to trigger a large failure from chalk cliffs in Normandy, France. Using 2D semi-probabilistic modelling they demonstrated that the infiltration resulting from previous heavy rainfall penetrated through fractures within the chalk rock mass, and accumulated, increasing pore pressures and generating localised stresses, eventually resulting in tensile and shear failure of the cliff.

In addition to the physical removal of material, marine and weathering processes acting on cliff rocks can cause a progressive deterioration of the rock surface, resulting in a decrease of bulk rock mass strength (Sunamura, 1992). In their examination of subaerial weathering controls of erosion of limestone and mudstone foreshores at Kaikoura Peninsula, NZ, Stephenson and Kirk (2000b) found in areas observed to have experienced weathering driven by wetting and drying the intact compressive rock strength to have decreased by up to 50%. Dupperet et al. (2005) undertook a series of laboratory experiments on samples of chalk from the Normandy coast, France, to examine the effects of water saturation, wetting and drying and salt crystallisation on the rock strength. The authors found a decrease in unconfined compressive strength of 40 – 50% for water saturation variation of only 10 - 17%. In addition, they observed wetting, drying, and salt weathering to result in micro-cracking and salt crystal build-up observed under the microscope, which resulted in decreased rock strength. Salt crystallisation within the chalk samples taken from the spray zone of the cliff face – notably above the elevation of inundation during high tides - was found to produce the greatest decrease in rock strength, ranging between 52 – 70%. Dupperet et al. (2005) witnessed significant variations in the level of strength degradation, determined by varying exposure to the different processes, including for

example the sample position in the cliff profile relative to inundation. Laboratory results corresponded well to those of the in-situ observations in the field.

Repeated wave impacts at the cliff face have been suggested to generate fatigue in the cliff rock mass, as repeated stress generation causes fracturing to occur at lower stresses than normal (Sunamura, 1992). The application of microseismic monitoring to coastal cliffs has demonstrated that in addition to the loading by direct wave impacts, wave movements across the foreshore produce a downward and seaward motion of the cliff (Adams et al., 2005; Young et al., 2011b). This cyclical loading of the foreshore and cliff by waves during high tides has significant potential to develop micro-cracking and strain accumulation within the cliff rock mass, leaving the cliff rock more susceptible to removal by wave erosion processes at the cliff face (Adams et al., 2005) (see Figure 2.8).

The irreversible strain accumulation and strength reduction of the cliff rock mass via dynamic loading increases vulnerability to failure, and therefore acts as a preparatory effect on the cliff face. Krautblatter and Dikau (2007) produced conceptual models of both the preparatory factors that degrade rock strength (which they refer to as backweathering) (Equation 2.2), and triggers of rockfalls (Equation 2.3).

Equation 2.2: $$r_{bw} = f(p, w, t) = f(to, g, h, c, b, t)$$

(Krautblatter and Dikau, 2007)

Where:

r_{bw} = rate of rock face backweathering

p = pre-weathering rock disintegration

w = weathering rock disintegration

t = time

to = topographic conditions

g = geological/geotechnical conditions

h = hydrological conditions

c = climatic conditions

b = biological conditions

Equation 2.3: $r_{rs} = f(e, i, t)$

(Krautblatter and Dikau, 2007)

Where:

r_{rs} = rockfalls

e = external drivers

i = internal drivers

t = time

These models demonstrate the numerous environmental and material controls of cliff erosion. However the vague terms used within the models mask the complexity of the variables that alter rock strength and control erosion, and the interactions between variables. These complexities make testing the direct effect of each of these sets of variables on cliff rock strength and erosion highly difficult. The preparatory model (Equation 2.2) does not consider dynamic loading from marine forcing as it was developed for inland mountain environments. However for coastal cliffs, the results of Adams et al. (2005), Lim et al. (2011) and Young et al. (2011b) indicate that marine dynamic loading should be a consideration of future studies of cliff erosion. Currently within coastal cliff studies there has been no further consideration of the dynamic loading effects identified by these initial microseismic studies, beyond that proposed by Adams et al. (2005) (Section 2.4.1.3).

Subaerial and marine processes trigger cliff failure via increased stress and strain within the rock mass. At some point a critical strain threshold is exceeded, causing failure (Rosser et al., 2007). In material where the rock strength is already degraded / is being degraded due to the factors in Equation 2.2 above, producing potentially highly fractured or weathered rock, environmental events can trigger failures by destruction of the rock bridges that connect blocks within the fractured zone to the rock mass, which can be determined by either the frequency or magnitude of the environmental forcing (Krautblatter and Dikau, 2007). Krautblatter and Dikau (2007) make the distinction between preparatory and triggering controls of rock mass failure, distinguished by the two equations, and they emphasise that the two do not often occur together.

As demonstrated by Equations 2.2 and 2.3, material characteristics also have preparatory and trigger controls of rockfalls. During brittle failure, once strain within a body of rock exceeds a critical threshold, strain accumulation accelerates and gradually a rupture is created, along which failure occurs (Main, 2000; Petley et al., 2005). This is controlled not by environmental influences but by the structural changes within the rock (Rosser et al., 2007), although the exact mechanisms are however uncertain with many models having been suggested (Main, 2000; Eberhardt et al., 2004; Amitrano, 2006). The progressive failure model has been used to explain non-coastal rockfalls and landslides (e.g. Eberhardt et al., 2004; Petley, 2004; Petley et al., 2005). And has also been used to explain observed coastal cliff failures (e.g. Amitrano et al., 2005; Rosser et al., 2007 and Senfaute et al., 2009). Rosser et al. (2007) observed patterns of precursory rockfall activity leading up to large failures and produced a qualitative model to explain this behaviour (Figure 2.9).

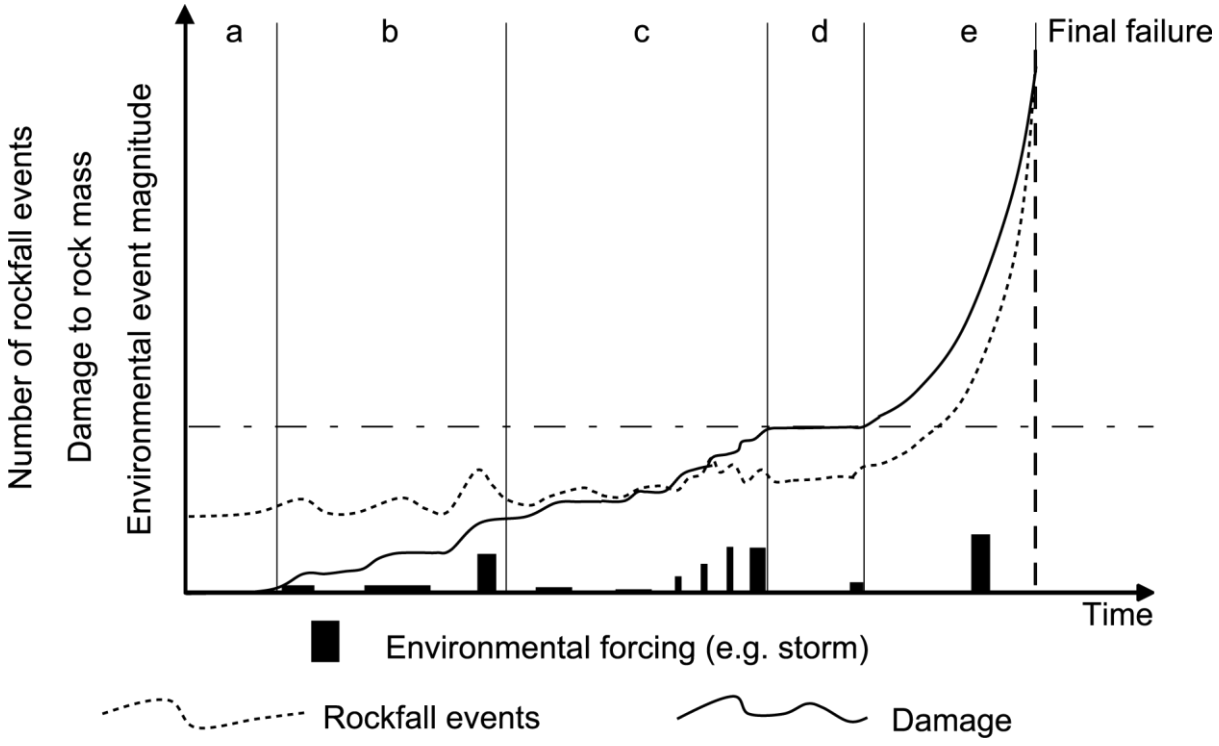

Figure 2.9: Schematic model of the development of a large slope failure, via a process of shedding of surficial material through rockfall and the accumulation of damage to the rock mass. From: Rosser et al. (2007).

a) Low levels of surface material detachment occur due to weathering and other relatively gentle environmental forcing;

b) Larger environmental events e.g. storms, result in increased rockfall activity, although most rockfalls are small, results in stress re-distribution and micro-fracturing within the rock;
c) Continued relatively quiet periods of background levels of failure are occasionally interspersed with larger environmental events and corresponding magnitude failures, producing further build-up of strain towards a critical threshold;
d) The rock strain may lie very close to the critical strain threshold without failure occurring if environmental conditions are quiet;
e) Once the critical strain threshold is exceeded, material controls determine failure timing and strain accumulates hyperbolically until the final failure.

Topography can have a preparatory effect on cliff materials, for example the removal of underlying material results in re-distribution of stresses and strain and eventual failure of surrounding material (Krautblatter and Dikau, 2007). Stock et al. (2012) attributed a sequence of rockfalls from the Rhombus Wall in Yosemite, California, to patterns of stress re-distribution and resulting crack propagation following an initial small failure. As cracks propagated from the initial failure area a series of larger rockfalls followed (740 m^3 over a few hours). Stock et al. (2012) observed continued progressive crack development in the zone of the previous failures, eventually resulting in a series of failures propagating out from this zone, as critical strain thresholds were exceeded, occurring over a number of weeks and months. This is potentially an important effect in coastal cliffs if higher rates of erosion occur at the cliff toe driven by waves than of the overlying material.

2.5 Summary

It is evident from this study that there are numerous environmental and material controls of cliff erosion, and that these controls can degrade cliff rock strength and therefore prepare the rock for failure, in addition to triggering failures.

Terrestrial laser scanning (TLS) and LiDAR enable high resolution monitoring and their application to coastal cliffs has improved understanding of cliff erosion in various materials. Observations of cliff behaviour from recent studies demonstrate the complexity of coastal cliff failure mechanisms. Cliff microseismic ground motions have been found to represent local wave conditions and hold significant potential to quantify environmental forces acting on a cliff. This study will explore the environmental controls of observed cliff erosion by combining monitoring

of erosion using TLS with monitoring of cliff top microseismics and exploring the relationships between the datasets.

Sunamura (2005) states that cliff rock resistance to erosion is time independent, however the continuous, cyclical loading of coasts by waves (both as impacts at the cliff face and from waves across the foreshore) in addition to weathering, indicates that rock resistance is in fact time dependent, with rock resistance dependent on time of exposure to environmental forces and material brittle failure characteristics.

By monitoring cliff erosion and concurrent environmental conditions and identifying relationships between them, in addition to laboratory experiments of rock strength and failure characteristics during varying environmental forcing, improvements in understanding of coastal cliff failure mechanisms can be made.

A number of specific questions have arisen from the above discussion regarding suitable approaches to monitoring marine and subaerial forcing at coastal cliffs and the environmental controls of hard rock cliff erosion:

- Do regional-scale environmental datasets accurately represent conditions at the cliff?
- If not, then what are the marine and atmospheric conditions at the coast relevant to cliff erosion?
- How can we more accurately measure or estimate these in harsh and inaccessible cliff environments?
- Can we use microseismics as proxies for a wide range of forces, including non-marine sources, acting on the cliff, and, can we find relationships between observed conditions and cliff erosion?
- Do current models of controls of coastal cliff erosion, such as those based upon Sunamura's cliff toe erosion model or the tidal inundation duration model accurately represent the controls on cliff erosion?
- What effect does dynamic loading of foreshores and cliffs by tides and waves have on rock mass strength and cliff erosion?
- And can this dynamic loading effect trigger rockfalls directly?

Chapter 3: Approaches and field site used to explore erosion, marine and atmospheric forcing at a coastal cliff

In order to improve understanding of the environmental controls of coastal cliff behaviour, both the nature of cliff change and environmental forces acting on a cliff need to be monitored. As discussed in Chapter 2 there have been various approaches to both of these, yet to date there is a lack of detailed, high resolution datasets to test our assumptions of how rocky coasts erode. Terrestrial laser scanning (TLS) has been demonstrated to be capable of capturing high-resolution, accurate 3D representation of coastal cliff faces which, when collected repeatedly over time, can provide an invaluable measurement of cliff change activity across the whole cliff face (Rosser et al., 2007; Collins and Sitar, 2008; Lim et al., 2010a). Microseismic ground motions have been shown to reflect tide and wave activity at the base of coastal cliffs (Adams et al., 2002; Adams et al., 2005), within shallow coastal waters, and beyond (Haubrich et al., 1963; Hedlin and Orcutt, 1989). Such data hold significant potential to explore and provide a relative measure of environmental forces and processes acting on coastal cliffs.

This chapter describes the methods and field site at Boulby on the North Yorkshire coast, used in this study to address the gaps in understanding identified in Chapter 2 and to achieve the research aims and objectives set-out in Chapter 1. Cliff microseismic ground motions were monitored, using an array of cliff top seismometers, to be used as proxies for environmental forcing at the cliff. This was combined with monitoring of cliff face erosion using TLS. This chapter describes the instruments and field set-ups, the data collection and processing techniques, analysis techniques and data quality.

The monitoring period of this study extends over two years from July 2008 to July 2010, over which time rockfall activity and microseismic ground motions have been monitored at the cliff at Boulby. Datasets of wave, tide and wind conditions during the monitoring period have been obtained from the respective national data archives. These datasets have been used to identify the environmental conditions generating recorded microseismic ground motions, and to test how well regional-scale environmental datasets represent conditions at the cliff when compared to the microseismic data. The usefulness of both datasets in exploring relationships between environmental conditions and cliff change behaviour is examined in later chapters.

3.1 Cliff top microseismic ground motions

3.1.1 Data collection approach

The marine generated ground motions observed by previous studies have been shown to cover a wide frequency band, from ocean wave periods of seconds, to high frequency shaking due to wave impacts (Hedlin and Orcutt, 1989; Adams et al., 2002; Adams et al., 2005). In addition, longer period infragravity waves of periods > 20 s have been shown to be important sources of energy within surf and swash zones (Guza and Thornton, 1982; Holman and Sallenger, 1985). To cover this range, broadband seismometers have been used here. The instruments used were Guralp 6TD velocity seismometers provided on loan by SEIS-UK, the NERC seismic equipment pool. The 6TDs have a frequency response of 30 s to 100 Hz and have three masses (components), so can measure vertical ground motions (Z), and horizontal ground motions in two directions, i.e. north-south (N) and east-west (E). The 6TDs were chosen above other broadband seismometers because they are robust (able to function in temperatures of -20 to 85^{o} C); self-contained, with the instrument containing sensor, digitiser and 3 GB of data storage; small (height 240 mm, diameter 150 mm); lightweight (2.7 kg) (SEIS-UK, 2005) and relatively quick and easy to deploy, as they can be placed in a shallow hole in the ground and do not require a solid rock base. Data downloads are done at the ground surface such that the seismometers are not disturbed.

3.1.2 Field set-up

As the 6TDs can sample at rates of 1 - 200 samples per second (sps), initially a sample rate of 200 sps was used. However this meant downloads were required every 2 - 3 weeks and that the data files were so large (1.8 MB per hour per component) that it hindered trials of data processing in the software packages that were being used (Matlab and Stata). After seven months the sample rate was reduced to 100 sps (100 Hz), which with a nyquist frequency of 50 Hz, meant that the high frequency signals generated by wave impacts, identified by Adams et al. (2005) to be around 20 Hz, were still within range. This change in sampling frequency did not result in a decrease in data quality. At 100 sps the data had to be downloaded approximately every six weeks. Data from the instruments was downloaded to an external hard drive using a hand-held computer, which was used for all communications with the seismometers, without disturbing the instrument installation. At each download the cables were all checked for rodent or weather damage, and the masses and GPS were checked to be working.

Five 6TDs were used and placed in the glacial till on the cliff top in a line normal to the cliff edge (Figure 3.1). This array was used to examine the ground motion decay with distance from the cliff edge, previously observed in different cliff materials by Adams et al. (2005). Each seismometer was set-up in an identical manner, and required a 0.8 m deep hole with a diameter of c.0.3 m, lined with a basal layer of sharp sand approximately 0.05 m deep. The seismometers were aligned to the north and placed within a large plastic bag to keep them clean. Each seismometer was powered by a 12 volt car battery connected to 2 x 20 watt solar panels. On the ground surface each seismometer was accompanied by a large weatherproof box which contained all cables, the battery and had the GPS antenna attached (Figure 3.1). The GPS was used to record time. The two cables from each seismometer were fed up through the ground and into the box once the seismometers were buried (Figure 3.2). These consisted of a cable to connect via USB to an external hard drive when downloading the data, and a cable to a 'breakout' junction box that was used to connect power, GPS and hand-held computer to the seismometer (Figure 3.2). When data wasn't being downloaded both the connectors for the computer and hard drive were capped to prevent water damage.

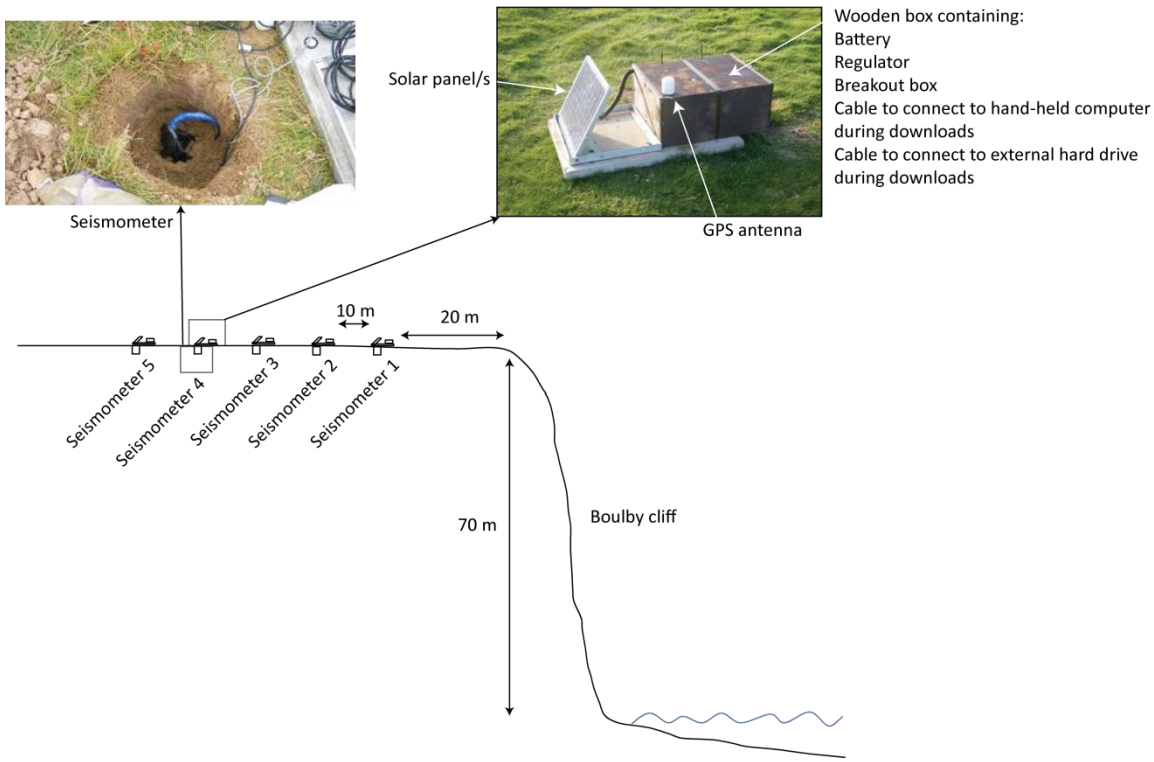

Figure 3.1: Profile of Boulby cliff with locations of the five cliff top seismometers. Each seismometer is buried in a hole approximately 0.8 m deep in glacial till and is accompanied by power sources and communications stored at the ground surface adjacent to the seismometer.

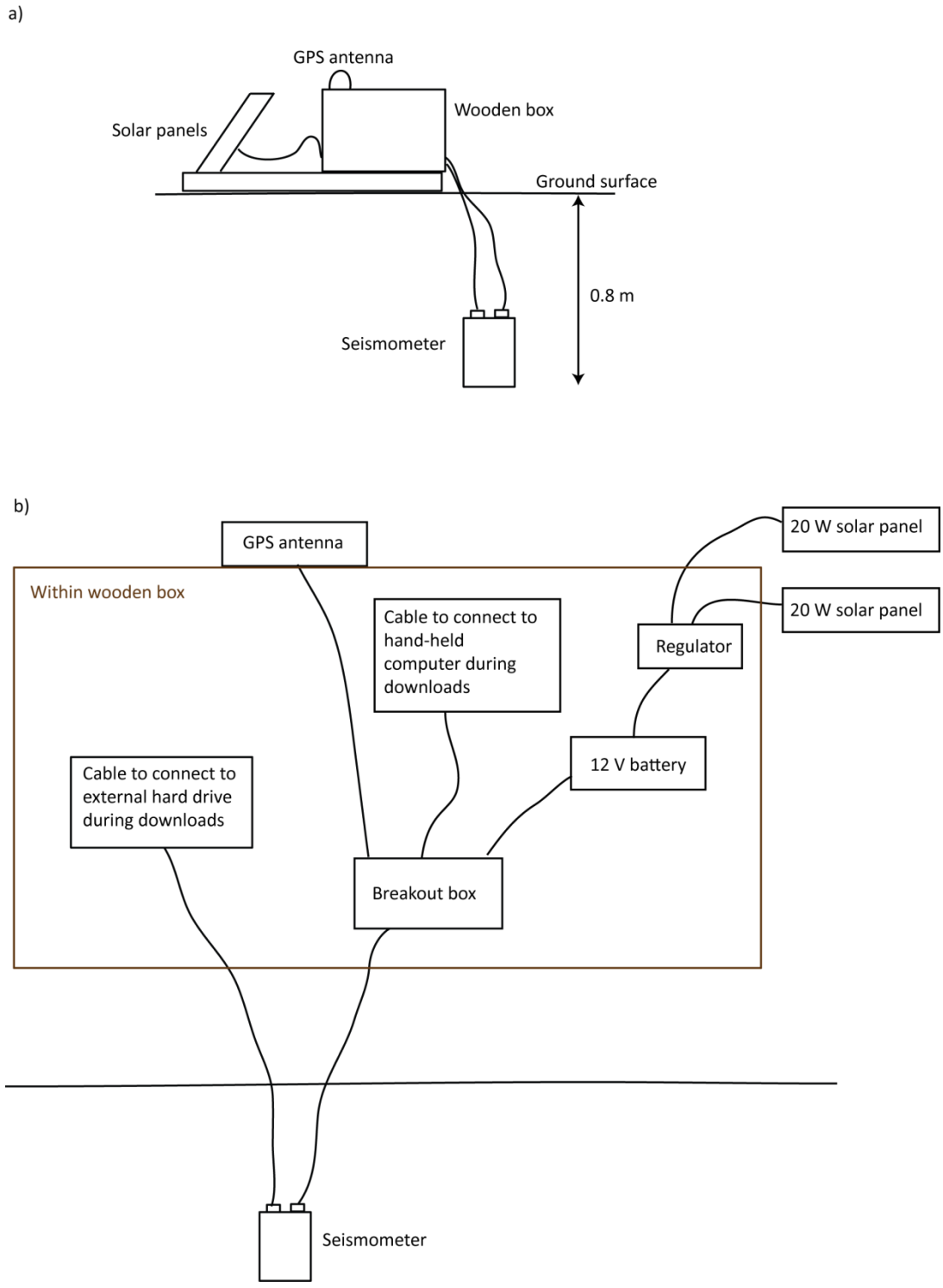

Figure 3.2: a) Profile of the seismometer set-up; b) Seismometer cabling, communications and power set-up.

There were a number of maintenance issues with the 6TDs which meant they had to be visited more regularly than the download interval of once every six weeks. The clay content of the till meant that some tilting occurred after installation, and water logging was also a problem at

seismometer 3, which resulted in the seismometer being out of action for long periods of the campaign.

3.1.3 Data quality

In addition to the equipment, SEIS-UK provided support and advice with installation, equipment maintenance, data management and processing. Data was backed up on SEIS-UK's server, on which a number of pieces of software were available and used for processing of the seismic data. One of these was PQLX, which is designed for analysis of site seismic noise and data quality (McNamara and Buland, 2004). PQLX calculates estimates of power spectral density (PSD) for frequencies across the full spectrum recorded (0.02 – 200 s). PQLX also calculates the probabilities of the different power values for each frequency, which can be used to explore the variability in power across the full spectrum over a specified period of time. McNamara and Buland (2004) provide a detailed explanation of the steps taken to calculate the PSD estimates and to produce the probability plots. However, in summary - PQLX calculates the average PSD for overlapping hours of data using a fast fourier transform with the output as decibels (dB) (calculated as $10 \log_{10}((m/s)^2/Hz)$); the probability of occurrence of a given power at each period is then plotted and compared to the high and low noise models of Peterson (1993) (McNamara and Buland, 2004). The spectral power probability plots of components Z, N and E of seismometer 1 are shown for the period 14/05/10 – 05/06/10 (Figure 3.3).

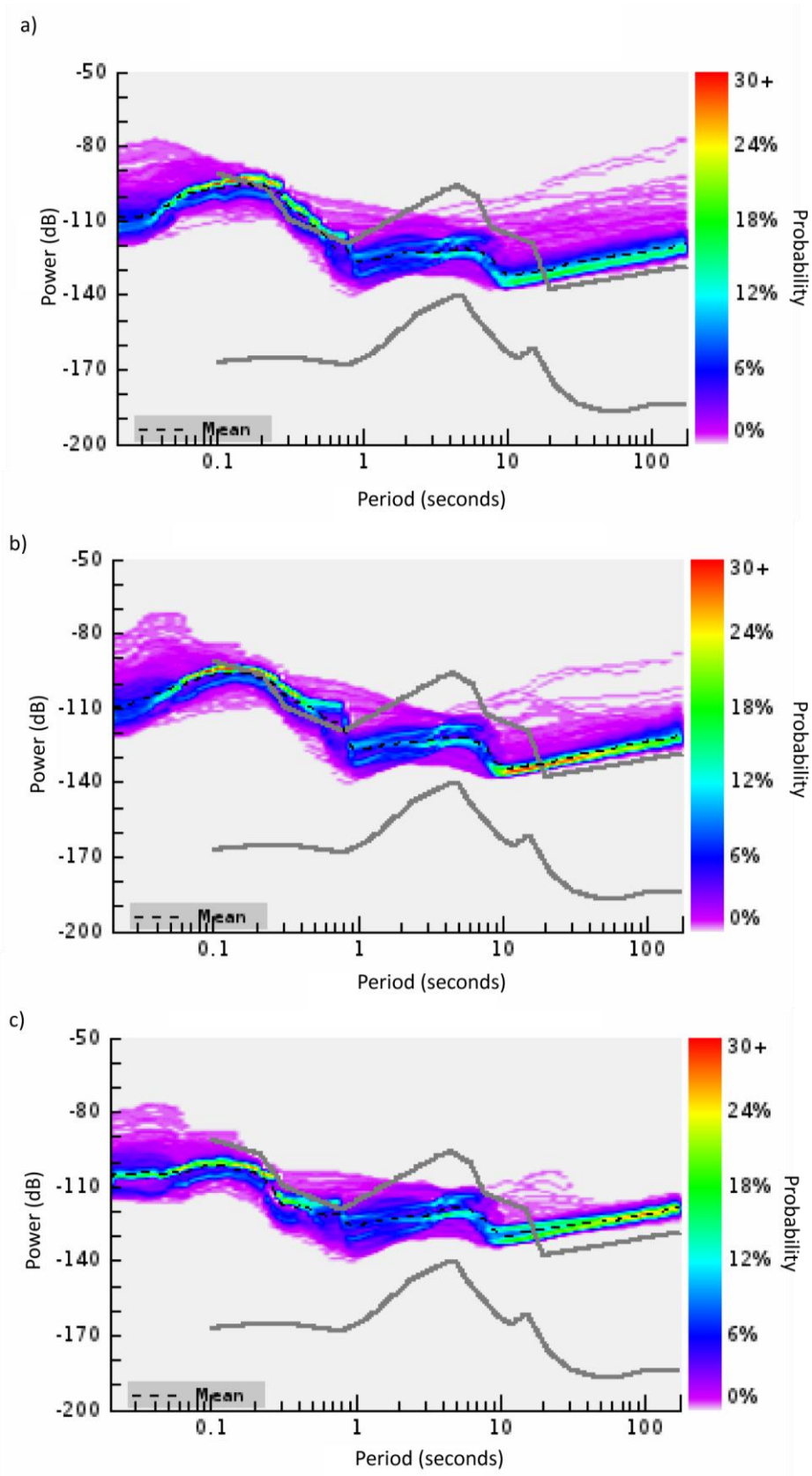

Figure 3.3: Probability plots of PSD for seismometer 1 for the period 14/05/10 – 05/06/10, for components: a) E (horizontal E-W); b) N (horizontal N-S); c) Z (vertical). Grey lines denote Peterson's (1993) high and low noise models. The dashed black line denotes mean probability.

The PSD probability plots (Figure 3.3) show that power across the spectrum is high compared to the global noise models, particularly at the high frequency (> 1 Hz / < 1 s) and low frequency (< 0.05 Hz / > 20 s) extremes, where the highest probability power lies above the bounds of the high noise model. This is anticipated to be due to the large amounts of environmental 'noise' at the site, including winds and waves, which are – encouragingly - the microseismic ground motions in which this study is interested. Ocean wave generated microseisms are typically considered 'noise' by seismologists. The double-frequency (DF) microseism peak can be identified, at around 5 s (0.2 Hz), and the highest probability power lies within the middle of the noise model values. The primary microseism peak, which typically occurs around 10 s (0.1 Hz), is however obscured by distinctive bands of high probability power that occur ≥ 10 s. This band features in all three components, although lies at lower power values in the two horizontal components as compared to the vertical. The tightly constrained signal power and consistent probability of occurrence indicate that this is generated by an unnatural source, and is believed to represent the noise floor of the instrument. This suggests that the lower powers of the ≥ 10 s period ground motions are obscured by the noise generated by the instrument, and so not all of the ground motion characteristics at periods longer than this were recorded. The instruments were found to be noisier than indicated by the manufacturer's specifications. The high probability recorded at the short periods < 1 s (> 1 Hz) represent noise generated by machinery nearby to the seismometers, as explained in Chapter 4. The PSD probability plots for the remaining four seismometers are provided in Appendix 1 for comparison.

In the Z component there is little activity at powers above the noise floor in the signals > 20 s, showing that the noise floor dominates at longer periods (Figure 3.3 c). However, in the horizontal components, particularly the E-W component, there is significant activity at higher powers above the instrument noise floor, indicated by the dark blue and purple bands (Figure 3.3 a). This indicates that natural sources of long-period ground motions, such as infragravity waves, produce ground motions mainly in horizontal directions, and these can occur at power levels above the noise floor. This suggests that the long-periods can still be examined in the horizontal, and particularly the E-W, components.

Other sources of noise typically occur at long or short periods. Significant sources of man-made noise at the site are traffic (< 1 s / > 1 Hz), from the road approximately 300 m landward from the seismometers; people walking around in the field, which can produce broadband noise; and the machinery operated by the adjacent Boulby mine, mentioned above. Wind can also generate high frequency noise. This can be caused by wind turbulence against topographic features, which is of interest to this study, or due to shaking of protruding objects (McNamara

and Buland, 2004; Bormann, 2009), which at the field site consists of the solar panels and fence posts near to the cliff edge. Wind seismic signals are broadband, ranging from 1 to 65 Hz; their amplitudes increase non-linearly with increasing wind speed; and they have been observed to increase significantly when wind speeds exceed a threshold of around 3 - 4 ms^{-1} (Young et al., 1996). The high variability of wind noise therefore makes identifying the specific source of the signals difficult. Whilst horizontal ground motions may represent onshore winds buffeting the cliff face, this may also represent the shaking of the solar panels. It is therefore anticipated that some of the signal representing wind forcing on the cliff also represents that generated by shaking of field equipment.

Signals created by distant earthquakes or other seismic sources such as lightening or military activity can occur at high power levels above ambient local noise across the full spectrum (McNamara and Buland, 2004). Large distant earthquakes typically produce long-period surface waves > 10 s, whereas smaller events create higher frequency signals < 1 s (McNamara and Buland, 2004).

Long-period noise can also be generated due to gradual tilting of the seismometers due to shifts in the materials in which they are deployed (sometimes caused by temperature or moisture variations), and also due to gradual tilting of objects rooted into the ground, such as trees and fence posts (McNamara and Buland, 2004). Temperature and atmospheric pressure changes can also cause long period noise and daily or seasonal variations (Lay and Wallace, 1995). Long-period noise power can be much greater in the horizontal components than in the vertical, notably by as much as 50 dB, largely because of tilt as gravity couples into the horizontal ground motion component, but not the vertical (Bormann, 2009).

3.1.4 Variation between the seismometers

Attenuation of seismic waves increases with distance from the source. Attenuation occurs via the geometric spreading of waves and also due to the material characteristics through which the wave travels. Geometric attenuation occurs as waves travel as spherical (body waves) and circular (surface waves) wave fronts away from the source. As the radius increases with increasing distance from the source the area over which the seismic energy is distributed grows (Stein and Wysession, 2003). The 3D spreading of body waves, compared to the 2D spreading of surface waves means that body waves attenuate more rapidly than surface waves as the distance increases from the source (Lowrie, 1997). Anelasticity of the materials through which

the waves travel causes friction and transfer of kinetic energy from the wave as heat energy to the surrounding material via absorption, and this can result in the permanent deformation of the material (Stein and Wysession, 2003). Anelastic attenuation varies with signal frequency, with higher frequencies attenuating quicker than lower frequencies (Lowrie, 1997). Attenuation also occurs as wave energy is dissipated via refraction, diffraction and reflection that occur at boundaries between different materials (Stein and Wysession, 2003).

Whilst a detailed consideration of attenuation of the different signals is beyond the scope of this project, the comparison of different frequency power between the five seismometers enables examination of the ways in which the signals vary with seismometer location, i.e. instrument distance from the cliff edge. The signals recorded at each seismometer are the sum of the original ground motion plus the effects of the rock and till properties plus the geometric spreading effect over distance plus instrument effects such as the damping, amplification and noise. The path that each of the seismic waves from a variety of sources has travelled to reach each seismometer will vary, and therefore the rock and till conditions through which they travel will also vary, which will affect the signals recorded. This is demonstrated by the higher power values recorded at seismometer 3 across the instrument frequency spectrum (Figure 3.4), believed to be due to the regular waterlogging at this section of the field, increasing seismic wave velocities (Mavko et al., 1998). In addition the exact source locations of the different signals are at this stage unknown.

Comparison of the mean power of a selected number of frequencies from across the spectrum, demonstrate the variability in signal power at the different seismometer locations, caused by the varying conditions through which the waves travel and by individual instrument effects (Figure 3.4). In the E - W component at each seismometer there is a slight decrease in signal power with increased distance from the cliff edge, occurring at the frequencies 12.5, 0.1, 0.07 and 0.014 Hz (Figure 3.4a). The 1 and 0.2 Hz frequencies show very little variation between instruments. The 50 Hz frequency actually appears to be slightly higher at the instruments further away from the cliff. This frequency sits within the range of high-frequency wind noise, and so the pattern of power distribution between instruments may represent variations in wind noise between locations. In the Z component (Figure 3.4b) the patterns across the different seismometers vary to those of the E component. The highest frequency of 50 Hz and the lower frequencies of 0.1, 0.07 and 0.014 Hz have greater power at the seismometer nearest the cliff edge, whilst the 1 and 0.2 Hz signal power shows little variation across the seismometers. The 12.5 Hz frequency has very similar signal power at the first two seismometers, but is lower at the last two.

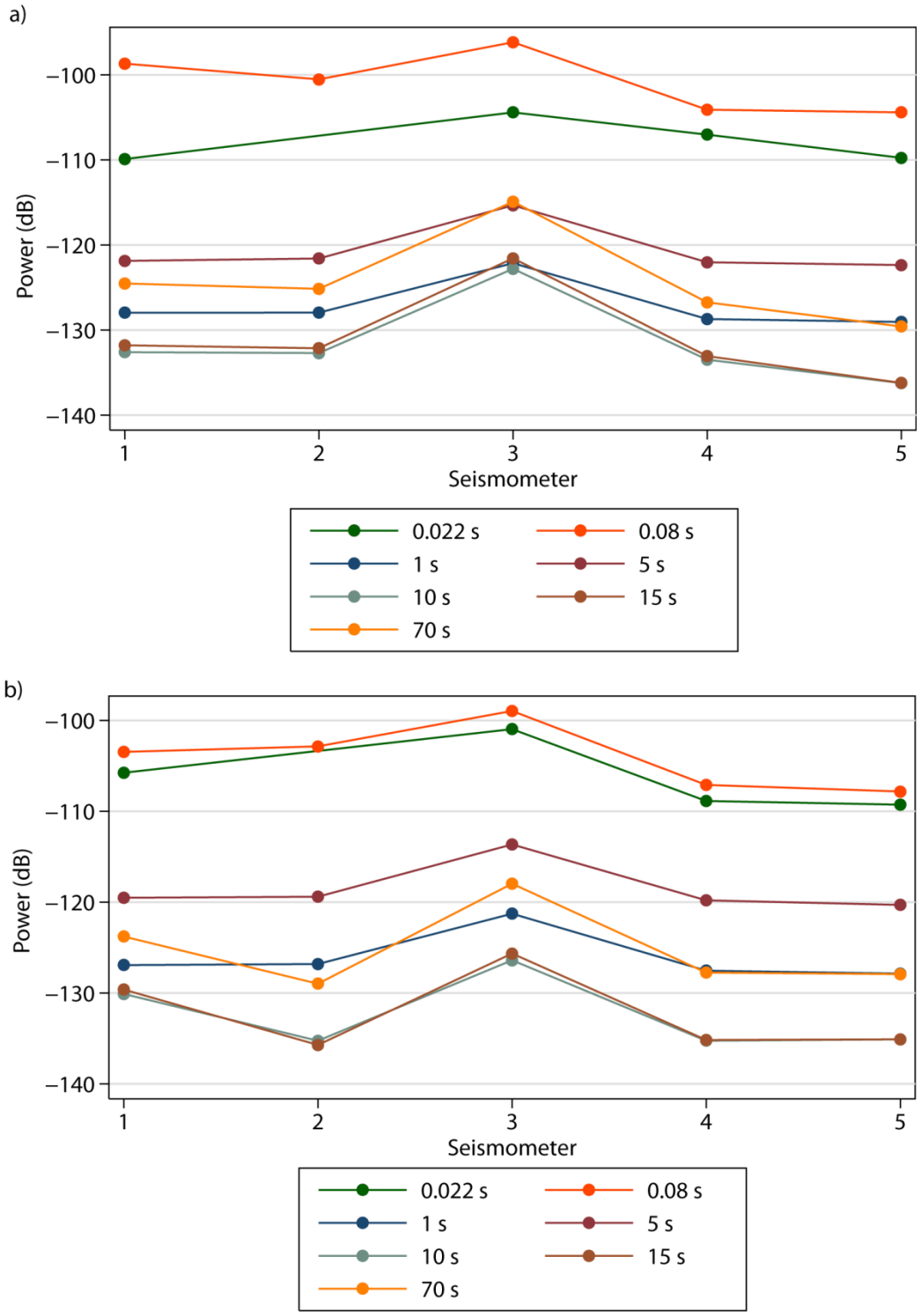

Figure 3.4: Comparisons of mean power for seven selected ground motion periods at the five seismometers with increasing distance from the cliff edge, in the: a) E component; and b) Z component. Seismometer 1 is closest to the cliff edge, the seismometers are then spaced 10 m apart (see Figure 3.1). Seismometer 2 is missing for the 0.022 s period as this instrument was not recording the shortest periods.

Comparison of the different frequency signal power at each of the seismometers shows that typically the highest values are recorded at seismometer 1, closest to the cliff edge. This is believed to be due to the lower distance between the seismic sources upon and below the cliff and this instrument, resulting in less potential for signal attenuation through the cliff material. The volume of data generated by sampling on three components at 100 Hz for two years forced the inclusion of only one seismometer for the remainder of the study; Seismometer 1. Again, due to the volume of data and the similarities in signals in the N and E components, only one of these components will be examined in addition to the vertical component, Z. The E component was chosen as this direction best represents the dominant direction of incoming waves and the tides relative to the alignment of the cliff line.

3.1.5 Field problems

A number of problems were encountered during the field monitoring period. Seismometer cabling and connections provided the greatest difficulties. Firstly, the addition of the seismometers to the field provided a novel and exciting food source to local rodent residents; a problem soon overcome by the replacement of the original containers with larger, sealed wooden boxes and conduit into the ground. But by far the greatest problem was water seeping into the cable connectors on the seismometers, corroding contacts. The second greatest problem was power. One solar panel was initially used for each seismometer in the first winter, but these proved insufficient and so second panels were added. Furthermore, the low winter temperatures resulted in battery failure on a few occasions. Finally, water-logging at seismometer 3, and water repeatedly getting into cable connectors, resulted in some gaps at this station throughout the monitoring period (Figure 3.5). Seismometer 1 had the fewest data gaps, which aided the selection of the best instrument for this study.

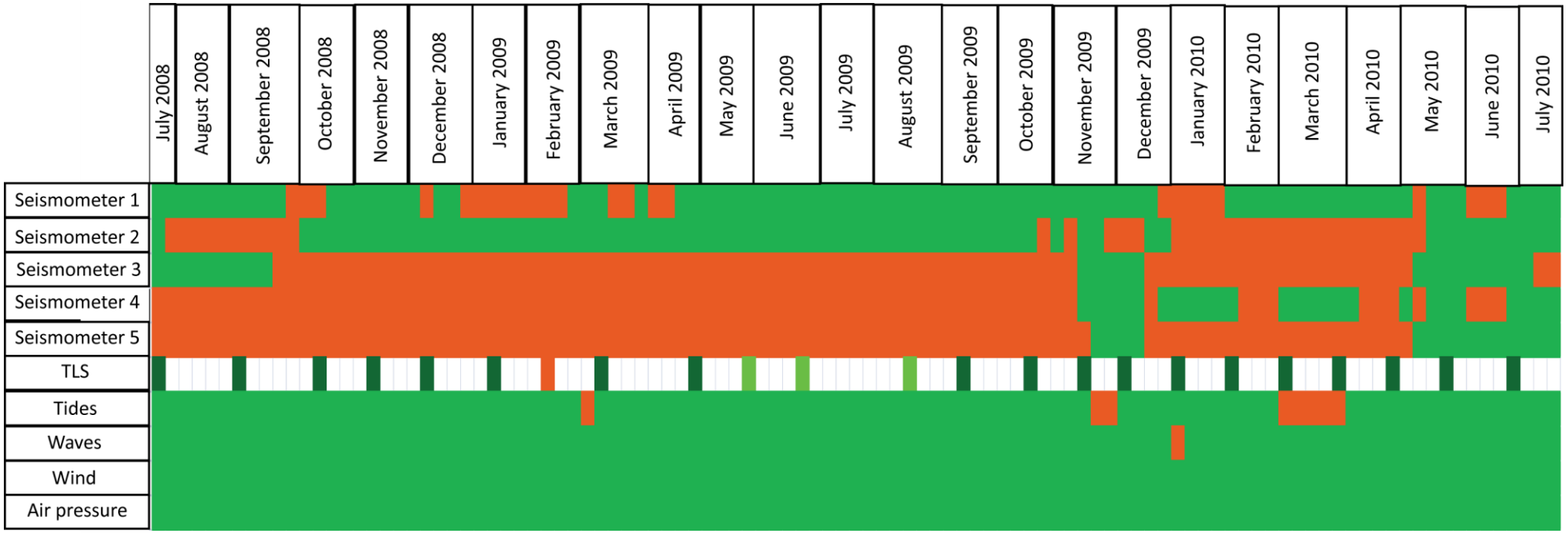

Figure 3.5: Gannt chart of data collected from the five seismometers, the laser scanning (TLS), and collected from the regional-scale datasets of tides, waves, winds and air pressure. Green indicates data was obtained, orange indicate data gaps. For the TLS dark green indicates the Trimble scanner was used, light green the MDL.

3.1.6 Data processing

The seismic data was processed in the time domain to examine the ground motion velocity, and in the frequency domain to examine the power and energy of different frequencies of ground motion. Various processing stages were required for each dataset to produce the variables needed for the analysis. A number of different software packages were used to process and analyse the data, including Matlab, Stata and PQLX.

3.1.6.1 Microseismic data in the time domain

Seismic data is rarely treated as time series data in the same way as is common for other environmental datasets. The huge volume of data due to the high-resolution sampling rate and length of monitoring period made initial processing of the velocity data slow. Critically, this study was interested in the data commonly removed as noise by conventional seismological studies, so much of the seismology software was poorly suited to this analysis. Establishing a technique to manage the velocity data and produce file sizes that could be useful for analysis therefore took considerable time. Seismic data is also usually considered over very short time periods (minutes), indeed other studies exploring coastal cliff microseismics have presented only minutes, hours or days of data (e.g. Adams et al., 2005; Young et al., 2011b). However, key to this study was exploring the long-term behaviour over the two-year monitoring period, and producing datasets that could be correlated with time series of environmental and rockfall datasets that were monitored at lower temporal resolutions, but over a period with sufficient variability to observe drivers and response.

The 100 sps velocity data therefore needed to be reduced in resolution, to minute and hourly values, so that it could be analysed over the whole monitoring period. The environmental datasets were sampled at different resolutions the lowest of which was hourly, therefore hourly values of the ground motion velocity were needed so that regression analyses could be undertaken with the environmental datasets.

A number of processing steps were needed to get the raw ground motion amplitude data into the desired minute and hourly resolutions of velocity (Figure 3.6). As previously discussed, there are a number of known seismic noise sources at the site. People walking and driving around the field resulted in noise across the spectrum and so all days when people were known to be in the field either downloading or maintaining the seismometers, or the other equipment in the field,

were removed from the datasets. In addition days where errors were caused by rodent, water or power problems were also removed.

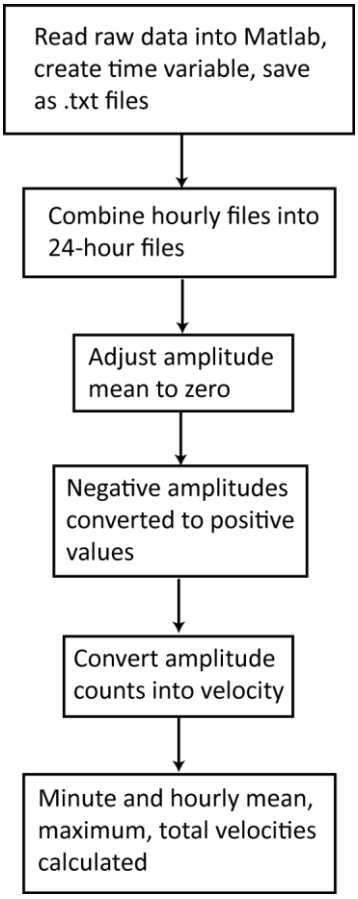

Figure 3.6: Workflow of the processing steps of the microseismic data to produce the minute and hourly resolution time series of ground motion velocity.

The first step towards producing the minute and hourly velocity values was to get the raw seismic data into non-seismology software where processing could be undertaken (Figure 3.6). The raw seismic data could be downloaded from the seismometers in a number of formats, one of which were .gcf files which could be read into Matlab using code provided by the seismometer manufacturer, Guralp. This code was incorporated into a script to automate the processing of the 17,544 hour files for the 731 days of the monitoring period that had no data problems. The Guralp code and the script are provided in Appendix 2 and 3. The script was used to read in the hourly 100 sps files, to produce a time variable from the starting time-stamp provided for each file, and save the files as text files. The raw amplitude of the hourly files was presented as amplitude counts (Figure 3.7a). These were then combined into daily 24-hour files using Windows' command line batch commands. The raw ground motion amplitude then needed to be converted into volts using the seismometer component's digitising factor, and

then converted into velocity using the seismometer component's sensitivity, both of which were provided by SEIS-UK. This was done in Stata, in addition, before converting the amplitude counts to velocity the mean was adjusted to 0 to adjust for the varying offset of the components' masses, and the negative counts converted to positive values ready for the later regression analyses. In Stata, minute and hourly values of the velocity were calculated. To avoid aliasing, the distortion of a signal due to sampling, the minute and hourly mean, maximum and total velocity were calculated rather than sampling the 100 sps data at minute or hour intervals. These minute and hourly statistics of the velocity were then ready for examination as time series and for regression against specific environmental and rockfall variables (Figure 3.7b and c). These steps were undertaken for all three components. The Stata script for these steps is in Appendix 4. The regression analyses method is described in Section 3.1.6.2.

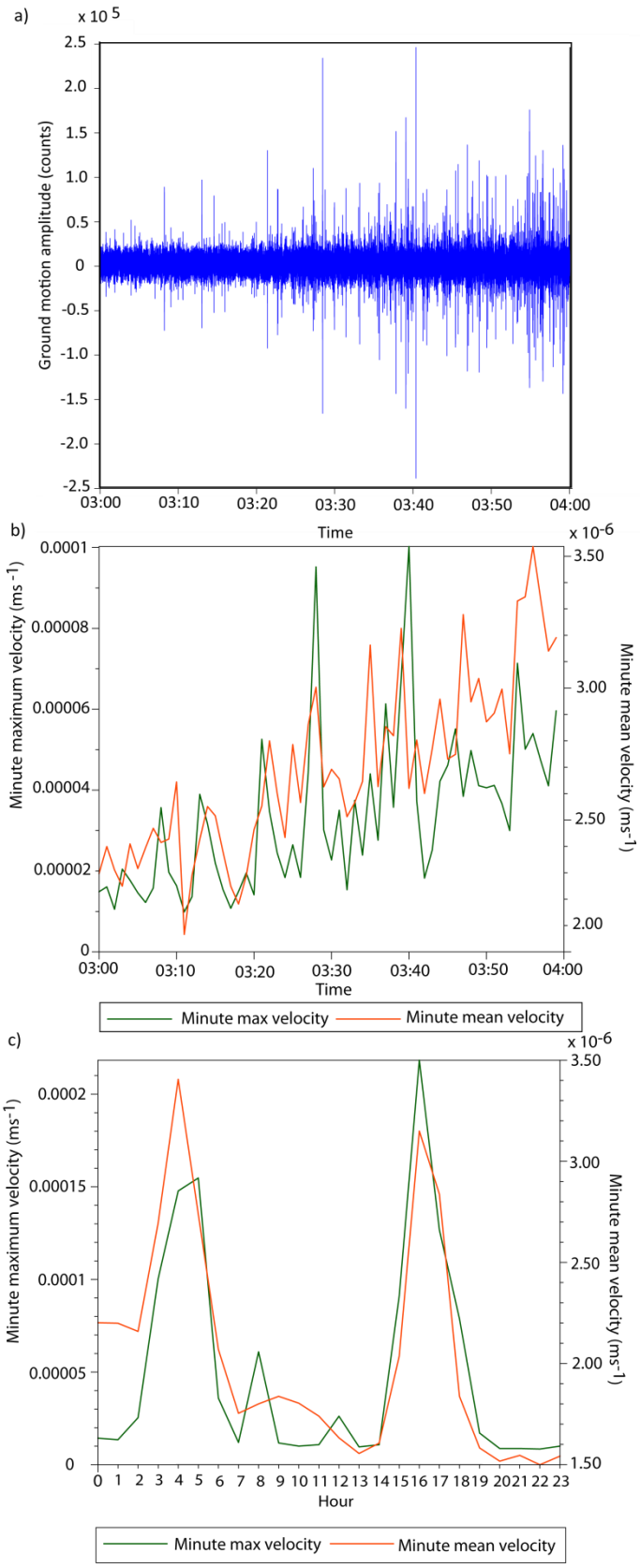

Figure 3.7: Examples of the different stages of the ground motion data in the time domain: a) 1 hour of the raw amplitude as counts; b) 1 hour of the minute maximum and minute mean velocity; c) 1 day of the hourly maximum velocity.

3.1.6.2 Microseismic data in the frequency domain

PQLX was used to calculate hourly or 30-minute PSD values across the spectrum of monitored ground motion frequencies. To do this a number of processing steps were required (Figure 3.8). Scripts were provided by SEIS-UK for the first five steps in Figure 3.8, and all processing was undertaken on their Linux server. First the raw .gcf files had to be converted to miniseed file format for use in PQLX. A dataless volume then had to be created which provided information regarding the individual seismometer's location, frequency range, components' digitising factor and sensitivity. Miniseed file headers were then produced which had to be checked to match those in the dataless volume. Once the full two-year dataset was converted and checked the PQLX database could then be created, and PSD values extracted. The code to extract the PSD values from the PQLX databases is in Appendix 5a. For each hour / 30 minutes PQLX provided PSD values for 106 frequencies for the 100 sps data, ranging from 0.02 – 178.67 s, and 114 frequencies for the 200 sps data, ranging from 0.01 - 178.67 s.

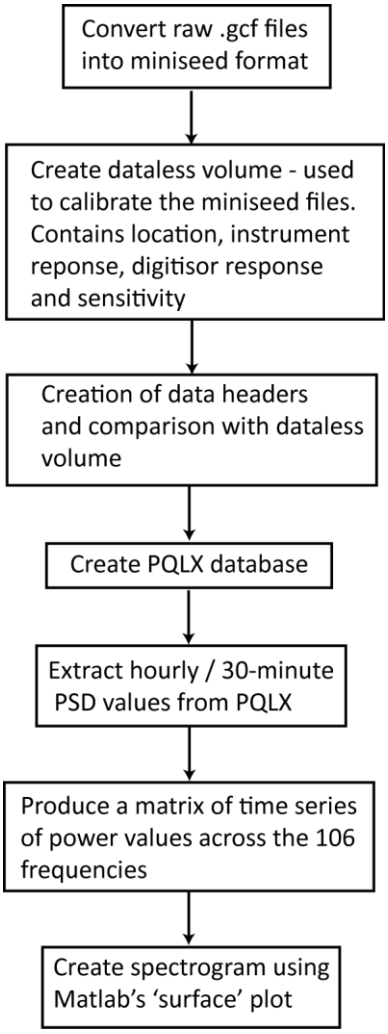

Figure 3.8: Workflow of the processing steps to produce the hourly / 30-minute power spectral density (PSD) values across the monitored spectrum of ground motion frequencies.

These data were first analysed by presenting them as spectrograms (Figure 3.8 steps 6 and 7), which are visually striking and provide an effective approach to explore the characteristics of the different frequencies, enabling direct comparisons of the powers across the frequency spectrum, and to examine temporal patterns (Figure 3.9). The spectrograms were produced using Matlab. A matrix of the time series of the powers across the 106 frequencies produced for the 100 sps data was created for each time period of interest, and the spectrograms were created as 'surface' plots. The Matlab code to produce these images is in Appendix 5b. The spectrograms enabled identification of a number of distinct frequency bands, associated with different environmental conditions, these are explored in Chapter 4. Spectrograms were examined over a number of different lengths of the monitoring period, from individual days, to the full two-year dataset. For the daily spectrograms the 30-minute PSD values were used, and for all other time periods the hourly values were used.

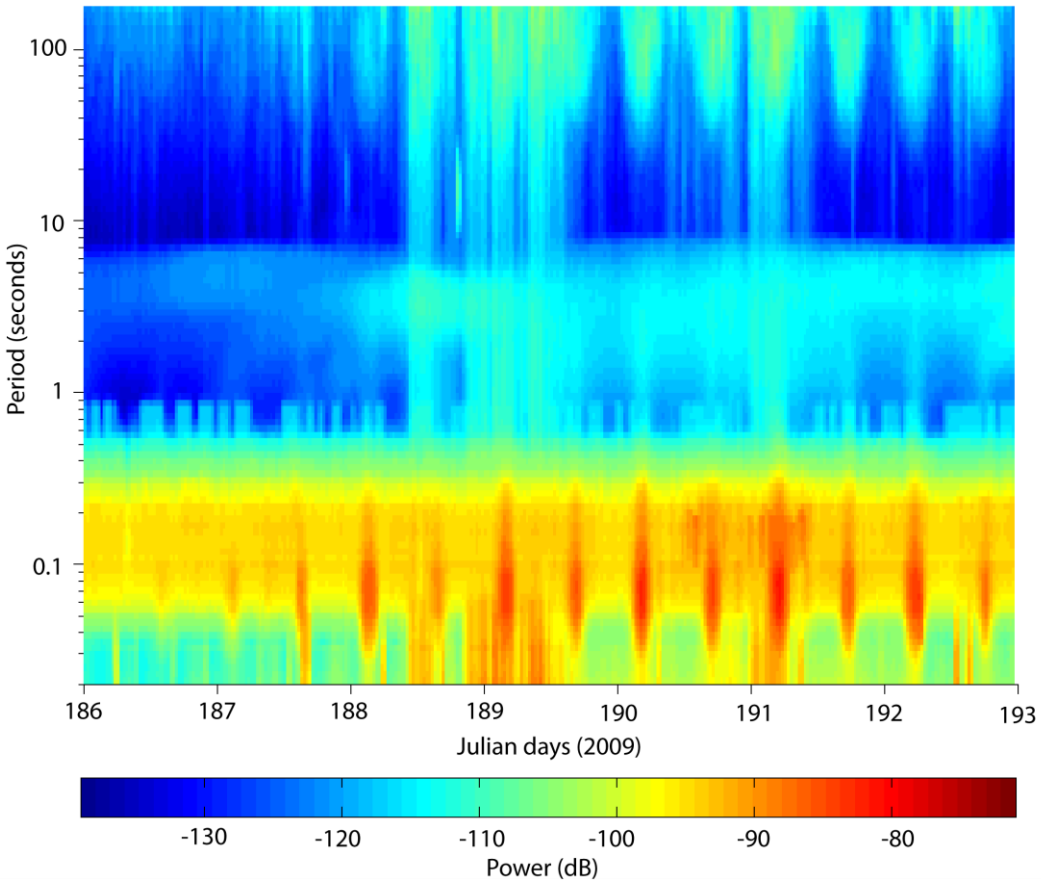

Figure 3.9: Example of the spectrograms produced to explore the cliff ground motions. A number of distinct frequency bands can be identified, explored in Chapter 4.

In addition to the power of different ground motion frequencies, the energy values were also explored. Ground motion frequency power tells us the relative rate at which energy is transferred to the cliff from the sources represented by the different frequencies, and energy values enable comparison of the total relative contributions from each source. From the hourly power spectral density (PSD) values energy was calculated using the calculations below:

power as dB = 10 x $\log_{10}$ $((m/s)^2/Hz)$

power as dB = 10 x $\log_{10}$ (power in watts)

power in watts = $10^{(\text{power in dB}/10)}$

power in watts = energy transferred/time taken

energy transferred = power in watts x time taken

Where the time taken is the period (seconds) of the ground motion frequency being examined. Statistics of the different ground motion frequencies' power and energy were analysed in Stata.

Regression analyses of both the power and energy of a number of frequencies, selected to represent different sources of environmental forcing (discussed in Chapters 4 and 5), and the ground motion velocity, was undertaken against various environmental and rockfall variables. All regression analyses were done in Stata. Numerous regression models were run to test for specific relationships between microseismic ground motion frequencies, environmental and rockfall variables, and so the regression analyses were automated, using the 'regress' and 'estimate' combination of commands in Stata. Before the regression analyses, the data were checked to satisfy the assumptions of regression (discussed in Burt et al., 2009). The automated outputs of the regression models indicated the statistically significant results, significant at $p < 0.05$, $p < 0.01$ and $p < 0.001$. Only statistically significant relationships are presented in the results chapters, and the associated p values are given with the results. The following regression diagnostics were checked for the statistically significant results: normality of the residuals, homoscedasticity, and multicollinearity in the multiple regression analyses. As the data are time series there is undoubtedly autocorrelation within each dataset, however this was a key characteristic of the data caused by seasonality and shorter-term variability of the environmental conditions that were of interest and so was not removed.

3.2 Cliff face erosion

3.2.1 Data collection approach and field set-up

To monitor rockfall activity from the cliff, the cliff was scanned every 4 - 8 weeks using a terrestrial laser scanner (TLS), collecting point clouds of the cliff surface, which were then processed to produce a 3D surface of the cliff. The matching of successive scan surfaces enabled the calculation of volumes of change across the cliff face, which were extracted as individual rockfalls.

Initially a Trimble GS200 terrestrial laser scanner (TLS) was used, however problems with the scanner meant that for a few months during the monitoring period the Trimble was returned to its manufacturers, and in its absence a MDL LaserAce 600 scanner was employed (see Figure 3.5 for time series of scanner deployment). Both scanners calculate the distance to a surface using the time-of-flight of the return of a laser pulse reflected from the surface back to the scanner. The specifications of the two scanners vary (Table 3.1), yet the output data is comparable when operated at this scale. Motorised mirrors within the scanners are used to direct the laser pulse across the entire surface area specified, moving as either horizontal or vertical swathes across

the surface, with the spacing at which points are collected specified by the user. The point clouds produced by the scanners provide 3D coordinates of each of the points collected across the surface.

Table 3.1: Terrestrial laser scanner specifications

	Trimble	MDL
Speed of point collection	Up to 5,000 points per second	250 points per second
Beam width	0.003 m at 50 m	0.046 m
Accuracy - measurement Precision- measurement Precision - angle/pan and tilt	0.0015 mm at 50 m	 0.1 m at 700 m 0.01^{o}
Laser wavelength	Green	905 nm (Red)

The methods of TLS data collection and processing used were developed by Lim et al. (2005), Rosser et al. (2005) and Lim (2006). To collect the point cloud the scanner was levelled upon a tripod over a survey nail located in the foreshore, normal to the centre of the scanned width of monitored cliff, at a distance of 110 m from the cliff toe. This reduced occlusion over the majority of the monitored section and also negated the need for multiple scans of the surface (Lim, 2006). The width of cliff scanned was 88 m and height of 55 m, producing a projected scan area of 4,840 m^2. The initial scan point spacing resolution used was 0.125 m, as originally six different sites were being scanned for the project and so time available for scanning was limited due to the tides. Later, when it was decided only one site was being used, the resolution was increased to 0.075 m. Although the steep (near-vertical) cliff faces meant that installing ground control points (GCPs) on the cliff was not possible, previous studies at the site have demonstrated that large sections of the cliff across the scan width are stable enough to be used as control points between successive surveys, and so these points were checked during the alignment of successive scans (Lim et al., 2005; Lim, 2006).

3.2.2 Data processing

The workflow of TLS data processing steps are shown in Figure 3.10. A number of different software packages were used for the different steps of the analysis. Initially Archaeoptics Ltd Demon software was used to clean up the point clouds. The MDL scanner files could be opened directly into Demon, however the Trimble scanner files first had to be opened in Realworks

(Trimble's processing software) and exported as ASCII files for use in Demon. In Demon erroneous points were removed from each of the point clouds, sometimes caused by birds flying in front of the cliff for example (Lim et al., 2005; Rosser et al., 2005; Lim, 2006), and the scan areas were trimmed down to remove any coverage of the till at the cliff top and to the width defined by two distinctive cliff face features at either edge of the scan. Each of the point clouds was then transformed to ensure that the cliff face was oriented towards the positive Z axis direction, with Y vertical (up) and X horizontal distance across the coastline (Lim et al., 2005; Rosser et al., 2005; Lim, 2006) (Figure 3.11).

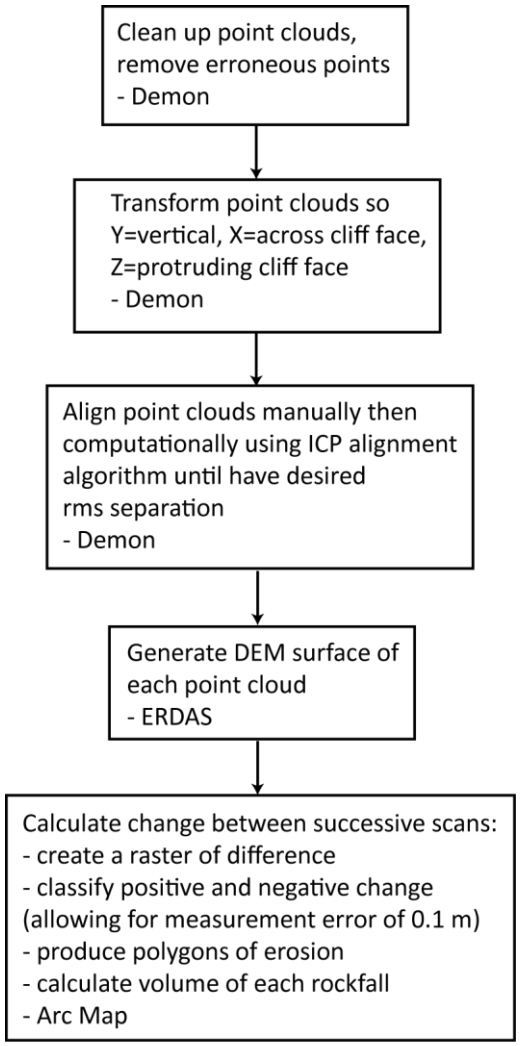

Figure 3.10: Workflow of TLS data processing

In Demon each of the point clouds was aligned to the first scan, captured in July 2008. This overcomes any errors due to variations in positioning or orientation of the scanner during point cloud collection (Lim et al., 2005). Alignment was initially done manually by dragging the clouds, and then computationally using a least squares iterative closest points (ICP) alignment

algorithm, which produces a root mean square (rms) separation between the two point clouds (Lim et al., 2005). This was repeated until an rms value of 0.04 m was achieved, the lowest that could be achieved with the survey point spacing. The point cloud matching is based on the distances between the majority of points across the two clouds and therefore because of the large area of the scanned cliff surfaces, actual surface change does not influence the matching (Lim et al., 2005). Distinct features on the cliff face, observed by previous studies by Rosser et al. (2007) and Lim et al. (2010a) not to have changed over the previous long-term monitoring they undertook at the site, were used as GCPs to check the alignment of each of the scans to the first scan during the matching of point clouds. These were viewed from multiple angles to visually confirm the best-fit alignments identified by the rms separations calculated.

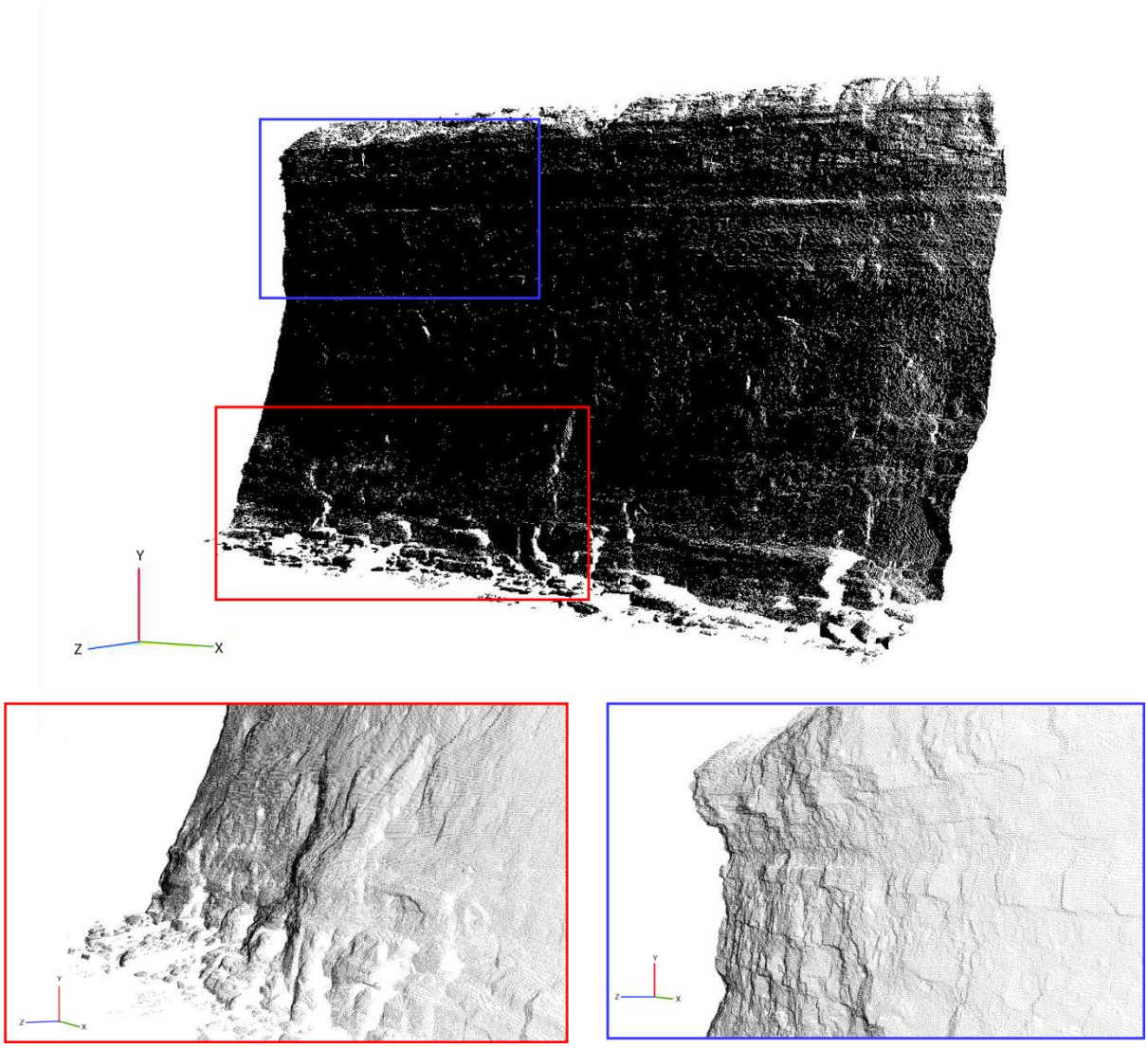

Figure 3.11: Example point cloud of the cliff face produced by the laser scanners. The red box shows a close-up of the point cloud detail at the cliff toe, here protruding sections of the cliff toe can be seen. At the lowest sections of the toe greater occlusion occurs caused by boulders lying on the foreshore in front of the cliff – this lowest section was not included in the rockfall calculations. The blue box shows a close-up of the top of the cliff. Here the blocky sandstones and siltstones protrude over the weaker shales beneath.

The X, Y, Z coordinates of the aligned point clouds were then imported into ERDAS Imagine software to generate 3D raster images of each of the point clouds (i.e. DEMs) of the cliff face (Lim et al., 2005). A linear rubber sheeting interpolation function was used to produce a raster from the point cloud coordinates using ERDAS's surfacing tool (Figure 3.12). A grid resolution of 0.125 m was used (as corresponds to the maximum point spacing used).

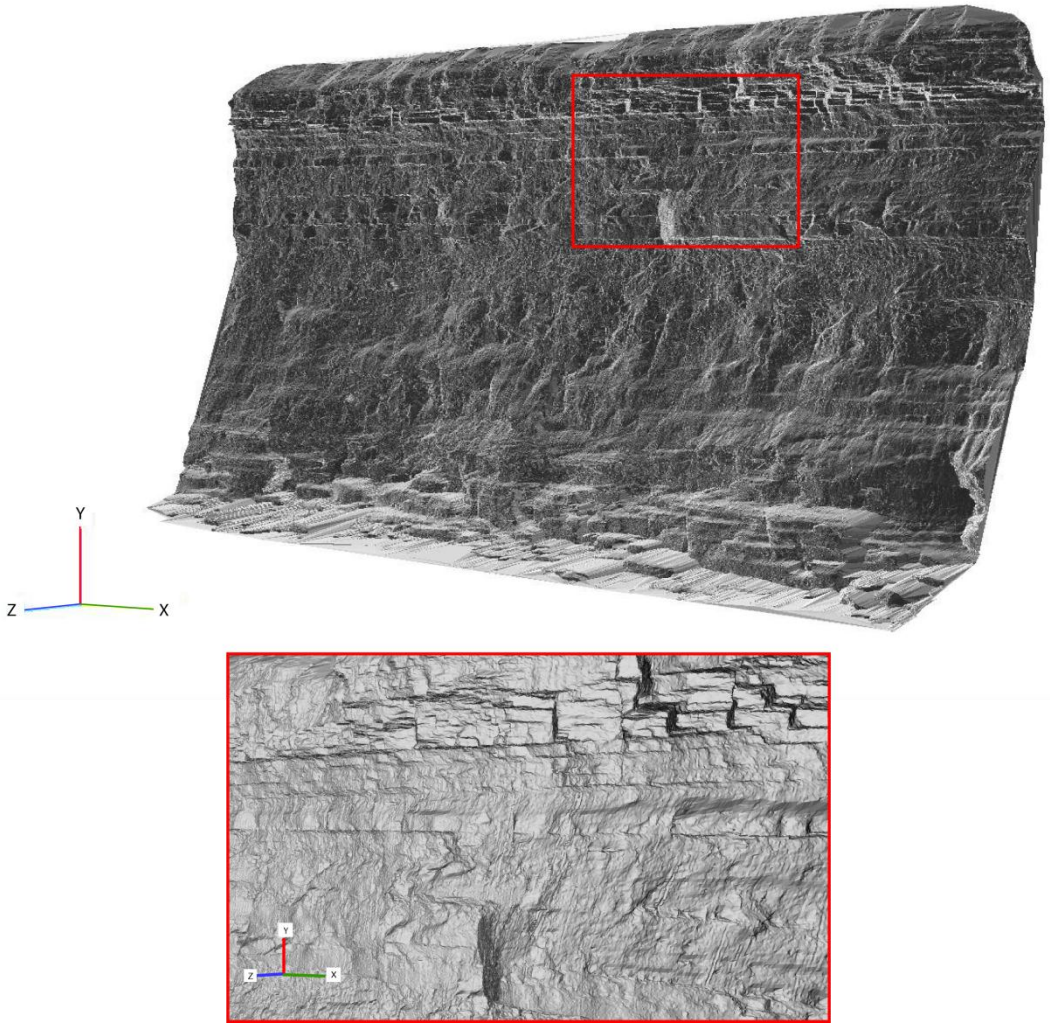

Figure 3.12: Example DEM surfaces of the cliff face generated from the point clouds. The red box shows a close-up of the cliff top. The blocky character of the siltstones and sandstones here is evident and different layers are clearly defined.

Once the DEMs of the cliff face had been created for each scan, change between successive scans was defined and rockfall volumes calculated. To do this the Spatial Analyst tools in ESRI Arcmap were used, methods used by Rosser et al. (2007) and Lim et al. (2010a). First, a raster of difference between each pair of successive TLS scan surfaces was generated using the Spatial Analyst 'raster calculator' tool by subtracting the first scan of the pair from the second scan (Figure 3.13a). From the difference image areas of positive and negative change were identified using the 'reclassify' tool. In identifying positive and negative change a mask was created that accounted for a measurement error of 0.1 m mainly arising from the precision of the MDL scanner. This value has been used by previous studies at the site using the same equipment and currently better data is not available to account for the accuracy and precision of these

scanners. Polygons of areas of individual rockfalls (negative change i.e. erosion > 0.1 m) were generated and using the difference raster, and using the Zonal Statistics function, the volume of each individual rockfall was calculated (Figure 3.13b). The DEM grid resolution of 0.125 m and minimum depth change of 0.1 m produced a minimum rockfall volume that could be detected of 0.00156 m^3.

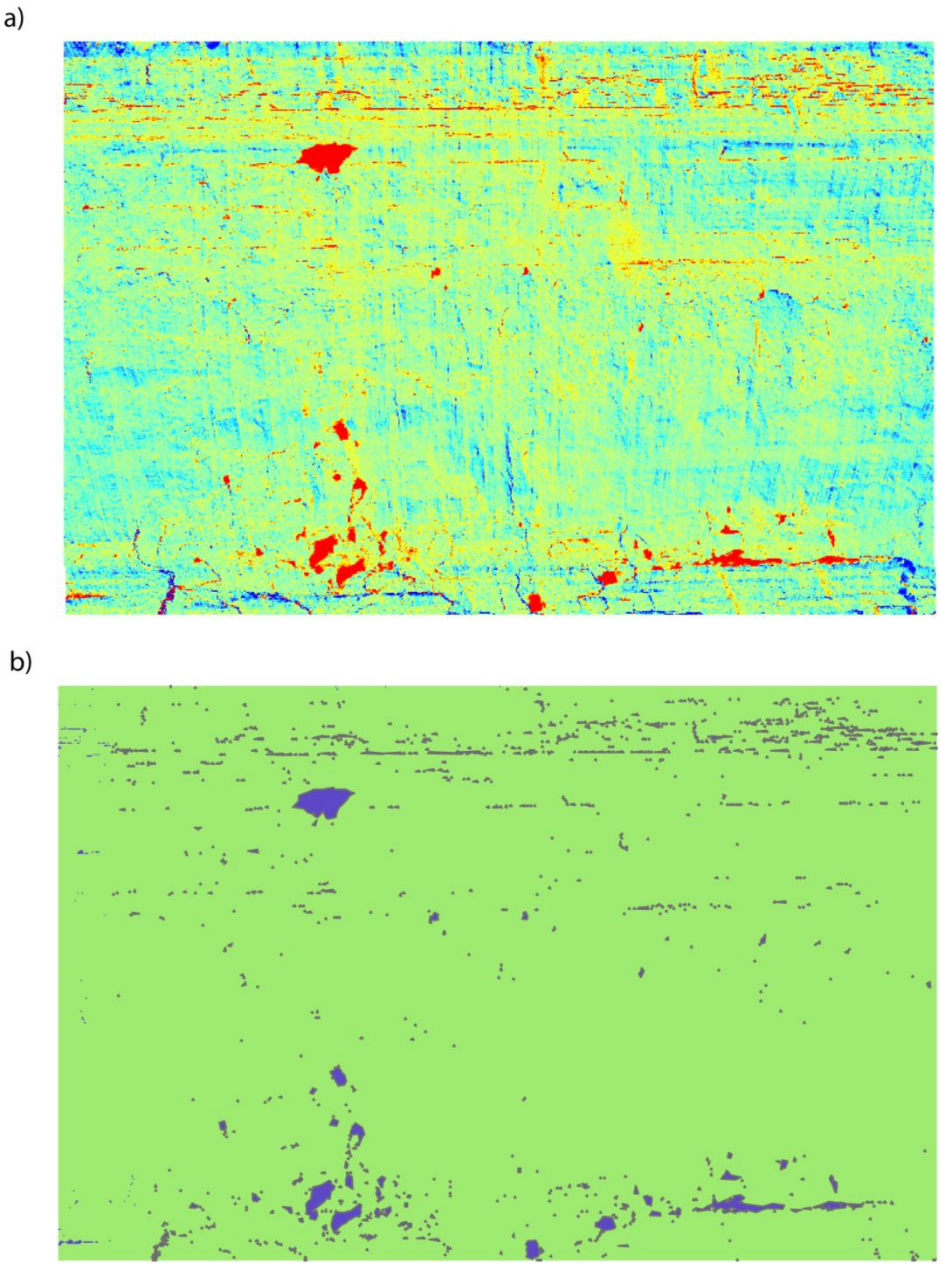

Figure 3.13: Calculating change across the cliff face from successive TLS scans: a) Example of the difference raster calculated between two successive scans. Dark blue indicates positive change which is focussed on ledges of mudstone near the toe and at the top indicating deposition of till on the protruding sandstone. Red indicates negative change i.e. erosion, larger blocks of which are focussed in the lower section of the cliff during this month; b) Rockfall polygons showing a number of large rockfalls have occurred during this month, between September and October 2009. Smaller rockfalls commonly occur along protrusions which demarcate the bedding planes between different layers of sandstones and siltstones at the cliff top.

For each TLS monitoring period, and for the whole two-year monitoring period, statistics of the rockfall volumes were calculated in Stata (mean, maximum, standard deviation and total

rockfall volumes). These are analysed in Chapter 7 and were also regressed against various seismic and environmental datasets, also analysed in Chapter 7.

3.2.3 Data quality

A number of factors during data collection and processing can determine the accuracy of the generated surfaces in representing the cliff face. The strength of the TLS signal return is determined by surface characteristics which influence the reflectance of the laser beam, including surface colour, wetness, roughness, and mineral composition, in addition to the atmospheric influence on ambient light conditions (Lim, 2006; Sturzenegger et al., 2007; Hodge et al., 2009). The lower section of the cliff exposed to the sea is frequently wetter than the upper sections of the cliff, which was observed to sometimes result in lower point returns in this portion of the cliff. However the successive scans each aligned with an rms separation of 0.04 m suggesting that localised poor reflectivity did not significantly hinder the precision of scan alignments.

On highly uneven surfaces, or when scanning at high incidence angles, occlusion can cause gaps in the final point cloud (Buckley et al., 2008). This was observed to be a greater issue at the edges of the scans, where incidence angles were higher, and at the cliff toe caused by boulders directly in front of the cliff on the foreshore. In addition, the sandstones in the upper sections of the cliff commonly have widely-spaced, blocky protrusions that cause some occlusion of the cliff above them, particularly at the top where combined with higher incidence angles.

Divergence of the laser beam over distance can result in the enlarged footprint of the laser overlying an uneven surface (Schürch et al., 2011). The point that is registered by the scanner is the strongest part of the return signal, which when the footprint is spread over an uneven surface may not produce the most accurate replication of the surface. In addition, high incidence angles can result in the spreading of the beam footprint over the rock surface, adding further error to the precise location of the point. These effects can be reduced by minimising the point spacing, in addition to the range and incidence angles between the scanner and cliff.

To minimise these sources of error and to obtain as accurate a representation of the cliff surface as possible, the scanner location and scan width were selected to minimise the incidence angles, whilst staying well within the distance range limit of the instruments. During processing of the data a rectangular section of cliff was used to delimit the area from which rockfalls were identified. This did not include the very top of the cliff / edges of the scan area,

where occlusion and high incidence angles were deemed to be problematic, nor the lowest metre of the cliff where boulders were a problem, and to avoid any inaccurate change calculations caused by scans not overlapping fully. The dynamic nature of coastal cliff environments meant that little could be done to control the features that determine surface reflectivity, which undoubtedly were variable between each scan, as determined by weather conditions which controlled the light and cliff face moisture conditions.

Errors can also be caused during processing of the TLS data during alignment of the successive scan surfaces and generation of the DEMs (Buckley et al., 2008; Hodge et al., 2009). Although the steep face of the cliff meant that installing GCPs on the cliff face was not possible, there are distinct features across the cliff face which have remained stable for a number of years and which were effectively used as GCPs during alignment of the point clouds. These were selected across the cliff face, in the four corners and centre, and were visually inspected from different angles to check alignment. The rms separation between the surfaces is lower than the point spacing, and so is considered acceptable. Variations are likely to occur during surface generation, as points collected within the point clouds will fall on different locations in each scan collected. This effect can be reduced by using a finer resolution scan.

It is recognised that to develop this approach of monitoring coastal cliffs using TLS, significant work is needed to test the error sources and accuracy of the techniques used and resulting datasets. Much work has been undertaken on this, as reported in Lim et al. (2009). As this project is focussed on the development of the application of microseismics to coastal cliffs, this was considered to be beyond the scope of this project, and the error limit previously established by Lim et al. (2009) at this site has been adopted.

3.3 Regional-scale marine and atmospheric datasets

Regional-scale datasets of tide, wave and weather conditions were obtained and used to examine these conditions during the two-year monitoring period.

Offshore wave data have been obtained for the Cefas wave buoy off the coast of Tees (30 km off the Tees coast, 22 km NNE of the cliff) (Figure 3.14), which sits in approximately 66 m depth of water. The buoy is a directional waverider buoy and provides readings of significant wave height, wave direction, wave spread, average wave period and peak wave period over 30 minute intervals. To obtain estimates of wave conditions in the shallow coastal waters and at

the cliff the wave buoy data was modelled to account for transformation over the local bathymetry, this is described in detail in Section 3.4.

Tide heights at the study site at Boulby were modelled linearly from the National Tide Gauge Network data collected at Whitby (15 km south along the coast) and North Shields (63 km north along the coast) (Figure 3.14). The Whitby tide gauge is a bubbler tide gauge which measures tide level using air pressure changes within a pipe which changes with pressure of the water column above it, and at North Shields a float tide gauge is used which measures the changes in height of a float within a stilling well (Proudman Oceanographic Laboratory, 2011). The tide gauge data provides measured tide heights and tide residuals at 15 minute intervals. 'Predicted' Boulby tides were modelled from the predicted Whitby and North Shields tide heights. The tide residuals from North Shields were then added to the predicted Boulby heights to account for meteorological effects on tide levels during the monitoring period. Although Whitby is closer to Boulby, the Whitby tide gauge levels are heavily affected by freshwater flow from the River Esk.

Wind velocity, wind direction and air pressure (adjusted for mean sea level) data have been obtained from the Met Office weather station at Loftus (3 km NW) (Figure 3.14). Mean values per hour are provided. The wind velocity has been reported to the nearest knot (converted to ms^{-1} for this study), wind direction is rounded to the nearest 10^{o}, and were measured by a Munro cup and vane (Met Office, 2011). Air pressure has been reported to the nearest 0.1 hpa, recorded by a precision aneroid barometer, and has been corrected for altitude to calculate the value at mean sea level (Met Office, 2011).

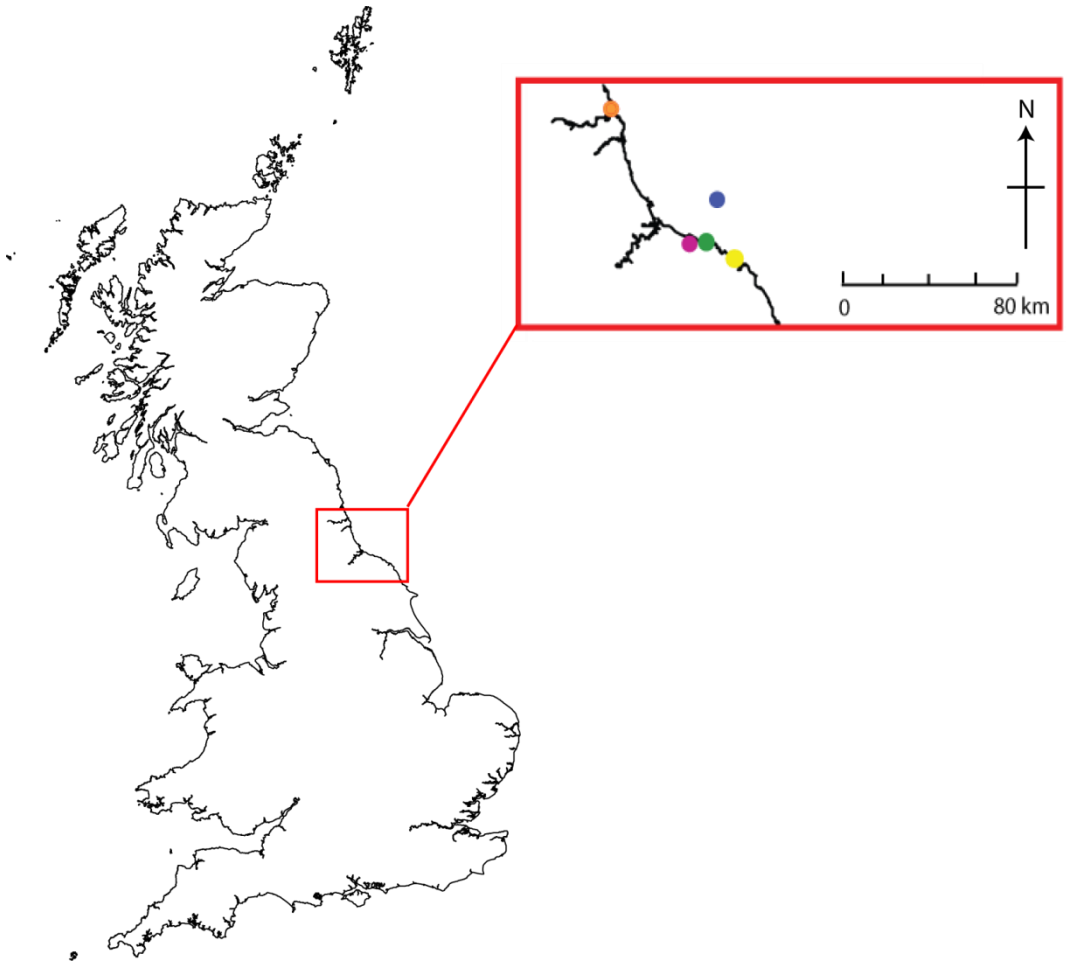

Figure 3.14: Monitoring locations of the different regional-scale environmental datasets used by this study, relative to the cliff at Boulby. Green dot = Boulby cliff; orange dot = North Shields tide gauge; blue dot= Tees wave buoy; pink dot = Loftus met station; yellow dot = Whitby tide gauge.

These data were used to examine the marine and atmospheric conditions at this stretch of coastline during the two-year monitoring period. The data were also used to test the combinations of environmental conditions that were generating the different frequency bands of ground motions, and relationships with the rockfall data were tested to examine how well regional-scale datasets can explain environmental controls of cliff erosion.

3.4 Wave modelling: Transformation of offshore wave data to the coast

3.4.1 Approach used

To explore the relationships between the ground motions and marine environmental conditions, an estimation of wave conditions near the cliff is needed. In the absence of

monitored wave conditions on the foreshore and at the cliff face, wave conditions from the Tees wave buoy (Figure 3.14) were modelled across the nearshore in front of the cliff, to estimate wave conditions as they shoal towards the cliff. This was done for the 1 km cross-shore profile of water depths seawards of the cliff (Figure 3.15). Because of the high tidal range at the study site and the long, shallow gradient foreshore, the proximity of waves to the cliff and their distribution of energy vary significantly over time. The breaking and surf zone can therefore extend 100s of metres seawards depending on tide and incoming wave conditions.

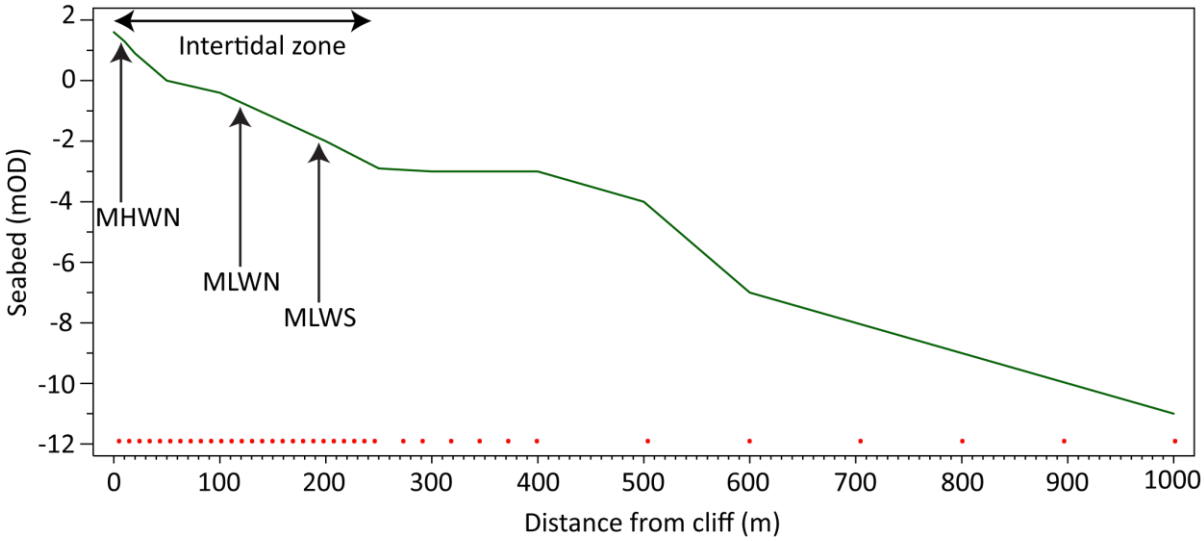

Figure 3.15: Cross-shore depth profile, 1,000 m seawards of the cliff. Red dots represent where wave characteristics were estimated by the model. The mean tide heights are those considering only tidal durations and not set-up and wave effects. MHWN = mean high water neap, MLWN = mean low water neap, MLWS = mean low water spring, MHWS is 0.94 m up the cliff face above the cliff toe (2.54 mOD).

Energy delivery from waves is most significant when waves are breaking (Sunamura, 1975). The breaking and surf zone delimits where maximum wave energy transfer to the coast occurs. Modelling wave conditions across the profile at the study site provides an estimation of wave characteristics such as height, breaking point, wave set-up, the widths of breaking, surf and swash zones, and their proximity to the cliff. Obtaining an understanding of these conditions, and their variation over time, is necessary to explain the variety of marine-related microseismic ground motions.

The wave transformation model used was based on that of Battjes and Stive (1985). The model considers energy dissipation of breaking random waves moving through a known profile of

water depths towards the coast. It does this by accounting for energy dissipation via turbulence that occurs in a wave bore as it breaks, an approach commonly used in wave transformation models (e.g. Thornton and Guza, 1983; Stive, 1984). This enables changes in wave energy flux (rate of energy density transfer) to be modeled through the profile, and the identification of the locations of increasing energy dissipation due to breaking. Decreasing water depth results in a reduced height at which waves break, and therefore in an increased proportion of breaking waves.

The model also accounts for changes in the mean water level that occur as waves break, called set-up and set-down, caused by the momentum flux of waves on sloping beaches / foreshores (Komar, 1998). This wave set-up and set-down is calculated by the model through the depth profile via integration of the momentum flux. As waves approach a sloping beach / foreshore and are preparing to break there is a shoreward increase in momentum which exerts stresses (called radiation stresses) that act in a number of directions (Davidson-Arnott, 2010). It is the shoreward radiation stress that represents the shoreward momentum flux which increases as the wave height increases towards the breakpoint (Davidson-Arnott, 2010). Wave set-up and set-down is a response to the changes in momentum flux as the wave approaches and passes the breakpoint and is caused as a pressure gradient or force is generated that balances the momentum flux (Komar, 1998). As the wave height increases and reaches the breakpoint there is an increase in momentum flux and a corresponding decrease in mean water level, i.e. set-down (Komar, 1998). Once the wave has broken the momentum flux decreases and there is a corresponding increase in mean water level, i.e. set-up (Komar, 1998).

The energy flux and momentum flux are integrated through the depth profile to calculate changes in wave height, wave set-down and set-up. The model runs through a 2D depth profile (Figure 3.15) determined from bathymetry data and calculates the outputs at 30 minute resolution, that of the input wave buoy data. Only waves travelling in onshore directions (285-125^{o}) were used in the model, which accounts for 75% of the wave buoy observations. However other than being onshore, wave directions were not considered in the 2D model. The input depths in the model profile vary through time to account for the tides.

A distance of 1000 m from the coast was used as the start point for the wave transformations as at this location, according to linear wave theory, the depths were still considered to be 'deep water' when compared to the wavelength. Therefore at this location, wave conditions were very similar to those at the buoy as the deep water meant no interaction between the seabed and waves had yet occurred. The spacing intervals of calculations in the profile were decreased

approaching the intertidal zone where more significant changes in wave characteristic occurred so more accurate model outputs for these areas could be attained (Figure 3.15).

Initial values of the wave height at 1000 m from the coast were obtained via shoaling the offshore significant wave heights measured at the wave buoy to 1000 m via standard Airy linear equation (see Equation A6.2 in Appendix 6). The energy dissipation is based on the fraction of waves that are breaking at each location in the depth profile, calculated from the ratio of wave height to estimated breaking wave height, based on a function of wave height to water depth. The model was created in Matlab. A detailed explanation of the modeling steps and equations used, together with the Matlab script, are provided in Appendices 6 and 7.

The model looped through the depth for the two-year wave dataset integrating both the energy flux and momentum flux to produce the key outputs, the rms (root mean square) wave height, wave set-up, energy flux and energy flux dissipation at each location within the profile (red dots in Figure 3.15). Once the waves broke then the predicted wave height was set to the breaking wave height for the rest of the depth profile up to the water's edge. This simulates real-world surf zones where broken waves travel through the surf zone and dissipate energy to the foreshore via bed friction and turbulence, resulting in decreasing wave height (Komar, 1998).

The modelled wave conditions provide an estimation of locations of wave breaking across the slope profile in front of the cliff. From these the likely spatial distributions of wave breaking, surf and swash zones and their associated energy dissipation processes have been identified. These zones match well with observations of calm and stormy conditions at the study site. However, it is important to remember that these are modelled conditions and in the absence of monitoring data of actual conditions within the profile the model outputs' accuracy cannot be tested.

3.4.2 Model quality

There are a number of limitations of the relatively simple wave transformation model used. The model accounts only for energy dissipation via turbulence that occurs during wave breaking, which is based on that of a wave bore (Stive, 1984). This means that it does not account for losses due to turbulence within surf bores that occur after breaking or to bed friction that occurs in the shallower parts of the surf zone and the swash zone. However, the decrease in wave heights that occurs shorewards of the first waves breaking indicates the occurrence of the surf zone and therefore the energy dissipation associated with it. The model also does not

account for energy dissipation due to refraction, reflection or diffraction whilst the waves shoal nor the effect of currents.

This relatively simple model approach was used because detailed bathymetry data was not freely available for the whole area in between the buoy and the coast. Also the 30-minute resolution and single location of the offshore wave buoy data meant that the resolution of input data was not sufficient for more complex wave refraction models, and that a 2D approach would need to be taken.

Also it is noted by Battjes and Stive (1985), who developed the original wave energy dissipation model that this was based on, that during large wave set-up gradients (which typically occur at the most seaward locations) that the set-up rise is too far seaward. The model was undertaken to produce estimations of wave conditions near the coast and at the cliff which could be used to explore the marine sources generating the ground motions. Therefore it is the relative values of wave conditions over space and time that are important for this analysis, rather than the absolute. The model outputs are deemed to provide a sufficiently accurate representation of observed wave conditions and therefore provide an extremely useful dataset to help explore the sources generating the microseismic ground motions of the cliff.

3.5 Field site

3.5.1 Location and geology

The study site is located at Boulby on the North Yorkshire coast, UK, approx 1.6 km north up the coastline from the village of Staithes (Figure 3.16).

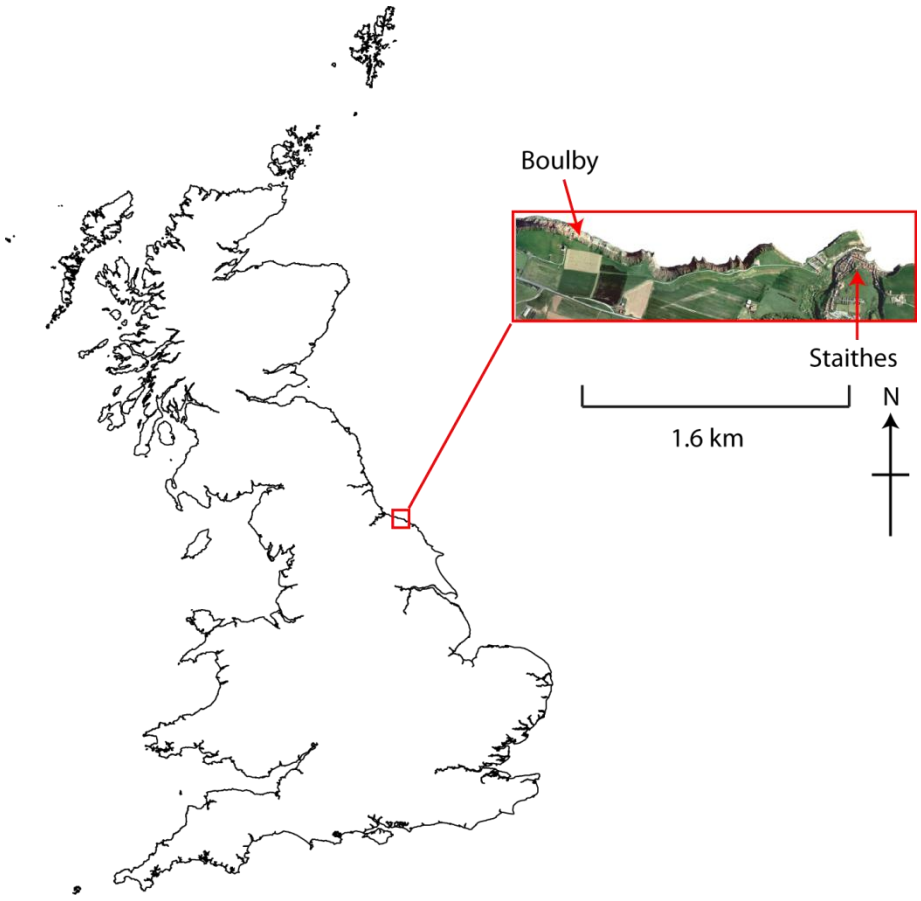

Figure 3.16: Field site location within Great Britain. Inset: location of Boulby relative to the village of Staithes.

The cliff is 70 m high and is formed of Lower Jurassic (Lias) rocks formed by sediments laid down by varying sea levels between 199.6 – 175.6 Ma (Rawson and Wright, 1992). The base of the cliff consists of mudstone overlain by silty shales and narrow layers of harder siltstone, sporadic ironstone and limestone, all of the Redcar Mudstone Formation, overlain by sandstones and siltstones of the Staithes Sandstone Formation (Rawson and Wright, 1992) (Figure 3.17a). The bedding layers between Boulby and Staithes dip gently from north to south. The rock is overlain by a glacial till approximately 10 m in thickness.

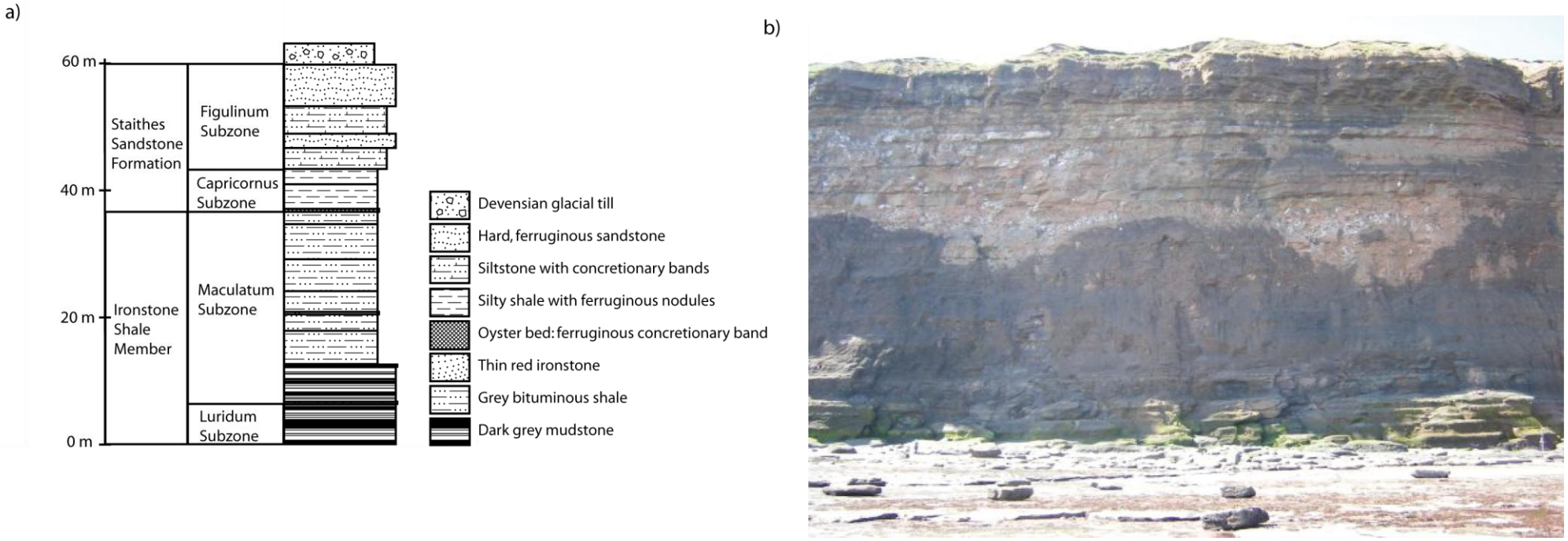

Figure 3.17: Boulby cliff: a) Schematic of the geology along this stretch of coastline; b) Photo of the monitored width of cliff at Boulby.

From the cliff photo it can be seen that the more resistant mudstone at the toe and the sandstones at the cliff top protrude beyond the weaker shales that lie between them (Figure 3.17b). When stood near the cliff an almost continuous stream of small fragments of shale can be heard and seen to be falling from the cliff face. Rosser et al. (2007) calculated different retreat rates for each of the key rock types from a 32 month dataset of monthly TLS monitoring of the coast between Boulby and Staithes, which corresponds well to the expected rates according to the relative strength material, structure and processes exposure: 0.0022 m a^{-1} for the mudstone; 0.0025 m a^{-1} for the shale; 0.002 m a^{-1} for the siltstone; and 0.006 m a^{-1} for the sandstone. From a 20-month monitoring period of the same stretch of coast, using a combination of TLS and photogrammetry, Lim et al. (2010a) calculated an average annual retreat rate of 0.065 m a^{-1} across this stretch of coastline and for the Boulby cliff a rate of 0.009 m a^{-1}.

Throughout the cliff profile the rock surfaces are heavily weathered, the lower sections of the mudstone surface are commonly smooth, attributed to abrasion from the sea. The mudstone also features a number of large concavities at different heights within the lower sections of the layer. Above the friable shales, the more resistant blocky siltstones and sandstones feature open joints. The upper parts of the cliff face are commonly stained red from till washed or blown over the cliff top, with recent failures leaving clean, easily distinguished, scars.

3.5.2 Geomorphology, marine and climate conditions

The mudstone at the base of the cliff makes up approximately the lowest 15 m of the cliff and is the only layer exposed directly to the sea and therefore marine erosive processes. The cliff has a wide mudstone foreshore which is the upper part of a gentle slope offshore. The foreshore is considered to be the intertidal zone which covers the upper 250 m of the slope. The foreshore has two steps of approx 0.2 m at around 50 and 100 m; the step at 50 m demarks a significant increase in foreshore gradient leading to the cliff toe (Figure 3.15).

The tidal range at the study site is macro-tidal at 6 m and tides are semi-diurnal. The gentle gradient of the foreshore combined with the large tidal range where MHWS reaches 0.94 m up the cliff face and MLWS is 200 m down the foreshore means the cliff exposure to marine conditions varies dramatically over a tidal cycle (Figure 3.18). This also means that all sections of the cliff are exposed to subaerial weathering processes, although for varying durations and the relative importance of the processes will vary. The lower zone reached by the sea is vulnerable

to erosion by wetting and drying processes as it is constantly submerged and exposed, in addition to salt weathering processes – possibly aided by the cyclical wetting and drying. Frost weathering is unlikely to occur in the lower sections of the cliff exposed to the sea due to the regular inundation by the sea and presence of salt, however these processes are likely to be more important in the upper sections constantly exposed to air temperature and moisture conditions. Wind erosion is also expected to be greater in the upper sections of the cliff more regularly exposed to strong onshore winds, which field evidence has shown also travel vertically and horizontally across the cliff face, producing multi-directional forces acting on the cliff. Across the monitored width of cliff no obvious seepage occurs, although to the immediate west of the scan water seeps almost permanently from the full height of the profile. To the immediate east of the monitored width of cliff lies a highly fractured tension zone which visibly extends approx half way up the cliff face.

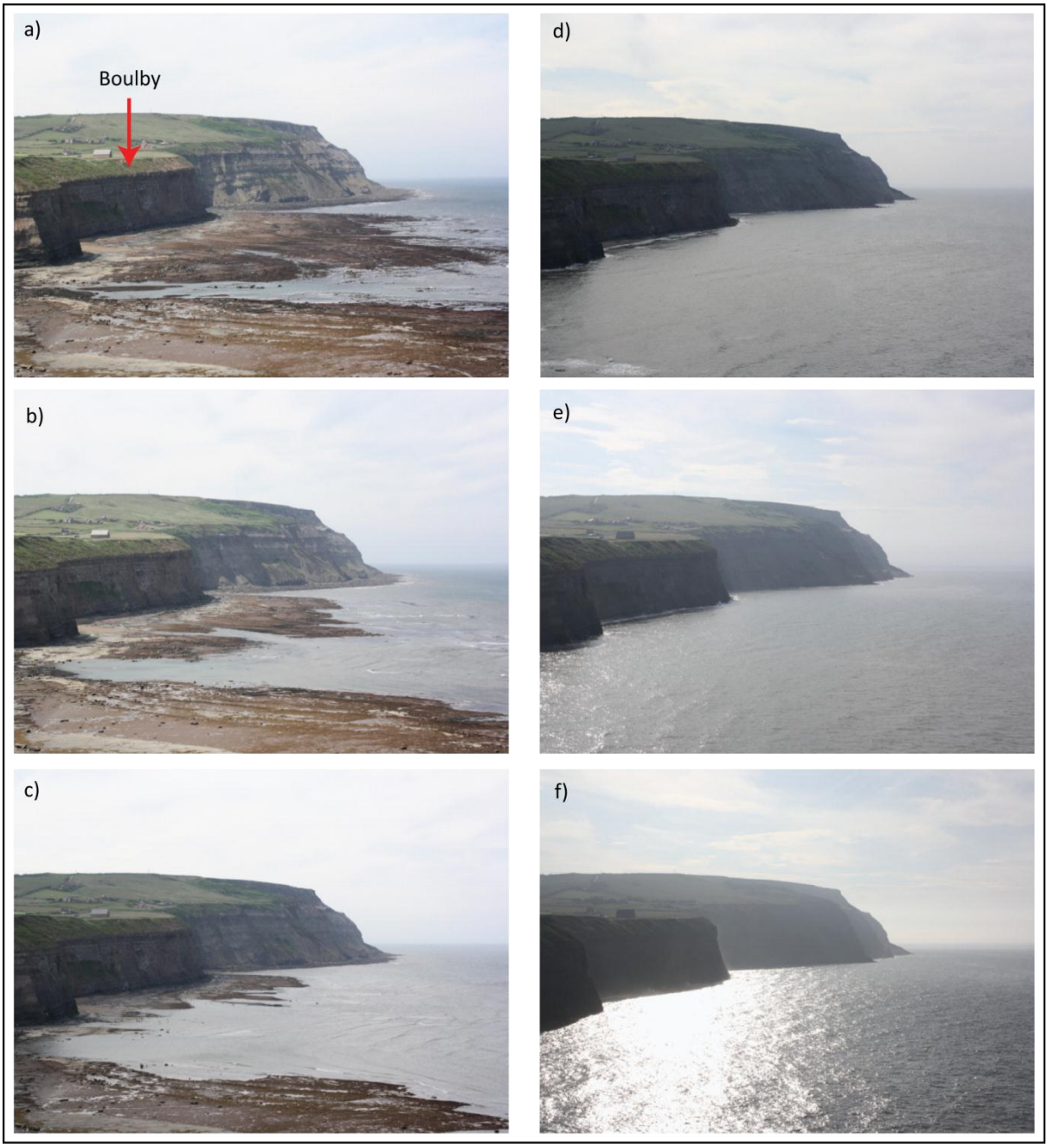

Figure 3.18: Spring tide heights at Boulby cliff: a) Low spring tide, approximately 200 m down the foreshore (-2 mOD); b) Rising spring tide moves across the foreshore; c) Mid spring tide, approximately 50 m from the cliff toe (0 mOD); d) Rising spring tide reaches cliff toe (1.6 mOD); e) High tide rises up the cliff face; f) High spring tide, approximately 1 m up the cliff face (2.5 mOD).

Large variations in wind velocities and directions occur over the North Sea with strong seasonality due to the North Atlantic Oscillation (NAO) (Ospar, 2000). These winds have a significant effect on the North Sea marine climate, determining wave heights, storm surges and currents, all of which have morphological implications. The North Sea marine climate is

considered to be a storm wave environment (Davies, 1980) and, although wave conditions are highly variable, during large storms local residents have said shaking of the cliff can be felt. The maximum fetch across the North Sea is approximately 860 km, which limits the heights of waves that can be generated within the North Sea basin. However, as the North Sea is open to the Atlantic, larger waves generated there do travel into the North Sea. The estimated 50-year return period significant wave height that reaches the NE England coast is 10 m, and estimated 50-year return period positive storm surge heights are 1.5 m (Huthnance, 1991).

The UK climate is heavily influenced by the pressure gradients of the NAO which determines the strengths of the prevailing westerly winds (Ospar, 2000). At the study site the greatest wind velocities occur during the winter months of November to March, as do the lowest air temperatures (Table 3.2). The north east coast is drier than most of the UK with an average annual rainfall of 545 mm. However cloud cover is typically high all year. Snow may occur during winter, and sea fog can occur all year round although clears up more quickly on summer days as temperatures increase. During the two-year monitoring period summer storms resulted in high intensity precipitation, generating some of the highest monthly precipitation values.

Table 3.2: Summary of monthly climate conditions at the Loftus meteorological station during the two-year monitoring period July 2008 – July 2010.

Month	Temperature (^{o} C)			Wind velocity (ms^{-1})		Relative humidity (%)	Precipitation (mm)
	Min	Mean	Max	Mean	Max	Mean	Mean
Jan	-4.6	2.28	9.7	6.73	20.6	90.55	36.7
Feb	-4	2.97	11.3	5.02	12.88	88.88	41
Mar	-3.2	5.74	16.1	6.01	18.54	82.12	27.3
Apr	-0.4	8.21	19.5	4.86	15.97	81.46	21.4
May	0.2	9.93	24.3	5.21	16.48	83.51	12.8
Jun	4.9	13.03	25.4	4.06	13.39	84.85	51.2
Jul	9	15.54	26.7	5.41	15.45	82.44	72.04
Aug	9	15.38	24.5	5.49	14.94	85.17	64.9
Sept	6.9	12.96	23.3	5.32	15.97	86.56	42.6
Oct	-0.5	9.62	18.7	6.53	20.09	89.33	45.4
Nov	-2.4	6.81	14.1	7.64	20.09	92.45	82.7
Dec	-7.1	3.35	11.3	5.93	17.51	93.02	46.9

A detailed examination of the marine and climatic conditions at the site during the monitoring period is presented in Chapter 5.

3.5.3 Human influences

The North Yorkshire coastline has been heavily influenced by mining and quarrying activity, both of the foreshore and cliff and deeper underground. During the 19th and 20th centuries the foreshores and cliffs were quarried for alum shale, ironstone and jet, resulting in lowering of foreshore platforms (Rawson and Wright, 1992). Evidence for this around the study area includes cart rutways, channels and protruding intact blocks of rock that indicate previous foreshore heights. It is unknown what, if any, quarrying activity took place at the foreshore at Boulby. However, mineral exploitation may explain some of the steps observed in the foreshore. Since the 1970s Cleveland Potash have been mining potash and salt deposits at depths below ground of around 1,000 m extending both kilometres inland and underneath the cliffs and out to sea. The mine buildings and shafts are situated approximately 600 m inland of the study cliff, and the tailings shaft sits in the field at the cliff top approximately 100 m from the cliff edge. During the mine's operation, a wide gradual subsidence bowl of maximum depth = 0.45 m centred roughly over this site of has developed since the late 1970s (Lim, 2006). Comparisons of erosion rates calculated by previous studies of this stretch of coast have however actually identified this section of cliff near the maximum subsidence, to be lower than the cliffs at Staithes where there is negligible subsidence, believed to be due to the greater resistance of the mudstones that form the cliff toe at Boulby as compared to the much weaker shales that form the cliff toe at Cowbar and Staithes (Lim et al., 2010a).

Whilst coastal management works have been undertaken around Staithes, there are no such works at Boulby.

3.5.4 Site selection

As discussed in Chapter 2 there have been a number of other studies into erosion of this stretch of coast, notably the long term monitoring using TLS undertaken by Rosser et al. (2007) and Lim et al. (2010a). The results of these studies challenge previous well-entrenched perceptions of coastal cliff change behaviour and indicate that cliff change is considerably more complex and diverse over time and space than considered by traditional cliff toe models, such as Sunamura

(1992). Key findings were: rockfall activity is distributed across the entire cliff face and not mainly at the cliff toe; there is an almost-constant activity of small scale rockfalls; and there is an absence of cliff toe notching or resulting cantilever failure. These behaviours have not been identified before because of the previous absence of techniques capable of monitoring the entire cliff face. The lack of statistical relationships between the observed rockfall behaviour and regional-scale environmental datasets has left questions regarding the environmental controls of cliff rockfall activity. This study therefore develops on from these previous studies and sets out to explore environmental controls of cliff rockfall activity via the application and examination of microseismic ground motions of the cliff that represent environmental forces acting on it, combined with monitoring of rockfall activity using TLS.

In order to continue the existing five-year long dataset of TLS monitoring, a site between Staithes and Boulby was to be chosen. The high tidal range of this stretch of coast extends up the cliff face, meaning that seismometers had to be installed at the cliff top. A site was needed where access to the cliff top was available, where there was sufficient space for an array of seismometers to be installed in a line normal to the cliff edge, and where there would be a low risk of disturbance and vandalism. Because of the specific requirements of the seismometers field set-up the Boulby site was chosen. CPL gave permission for the use of their field at the cliff top, which was large enough to accommodate the whole array, and was much more secure than other available sites.

3.6 Summary

The approaches, equipment and techniques used by the study described above have been used to address the research aims and objectives of this thesis, to improve understanding of the environmental controls of coastal cliff erosion. For two years the cliff top microseismic ground motions and cliff face rockfalls have been monitored in order to better constrain the environmental conditions directly at a cliff and the cliff response to these forcing mechanisms. The high tidal range and wide, gentle gradient foreshore, storm wave environment and strong seasonality of environmental conditions means that the cliff at Boulby is exposed to highly varied marine and subaerial conditions and therefore provides an excellent opportunity to explore how hard rock cliffs respond to a wide range of conditions. The TLS results of this study add to an already existing five-year dataset of hard rock coastal cliff erosion, which as it develops can provide us with continued improvements in understanding how hard rock cliffs change, an area which has previously been relatively neglected due to difficulties in monitoring

such steep slopes and comparatively slow rates of change. Microseismic ground motions are anticipated to provide an exciting, and previously unattainable, insight into the environmental forces acting on the cliff. A technique that from a cliff top location can provide a high-resolution representation of conditions both directly at the cliff, and more widely, and from marine and subaerial sources, providing a measure of both relative environmental forcing and cliff ground motion response.

In the following chapters the data produced from these cliff monitoring techniques, and from regional-scale datasets, will be examined and relationships between them explored, in an attempt to clarify environmental conditions at the cliff, unpick the interactions between environmental forcing and cliff materials, and to suggest the failure mechanisms producing the observed cliff behaviour.

Chapter 4: Exploring coastal cliff microseismic ground motions

The two-year dataset of coastal cliff microseismic ground motions collected during this study represents environmental conditions and resulting processes near to the cliff. The data provides an opportunity to gain insights into the interactions between local marine and atmospheric conditions acting upon the cliff. Fundamentally, the improvements offered by this dataset compared to previous coastal cliff studies is that rather than measuring environmental conditions themselves, it measures the cliff microseismic response to all external factors simultaneously. This has the benefit of enabling examination of the relative role of a variety of environmental conditions in generating microseisms, which is not reliant upon assumptions about the ways in which environmental data represents conditions actually at the cliff face.

The aim of this chapter is to explore and describe the different frequencies of ground motions monitored at the cliff. The data demonstrate significant variability throughout the two years, and within this a number of distinct frequency bands have been identified and compared to the corresponding time series of environmental conditions that are hypothesised to generate these microseisms. Specifically, the aim of the chapter is to identify and characterise microseismic signals, and to consider their variability through the monitoring period. These are examined in more detail in Chapter 6 via quantitative analysis in order to explore the processes and mechanisms generating observed ground motions.

4.1 Frequency bands of cliff ground motions

Spectrograms depict ground motions power across the range of frequencies recorded, and how these vary over time. Exploring ground motion in the frequency domain enables examination of varying frequencies and their response to environmental conditions. In Chapter 3 (Section 3.1.3), the frequency ranges of ground motions generated by various environmental phenomena was briefly described. Using this previous work, and comparing the time series of frequency power with tide, wave and wind conditions near the site, the environmental conditions generating the different ground motion frequencies can be identified. This approach both allows the relative contribution of the various forces and efficacy of the distal monitoring in representing the conditions at the cliff to be assessed.

A number of distinct frequency bands have been identified in the cliff ground motion data (Figure 4.1), as outlined below. Some ground motion frequencies are generated by natural

sources, whilst others are anthropogenic. For the remainder of the thesis the codes assigned to each frequency band are used for brevity.

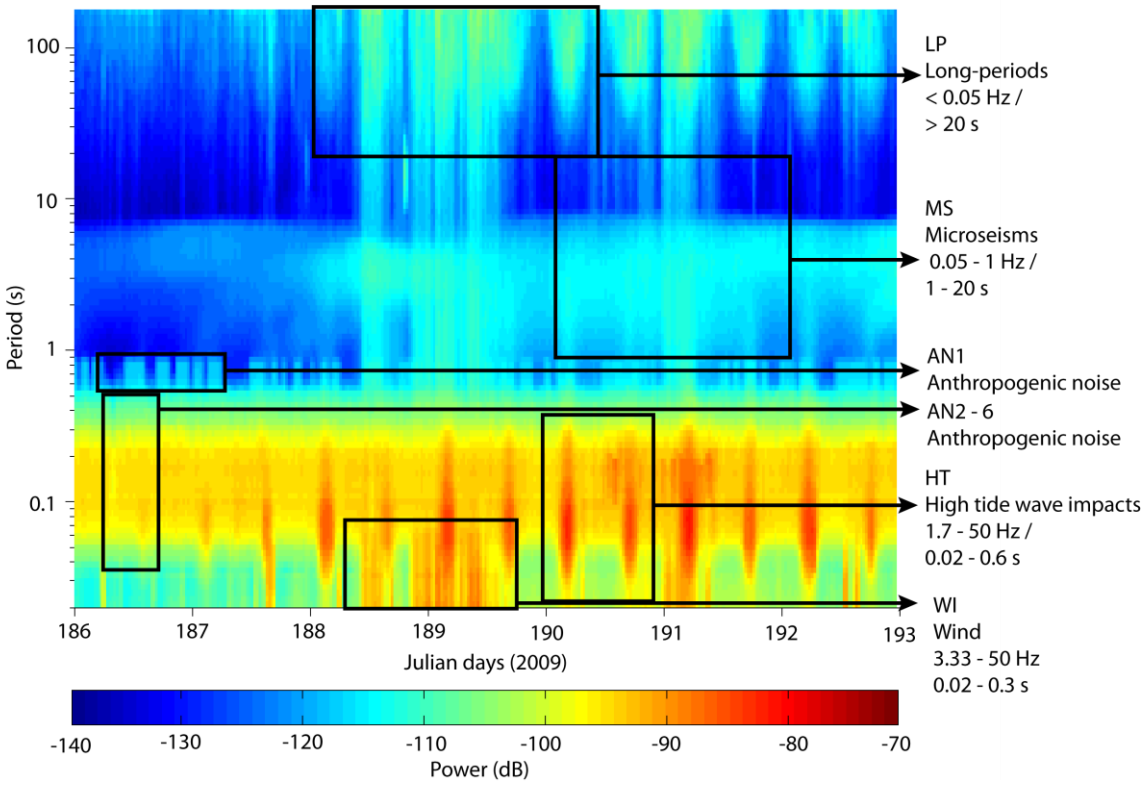

Figure 4.1: An example spectrogram from the dataset and the different bands of ground motion frequencies observed. Frequency power is presented in decibels (dB) calculated as $10 \log_{10}((ms^{-1})^2/Hz)$. Each of the black boxes highlights an example of the typical temporal and power characteristics of each frequency band.

Long-period frequency band (LP): There is a distinct range of long-period signals < 0.05 Hz (> 20 s), which have a distinct pattern, differentiating these from the microseisms (MS) (1 – 0.05 Hz / 1 - 20 s) by a band of low powers (approximately -130 dB) at around 0.1 Hz / 10 s. Increases in LP power often occur with simultaneous increases in the microseism (MS) frequency range and high power high tide (HT) or wind (WI) frequencies (explained below). The frequency of these LP signals and their association with tides and incoming wind and wave characteristics suggests that the LP frequency band represents long-period ocean waves called infragravity waves. Infragravity waves lie within the period range of 0.05 – 0.003 Hz / 20 - 300 s and are generated as groups of swell waves from distant storms arrive at the coast resulting in 'surf beat' an increase and decrease of the mean sea level at the period of the groups (Munk, 1949; Tucker, 1950).

Microseism frequency band (MS): Microseisms are widely acknowledged to be generated by sea waves near the coast, and take two forms:

- ***Primary microseisms*** are microseismic waves that have the same periodicity as the incoming ocean waves (Haubrich et al., 1963);
- ***Double frequency (DF) microseisms*** are generated by the constructive superposition of waves of the same periodicity travelling in opposite directions (Longuet-Higgins, 1950). Waves travelling from different directions can be generated either by storms of varying wind directions generating waves heading in multiple directions or by the meeting of landward waves with those reflected from the coast (Longuet-Higgins, 1950).

The microseisms can be clearly distinguished in the spectrogram in the period range of 1 - 0.05 Hz / 1 - 20 s. The MS frequency band power corresponds well to the increased power at the high and low frequency bands (non-anthropogenic) e.g. LP, HT and WI frequencies, which are all associated with incoming waves and / or wind.

Anthropogenic frequency band (AN): Within the high-frequency range 1.1 - 25 Hz / 0.04 - 0.9 s there are six discrete frequency bands that have constant frequency power. This suggests that these features are generated by anthropogenic activity, the most likely source of which is the Boulby mine, which functions 24 hours per day. As a result, these anthropogenic signals are not considered further in the analysis:

AN1: There is an intermittent short-period signal tightly constrained within the frequencies 1.1 - 2 Hz / 0.5 - 0.9 s. Both the frequency range and the power values have an 'on / off' nature, with powers at around -115 dB or -130 dB, rather than the gradual increase and decrease of the signals from natural sources. It is possible that this signal is a response to a pump or motor in the nearby tailings facility, approximately 150 m from the monitoring site.

AN2 - 6: Between 2 - 25 Hz there are five frequency bands whose power values vary throughout this frequency range but remain constant throughout the monitoring period.

There are two different types of high-frequency bands that are clearly driven by environmental conditions, rather than anthropogenic sources. These are high-power events that overlap with the high-frequency anthropogenic signals (AN1 - 6). Naturally generated high-frequency signals have increases in power that coincide with increased power in the microseism (MS) and long-period (LP) bands, suggesting that the signals are related:

High tide frequency band (HT): Regularly occurring high-power signals around -85 to -95 dB are monitored in the frequency range 1.7 - 50 Hz / 0.02 - 0.6 s. As shown later, these occur during

some, but not every, high tide. Adams et al. (2005) observed a coastal cliff ground motion signal at 20 Hz / 0.05 s representing high-frequency ringing of the cliff mass in response to direct wave impacts against the toe. It is anticipated that the HT frequency band observed here represents the same phenomenon.

Wind frequency band (WI): Sporadic increases in power that have similar values to the high tide frequencies (HT), occur within the 3.3 - 50 Hz / 0.02 - 0.3 s frequency band. Young et al. (1996) identified that wind velocities of 3 ms^{-1} and stronger result in a significant increase of seismic energy delivery to the ground surface at frequencies of 15 - 60 Hz / 0.066 - 0.017 s, although found signal amplitude to be non-linear with wind velocity. Other studies (e.g. Bungum et al., 1985; Given, 1990; Gurrola et al., 1990), observed wind seismic signals at lower frequencies, reaching as low as 1 Hz for winds above 3 ms^{-1} (Withers et al., 1996). Wind velocities above 3 ms^{-1} are frequent at the study site. The intermittent, high-power, high-frequency and stochastic nature of this frequency band, and commonly its coincidence with wave-generated frequencies, suggests that this frequency band represents the influence of wind upon the monitored cliff.

4.2 Exploring the time series of frequency band characteristics

To examine the seismic signals identified above in more detail, the ground motion data have been considered at different timescales (days, months and the full two-year dataset). For each monitoring period examined, the data are presented as spectrograms alongside a time series of tide, wave and wind conditions monitored near the site, to identify the environmental conditions generating each microseismic frequency band. The ground motion velocities are also presented, which represent a combined seismic signal composed of all the frequencies recorded. The three ground motion components (N, E and Z) and signal power differences between them are examined to characterise microseismic response to environmental conditions.

4.2.1 Daily frequency band variations

Three individual days with a range of environmental conditions are presented to showcase the diversity of environmental forcing at the cliff and resultant ground motion characteristics generated (Figure 4.2). These are examples with spring tides, demonstrating the effects of wave heights and wind velocities.

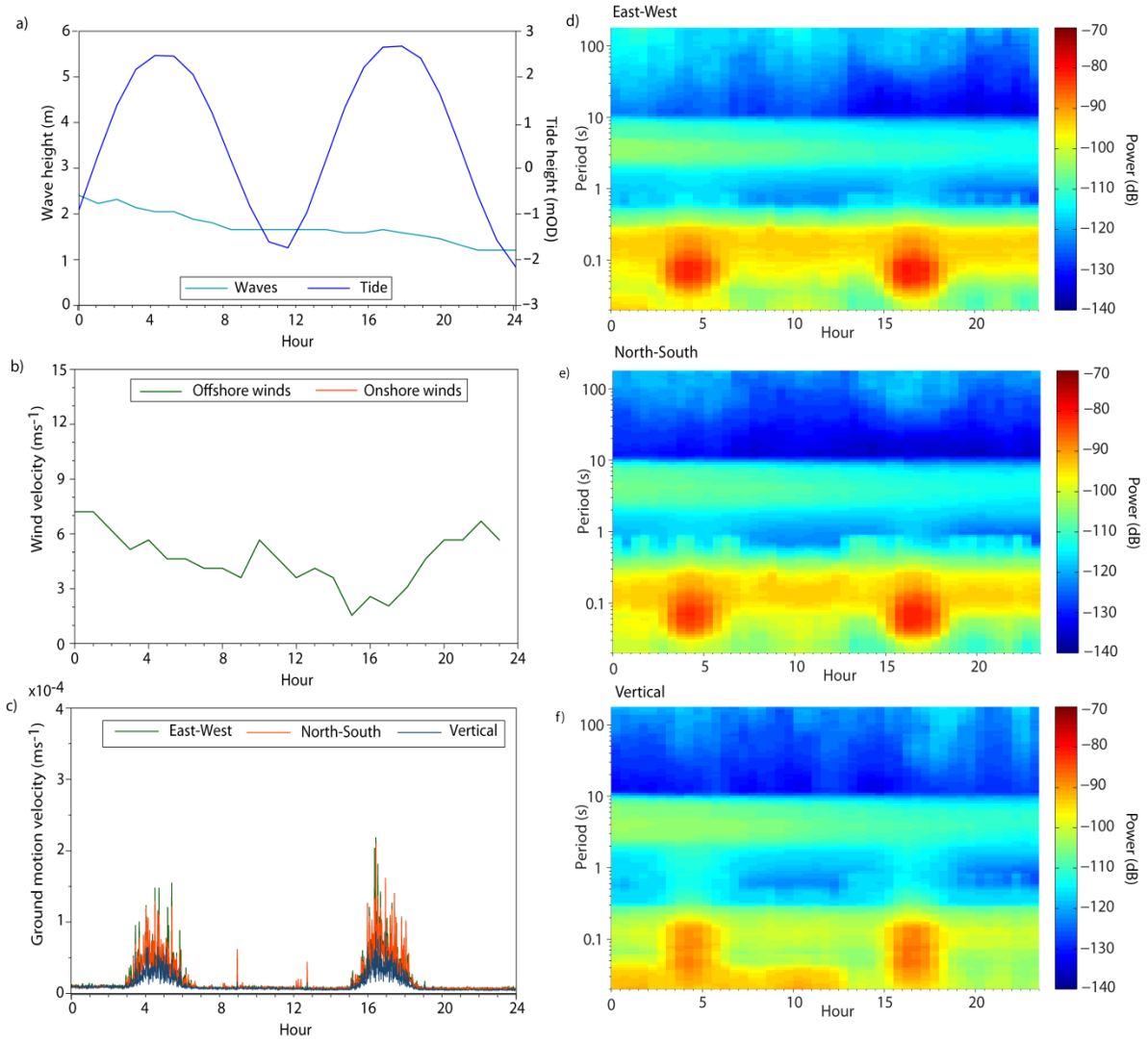

Figure 4.2: Spectrograms and environmental data for 04/12/09. a) Hourly max tide height modelled for Boulby and hourly max wave heights obtained from the Tees wave buoy (Figure 3.14); b) Mean onshore and offshore wind speeds monitored hourly at Loftus (Figure 3.14); c) Ground motion velocity for all three components; d) East-west component spectrogram; e) North-south component spectrogram; f) Vertical component spectrogram.

The most distinctive features in this first example are the two high-frequency high-tide (HT) signals evident in the spectrograms for each component (Figure 4.2d, e & f), that match the time of the high tides (Figure 4.2a). The high-frequencies of these signals suggest a ringing response of the cliff to direct wave impacts enabled by increased inundation depths during high tides, as suggested by Adams et al. (2005). Each HT signal lasts four hours, which corresponds to the tidal inundation of the cliff toe that occurs at heights above 1.6 mOD. Throughout both HT events, signal power gradually increases, peaks, then decreases, indicating that as the tide rises and falls, so does the rate of energy transfer to the cliff.

The increased power associated with high tides extends into longer-periods of 1 - 0.5 Hz / 1 - 2 s. This suggests that when the sea is at the cliff it generates cliff ground motions across a wide frequency range, which may reflect the different processes acting on, or near to the cliff during high tides. Energy delivery to the cliff in this frequency band is clearly modulated by tidal height.

High power in the WI frequency band in the vertical component (Z) (Figure 4.2f) is observed during the first half of that day, but barely features in the horizontal components (E and N) (Figure 4.2d & e). During this time wind velocities were above 3 ms^{-1}, the same threshold velocity that has been identified by a number of studies to result in seismic noise (e.g. Withers et al., 1996; Young et al., 1996). WI signal power does not show a clear relationship with wind velocity, with increasing velocities in the later hours not matched by increased power in the WI frequency band. This may be due to variations in wind direction, or may indicate that the wind data doesn't accurately represent conditions at the cliff, or reflects the non-linear relationships observed elsewhere (Young et al., 1996).

The ground motion velocity (Figure 4.2c) depicts the total ground motion of the cliff, across all the frequencies within the spectrograms. Interestingly, the only significant features apparent in the dataset are the two high tides. These reflect the higher power in the long-periods LP and high-frequency HT bands associated with the timing of the high tides.

In the second example day, increased signal power occurs in all naturally generated frequency bands across the spectrum (Figure 4.3). The power increases during the day, suggesting that a storm reached the coast which increased in magnitude as the day progressed. The high power of the WI frequency band reflects the high onshore wind velocities (Figure 4.3b). The high power in LP, MS and also HT probably represent increased wave energy resulting from the increased wave heights (Figure 4.3a), which are transferred towards the cliff by the strong onshore winds.

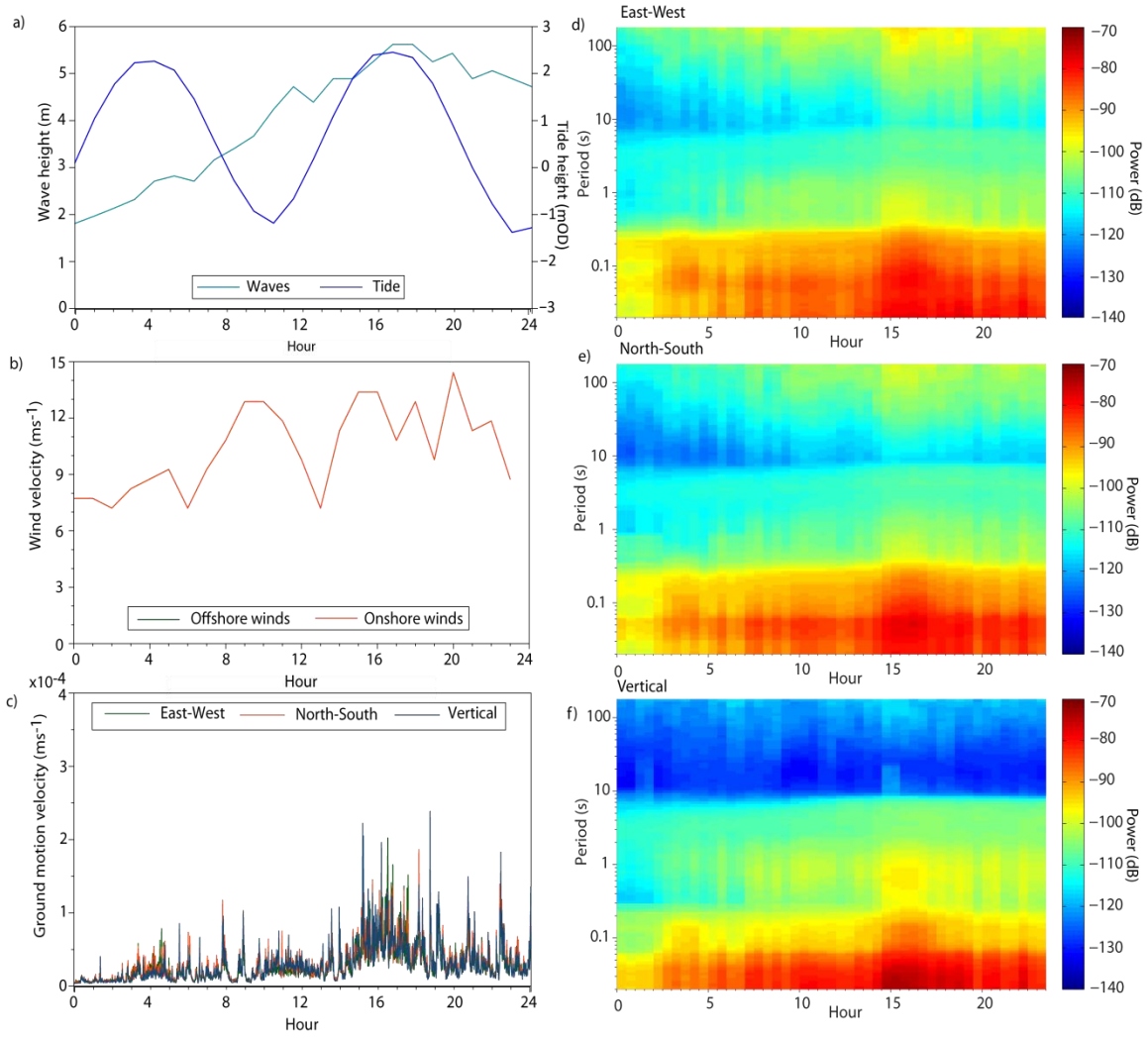

Figure 4.3: Spectrograms and environmental data for 17/12/09. a) Hourly max tide height modelled for Boulby and hourly max wave heights obtained from the Tees wave buoy (Figure 3.14); b) Onshore and offshore wind speeds monitored hourly at Loftus (Figure 3.14); c) Ground motion velocity for all three components; d) East-west component spectrogram; e) North-south component spectrogram; f) Vertical component spectrogram.

The increased power across the LP and MS frequency bands suggests ocean waves of a range of periods arrive at the coast. The longer period MS and LP signals indicate the arrival of swell waves that are generated at distant (> 100 km) locations, and the shorter periods of the MS range indicate the presence of waves that are generated more locally. The increased power across all frequency bands throughout the later part of the day match the timing of the more energetic wind and wave conditions (Figure 4.3). This suggests storm surge is forcing the waterline closer to the cliff than would be the case under purely tidal forcing. This enables more energy to be transferred further up the foreshore slope and nearer to the cliff toe as compared to a normal tide.

In all frequencies the maximum power occurred during the afternoon high tide, which coincided with peak wave heights and near maximum wind velocities. This may suggest that the increased sea levels associated with the storm surge enabled the high tide to transfer wave energy higher up the cliff, resulting in more energy transfer directly to the cliff face.

The increased high tide HT power again extends into longer periods, up to 1 - 2 seconds, particularly in the vertical Z component (Figure 4.3f). This may indicate wave processes (such as wave breaking or generation of void pressures) either directly at the cliff face, or on the foreshore slope directly beneath the cliff toe. The HT frequency band during the tidal high is not as distinct as in the first day example above (Figure 4.2) due to the higher power in the high frequency band occurring throughout the day. The high powers in these high frequencies suggest that the greater wave energy generates the HT ringing phenomenon on the foreshore when water levels were high as a result of the storm surge accompanied by large waves. The power at the higher frequencies most likely represents the marine driven HT ringing, in combination with increased wind energy transfer to the cliff, as represented by the overlapping frequencies of the WI band (Figure 4.3).

The LP signals in this example, particularly in the horizontal directions, indicate that during storms increased amounts of long-period infragravity wave energy is delivered to the coast. The suggested storm surge scenario means that this energy is dissipated in particular in the shallow waters on the near-horizontal foreshore, as observed by a number of previous studies (e.g. Guza and Thornton, 1982; Holman and Sallenger, 1985).

The ground motion velocity depicts the increase in energy delivery in the second half of that day, with the greatest velocities occurring during the combined high tide, larger waves and wind speeds (Figure 4.3c). The similar velocities of the Z, N and E components suggest it is the high power, high frequency wind (WI) and wave (HT) frequency bands that contribute most to the overall ground motion velocity, particularly as the long-period (LP) Z component power is much lower than that monitored in the horizontal components.

Examining the directions of ground motion of each frequency band can provide insight into the processes generating the ground motions. To identify the dominant directions of each of the frequency bands ground motions, the spectrograms of the different components were subtracted from one another and the differences in power between the components examined (Figure 4.4):

- The microseisms (MS) frequency band produces greater power in the vertical direction as compared to the horizontal (Figure 4.4b & c). This is because these signals result from

the interaction of vertically-acting, wave-driven pressure fluctuations with the seabed (Friedrich et al., 1998);

- The wind frequency band (WI) power is also stronger in the vertical component, the direction upon which wind seismic noise studies focus (e.g. Young et al., 1996; Withers et al., 1996), suggesting the signal is typical of wind seismic signals generated at the ground surface;
- The anthropogenic AN1 - 6 and high tide (HT) frequency bands have greater power in both horizontal components. The dominance of the HT frequencies in the horizontal directions is believed to be due to this being the direction of loading by the waxing and waning tide, and due to wave impacts acting horizontally against the cliff toe;
- The long-period (LP) frequency band power is greatest in the horizontal component, and notably so in the E - W direction in this example. This suggests that this is the dominant incoming direction of swell and infragravity waves during this period. The dominance of horizontal ground motion is believed to represent loading of the foreshore with long-period wave energy by tides;
- Within the difference images (Figure 4.4) it is clear where the instrument noise floor is reached at approximately 10 s by the sudden change in dominant ground motion direction (from vertical to horizontal once periods > 10 s). This feature occurs because the noise floor of the Z component occurs at higher powers than in the E and N components and therefore a greater proportion of the Z component MS and LP signal power is obscured.

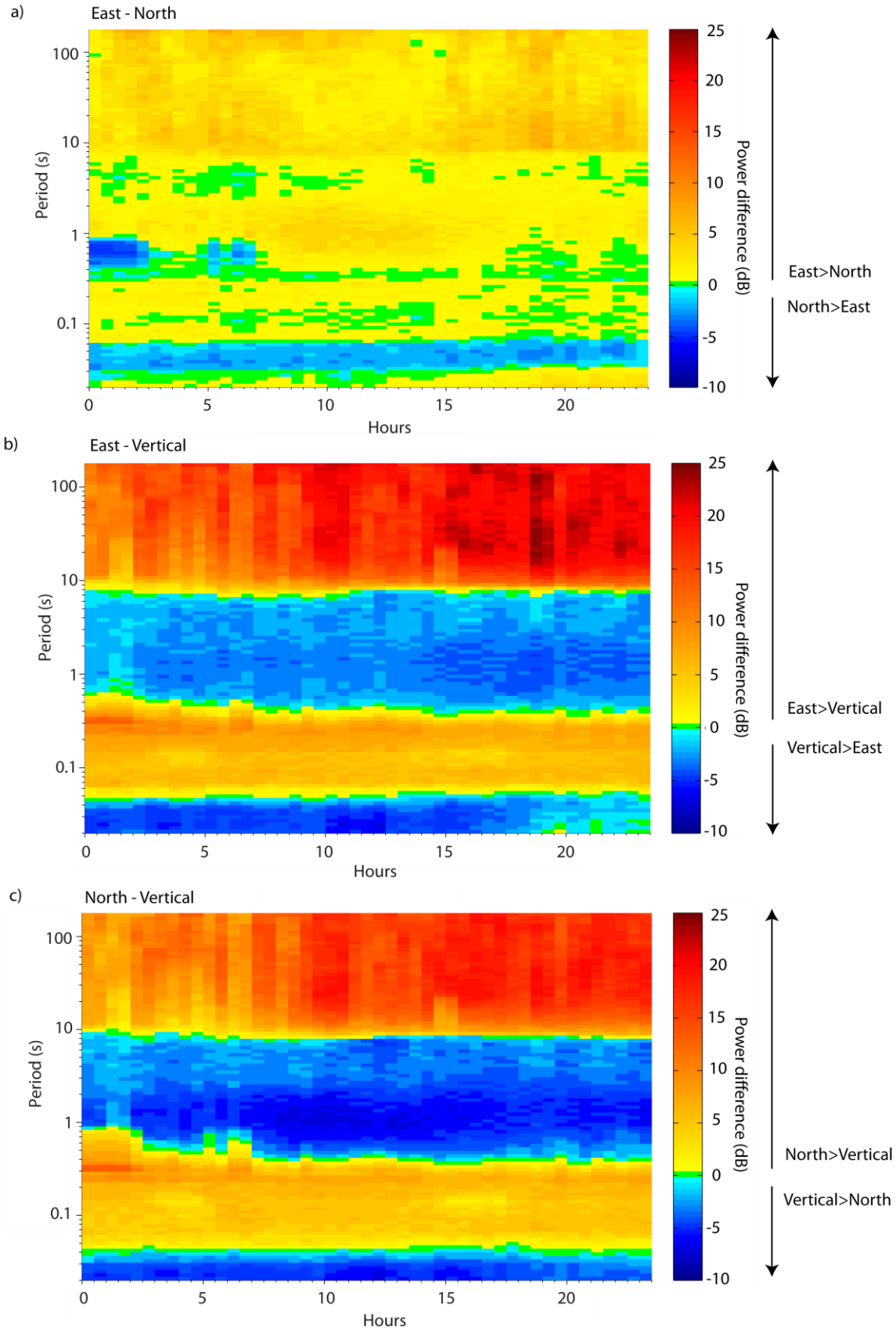

Figure 4.4: 17/12/09 Differences in power between the a) E and N components; b) E and Z components; c) N and Z components.

The third example day shows relatively quiet environmental conditions and corresponding low signal power in each of the ground motion frequency bands (Figure 4.5). Despite being a spring tide with heights similar to those of the other example days (Figure 4.5a), there is no discernable HT signal. This is likely due to the low wave heights and therefore a lack of incoming wave energy. This example shows that energy transfer to the cliff is not controlled only by tide height, and that energy transfer is dependent on the wave conditions that occur during the high tides. This is significant as tidal inundation models are often used within cliff erosion models to indicate where and when wave energy, and therefore where erosion, is focussed on the cliff face (e.g. Trenhaile and Layzell, 1981; Walkden and Dickson, 2008). This result demonstrates that if erosion is a function of marine energy, then the relative efficacy of energetic as compared to non-energetic marine conditions is not expressed in inundation models alone.

There is no WI signal generated by the low onshore / offshore winds, which here are typically below 3 ms^{-1} (Figure 4.5b), the velocity suggested by Young et al. (1996) to be the threshold for generating seismic noise at the ground surface.

The ground motion velocity graph (Figure 4.5c) depicts the low velocity ground motions during this day due to the low power signals across the whole spectrum of frequencies monitored. There are no significant peaks above background levels. This example demonstrates that background levels of ground motions are generated by anthropogenic AN and low power MS and LP activity, which all vary little throughout the day.

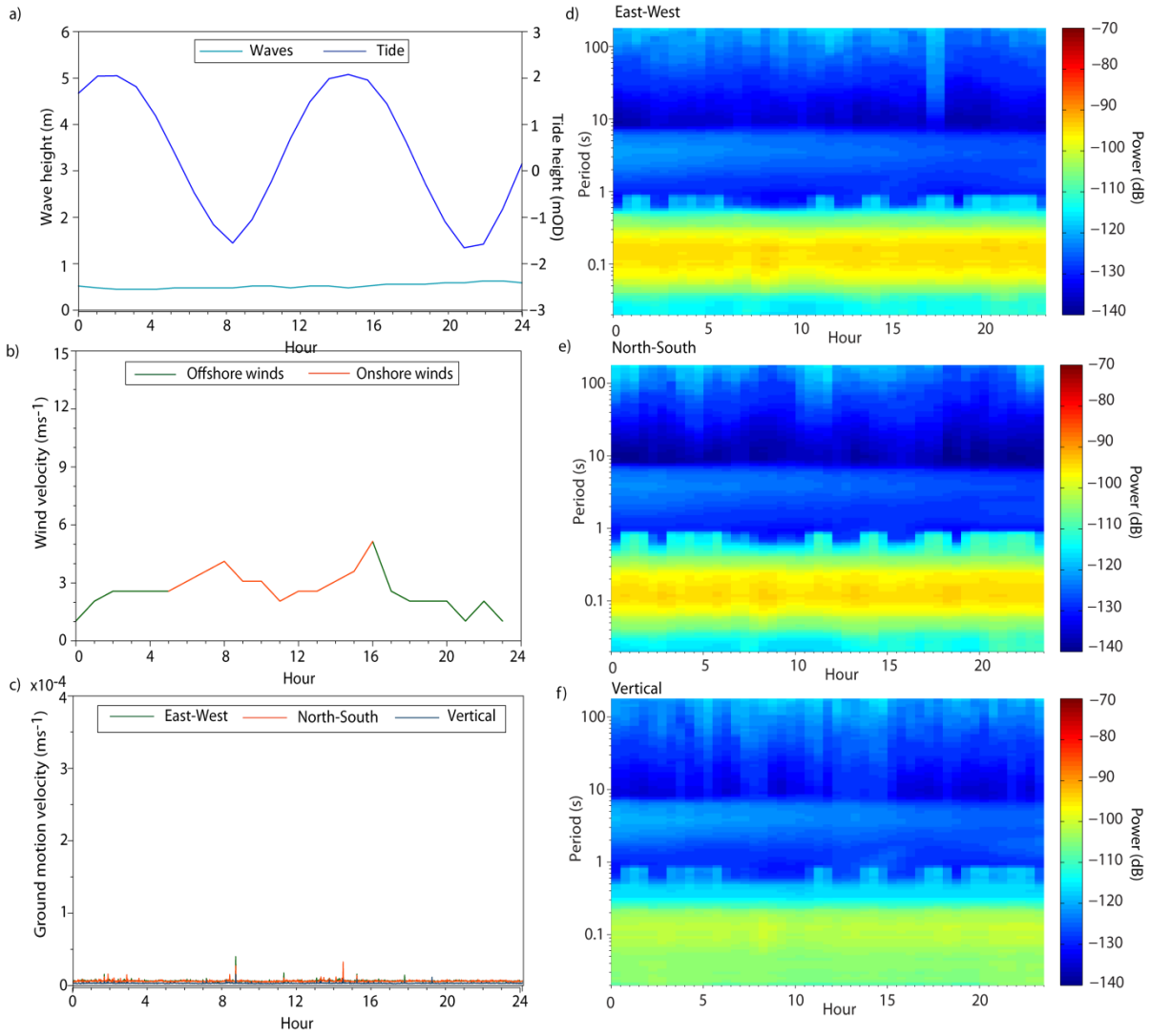

Figure 4.5: Spectrograms and environmental data for 21/06/09. a) Hourly max tide height modelled for Boulby and hourly max wave heights obtained from the Tees wave buoy (Figure 3.14); b) Onshore and offshore wind speeds monitored hourly at Loftus (Figure 3.14); c) Ground motion velocity for all three components; d) East-west component spectrogram; e) North-south component spectrogram; f) Vertical component spectrogram.

4.2.2 Seasonal frequency band variations

4.2.2.1 Summer month example

The ground motions generated by environmental conditions during a relatively quiet summer month (Figure 4.6) can be explored by examining data from June 2009. During this month two full neap-neap tidal cycles occurred, with the spring tides occurring around the 10th and 26th June.

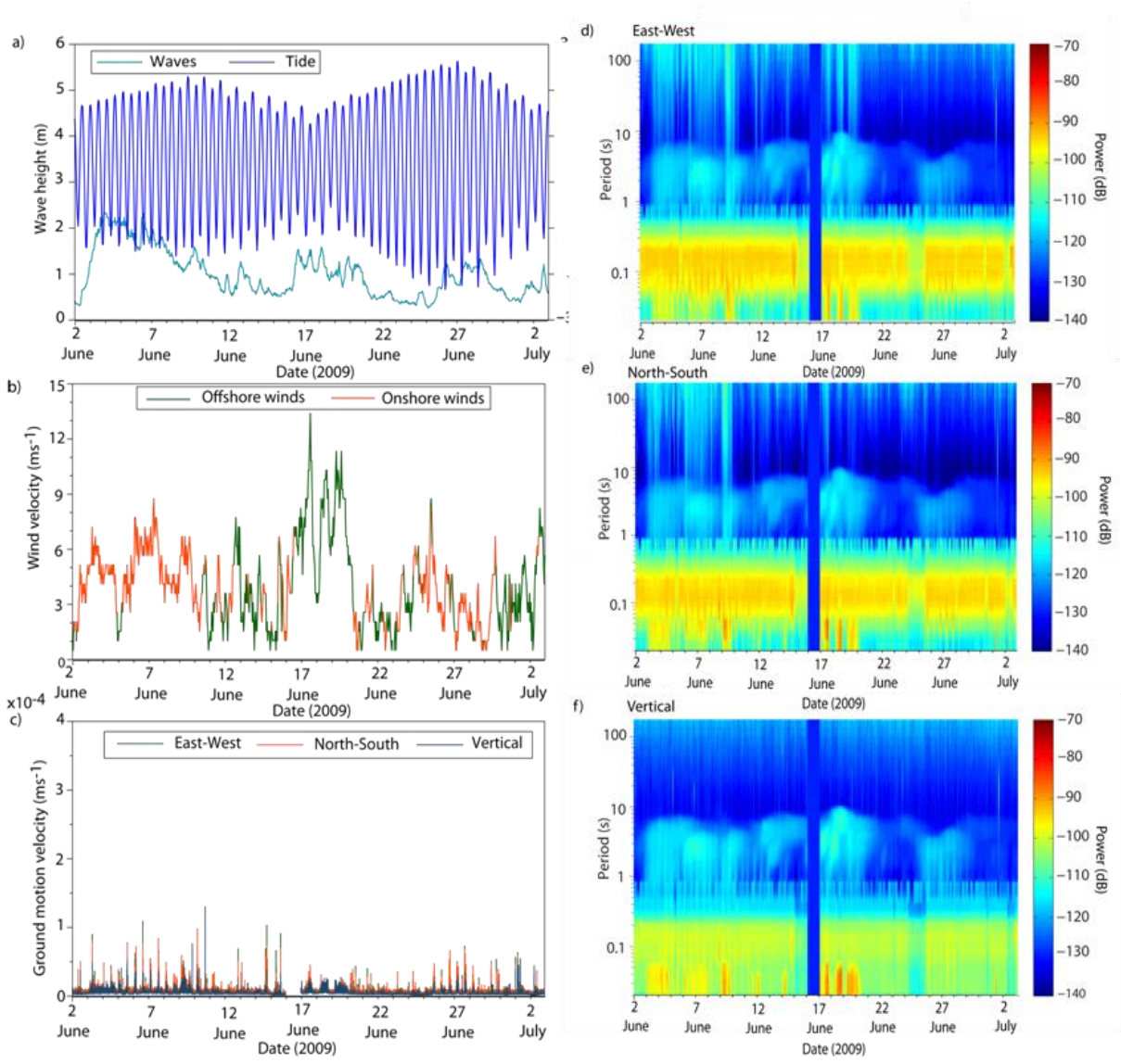

Figure 4.6: Spectrograms and environmental data for the summer month 02/06/09 – 02/07/09. a) Hourly max tide height modelled for Boulby and hourly max wave heights obtained from the Tees wave buoy (Figure 3.14); b) Onshore and offshore wind speeds monitored hourly at Loftus (Figure 3.14); c) Ground motion velocity for all three components; d) East-west component spectrogram; e) North-south component spectrogram; f) Vertical component spectrogram. The 16th June contained noise across the spectrum as there were people working in the seismometer field on this day. The power values have been replaced with a null value, represented by the blue band.

Examining spectrograms over monthly timescales enables the identification of longer events that result in energy transfer to the cliff, and the corresponding conditions that generate them. In this summer-month spectrogram it is clear that there are a number of higher energy events extending over multiple days, which often have very different characteristics. To summarize:

- High power events occurred in all four (LP, MS, HT and WI) frequency bands (e.g. on 3rd – 9th June - Figure 4.6). In the horizontal components, higher power in the LP frequency band extended into lower frequencies, overlapping with the microseism band. This was a period of continually high wave heights, averaging 1.68 m (Figure 4.6a), and onshore wind speeds, averaging 5 ms^{-1} (Figure 4.6b), which together with the corresponding LP and MS frequency bands (Figure 4.6c - e) suggest the arrival of swell from a distant storm. The higher signal power in the HT frequency band demonstrates that energy transfer increases during high tides when waves can strike the cliff. These tidal signals can also be seen in the long-period (LP) and microseism (MS) bands, although they are not as distinct, indicating that energy transferred at the frequency of incoming surface waves and infragravity waves is concentrated on the foreshore during high tides. The WI frequency band power corresponds well with wind velocity above 3 ms^{-1}, resulting in increased power (e.g. 6th and 9th June). The apparent lack of sensitivity to wind direction suggests that: i. regardless of direction, a buffeting effect occurs at the vertical cliff face via turbulence; and / or ii. that the wind interferes with solar panels, ground cover and boxes at the surface of each seismometer installation.
- High power events occurred in the MS, LP and WI frequency bands but not in the HT frequency band, for example 17th – 19th June (Figure 4.6). High offshore wind velocities (Figure 4.6b), and higher than average waves at distance from the cliff (Figure 4.6a) during this time may explain these characteristics across frequency bands. The strong offshore winds can explain the lack of increased power in the HT frequency band as they could result in decreased coastal sea levels, drawing water away from the cliff (Davidson-Arnott, 2010). This would lower average sea level, reducing the ability of waves to reach the cliff, or alternatively the more shallow water may mean that waves break before reaching the cliff and therefore dissipate energy on the foreshore. The high power in the MS frequency band suggests large waves were present offshore, or on the seaward portion of the nearshore, yet they failed to reach the cliff due to the offshore winds. The higher power in the LP frequency band indicates that long-period wave energy can generate microseisms away from the cliff that are detectable at the cliff top seismometer. This may represent constructive interference between incoming waves with waves reflected off the coast or wind-generated offshore waves, causing infragravity waves to superimpose upon incoming swell waves to form standing waves off the coast. Standing infragravity waves will generate the LP ground motions via the DF microseism pressure fluctuations, and therefore can be generated in any water depth. The LP frequency band power during these events may as a result represent LP

energy conditions further offshore, where larger waves have been generated over a long fetch.

- High power events occurred in the MS and HT frequency bands, combined with low power in the LP frequency band, and no distinct WI frequency band, on for example 25th – 28th June (Figure 4.6). During this time average wave height was 0.85 m and, with spring high tides (Figure 4.6a) of nearly 3 mOD, the waves would have impacted directly onto the cliff face. The wind velocities were onshore, and averaged 3.05 ms^{-1}. The lack of long-period signals, the shorter-periods of the MS frequency band as compared to earlier in the month (17th, 18th June), combined with the smaller wave heights and lower wind velocities, suggests that the winds and waves were locally generated, as no swell waves were observed.

Comparing the occurrence of high power in the MS frequency band in the spectrograms (Figure 4.6d - f) with the wave data (Figure 4.6a), it is clear that greater microseism power occurs during times of increased mean wave heights, however there does not appear to be a clear linear relationship between the magnitude of wave height and that of microseism spectral power. This may indicate the presence of primary microseisms and / or DF microseisms during each of the different time periods, each of which have different signal amplitudes. As the ratio of primary to DF microseisms varies, so will the microseism amplitude, and therefore the power within the MS frequency band will fluctuate accordingly. The microseism periods in the spectrograms do correspond well to the wave periods from the wave buoy data, indicating the significance of primary microseisms in generating these signals.

The velocity graphs (Figure 4.6c) demonstrate the high power events generated by large waves during high spring tides impacting upon the cliff. The pattern of semi-diurnal peaks in power can be clearly seen within days 4th – 11th June, and 25th- 27th June. The strong wind events on days 17th – 19th are also evident, particularly visible in the Z vertical component.

4.2.2.2 Winter month example

Spectral power levels within the winter month of December 2009 (Figure 4.7) are significantly greater, on average by 10 - 15 dB, compared to during June 2009 (Figure 4.6). Notably, more powerful events occur across all four frequency bands (Figure 4.7).

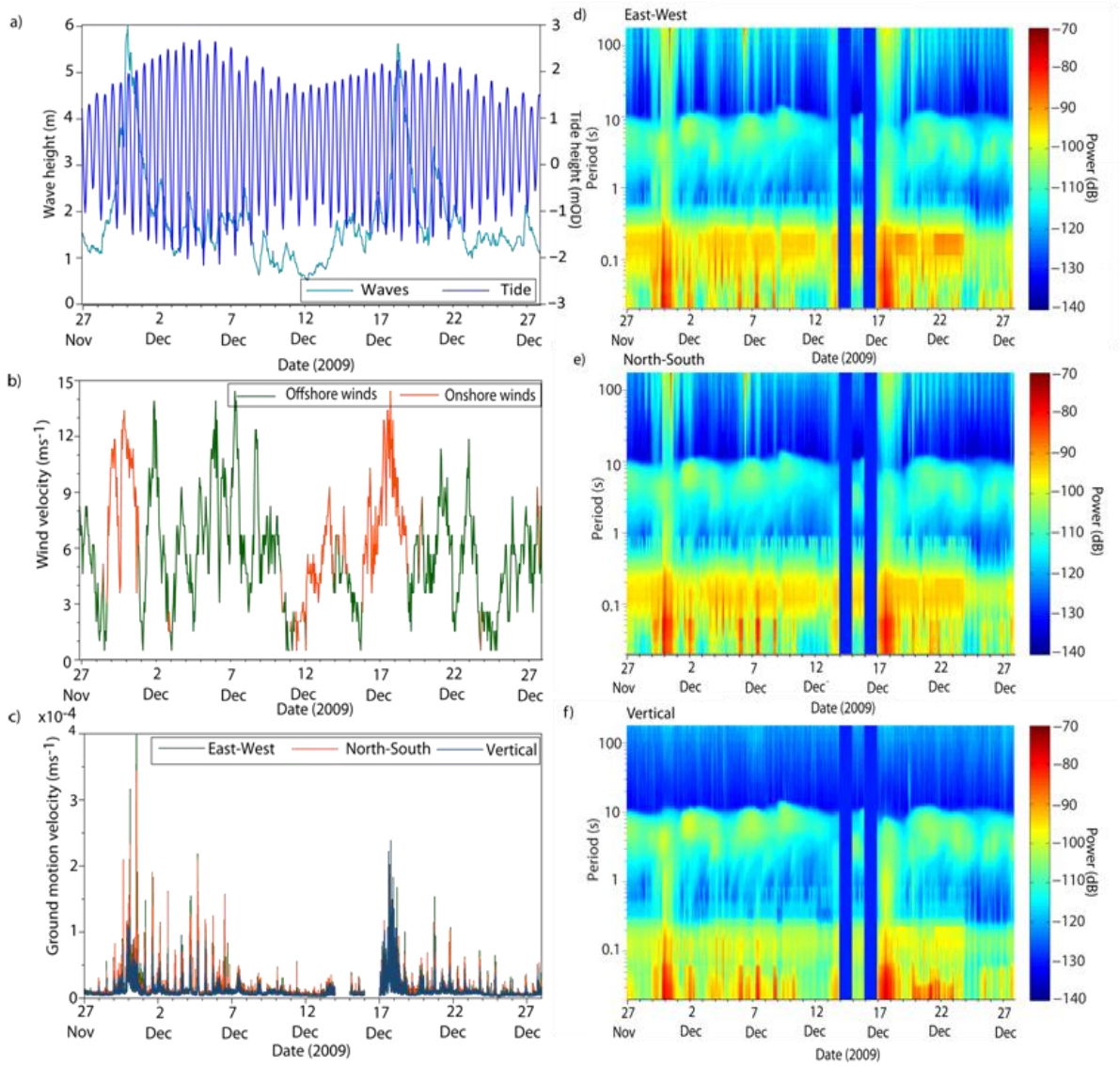

Figure 4.7: Spectrograms and environmental data for the winter month 27/11/09 – 27/12/09. a) Hourly max tide height modelled for Boulby and hourly max wave heights obtained from the Tees wave buoy (Figure 3.14); b) Onshore and offshore wind speeds monitored hourly at Loftus (Figure 3.14); c) Ground motion velocity for all three components; d) East-west component spectrogram; e) North-south component spectrogram; f) Vertical component spectrogram. The 14th and 16th December contained noise across the spectrum as there were people working in the seismometer field on these days. The power values have been replaced with a null value, represented by the blue bands.

There were two large storms during this winter month example (29th Nov – 2nd Dec and 17th – 18th Dec), which resulted in high power across the frequency spectrum. These storms demonstrate the same spectral characteristics as those in the summer month, however winter power levels are 10 - 20 dB higher. This means that during winter storms dramatic increases in energy transfer to the cliff occurs from the environmental conditions represented by the

different frequency bands. The wind speed and wave height averages are approximately double those during the summer example, explaining the increased power monitored during this winter month.

The range of frequencies and associated signal power within the WI frequency band are more varied with the higher and more variable wind velocities that occur during this winter example (Figure 4.7) as compared to the summer example (Figure 4.6). These features are within both the onshore and offshore wind direction sub-classes, and demonstrate a greater sensitivity of signal power to wind direction during higher wind velocities. The wind direction determines how and where the wind interacts with the cliff e.g. where turbulence is generated and buffeting occurs. These effects can occur at the cliff top ground surface, or on the cliff face, and can act in primarily horizontal and / or vertical directions. This diversity is reflected in the range of frequencies that the WI frequency band includes; notably the WI frequencies range is greater during onshore winds. This suggests that during onshore winds, winds transfer energy to the cliff via a variety of mechanisms or via a variety of directions. In the field there is evidence of winds blowing up and down the cliff face as the till from the cliff top stains the cliff face and also in winter months was found to coat the seismometers' solar panels and boxes. During strong onshore winds it is possible that winds travel in multi-directions across the cliff face, producing cliff shaking at a wide range of frequencies.

The HT frequency band power varies significantly across the winter month example; the HT signal is sometimes absent during high tides, even when there are waves (Figure 4.7). For example on 20th – 22nd Dec, average wave heights were 1.82 m and high tides were around 2 mOD, and the HT frequency band is clearly visible. However on 10th – 13th Dec the same tide heights occurred but wave heights averaged 0.92 m, resulting in no HT frequency band in the spectrogram. The day examples presented above demonstrate that HT frequency band characteristics are controlled by the coincidence of wave and tide heights. The summer day example above shows that high spring tides produce no HT frequency band if only very small surface waves are present. The winter day examples show that during high tides the amount of energy transferred to the cliff depends on wave height. However when sufficient wave heights are present, the tide also influences rate of energy transfer to the cliff as tide height controls the area of cliff face to which this energy can be transferred. The varied combinations of tide and wave heights that occur through the monitoring period can explain the variability in the HT frequency band observed across the winter month.

The velocity graph for December 2009 shows distinctive high tide peaks. The largest velocity peaks occur during the two storms on 29th – 30th Nov and 17th – 18th Dec, when high waves and onshore wind velocities are monitored.

4.2.3 Frequency band variation over the two-year monitoring period

The four frequency bands introduced in Section 4.1 are clearly distinguishable within the two-year spectrogram (Figure 4.8), where their long-term variation can be explored.

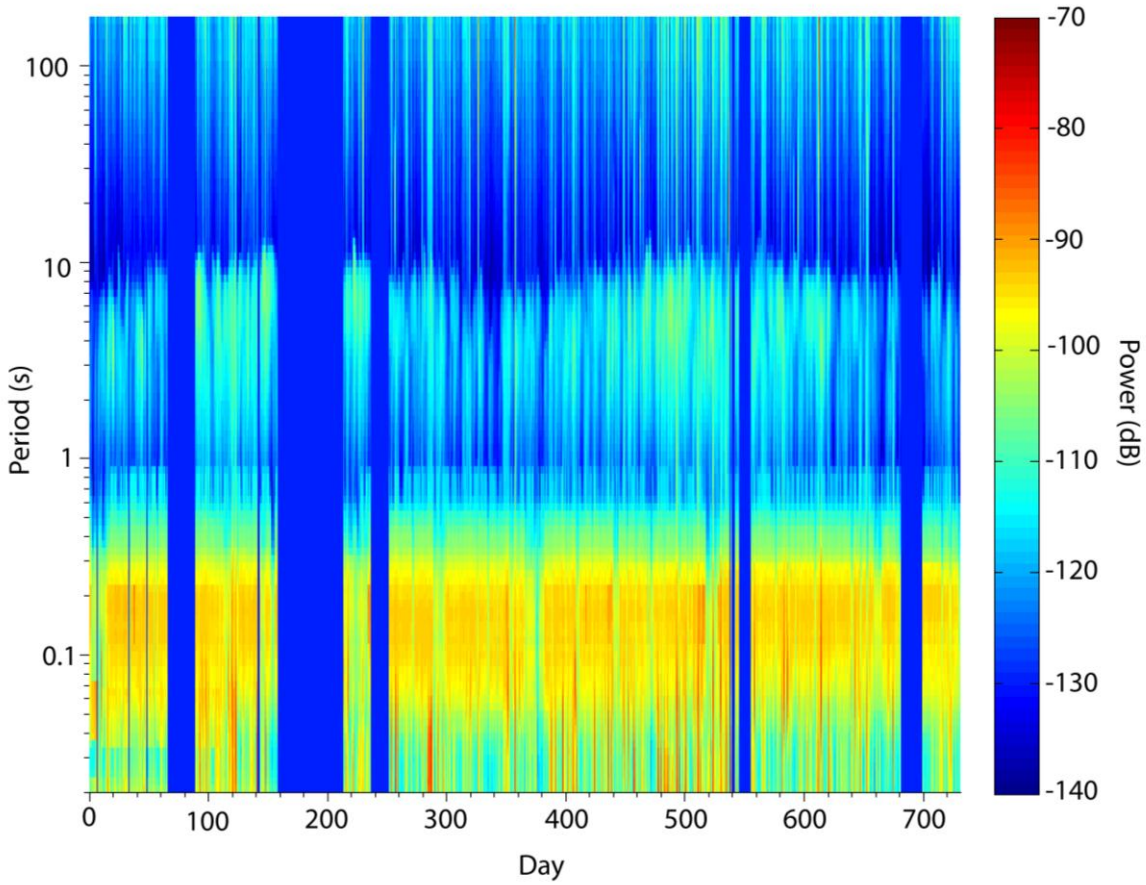

Figure 4.8: Two-year spectrogram for the east-west ground motions (E component). The power values for periods of missing data or errors have been replaced with a null value, represented by the blue bands.

The power of the LP frequency band is variable over time, typically ranging between approximately -130 dB to -97 dB (Figure 4.8). Higher power often occurs as a result of clusters of events, suggesting the occurrence of storms or stormy periods. This frequency band typically has greatest power at periods longer than 40 s. There is a clear seasonality with greater power monitored during the winter months at this site.

There is a very distinct seasonality in the MS frequency band. During winter months the highest power occurs (maximum is approximately -100 dB) across the full range of monitored frequencies, and also the bandwidth of responsive frequencies increases, with the higher power extending into longer periods up to 15 s. This contrasts with the shorter period ground motions during the summers, which have a maximum period of 8 s (Figure 4.8). Longer winter wave periods indicate swell waves generated by high wind velocities, which have travelled and developed over larger fetch distances. The greatest power is generated in the 2 - 10 s range (0.1 – 0.5 Hz), during the winter months. During the winter the combination of higher power of the LP and MS frequency bands, as well as the longer MS periods, suggest that these represent swell arriving from storm locations some distance from the coast.

Within the two-year spectrogram the consistent nature of the anthropogenic (AN) frequency band is clear and with no evidence of seasonal variation, supporting the conclusion that these signals are man-made (Figure 4.8). No correlations have been found with the timing or scheduling of works at the adjacent mine.

The high-frequency HT and WI bands remain difficult to characterise at this resolution (Figure 4.8). Typically increased power appears to occur concurrently with higher power in the MS and LP frequency bands.

4.3 Summary

Five distinct frequency bands of ground motion have been identified in the monitoring data collected at the cliff. The AN band is generated by anthropogenic sources, most likely machinery in the mine tailings shaft which is in the same field as the seismometer array. The remaining four frequency bands however are generated by naturally occurring nearby marine and atmospheric conditions. The frequency bands were initially identified using the frequency range occupied in tandem with the findings of previous studies that have identified the characteristics of microseismic ground motions generated by different marine and atmospheric variables. Qualitative comparisons between the spectral characteristics of each band with a concurrent time series of tide, wave and wind conditions has enabled further identification of the environmental conditions that generate the different frequency ground motions. Each frequency band represents a specific combination of environmental conditions, the relative magnitudes of which determine the energy transferred to the cliff, generating the microseismic ground motions monitored.

The four frequency bands are:

Long-period (LP) frequency band – believed to represent ocean infragravity waves, the energy from which is often focussed in shallow surf and swash zones.

Microseisms (MS) frequency band – ground motions generated by pressure fluctuations beneath incoming ocean waves, divided into primary and double frequency (DF) microseisms generated in varying locations and by different mechanisms.

High tide (HT) frequency band – wave impacts against the cliff, and foreshore during large storms, during high tides generate a high-frequency, high-power shaking of the cliff.

Wind (WI) frequency band – wind turbulence at the cliff top and cliff face generates high-frequency, high-power intermittent events of ground motions.

The findings demonstrate the complex nature of energy transfer to a cliff due to the range of environmental forces active and their interactions. The ground motion frequency bands are highly variable over time and are clearly seasonal, indicating more energy is transferred to the cliff during stormy winter conditions. The environmental processes that are generated by the combinations of marine and atmospheric conditions, and the mechanisms by which they generate the microseismic ground motions and therefore transfer energy to the cliff, are quantitatively examined in Chapter 6.

Chapter 5: Environmental conditions at the cliff

In order to clarify the processes generating the ground motion frequency bands observed in the spectrograms presented in Chapter 4, the corresponding marine and wind conditions during the monitoring period are explored. The aim of this chapter is to characterise the environmental conditions during the monitoring period that may potentially transfer energy to the cliff, and therefore generate the microseismic ground motions and drive cliff erosion.

The seismic signal characteristics and temporal variability through the monitoring period suggest that energy transferred to the foreshore, out to sea and at different locations on the cliff itself are detected by the cliff top seismometers. The sea transfers energy to the coast via a number of processes (e.g. orbital motion pressure fluctuations, wave breaking, surf and swash motions and direct impacts onto the cliff face), the location of which can vary with the tide and incoming wave and storm conditions. The effect of tides is particularly significant at the study site because the high tidal range and shallow gradient, wide foreshore enable processes that generate a seismic signature to operate over a large spatial extent.

This chapter is focussed upon identifying how marine conditions vary spatially across the nearshore, foreshore and at the cliff, and also how this varies over time. This is necessary to identify the areas where the different marine processes operate that generate the HT, MS and LP seismic signals. Undertaking a detailed exploration of marine conditions near the cliff is essential for improving understanding of interactions between wave processes and coastal cliff erosion.

5.1 Monitored environmental conditions

5.1.1 Local land-based wind conditions

The dominant wind direction at the site was south easterly to westerly (150 - 280^{o}) (Figure 5.1), occurring 63% of the time. The mean wind direction was south westerly (220^{o}) (Figure 5.2). The dominance of south westerly winds is typical for the UK (Smithson et al., 2002). However, the potential for these winds to generate waves that will influence the cliff is limited as these wind directions blow offshore and therefore have no fetch. Onshore winds make up only 37% of the monitored time, with similar frequencies occurring from all directions within this sector.

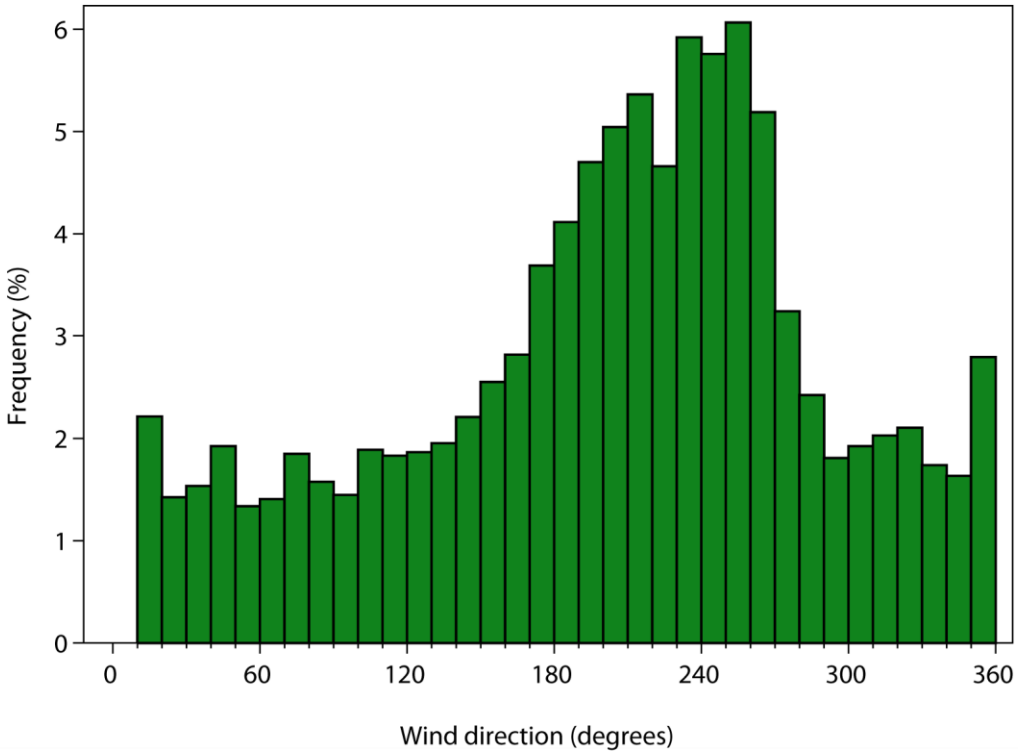

Figure 5.1: Frequency distribution of wind directions during the monitoring period 25/07/08 – 25/07/10 (recorded at Loftus met station). Wind directions are the hourly average and have been rounded up to the nearest 10° by the Met Office – this explains the absence of winds from 0 – 10°.

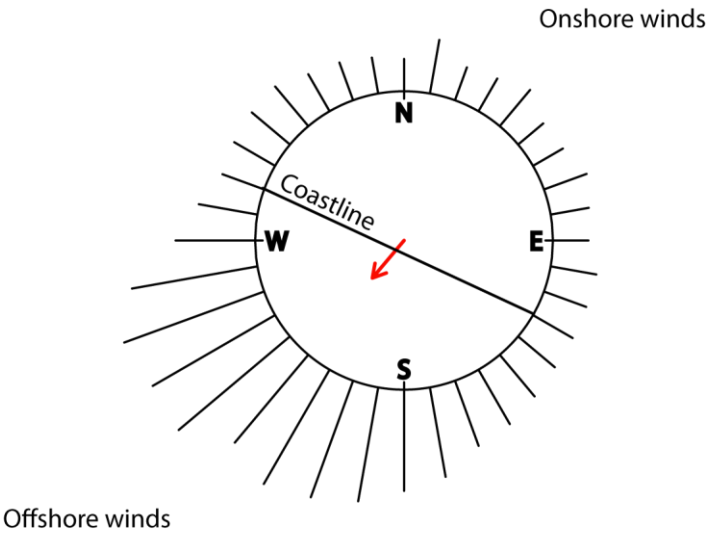

Figure 5.2: Frequency of wind directions and their orientation relative to the coastline. The most frequent winds, southerly to westerly, blow in an offshore direction. Mean direction is 220° with a vector strength of 0.33 (red arrow).

Mean wind velocities are in the range 4 - 7 ms^{-1} for all wind directions (Figure 5.3). The largest hourly maximum wind velocities are from the prevailing offshore wind directions and lie between 11 to 20.6 ms^{-1}. The highest onshore winds originate from the north-westerly to northerly directions (300 - 360°) and from the south east (130 - 150°) peaking at 16 ms^{-1}.

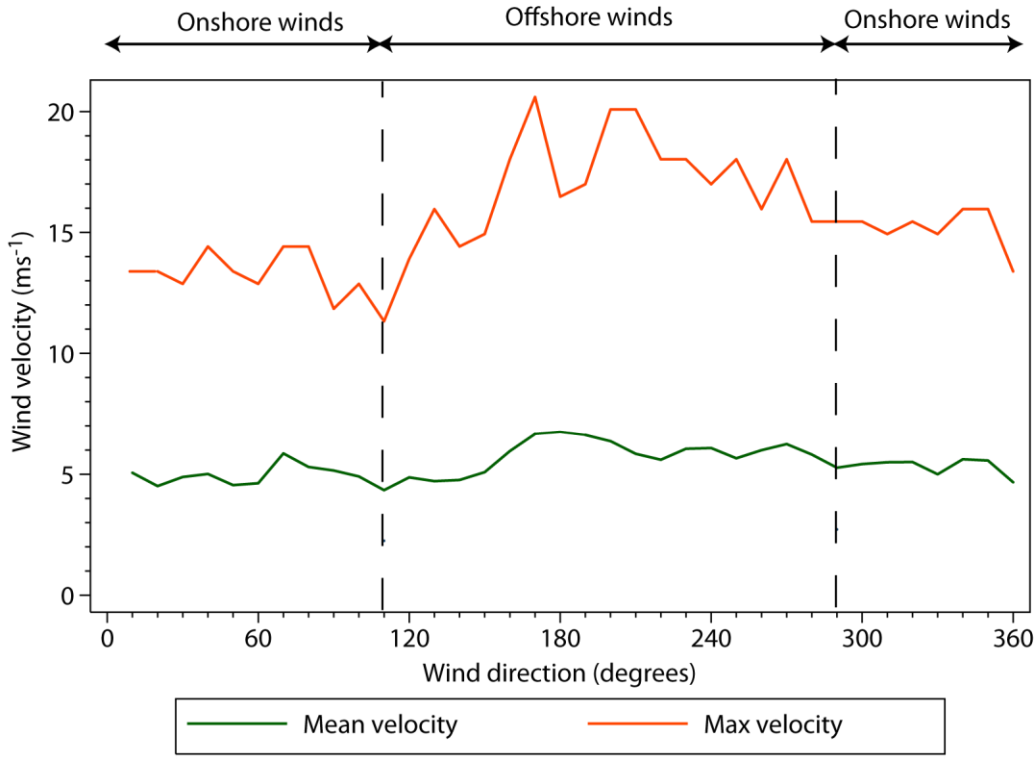

Figure 5.3: Mean and maximum wind velocities for varying wind direction (N.B. as before the wind directions have been rounded up to the nearest 10°).

The frequency distribution of the wind velocities from all directions conforms to the expected right skewed distribution typical of environmental variables (Figure 5.4) (Summerfield, 1991). Over 80% of wind velocities lie in the range 1 - 9 ms^{-1}.

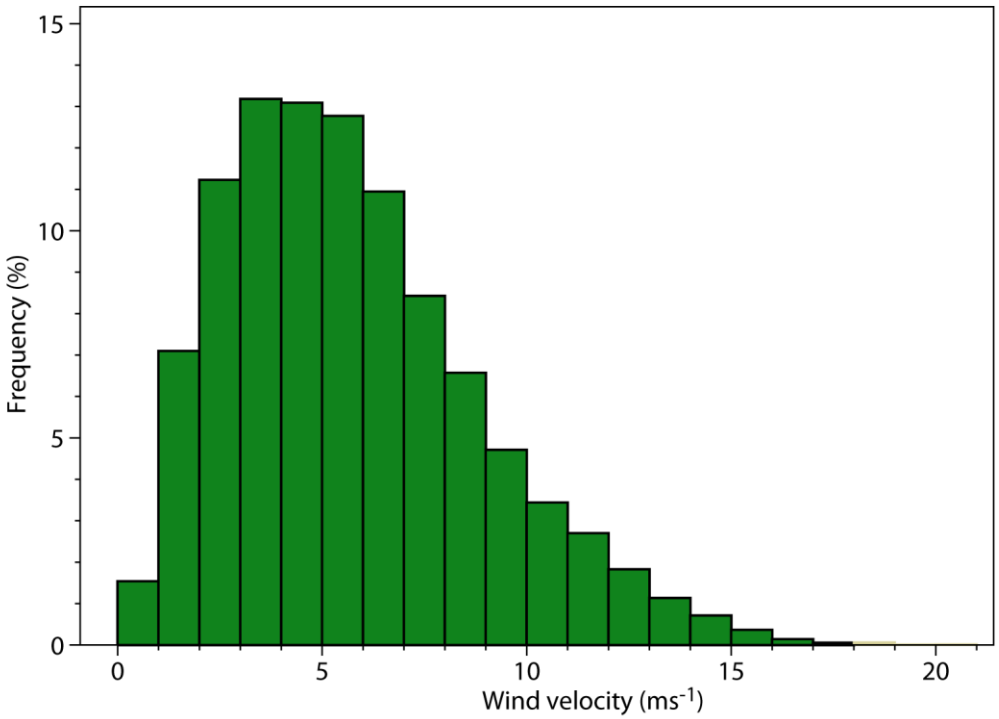

Figure 5.4: Frequency distribution of wind velocities from all directions.

In order to explore the seasonality of wind conditions, a smoothed (using a moving average) time series of wind velocity is presented (Figure 5.5). Wind velocities are characterised by peak velocities that occur in October - December and then decrease over the following six months, with lowest velocities typically occurring in May - July (Figure 5.5). These conform to expected patterns for this region, in which maximum wind velocities are expected in the winter months of November - February and minimum wind velocities in the summer months of May - September (Coelingh et al., 1998). These seasonal wind patterns are driven by contrasting air and sea temperatures – with cold air passing over relatively warm water in winter months creating unstable atmospheric conditions, the turbulence of which results in downward air momentum (Coelingh et al., 1998). In the summer warm air passes over relatively cool water, which creates stable conditions and less vertical mixing which in turn means lower wind velocities (Coelingh et al., 1998).

Wind and atmospheric pressure changes in the North Sea are governed by the pressure gradient of the North Atlantic Oscillation (NAO) (Ospar, 2000). The dominant westerly air circulation frequently contains lower pressure systems (Ospar, 2000), which result in increased sea levels. Higher wind velocities, larger wave heights and storm surges occur during winter, which are more stormy due to the stronger and more variable NAO (Wakelin et al., 2003).

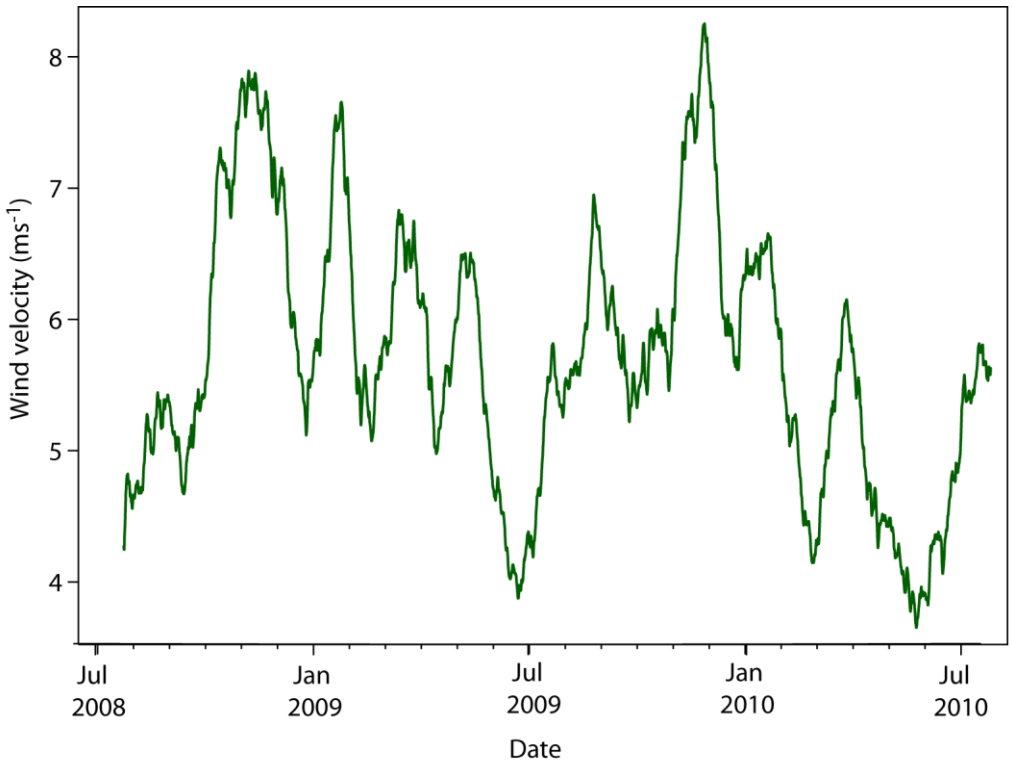

Figure 5.5: Wind velocities over the two-year monitoring period. Hourly mean velocities have been smoothed using a moving average over 30-day periods.

5.1.2 Wave conditions at the offshore wave buoy

Wave height, period and wavelength are determined by wind velocity, time and fetch over which the wind blows (Davidson-Arnott, 2010). As wind velocity, duration and fetch increase so do wave heights, periods and wavelengths as more energy is transferred from the wind to the sea surface (Davidson-Arnott, 2010). Therefore the potential fetch is significant in determining the magnitude of waves travelling towards the coast, and hence the energy which they transfer. The fetch at this site for most directions is limited by the boundary coasts of the North Sea, with a maximum fetch of approximately 860 km. However, between 1 and 18^{o} (N - NNE approx) the fetch extends much further into the Norwegian Sea, with its maximal extent being seasonally limited by sea ice cover.

Wave conditions were monitored at a wave buoy 30 km off the coast of the mouth of the River Tees, 22 km NNE from the study site (Figure 3.14). The majority of waves arrive at the buoy from northerly to easterly directions in the range 0 - 150^{o} (Figure 5.6) and have a mean of 40^{o} (Figure 5.7). These account for 80% of monitored waves and are the directions with the longest

fetch. From 150 - 330° (SE - NW) the fetch lengths to the buoy are short due to the close proximity to the coastline, which restricts the generation of waves from these directions.

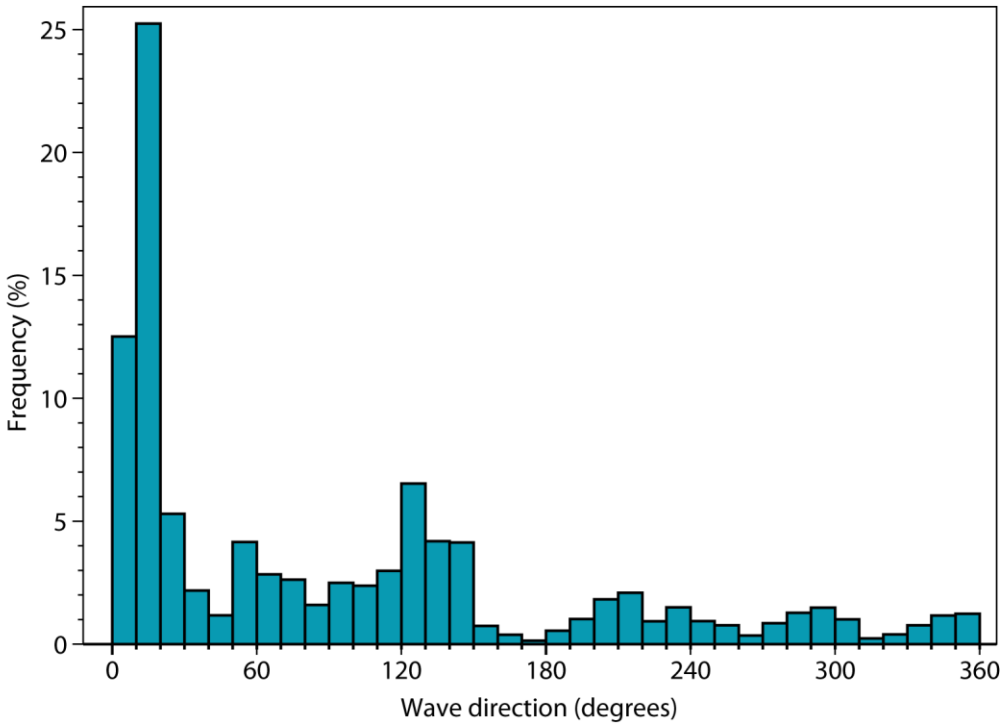

Figure 5.6: Wave directions measured from Tees wave buoy for the monitoring period 25/07/08 – 25/07/10.

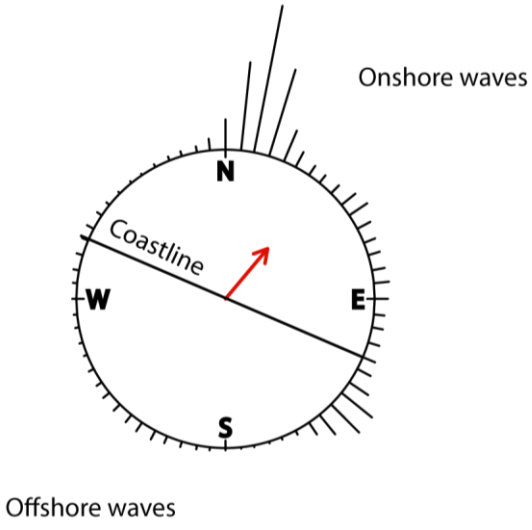

Figure 5.7: Wave directions relative to the study site coastline. The largest proportion of waves arrive from 0 - 150° which are the directions with the greatest fetch. Mean wave direction is 40° with a vector strength of 0.439.

The largest waves arrive from the directions 340 - 140° (NNW - SE) (Figure 5.8) which are directed onshore and lie within the range of directions with the largest fetches. Maximum wave heights from these directions exceed 4 m, peaking at 6.5 m. The maximum wave height for waves travelling in offshore directions is 5 m, although for most waves travelling offshore the maximum wave heights are below 3.5 m, due to the shorter fetches. The highest waves originate between 0 - 30° (N - NNE); the directions with the largest fetches.

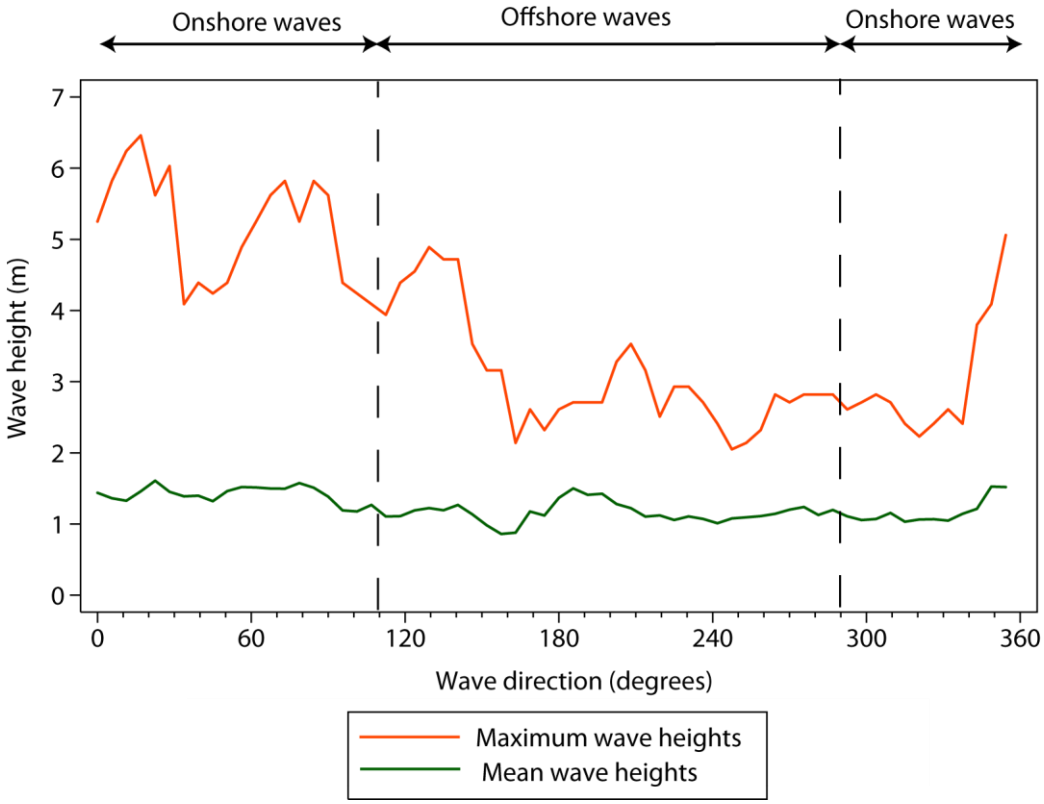

Figure 5.8: Average and maximum wave heights for varying arrival directions.

The frequency distribution of wave heights at the wave buoy (Figure 5.9) also demonstrates the right skewed distribution typical for environmental processes (Summerfield, 1991). Over 80% of waves are <= 2 m high. Large waves of >= 4 m (max recorded was 6.5 m) make up only 5% of the recorded waves.

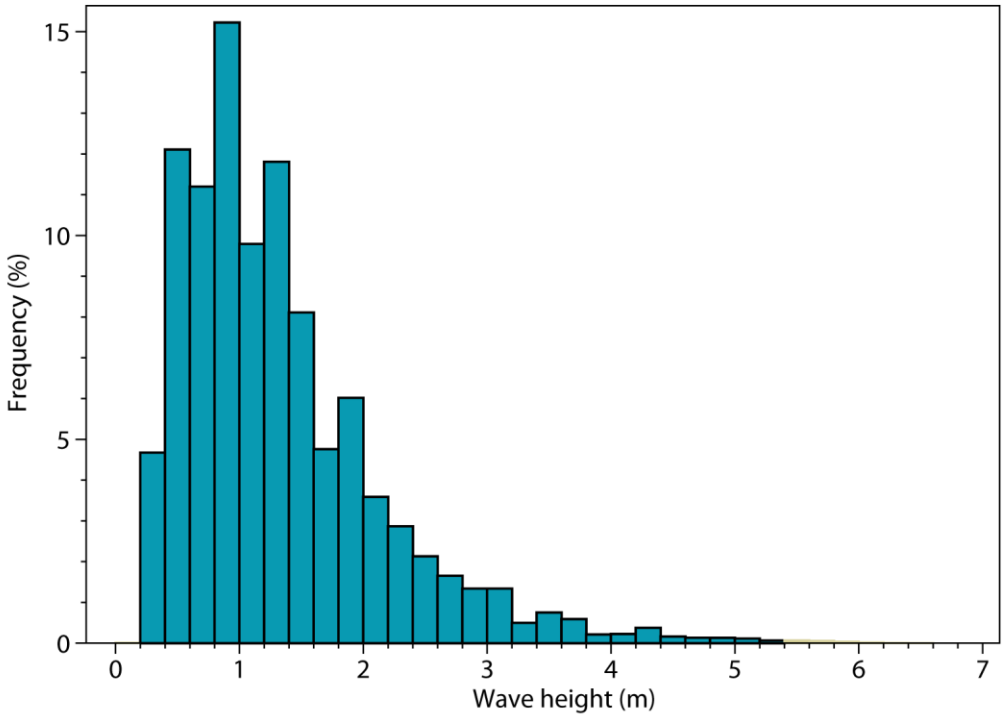

Figure 5.9: Frequency distribution of wave heights monitored at the Tees wave buoy.

The available fetch over which waves can travel determines the wave periods that can develop. The relatively limited fetch of the North Sea limits the periods generated although waves that have travelled over greater distances can enter the North Sea from the North Atlantic. The wave buoy provides statistics of the wave characteristics over 30 minute intervals and mean and max wave periods were provided (Figure 5.10). The mean recorded wave period at the buoy is approximately 5 s, and the most frequent period was 3 - 4 s (Figure 5.10a). Maximum wave periods recorded at the buoy extend to 18 s, however only approximately 8% had periods >12 s (Figure 5.10b).

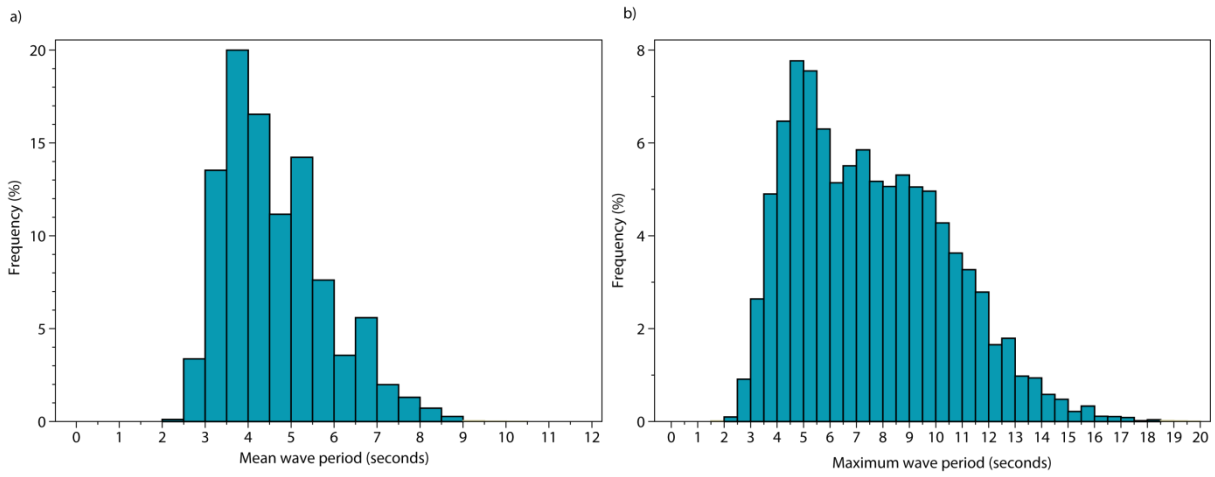

Figure 5.10: Frequency distributions of wave periods (calculated over 30-minute intervals) monitored at the Tees wave buoy. a) Average wave period; b) Maximum wave period.

The wave heights clearly show seasonality, with greater wave heights occurring between October and March (Figure 5.11). These occur with the highest wind velocities (Figure 5.5), with more stormy conditions occurring during autumn and winter.

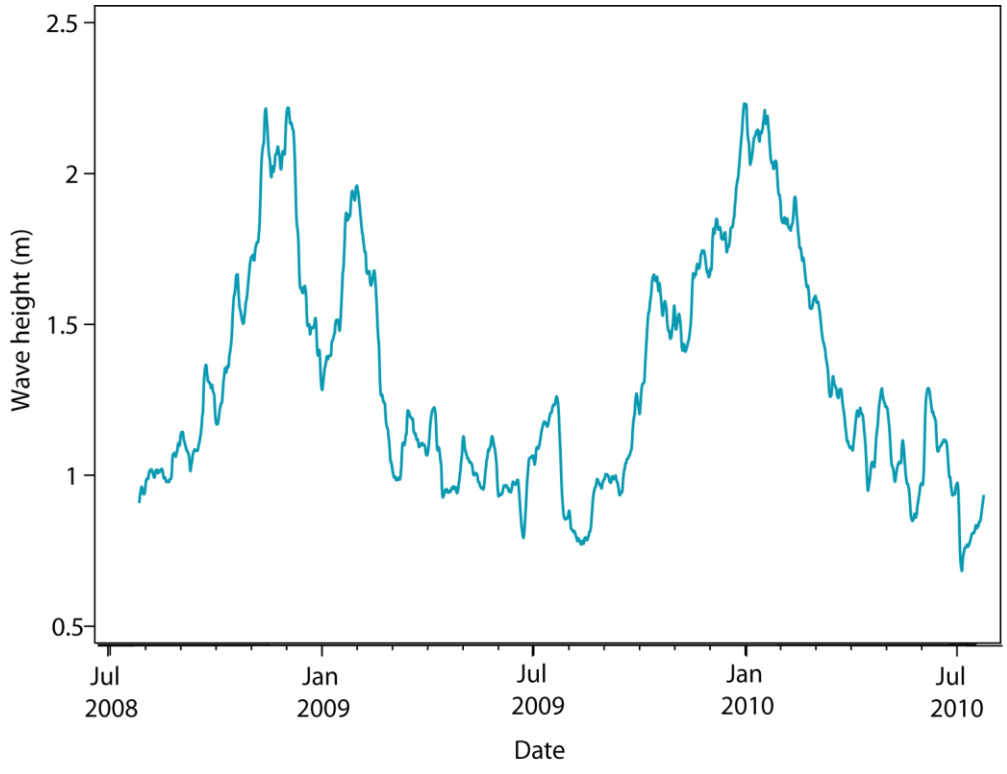

Figure 5.11: Wave heights over the two-year monitoring period. 30-minute mean heights have been smoothed using a moving average over 30-day periods.

5.1.3 Tides

The frequency distribution of tide heights (Figure 5.12) includes meteorological effects on the tides such as storm surges. The frequencies of the tide heights depict the amount of time the still water level spends at different locations in the intertidal zone, commonly termed the inundation duration. The wide foreshore of the study site means that the intertidal zone extends over 250 m. As the mean high neap tide level is just below the cliff toe, this means that only during high spring tides does the still water level reach the cliff face (not accounting for waves) (Figure 5.12). The sea only reaches the cliff when tide heights reach 1.6 mOD which means for the majority of the tidal cycle the sea is not in contact with the cliff face due to the large tidal range and long, gently sloping foreshore. Tidal inundation only occurs at the cliff face for 20% of the monitoring period.

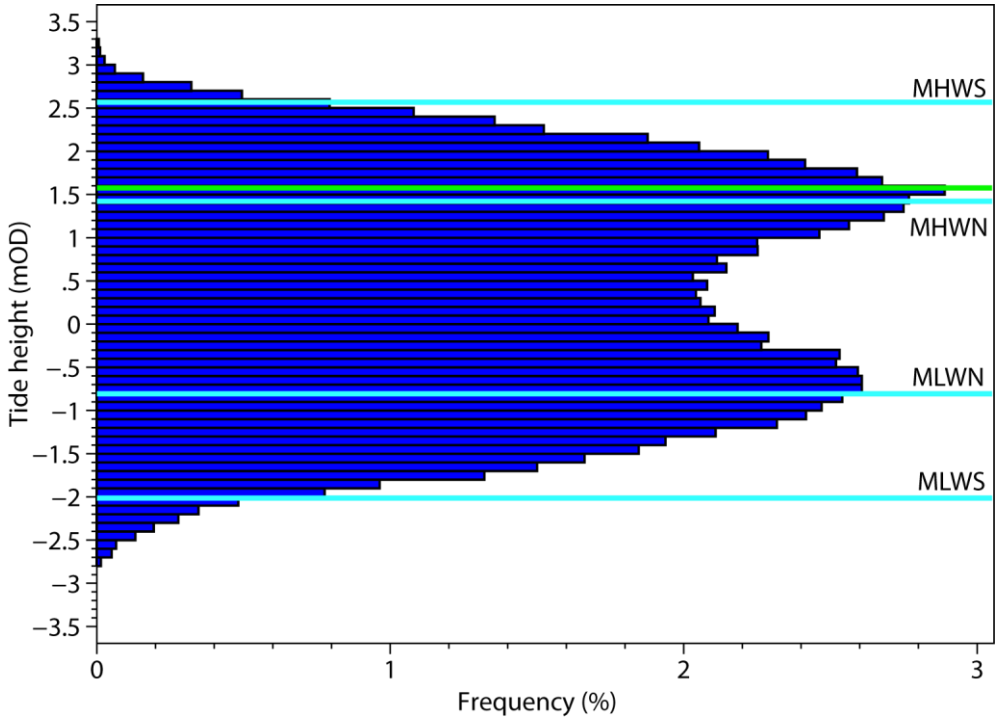

Figure 5.12: Tide frequency distribution for Boulby. Tide heights are modeled for Boulby from predicted tides for gauges at North Shields and Whitby (63 km north and 15 km south of Boulby respectively), with the North Shields residuals added to account for meteorological effects. The green line indicates the cliff toe, all tide heights above this occur at the cliff face. The light blue lines indicate the neap and spring mean low and high tide heights: MLWS = mean low water spring; MLWN = mean low water neap; MHWN = mean high water neap; MHWS = mean high water spring.

The tidal residuals, which are the monitored minus the predicted tide levels, help identify meteorological effects, such as storm surges, air pressure and sea surface temperatures, on tide

heights. In coastal areas, strong onshore winds typically result in increased sea levels recorded at tide gauges as water is pushed up against the coast, whereas strong offshore winds typically result in decreased monitored sea levels (Davidson-Arnott, 2010). Sea levels do not adjust immediately to changes in atmospheric pressure and instead change with overall pressure changes over a larger regional area (Davidson-Arnott, 2010).

The tide residuals show increased positive values during the winter months (October to December) (Figure 5.13). Positive values indicate increased sea levels due to meteorological effects, such as storm surges, where onshore winds and low air pressure raise sea levels at the coast. Negative tide residuals over the spring months of March to May indicate drops in sea level, generated by strong offshore winds or high air pressure (Figure 5.13). In the North Sea the increased storminess in winter, and the resultant surges, are driven by wind and pressure conditions determined by the variability of the NAO (Wakelin et al., 2003). The mean residuals are largely positive indicating that air pressure and wind conditions across the North Sea favour increases in sea level at the site.

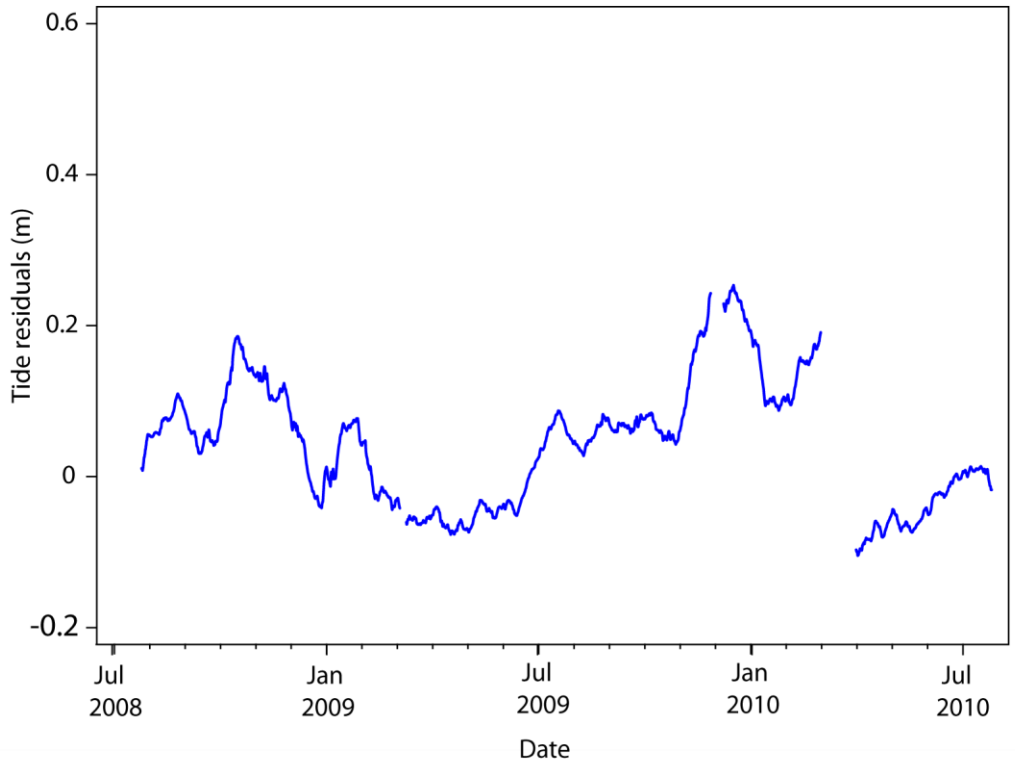

Figure 5.13: Tide residuals over the two-year monitoring period. 15-minute mean residuals have been smoothed using a moving average over 30-day periods. The gap in March 2010 is due to a 30-day gap in the recorded data during this month.

5.2 Wave transformation model results

In this section nearshore wave conditions at the cliff that have been modelled from the offshore wave conditions monitored at the Tees wave buoy are explored. The model is based on the wave energy dissipation model of Battjes and Stive (1985), details of which are provided in Chapter 3 (Section 3.4). The results from the wave transformation model enable the exploration of wave height, set-up, energy flux and dissipation across the nearshore. The modelled wave conditions indicate how wave characteristics measured at the wave buoy transform due to shoaling as they travel towards the cliff through decreasing water depths. The combinations of tidal, offshore wave and depth profile variability result in highly diverse wave characteristics throughout the nearshore, both spatially and temporally.

5.2.1 Modelled wave heights

Modelled wave heights across 1000 m of the nearshore (Figure 5.14) change in response to decreasing water depth. The maximum, mean and standard deviation of the wave heights all decrease from 250 m towards the coast, which indicates wave height becomes increasingly depth-limited in the intertidal zone. Interestingly there is an increase in maximum wave height landwards from 1000 m, peaking at 4.25 - 6.98 m between 500 - 1000 m. As waves move into decreasing water depths and begin to shoal, wavelengths decrease and heights increase. Waves break once they reach a limiting steepness, determined by the ratio of wave height to wavelength. Larger waves typically have longer wavelengths and therefore they start shoaling in deeper water and therefore break further out to sea. The increase in maximum wave heights between 500 and 1000 m therefore suggests that at these locations, the largest waves are breaking. The continuous decrease in maximum wave heights shoreward of 700 m suggests that the maximum wave heights continue to be limited by the decreasing water depth. The mean wave heights indicate that smaller waves start shoaling, and therefore break, much closer to the cliff than the largest waves.

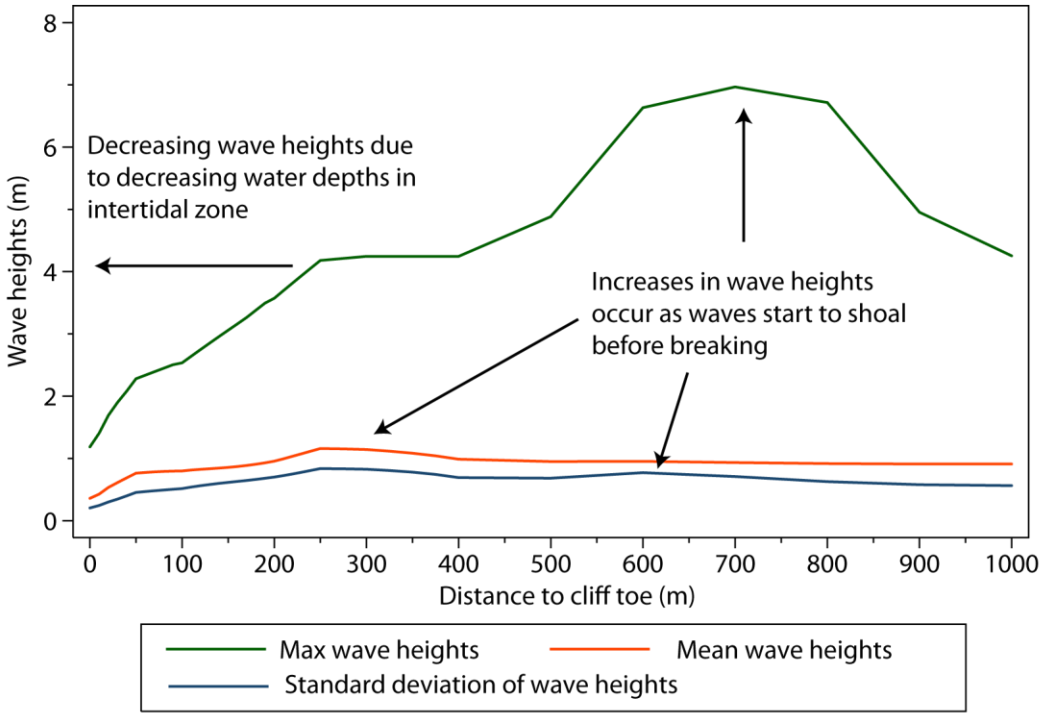

Figure 5.14: Modelled wave heights across the nearshore (normal to cliff).

These results demonstrate the variability of wave conditions across the nearshore and foreshore profile due to tidal inundation, bathymetry and foreshore topography controls on water depth, and incoming wave conditions. The results indicate that large waves reach the coast and travel across the nearshore – at 600 m from the cliff waves can be over 6 m high and even at 200 m waves as high as 3.5 m occur. These conditions will deliver significant energy to the coast, and have the potential to be highly effective in eroding both the foreshore and cliff.

Figure 5.14 demonstrates that the largest waves start to break at around 700 m from the cliff, and continue to do across the nearshore. In the model used to calculate the wave heights, a variable Q was used which indicates when waves within a model run begin to break. Within a model run, when Q first equals 1 this indicated that waves had started to break, after this point the height at which waves break will decrease due to the decreasing water depth. The frequency of Q = 1 can therefore be used as an indicator of where wave breaking and surf conditions are concentrated within the nearshore (Figure 5.15). The amount of wave breaking increases, as would be expected, as the waves get closer to the coast and the water depth decreases. The increased frequency of Q = 1 in the 400 m in front of the cliff toe, indicates that this section of the nearshore experiences most frequently the turbulent conditions that characterise the wave breaking and surf zone. These are the areas in which the majority of energy is transferred to the seabed via turbulence and friction.

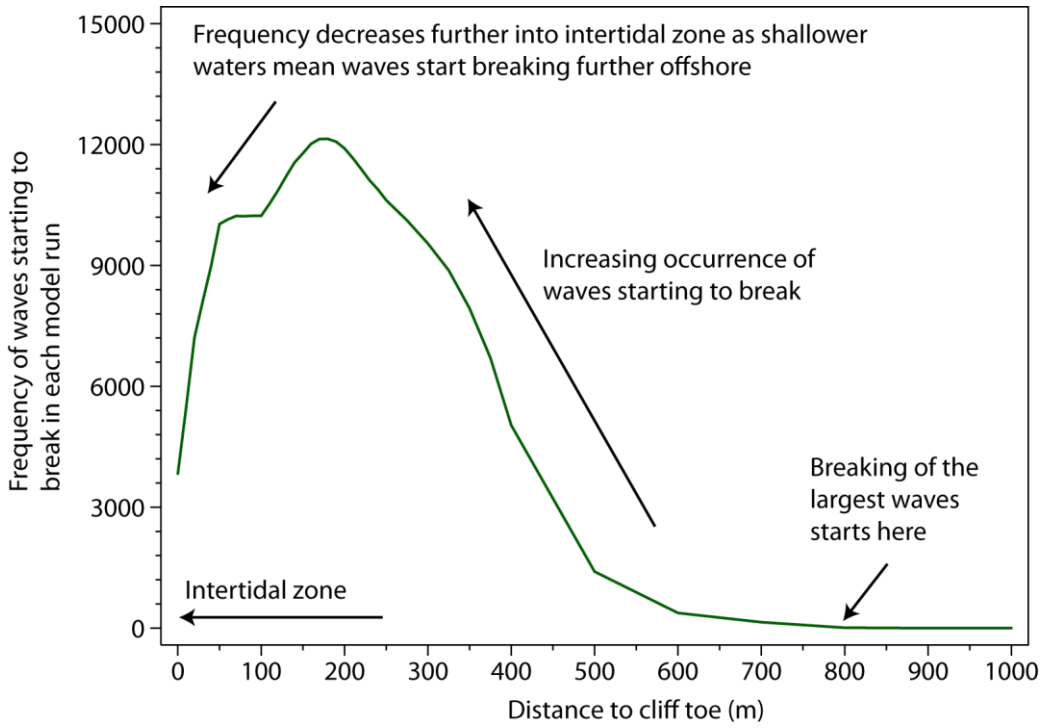

Figure 5.15: Occurrence of wave breaking across the nearshore. Within each model run the point within the nearshore when waves start to break is indicated by Q = 1. The frequency of Q = 1 across the nearshore are plotted here for the two-year monitoring period.

5.2.2 Modelled wave set-up and set-down

A decrease in mean water level (set-down) occurs just before, and as, waves break, followed immediately by an increase in water level (set-up). The pattern of mean water levels across the nearshore (Figure 5.16) suggests that the majority of wave breaking occurs between 400 - 200 m as set-down of the mean water level occurs followed by set-up post-breaking. The maximum set-up occurs at the waterline (Komar, 1998) and this is evident in both the mean and maximum set-up heights. The shoreward increase in the standard deviation of water level change reflects the increasing occurrence of wave set-down and set-up effects moving inland across the foreshore profile, as water depths gradually decrease and increasingly more waves break. The maximum water levels increase markedly at 600 m which indicates post-breaking set-up caused by the breaking of the larger waves in the zone between 600 - 1000 m. The lack of set-up seawards of 600 m suggests that the large waves are breaking nearer to 600 m than 1000 m. The maximum set-up heights continue to be high, up to the cliff toe, suggesting that during

stormy conditions water levels from 600 m across the nearshore to the cliff face can be up to 1 m higher than that of the still water tidal depths.

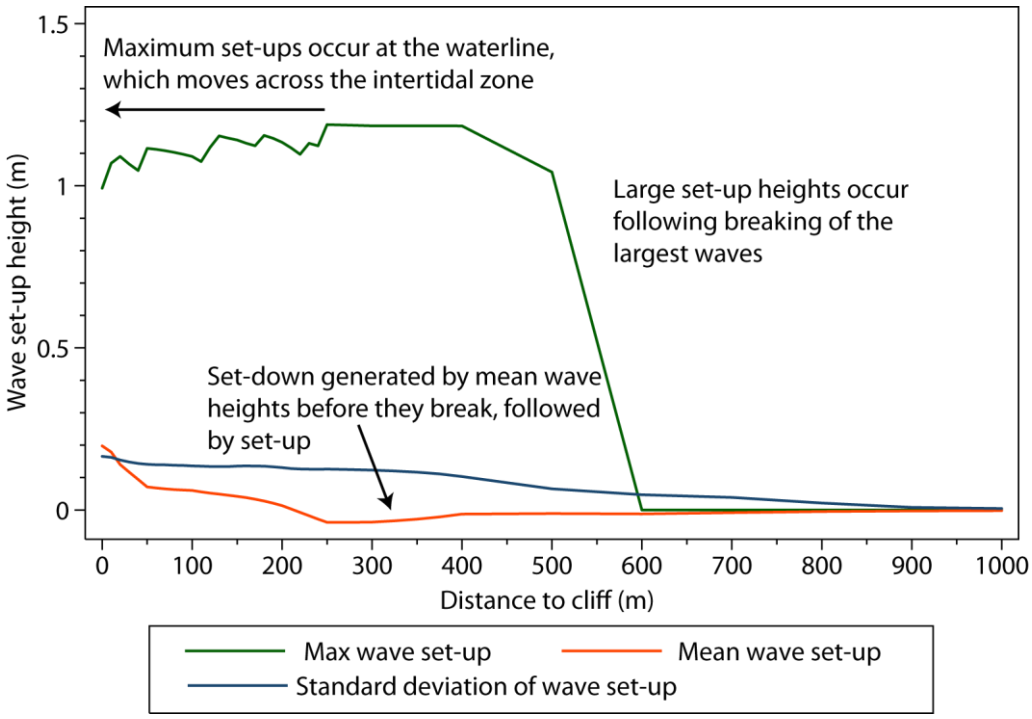

Figure 5.16: Modelled wave set-up heights across the nearshore (normal to cliff).

Comparing the waterline set-up heights against the offshore wave heights it is clear that larger waves result in greater set-up heights at the waterline (Figure 5.17). This is because set-up is generated by the shoreward momentum flux, determined by the amount of wave energy, and therefore wave height. The high set-up water levels generated by the largest waves breaking at around 600 m enable larger waves to travel closer to the cliff due to the increase in water depth. As wave energy is proportional to the square of wave height, considerably more wave energy can be transferred to the cliff during stormy conditions of high set-ups.

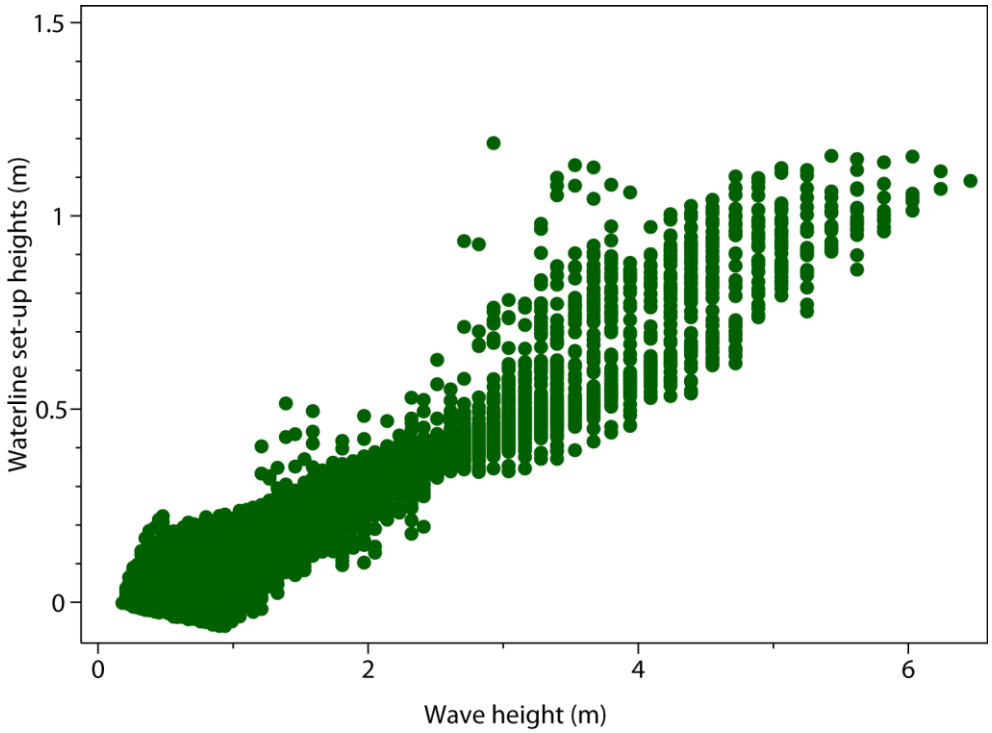

Figure 5.17: Relationship between offshore wave height and set-up of the waterline.

5.2.3 Modelled wave energy (energy flux and energy dissipation flux)

The energy flux is the rate at which the wave energy is transferred by the moving waves. It remains constant within a wave until the wave breaks and energy is dissipated (Komar, 1998). Larger waves have greater energy as wave height is related to energy via Equation A6.9 (in Appendix 6). Therefore, the locations of the largest maximum energy flux indicate the occurrence of the largest waves where greater wave energy is available for transfer (Figure 5.18). The decrease in maximum energy flux towards the coast reflects the depth limitation of maximum wave heights, and therefore limits on the available energy in the waves.

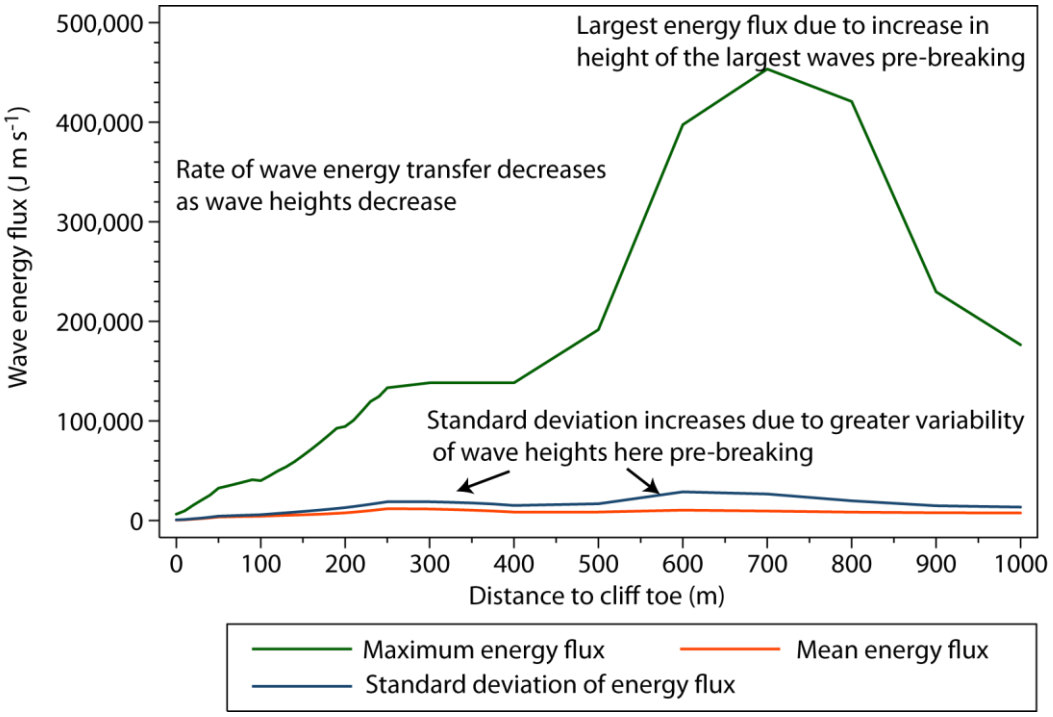

Figure 5.18: Modelled wave energy flux across the nearshore (normal to cliff).

The model only considers energy dissipation due to turbulence as waves break (Battjes and Stive, 1985), therefore the energy dissipation flux across the nearshore clearly indicates energy dissipation in the two dominant zones of wave breaking (Figure 5.19). The highest energy dissipation flux occurs between 800 and 500 m and reflects the breaking of the largest waves in this area, which have the greatest potential energy. As waves break the potential energy within the elevated water in the wave crest is converted into kinetic energy generating turbulent conditions and the formation of surf bores. The relatively low energy dissipation flux (Figure 5.19) compared to the energy flux (Figure 5.18) indicates that rates of wave energy dissipation are much lower than rates of energy transfer by the waves. These results indicate that low levels of energy are being dissipated during wave breaking and considerable wave energy continues to be transferred forwards towards the cliff. As the model only accounts for energy dissipation due to turbulence at the point of breaking, the results suggest that most of the energy must be dissipated nearer to the cliff by other mechanisms, such as turbulence and seabed bottom friction in the shallow waters of the surf and swash zones. Energy transferred to the seabed in the shallow waters has greater potential to affect the cliff.

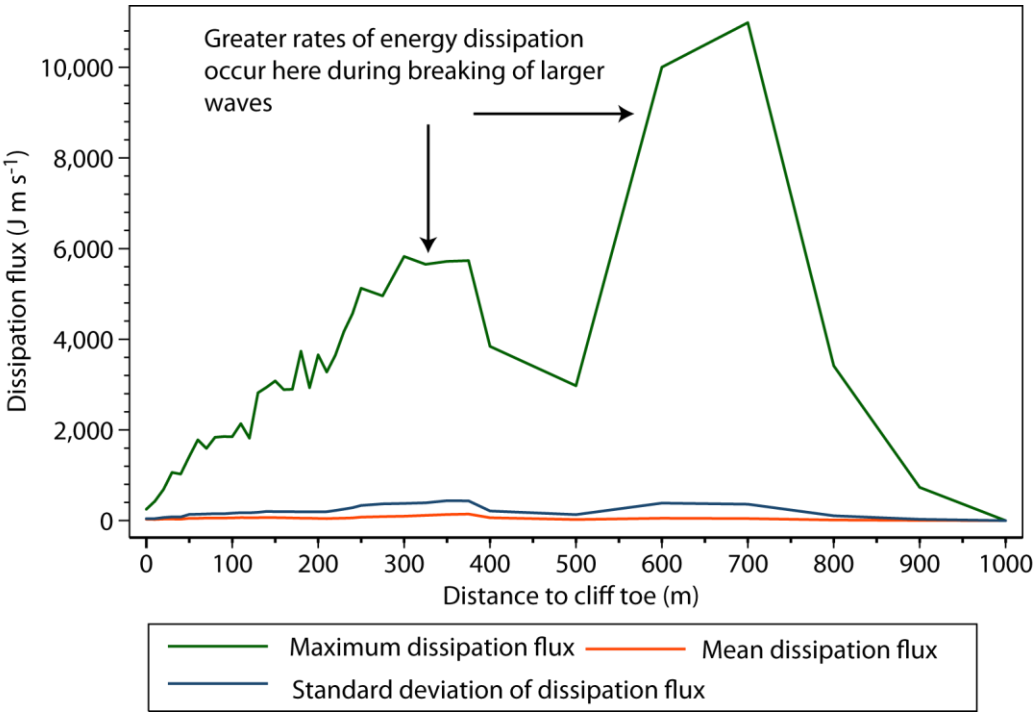

Figure 5.19: Modelled wave energy dissipation flux across the nearshore (normal to cliff).

Throughout the nearshore profile the energy flux (rate of energy transfer by the waves) is significantly greater than the rates of energy dissipation. The rate of dissipation is approximately 2 - 5% of the rate of energy being transferred through the water by the waves. The model only accounts for dissipation via turbulence and bubbles that occur as waves are breaking (as in a wave bore, via a hydraulic jump), it therefore underestimates dissipation as it does not account for other forms of energy dissipation caused by friction between the increasingly horizontal orbital water motions within the wave and the seafloor as waves move through decreasing water depths. The model also does not account for dissipation that occurs post-breaking in the surf and swash zones via turbulence within the surf and due to bottom friction at the seabed. The energy dissipation flux therefore represents energy dissipated within the water and the decrease in energy carried forward in the broken wave as it continues into the surf zone.

These results demonstrate the significant control that tides and bathymetry at this site have in determining where wave breaking occurs due to the large tidal range and long, shallow gradient foreshore. These physical conditions mean that the wave breaking occurs and varies over a large area creating extensive breaking and surf zones, typical for sites with similar foreshore characteristics (Thornton and Guza, 1983).

5.2.4 Waterline location across the intertidal zone

As discussed in Chapter 2 tidal inundation models have been used to indicate where the waterline spends the greatest amount of time and where wave energy delivery, and therefore erosion processes, are likely focussed (Trenhaile and Layzell, 1981; Carr and Graff, 1982; Trenhaile, 2000). Tidal inundation models however do not take account of wave set-up, wave heights nor storm surges (if using predicted tides) which each also determine the sea level and therefore the distribution of wave energy on the foreshore and cliff. Consideration of these features is particularly important at storm wave dominated coasts, such as those of the North Sea.

When wave and set-up heights are added to tide heights at the study site the waterline position shifts landwards (Figure 5.20), and therefore the frequency distribution of the waterline position within the intertidal zone varies to that forced by the tide heights only i.e. the tidal duration model (see Figure 5.12). The water line spends more time at the cliff face because water levels extend vertically up the cliff face once they can traverse no further landwards. Because the MHWN tide lies just seaward of the cliff toe, the addition of wave heights and set-up to this most frequently occurring tide height (see Figure 5.12) has a significant effect on the inundation duration of the water at the cliff face (Figure 5.20). This results in an 11% increase in cliff face inundation frequency, with just over 30% of all tides reaching the cliff face (Figure 5.20).

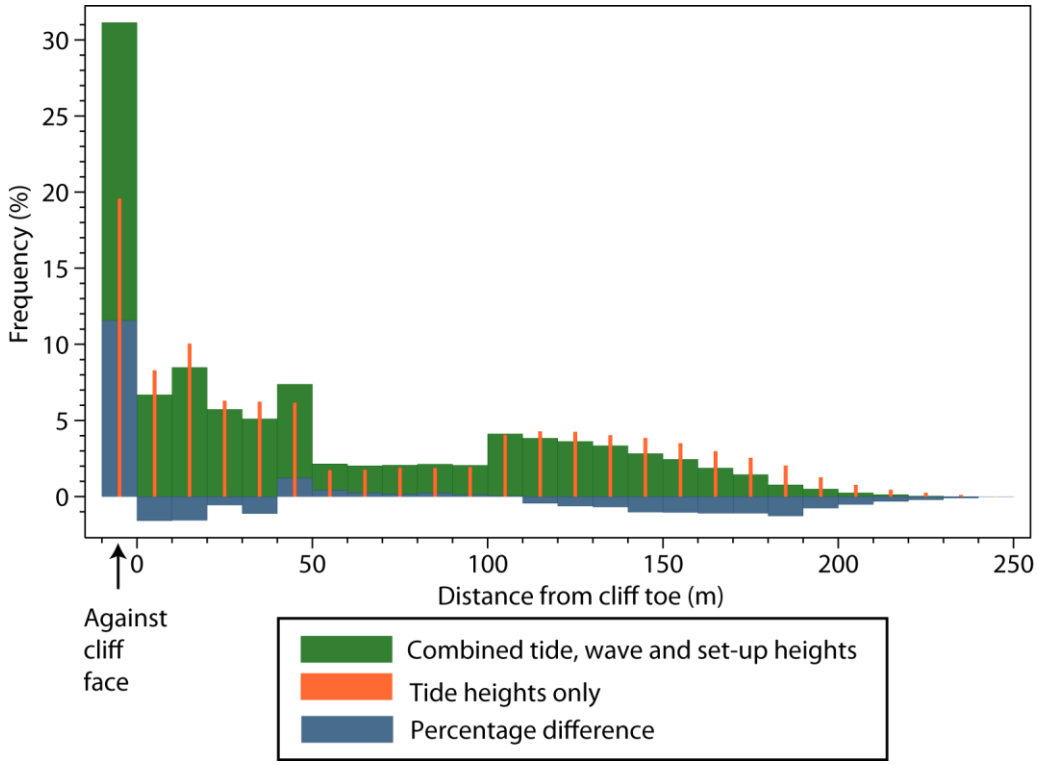

Figure 5.20: Frequency distribution of waterline location along the foreshore and at the cliff face. This represents conditions monitored during the two-year monitoring period and will vary depending on the wave and surge conditions during subsequent monitoring periods.

Considering the effects of wave conditions in addition to tide heights provides a more accurate indication of how the sea is distributed across the foreshore over time. These changes in waterline location frequency have implications for where and when energy delivery is focussed, most significantly for this study is the amount of time the sea is able to impart energy directly to the cliff face.

5.2.5 Vertical variation in inundation at cliff face

The sea spends an additional 11% of the time in contact with the cliff face when wave heights and set-up are added to tide heights (Figure 5.20). By adding wave and set-up heights to the tide height, the height of cliff face exposed directly to waves increases by 1.4 m (Figure 5.21). There are two peaks in increased height frequency (blue bars): the first is at 2.2 mOD (0.6 m above the cliff toe) and is likely to indicate the combinations of average wave sizes and their associated set-up upon the cliff face with the most frequently occurring MHWN tides; the second peak is at 3 mOD (1.4 m above the cliff toe) which may represent the most common storm wave conditions that occur at the cliff as above this height the frequency decreases suggesting higher wave conditions become increasingly rare.

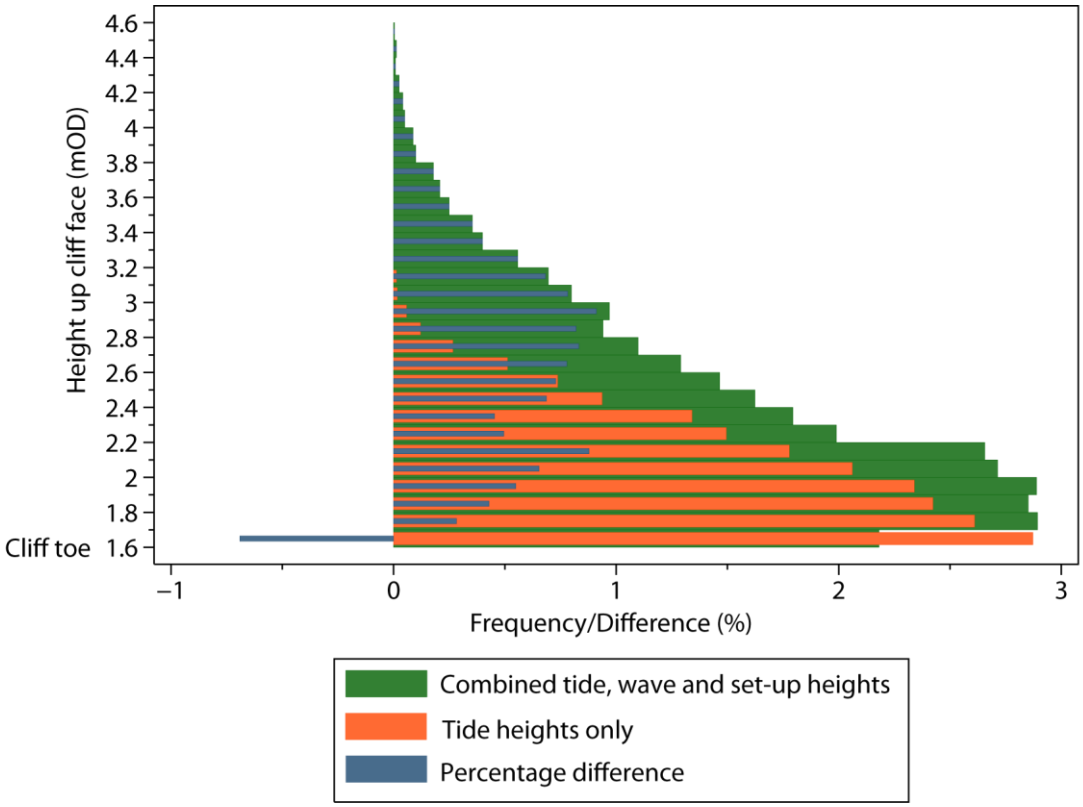

Figure 5.21: Frequency distribution of water levels at vertical locations on the cliff face. Comparison of the Boulby modelled tide heights only (orange) with the combined heights of tides, waves and set-up (green), and the difference between them (blue).

These results have the greatest implications for change of the cliff because both energy transfer and the associated erosive processes will occur more frequently directly at the cliff face. The greater extent of cliff face exposed to the sea by combined tide, set-up and wave heights compared to the highest tide-only level will result in a much greater area of the cliff surface exposed to highly energetic and erosive conditions, well beyond the extent identified by the tidal duration model (Figure 5.12).

5.3 Summary

The results demonstrate the high variability of marine conditions near the cliff during the monitoring period. Variability in marine energy delivery is significantly controlled by local bathymetry and foreshore topography, and the high tidal range (6 m) spread over 250 m of a wide, gentle gradient foreshore. The result is that the exposure of the foreshore and cliff face varies significantly over short, hourly timescales, resulting in rapid changes in the proximity of marine energy sources to the cliff. Marine energy is also dissipated over a wide spatial extent, throughout the tidal cycle. The NAO results in variable climatic conditions at the cliff. Winds,

waves and storm surges show strong seasonality with stormier conditions, and therefore greater energy delivery from all forcing mechanisms, occurring during winter months. Onshore winds and the arrival of swell and large storm waves at the coast results in highly energetic conditions which, as demonstrated in Chapter 4, transfer significant energy to the cliff generating ground motions over a range of characteristic frequencies.

The wave transformation model provides estimates of the wave characteristics throughout the nearshore zone during the monitoring period. The addition of the modelled wave and set-up heights to tide heights demonstrates that the distribution of water levels across the intertidal zone varies significantly to that of simple tidal inundation models, and critically enables increased energy transfer directly to the cliff. Therefore although the results demonstrate the strong control tides have over the locations of wave breaking, they demonstrate that considering tide heights alone does not provide an accurate depiction of energy distribution within the intertidal range, as suggested by Trenhaile and Layzell (1981). This is significant as tidal duration models have been used as the basis of models to identify the distribution of wave energy and cliff erosion (e.g. Trenhaile, 2000; Walkden and Hall, 2005).

The findings of this chapter demonstrate the nature of marine and atmospheric conditions near the cliff. The variables explored in this chapter are used in Chapter 6 to test the combinations of environmental conditions that generate the four frequency bands of ground motions identified in Chapter 4. The combinations of environmental variables that generate each frequency band, together with the frequency and power characteristics of the resulting ground motions, can provide insight into the processes that are transferring energy to the cliff and therefore potentially have a control on cliff erosion. Once the conditions and processes that the ground motions represent are identified, the control of these on cliff erosion can be tested.

Chapter 6: Environmental processes generating cliff microseismic ground motions

The marine and atmospheric conditions near the cliff identified in Chapter 5 provide an indication of the nature of environmental forces acting on the cliff. Constraining more specifically the conditions directly at the cliff and how these environmental forces interact with the cliff, is fundamental to improving understanding of environmental controls of cliff erosion. The four microseismic frequency bands identified in Chapter 4 may provide useful proxies for the environmental conditions and processes that act on the cliff and in addition the ground motion characteristics themselves provide information regarding the nature of interactions with the cliff. The frequency bands could therefore provide a measure of the relative forcing of the different environmental processes that generate them. In this context, the aims of this chapter are to:

- Identify the marine and atmospheric processes and mechanisms that transfer energy to the cliff and generate the different frequency ground motions;
- Compare the relative power and energy transferred to the cliff from the different frequencies and therefore, by proxy, the various environmental processes.

It is hypothesised that using microseismic data to represent the environmental processes might provide a better means of identifying environmental controls of coastal cliff erosion.

To address the first chapter aim, the marine and atmospheric variables that generate the microseismic frequency bands are quantitatively tested using multiple regression analysis. The previous chapter showed that marine conditions vary temporally and spatially due to the relatively large tidal range, foreshore extent, seabed topography, and the wave and weather conditions. The microseismic frequency bands identified in Chapter 4 also show considerable temporal variability in power, with some frequencies showing strong tidal signals, suggesting the processes generating the ground motions are spatially distributed across a variety of source locations. Therefore the modelled marine variables across 1000 m of nearshore, in addition to conditions at the wave buoy, are used in the regression analyses to examine what marine conditions where are generating the microseismic ground motions. Section 6.1 explains the approach used, and the results are presented in Section 6.2.

To address the second chapter aim, energy has been calculated from ground motion frequency power, and the relative power and energy contributions of the different frequency bands are examined. It is anticipated that exploring power and energy of the different frequencies will provide a greater insight into how the various environmental processes represented by the

frequencies influence the cliff. Section 6.3 examines the relative energy contributions of each frequency considered, and therefore considers the relative efficacy of the different environmental processes represented, in generating cliff microseisms.

6.1 Approach used to identify the environmental conditions generating cliff microseismic ground motions

Regression analyses have been used to test the marine and atmospheric conditions that generate each of the frequency bands of ground motions. Specific frequencies from the four frequency bands have been examined to explore the environmental conditions and processes that generate them. The power of each ground motion frequency has been regressed against the environmental variables explored in Chapter 5. Frequency power, rather than energy, is used because power (the rate of energy transfer) provides better insight into how energy is transferred to the cliff, and therefore is more useful in identifying the processes generating the ground motions. Because of the spatial variability of the marine variables (identified in Chapter 5), the area seaward of the cliff therefore also needs to be examined to identify the environmental processes and sources generating ground motions (Figure 6.1). To this end the conditions that generate the microseismic frequency bands are explored at the cliff, across 1,000 m of the nearshore and further seaward at the wave buoy (Figure 6.1).

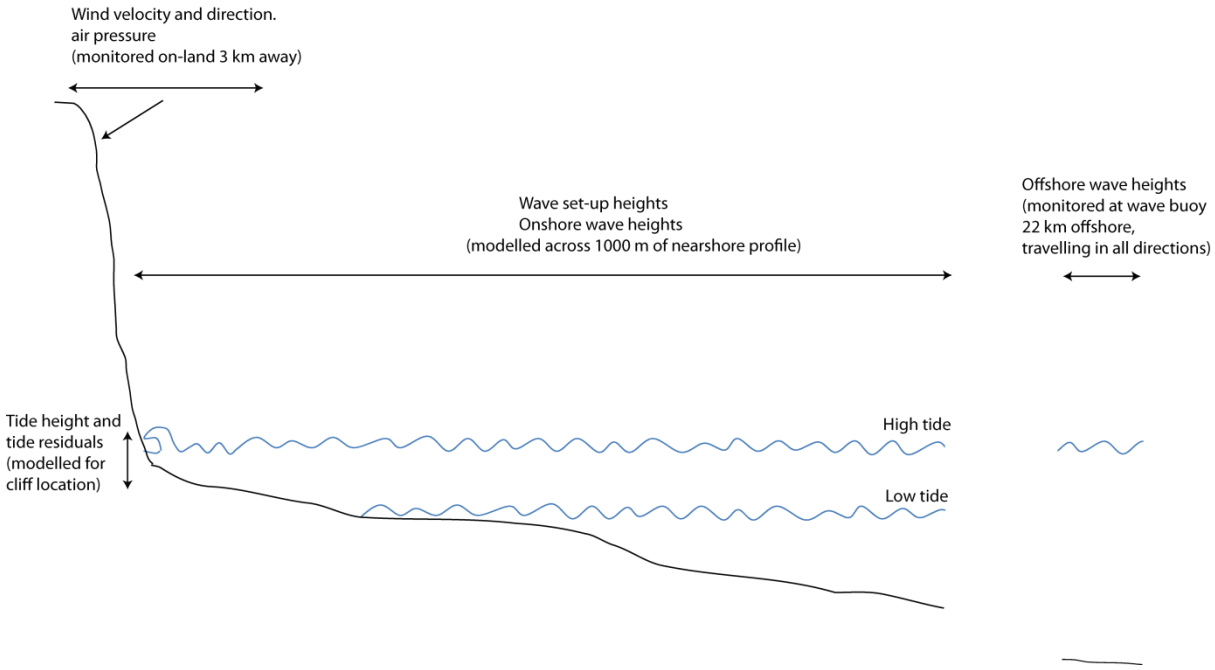

Figure 6.1: The spatial extent and environmental datasets tested to identify the processes and mechanisms generating the microseismic ground motions (not to scale).

The wave and set-up heights across the nearshore were modelled at varying intervals between 1000 m and the cliff - at 100 m intervals from 1000 - 300 m, then at 250 m, 200 m, 150 m, 100 m, 50 m, 40 m, 30 m, 20 m, 10 m and at the cliff toe. Regression analyses have been undertaken between the power of the ground motion frequencies and conditions at each of these locations across the nearshore, as well as at the wave buoy, to constrain where the ground motions are being generated. This is important to distinguish the ground motions generated by waves at the cliff toe, as observed by Adams et al. (2005), from those generated further from the cliff, for example primary microseisms generated further seawards within the nearshore e.g. Hedlin and Orcutt (1989).

Seven specific frequencies have been selected from across the monitored spectrum. The frequencies were selected as those considered to best represent the four different frequency bands, based on their power, temporal variability and periodicity, and observations from the previous literature (Table 6.1).

Table 6.1: The frequencies / periods used to test the environmental conditions generating the different ground motion frequency bands. Frequency power in the dominant direction of ground motion was used in the analysis. N.B In the microseism (MS) frequency band a number of frequencies were selected to explore the variability within this broad range.

Frequency band	**Frequency/Period used**	**Dominant direction of ground motion (seismometer component)**
Wind (WI)	45.5 Hz/ 0.022 s	Vertical (Z)
High tide (HT)	12.5 Hz/ 0.08 s	Horizontal (E-W)
Microseism (MS)	1 Hz / 1 s 0.2 Hz / 5 s 0.1Hz / 10 s 0.07 Hz / 15 s	Vertical (Z) Vertical (Z) Vertical (Z) Horizontal (E-W)
Long period (LP)	0.01 Hz / 70 s	Horizontal (E-W)

The power of these ground motion frequencies represents the combined effects of the available energy from the different sources; the interactions between the sea, air and the local geomorphology; the lithological effects on frequency propagation e.g. attenuation or amplification; and the instrument effects e.g. frequency response. The individual ground motion frequencies are referred to by their periods (in seconds) for the remainder of the thesis as these more clearly relate to the wave conditions that generate each band.

Multiple linear regression analysis has been used to identify the environmental conditions that are generating the seven seismic frequencies and to test their relative contributions to the frequency power. R^2 values and beta coefficients derived from the regression models for each are presented. The regression model R^2 value is used to test how well the combinations of environmental conditions can explain the variability in the frequency power e.g. R^2 of 0.5 implies that 50% of the frequency power variance can be explained by this combination of environmental variables, assuming independence of variables, and that the regression model and variables satisfy standard regression diagnostics. All of the R^2 values presented are statistically significant ($p < 0.001$) given the large numbers of samples analysed; i.e. only the environmental variables that are found to be statistically significant in explaining the signal power are presented in each model.

Different combinations of the environmental variables were regressed against seismic frequency power to define an optimum model. A hypothesis has been set for each frequency stating which environmental conditions are anticipated to generate each set of ground motions. These hypotheses have been tested using different combinations of environmental variables whose characteristics, e.g. frequency, timing and strength, are similar to those of the seismic frequency. The best fit combinations of variables are presented here. The R^2 values and beta coefficients are derived for environmental conditions at defined distances from the cliff toe to explore which processes are generating each seismic frequency, and where.

The relative contribution of each of the significant environmental variables to the frequency power is explained by their beta coefficient values, which are the standardized regression coefficients reported for each variable. The beta coefficients are a standardised measure of the relative strength of each independent variable in the regression model in explaining the dependent variable i.e. how each environmental variable affects the microseismic frequency power. Beta coefficients are measured in standard deviations of the variable units. The beta coefficient values represent the standard deviation increase or decrease of the dependent variable (microseismic frequency power) with one standard deviation increase of the independent variable (environmental variable e.g. wind velocity). For example, in Figure 6.2, at the cliff there is a 0.8 increase in standard deviation of the frequency power with one standard deviation increase of wave set-up. In the same example (Figure 6.2) a one standard deviation increase in the wave heights however only results in a 0.45 standard deviation increase in frequency power and therefore at the cliff. Thus, in this example, set-up has a greater influence on the frequency power.

The analysis of each seismic frequency is presented as follows:

- Presentation of the results of the regression models (the R^2 and beta coefficient values) across 1000 m of the nearshore normal to the cliff;
- The key findings – i.e. which environmental conditions and processes are important, the mechanisms by which they generate the microseismic frequencies, and where;
- Comparison of these findings with those of other studies that have observed the same microseismic ground motions in different scenarios. This is necessary as not all the ground motions have been previously explored in the context of coastal cliffs. In order to fully explain how the combinations of environmental conditions, and resulting processes, are generating the ground motions it is necessary to validate these observations against those of seismology studies that have explored these frequencies in different contexts. This interpretation is covered here as it is specific to these results

and not to the main discussion chapter of this thesis, which addresses these findings in the context of coastal cliff erosion.

6.2 Identifying the environmental conditions and processes that generate the ground motion frequencies

6.2.1 General observations

Wave height and set-up contribute to the power of each of the seven frequencies, although the relative significance to each frequency varies. There is a pattern in the relative contributions of wave and set-up heights across the 1000 m nearshore profile. This is due to variations in the seabed topography which, together with water depths, determines the distribution of location of breaking and therefore wave and set-up heights.

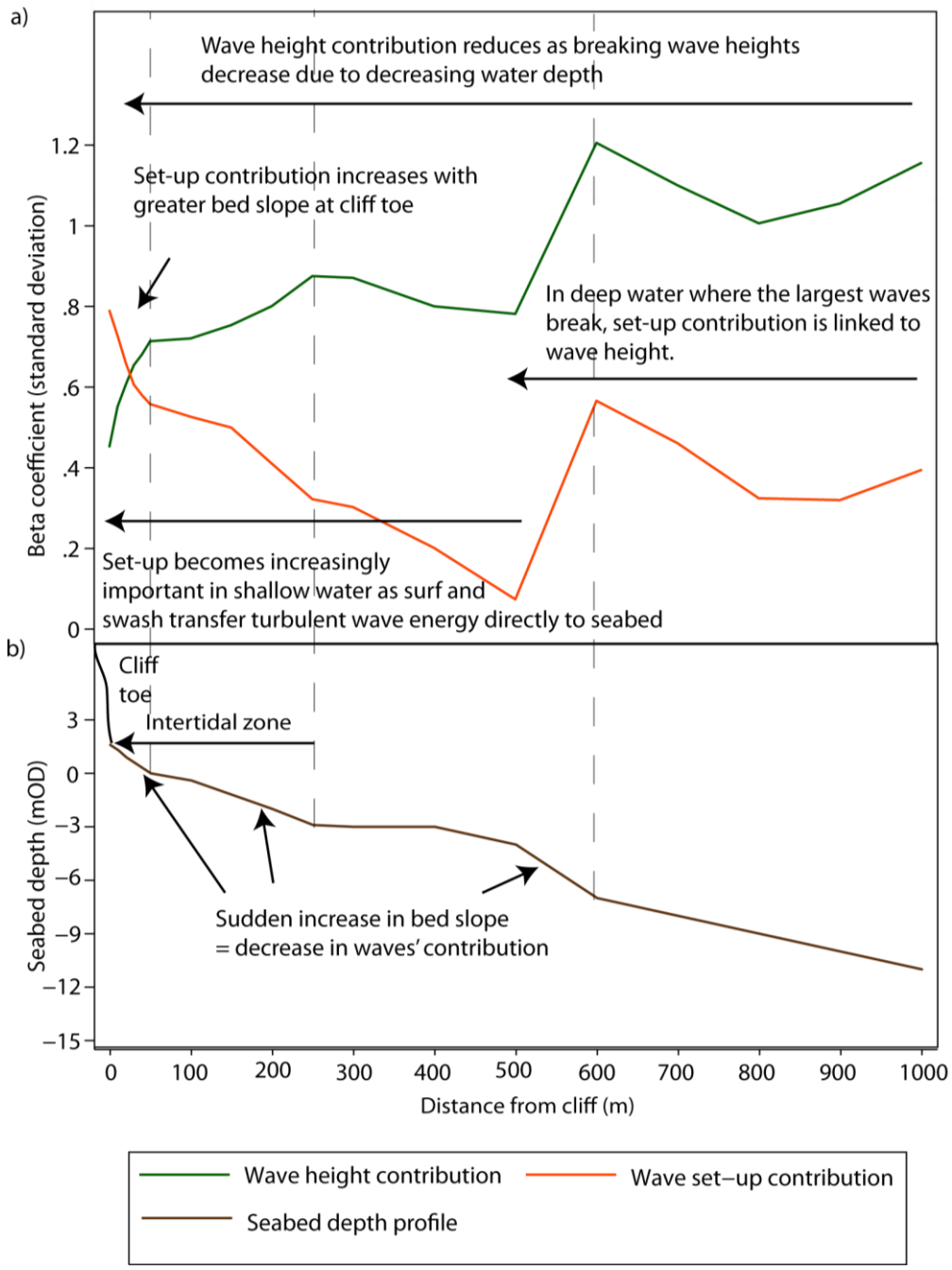

Figure 6.2: Typical pattern of wave height and set-up relative contributions to the ground motion frequency power across the nearshore and their relationship to local bathymetry. a) Typical pattern of wave height and set-up height regression beta coefficients across the nearshore. b) The seabed depth profile across 1000 m of the nearshore. The sea bed morphology across the nearshore profile has a significant effect on the contributions from wave heights and set-up to frequency power via its effect on the breaking location of waves of different heights. Dashed lines represent significant changes in seabed slope, which affect the wave height and set-up contributions.

The distribution of wave heights across the profile reflects the breaking locations of waves of different magnitudes. As wave height is proportional to wave energy, the larger waves transfer greater amounts of energy in the deeper water as they break. Set-up, and therefore surf and swash, become increasingly important to generating the microseismic frequency power in the intertidal zone across the foreshore. The relatively shallow waters of the intertidal zone mean the surf and swash can deliver turbulent energy directly to the foreshore and cliff face.

The pattern of wave height and set-up across the profile demonstrate the significance of foreshore and tidal characteristics in controlling where wave breaking occurs and therefore where wave energy is transferred to the seabed in relation to the cliff. These results show that at this site sufficient wave energy is delivered across the foreshore and seabed away from the cliff face to generate ground motion of the cliff. The greatest contribution from the largest wave heights and the set-up in the deepest zone of the profile indicates that during wave breaking and in the surf zone energy is transferred through the water column to the seabed.

6.2.2 The wind (WI) frequency band: 0.022 s period signal

The 0.022 s (45.5 Hz) period seismic signal is used here to explore the environmental conditions and processes generating the WI frequency band of ground motions. In the spectrograms of Chapter 4 the WI frequency band is characterised by: sporadic high power bursts that typically lie in the period range of 16.7 – 50 Hz / 0.02 - 0.06 s; power is commonly greater in the vertical direction (Z component); the frequency of occurrence and power are both greater in the winter; and sometimes the signal is accompanied by corresponding increased power across the entire frequency spectrum. These characteristics match those observed by studies of wind seismic noise (e.g. Withers et al., 1996; Young et al., 1996; McNamara and Buland, 2004). It is therefore hypothesised that the WI signal is generated by wind loading the cliff.

The beta coefficients show that the hypothesis is largely correct as the variable that contributes most to the signal power is wind velocity (Figure 6.3). Wind generates seismic signals via turbulence caused by friction at the ground surface and over topographic features (Bormann, 2009; McNamara and Buland, 2004). At the cliff this signal can therefore be generated at the cliff top ground surface and at the cliff face (Figure 6.4). In the field there is evidence of wind travelling up over the cliff top as there is regular coating of the seismometer solar panels and boxes by red dust blown up from the glacial till at the cliff face. The presence of the boxes and solar panels above the seismometers increase ground friction and therefore generate additional turbulence around them. In addition the wind probably results in high frequency shaking of the

protruding equipment, which couples into the ground (McNamara and Buland, 2004). However, the highest R^2 values are produced by the model containing onshore winds, which implies that in addition to turbulence at the cliff face, wind loading also transfers energy to the cliff via buffeting (Figure 6.4).

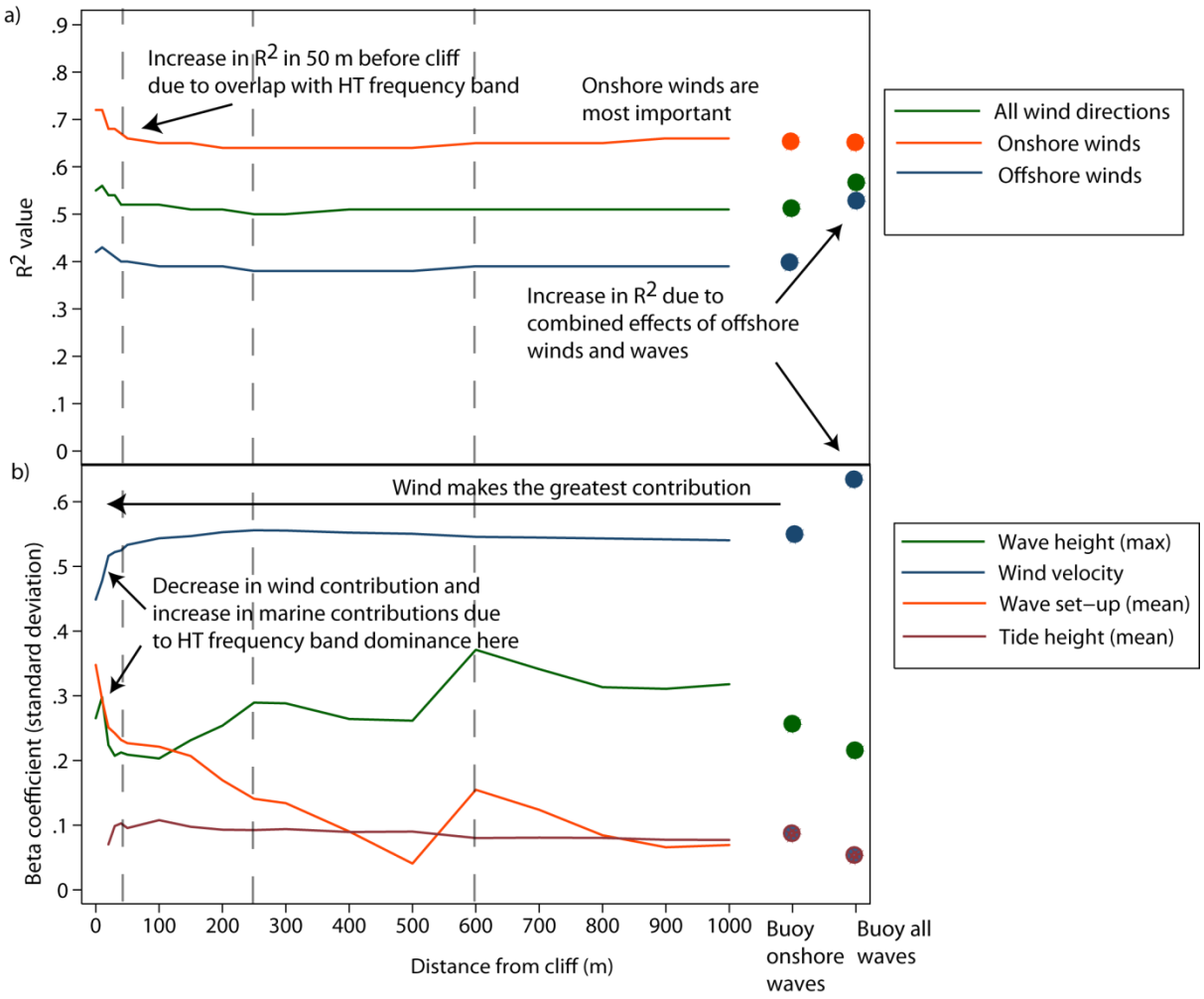

Figure 6.3: The best fit multiple regression model outputs of the 0.022 s (WI) signal: a) R^2 values of the regression models indicate how well the combination of environmental variables explain the signal power. To test the effect of wind direction, onshore winds, offshore winds and winds from all directions were included; b) Beta coefficients of the regression models indicate the relative contribution of the environmental conditions to the signal power. Dashed lines represent significant changes in seabed slope which affect the wave height and set-up contributions. Dots represent the conditions at the offshore wave buoy.

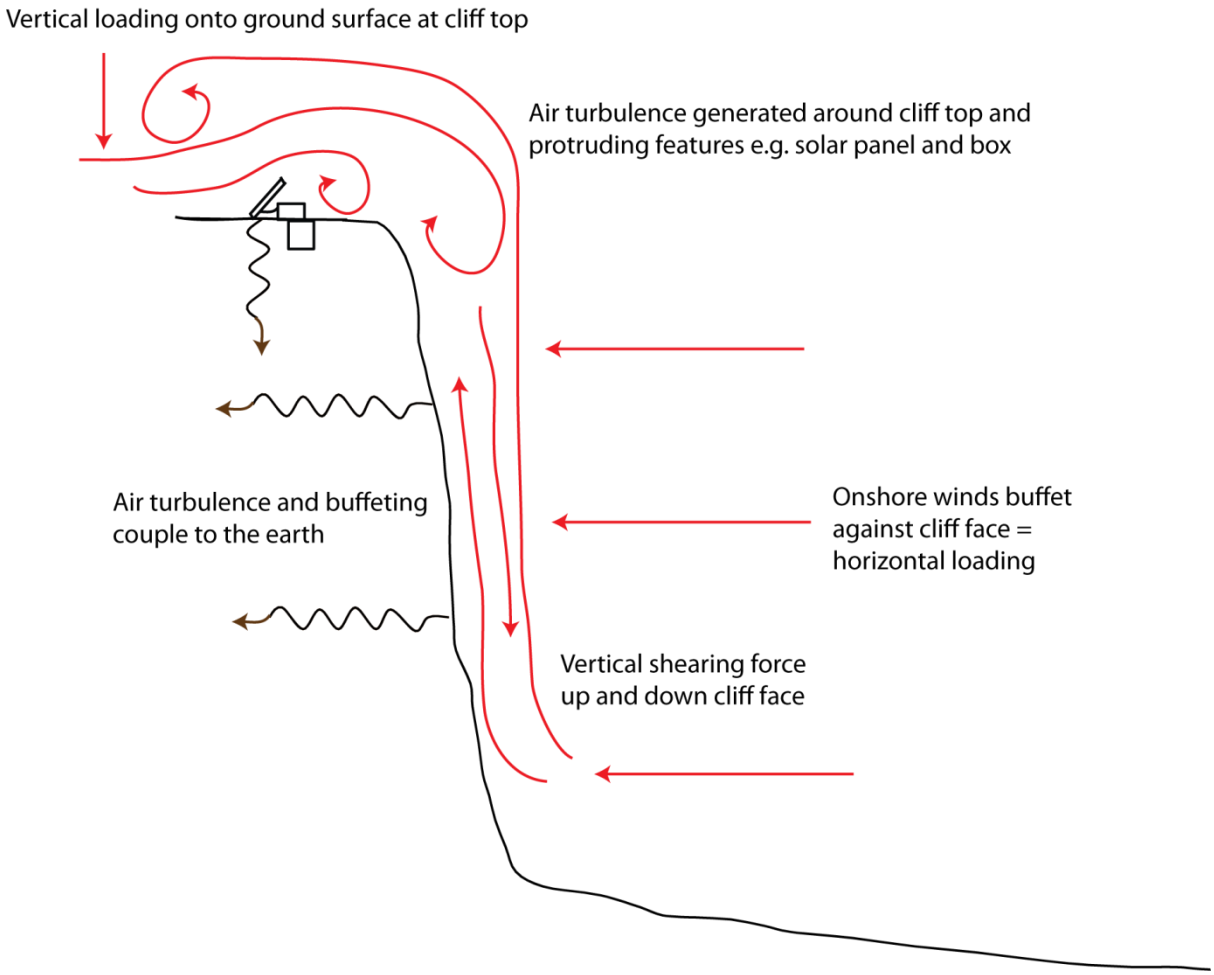

Figure 6.4: Mechanisms of wind energy transfer at the cliff. Energy from wind is transferred to the cliff both vertically and horizontally. The vertical ground motion at this period is believed to be generated by turbulence and vertical wind loading at the ground surface on top of the cliff, as well as due to vertical shearing at the cliff face. Horizontal loading also occurs at the cliff face from onshore winds, in addition to turbulence from winds travelling over the cliff top, generating horizontal ground motions at this period.

There is little variation in the R^2 values across the majority of the cross-shore profile (Figure 6.3) which suggests that the highly varied marine conditions across this zone have little bearing on this signal. However, the increase in R^2 values nearer to the cliff, and the increasing relative contributions of the tide, waves and set-up in this area, suggest that during high tides wave impacts against the cliff do contribute to this signal. This is believed to represent the overlap with the HT signal that also occurs at this period, the generating mechanisms which are explored fully in Section 6.2.3.

The modelled wave conditions used in the regression analysis include only waves travelling onshore; it is only at the buoy that waves from all directions are included. The higher R^2 values

at the buoy when offshore waves are included in the model and are therefore combined with offshore winds, suggest that the winds also generate this signal via interaction with the sea surface. Similar high frequency signals recorded on ocean bottom seismometers have also been found to correlate well with wind speeds, thought to represent acoustic signals generated by whitecaps on the sea surface or the breaking of waves in the open sea (McCreery et al., 1993).

The results show the hypothesis to be largely correct as the primary driver of the WI signal is onshore wind loading on the cliff. These results are important as they identify that energy is not only delivered to the cliff toe by the sea. Non-marine conditions can transfer energy to the cliff face and on to the top of the cliff, generating high-frequency ground motions. The relative contribution of wind compared to marine sources to the energy transferred to the cliff are examined in Section 6.3.

6.2.3 The high-tide (HT) frequency band: 0.08 s period signal

The HT frequency band occupies 2.5 - 50 Hz / 0.02 - 0.4 s and consists of distinct events of increased signal power (Figure 4.1). These high power peaks occur sporadically, yet often occur as groups at regular intervals of approximately 8 hours, lasting for around 4 - 5 hours. These temporal characteristics suggest a tidal control or modulation; this is supported by comparisons with time series of tide heights (Figure 4.2). However, these signal peaks do not feature for all high tides, and comparisons with time series of wave heights indicate that wave characteristics also significantly determine the HT signal. The signal powers are greatest in the horizontal component, which matches the direction of the incoming sea. The regression models will test the hypothesis that the HT signal is generated by high tides that are accompanied by energetic wave conditions impacting against the cliff face.

The importance of tides, wave and set-up heights to this signal, and the increasing R^2 values in the intertidal zone (Figure 6.5), indicate that it is processes associated with wave breaking within this area that are largely generating this frequency signal, with the location of these source conditions determined by the tide. These findings support the hypothesis above. The results show that wave and set-up heights are most important to the generation of the signal when the high tide is at the cliff face, indicating that it is wave processes directly at the cliff that contribute most to the signal power.

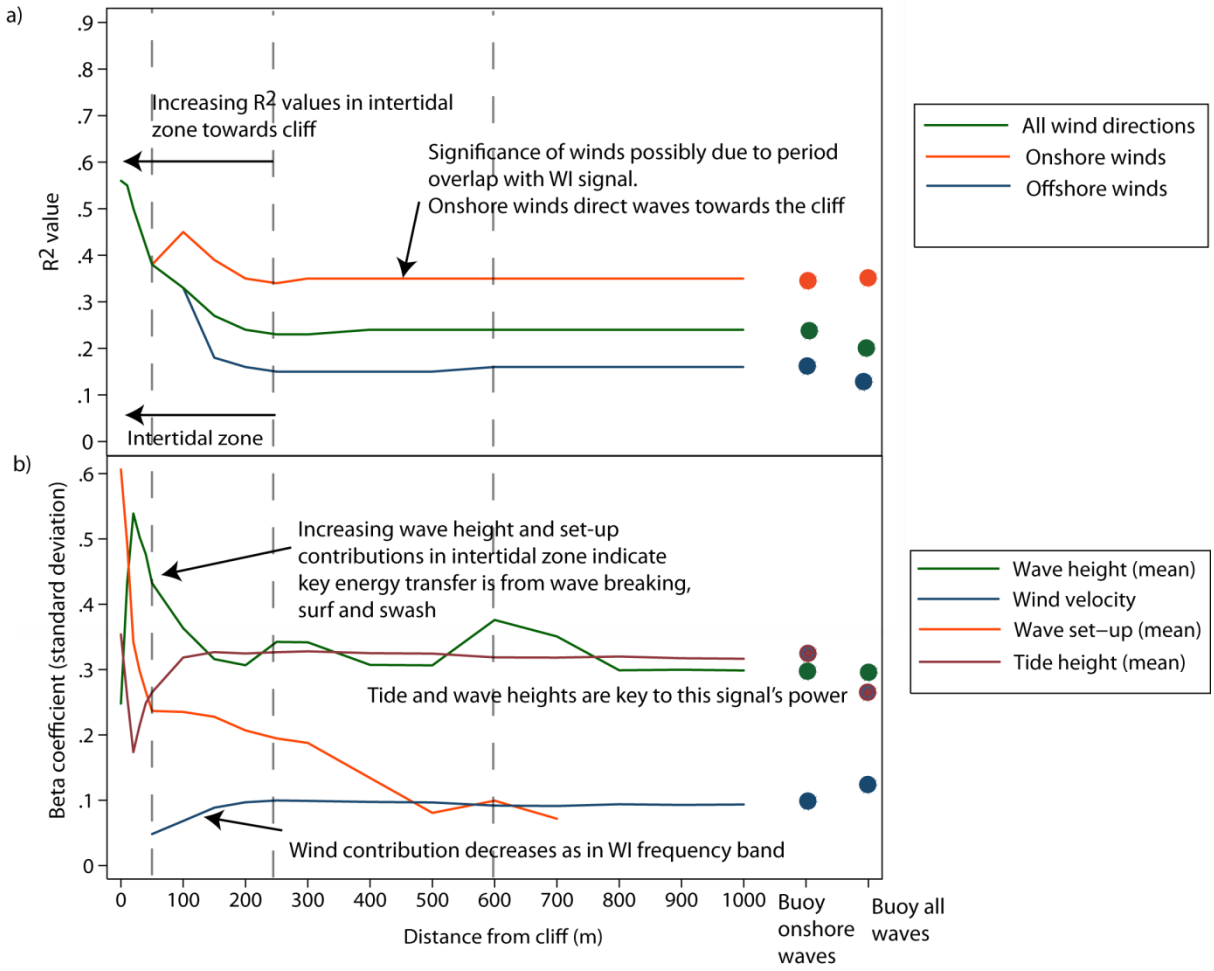

Figure 6.5: Multiple regression model outputs of the 0.08 s (HT) signal: a) R^2 values (To test the effect of wind direction onshore winds, offshore winds and winds from all directions were tested in the multiple regression models); b) Beta coefficients. Wave set-up was only statistically significant landwards of 700 m. Dashed lines represent significant changes in seabed slope which affect the wave height and set-up contributions. In the spectrograms these high tide increases in power are highly distinctive from the constant anthropogenic noise that also occurs at this period. The occurrence of this anthropogenic noise may explain the low R^2 values for this signal. Dots represent the conditions at the offshore wave buoy.

Wave energy is transferred to the cliff as waves impact against the cliff face via a number of mechanisms, in horizontal and vertical directions, the nature of which depend on whether waves are breaking onto the cliff face or before the cliff (Figure 6.6). Waves may break at the cliff face, but the modelling results in Chapter 5 indicate most will break before the cliff due to the long gentle gradient of the foreshore and decreasing water depths. Therefore it is commonly turbulent surf that is directed onto the cliff.

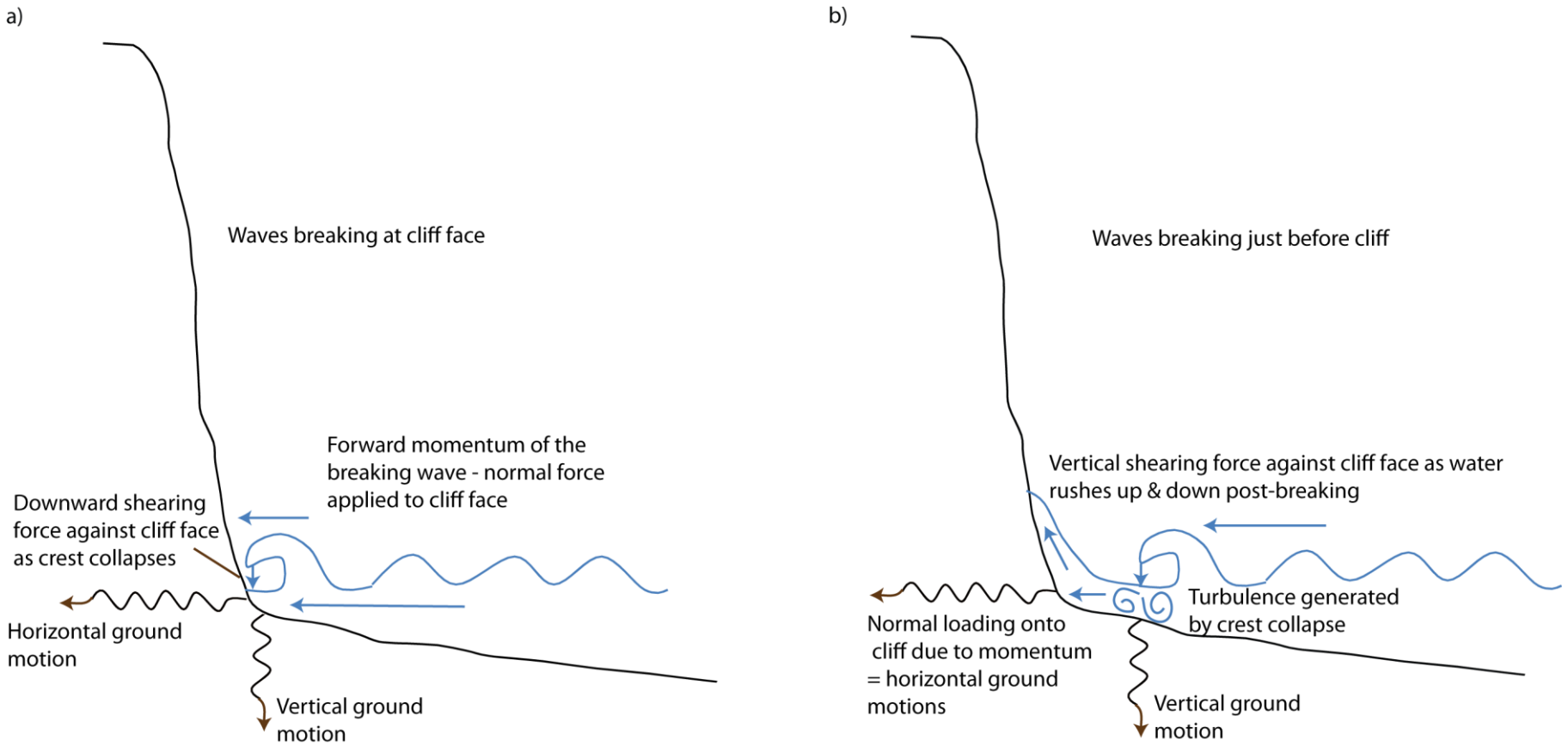

Figure 6.6: Mechanisms of energy transfer to the cliff potentially generating the HT frequency band. As waves break, vertical loading of the cliff face / foreshore occurs due to downward forces as the wave crest collapses. Horizontal normal loading of the cliff face also occurs due to forward momentum of the wave and the surface rollers of the surf bore that are generated at the point of breaking. Depending on the storminess of the marine conditions, this frequency band may be generated a) at the cliff face; or b) on the foreshore in front of the cliff.

The stronger signal powers of this frequency band occur in the horizontal component, demonstrating that more energy is transferred to the cliff via horizontal impacts and loading of incoming waves and surf against the cliff, rather than from the vertical shearing and collapsing wave crests. However, the vertical water movements against the cliff face will be important in removing cliff material via hydraulic processes and abrasion. This high frequency ringing of cliffs in response to wave impacts during high tides has also been observed by Adams et al. (2005) and Young et al. (2011b), who also noted it to be dominant in the horizontal direction of incoming tides.

The increase in R^2 values with decreasing distance towards the cliff suggests that more energy is transferred to the cliff when wave energy is delivered directly to the cliff face than with increasing distance down the foreshore. There is a distance decay effect due to the increased attenuation of microseismic energy with greater distance between the source and seismometer. Short period seismic waves attenuate quicker than longer period waves via anelastic attenuation, and the rapid increase in R^2 values across the intertidal zone towards the cliff, and particularly the increase in the last 50 m, supports the idea that this short period signal attenuates rapidly over distance. However, the increase in R^2 values across the intertidal zone does suggest that the processes that generate this signal occur across the whole foreshore, but the seismometer's position at the cliff top means that the energy recorded is higher the closer the source is to the cliff. Evidence that the processes generating the HT signal occurs across a wider area is in the stormy day example presented in Chapter 4 (Figure 4.3), where highly energetic conditions during storm surges appear to have generated the HT signal on the foreshore during lower tides.

The results indicate that the hypothesis is partly correct in that the HT signal is largely generated during high tides by energetic waves impacting against the cliff. However the R^2 results indicate that the signal can be generated by these conditions at the foreshore in front of the cliff as well as at the cliff face, although the strength of the relationship decreases with increasing distance from the cliff.

6.2.4 Microseism (MS) frequency band

Four different frequencies from the microseism (MS) frequency band of 0.05 - 1 Hz / 1 - 20 s have been selected to better constrain the mechanisms of energy transfer to the cliff at the periods of incoming waves.

6.2.4.1 The microseism (MS) frequency band: 1 s period signal

The 1 s signal was selected because it lies at the boundary between the microseism (MS) frequency band and the higher frequency, higher power HT frequency band. The signal period is shorter than the wave periods recorded at the buoy, and although increases in 1 s signal power sometimes occur with those at the longer MS signal periods, this is not always the case. In the spectrograms the 1 s signal power increases during stormy periods that create increased power across the whole spectrum (e.g. Figure 4.3), and also in the daily spectrograms higher power can also be seen to occur with the HT frequencies (e.g. Figure 4.2). The hypothesis to be tested by the regression analyses is that the 1 second MS signal represents wave breaking across the foreshore.

The pattern of R^2 values across the nearshore profile (Figure 6.7a) broadly matches those of the wave heights (Figure 6.7b). The 1 second MS signal is therefore believed to represent wave conditions across the nearshore and foreshore zone. The results suggest energy is transferred to the seabed, foreshore and cliff face via a number of wave-related processes.

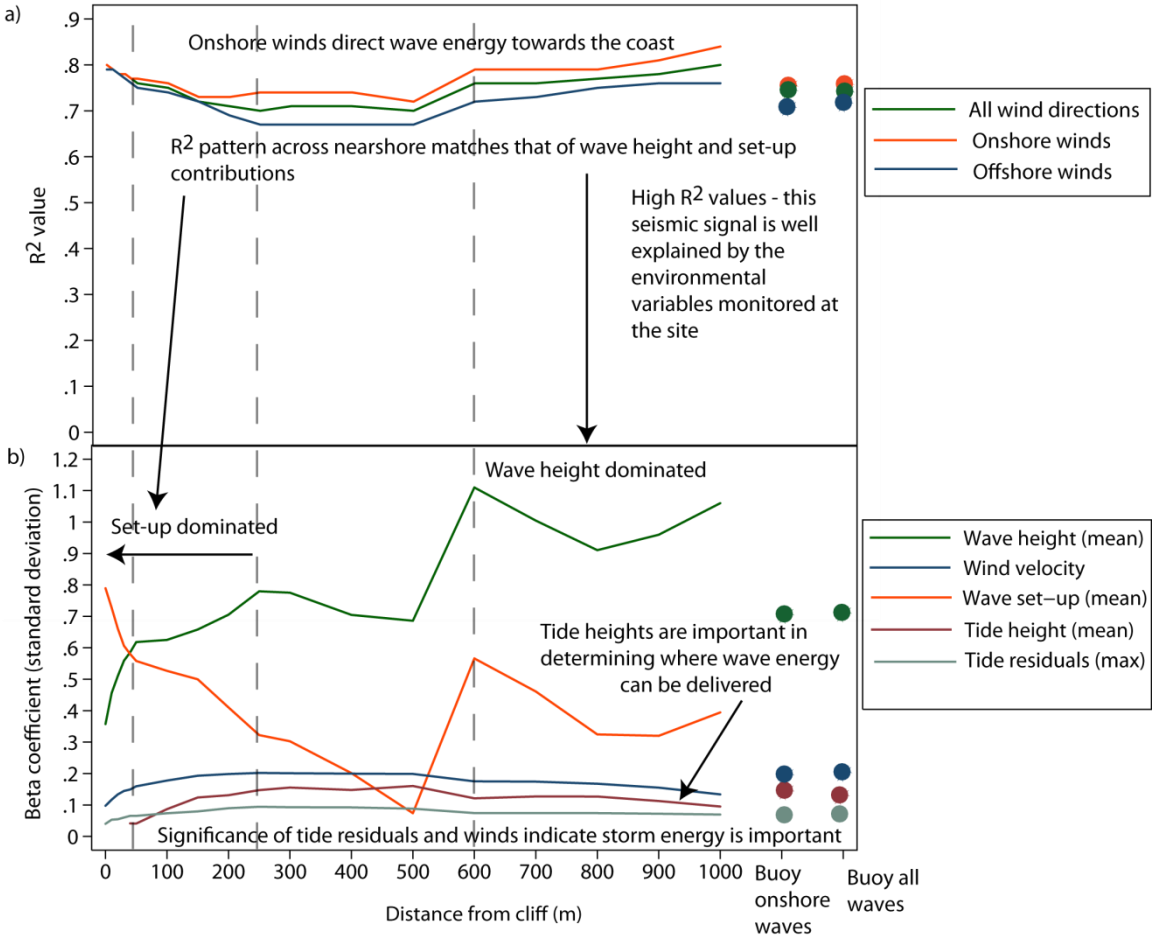

Figure 6.7**:** The best fit multiple regression model outputs of the 1 s (MS) signal: a) R^2 values (To test the effect of wind direction onshore winds, offshore winds and winds from all directions were tested in the multiple regression models); b) Beta coefficients. Dashed lines represent significant changes in seabed slope which affect the wave height and set-up contributions. Dots represent the conditions at the offshore wave buoy.

Wave periods monitored at the site range from 2 - 20 s. If the 1 s frequency is generated by microseism mechanisms then the 1 s microseisms at the site must therefore be double frequency (DF) microseisms, generated by the superposition of ocean waves of 2 s period. The generation of 2 s waves by gentle winds mean that superposition of these waves can occur quite easily as wind directions shift and waves travelling from opposing directions meet, as observed by other studies (e.g. Kibblewhite and Ewans, 1985). Alternatively waves reflected off the cliff face may superpose with incoming waves of the same period. Although such waves occur frequently, short-period ocean waves are of small magnitude as they are generated locally, and therefore their net amplitudes will only generate relatively low signal power compared to larger, longer period waves generated further away. Seismic signals of 1 s period are common at ocean floor seismic stations as the sea surface responds quickly to local winds

(Webb, 1998), and 2 s ocean waves have been observed to be easily generated by gentle winds. Such waves have been observed to form in 2.5 hours under only a 5 ms^{-1} wind (Webb, 1998), during which the wind would only need to run 45 km.

The significance of wave set-up suggests that the microseismic signal partly also represents processes that occur during wave breaking across the nearshore. These findings match those of McCreery et al. (1993) who observed wave breaking on nearby islands generating ocean bottom seismic signals around the 1 s (1 Hz) period. The generating process may be the downward forcing or shock pressure that occurs as waves break, with the 1 s periodicity caused by the repetitive breaking of incoming waves of different periods across the nearshore, possibly in one location triggered by a sudden decrease in water depth. This is suggested by the higher R^2 values in the breaking wave zone 600 - 1000 m from the cliff and in the intertidal zone (Figure 6.7), which in Chapter 5 were shown to be the main areas of wave breaking.

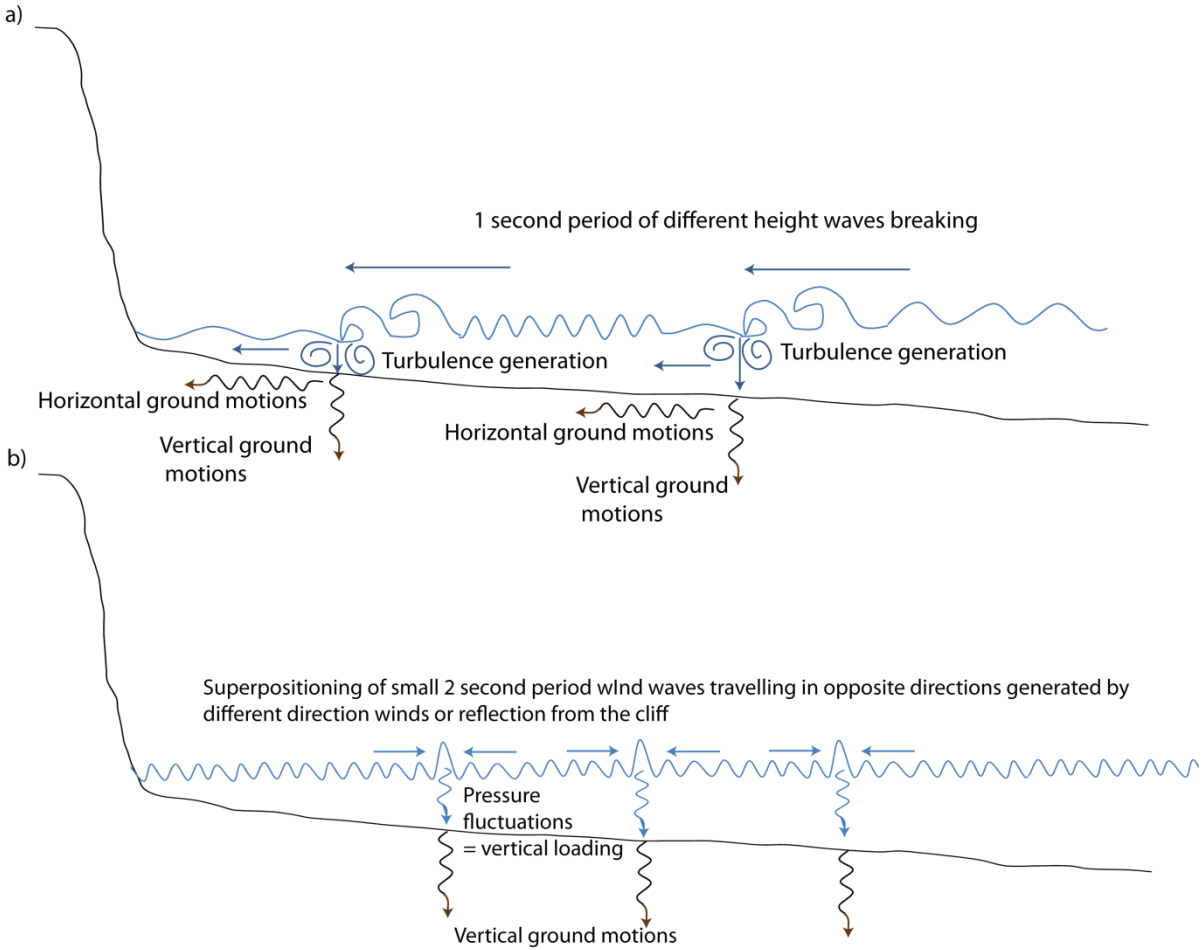

Figure 6.8: Mechanisms of energy transfer to the cliff potentially generating the 1 s MS frequency. This frequency may represent: a) The steady beat of waves of different heights breaking at different locations within the nearshore; b) the formation of small DF microseisms by the superposition of small, locally generated 2 second wind waves.

These results partially support the hypothesis above, however the results suggest the 1 s frequency may also represent DF microseisms generated across the nearshore by small, locally generated waves. The high correlation strength generated between the signal power and the sea conditions across the nearshore may suggest that 1 s frequency is the resonant frequency of the cliff, which develops in response to the sum of the different wave processes acting across the nearshore.

6.2.4.2 The microseism (MS) frequency band: 5 s period

The spectrogram of the two-year monitoring program (Figure 4.8) shows the highest signal power within the spectrum of wave periods recorded at the wave buoy to occur at around 5 s period. This is also the wave period typically associated with double frequency (DF) microseisms in global seismic noise models (e.g. Peterson, 1993). 5 seconds is also the mean wave period recorded by the wave buoy. Therefore it is anticipated that the microseismic signal at the same period could represent both primary and DF microseisms. It is uncertain to what extent 5 s DF microseisms are generated in the North Sea by swell waves of 10 s, as 10 s waves made up only 8% of the monitored maximum wave periods recorded at the buoy (Figure 5.10b). It is expected that the 5 s signal, together with the other seismic signals between 2 - 18 s (the range of wave periods recorded at the buoy (Figure 5.10)), represents primary microseisms generated by wave conditions of the same periods in shallow water near the coast. The hypothesis to be tested by the regression analyses is that the 5 s MS signal represents primary and double frequency microseisms generated near the coast.

The highest R^2 value occurs during offshore wind and wave conditions at the buoy approx 22 km from the coast (Figure 6.9). This suggests that this signal is generated largely beyond the nearshore where sufficient fetch enables offshore winds to generate waves. Conditions within the nearshore appear to only make a small contribution to the signal generation. The significant environmental variables in the model suggest that stormy wind and marine conditions generate this signal.

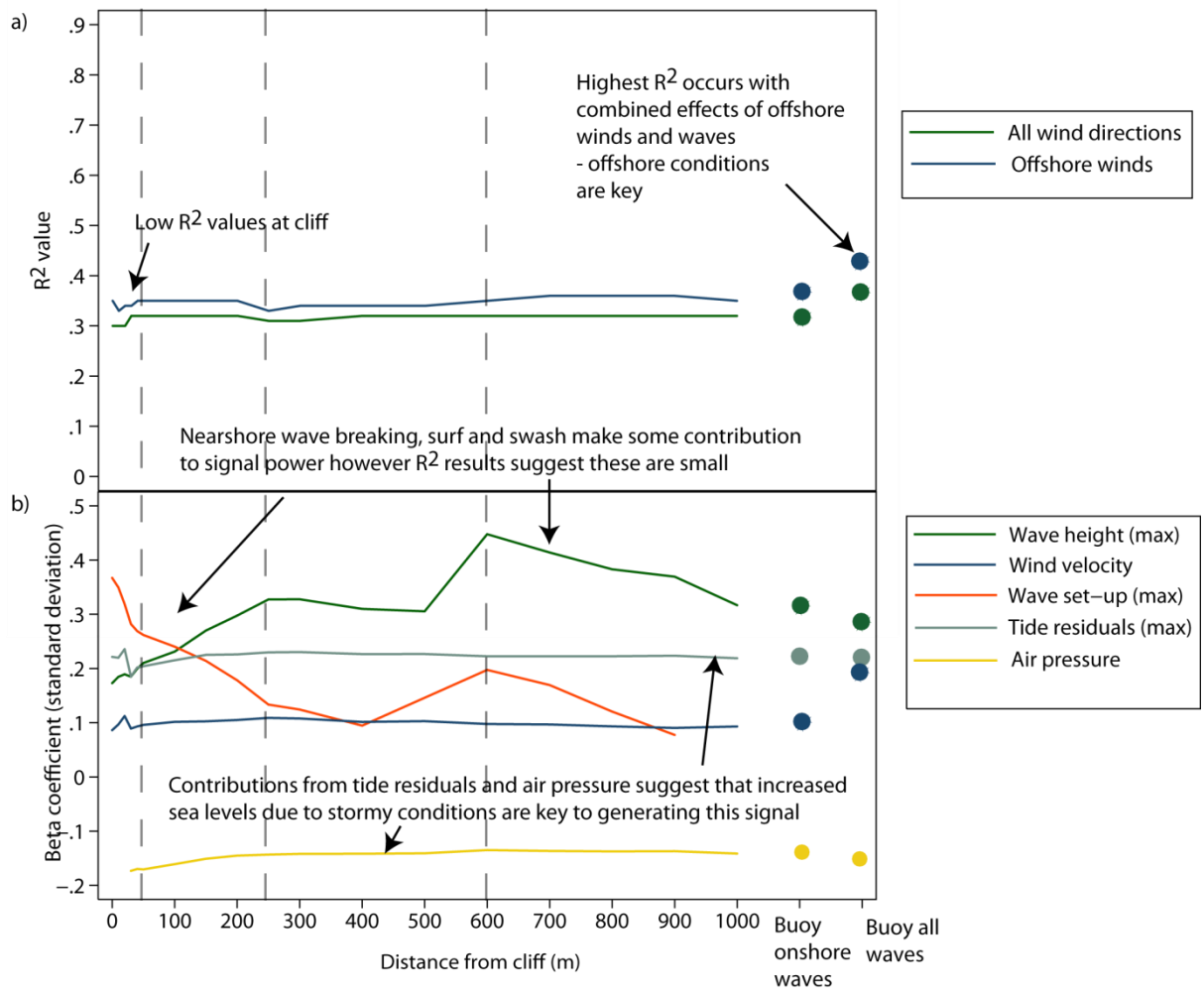

Figure 6.9: The best fit multiple regression model outputs of the 5 s (MS) signal: a) R^2 values (To test the effect of wind direction onshore winds, offshore winds and winds from all directions were tested in the multiple regression models.) Onshore winds are insignificant to the generation of the signal; b) Beta coefficients. Dashed lines represent significant changes in seabed slope which affect the wave height and set-up contributions. The low R^2 values indicate there are other variables, not used here, that contribute to the signal power such as wind and wave conditions further offshore in the North Sea. The negative beta coefficients of air pressure show that as air pressure rises, the signal power decreases, representing the decrease in sea level that occurs with rising air pressure. Dots represent the conditions at the offshore wave buoy.

The significance of the wave heights across the nearshore in generating the 5 s MS signal (Figure 6.9b) suggests that the signal is partially generated by primary microseisms within the nearshore. These are generated by waves of the same period (approximately 20% of waves recorded at the buoy have 5 s periods) via pressure fluctuations under the waves which couple into the seabed generating seismic waves (Hasselman, 1963) (Figure 6.10b). The higher R^2

values at the buoy however indicate that these are generated largely beyond the 1 km nearshore. The relatively shallow depths of much of the North Sea make it highly suitable for the generation of primary microseisms (Hedlin and Orcutt, 1989) and so 5 s primary microseisms generated beyond the 1000 m of nearshore may be generating this signal detected at the cliff top seismometer. The mean wavelength of 5 s period waves recorded at the buoy is 38.98 m, which would start to generate primary microseism signals in depths of approx 19.5 m assuming the pressure fluctuations begin to interact with the seafloor in water depths of half the wavelength (Bromirski et al., 2005). This water depth lies between that at the 1000 m extent of the nearshore examined here and the depth at the wave buoy (66 m approx) and so 5 s primary microseisms can be generated over a large area. A number of studies have detected primary microseisms generated at distant locations from their seismometer sites (e.g. Cessaro, 1994; Friedrich et al., 1998). The low R^2 values of these regression models may therefore mean that some of the microseisms detected at the seismometer are not generated at this stretch of coast in the conditions represented by the marine variables used in the model.

The high amplitude, distinctive peak in global noise models associated with DF microseisms at around 5 s periods (e.g. Peterson, 1993) may also explain the high power of the 5 s signal, which is poorly explained by the local environmental variables used in the regression models. DF microseisms of 5 s periods are generated by 10 s waves and are considered to be 'regional' i.e. generated by winds and waves within the same ocean basin (Webb, 1998). This is because at these periods these Rayleigh seismic waves do not travel as efficiently as at longer periods and therefore 5 s DF microsesisms generated further away will not be detected at this site (Webb, 1998). If the 5 s signal at the study site does represent DF microsesisms then they must therefore be generated within the North Sea basin. It is anticipated that these DF microseisms are generated in areas of open sea where multi-directional wave fields occur that enable the superposition of waves travelling in opposing directions (Webb, 1998) (Figure 6.10a). Alternatively these DF microseisms may be generated near the coast by the superposition of incoming waves with waves reflected from the cliff, however the low R^2 values across the nearshore suggest this is rare at this site, possibly indicating the coastal morphology and bathymetry of the coast are unsuitable for wave reflection. These findings indicate the hypothesis is true.

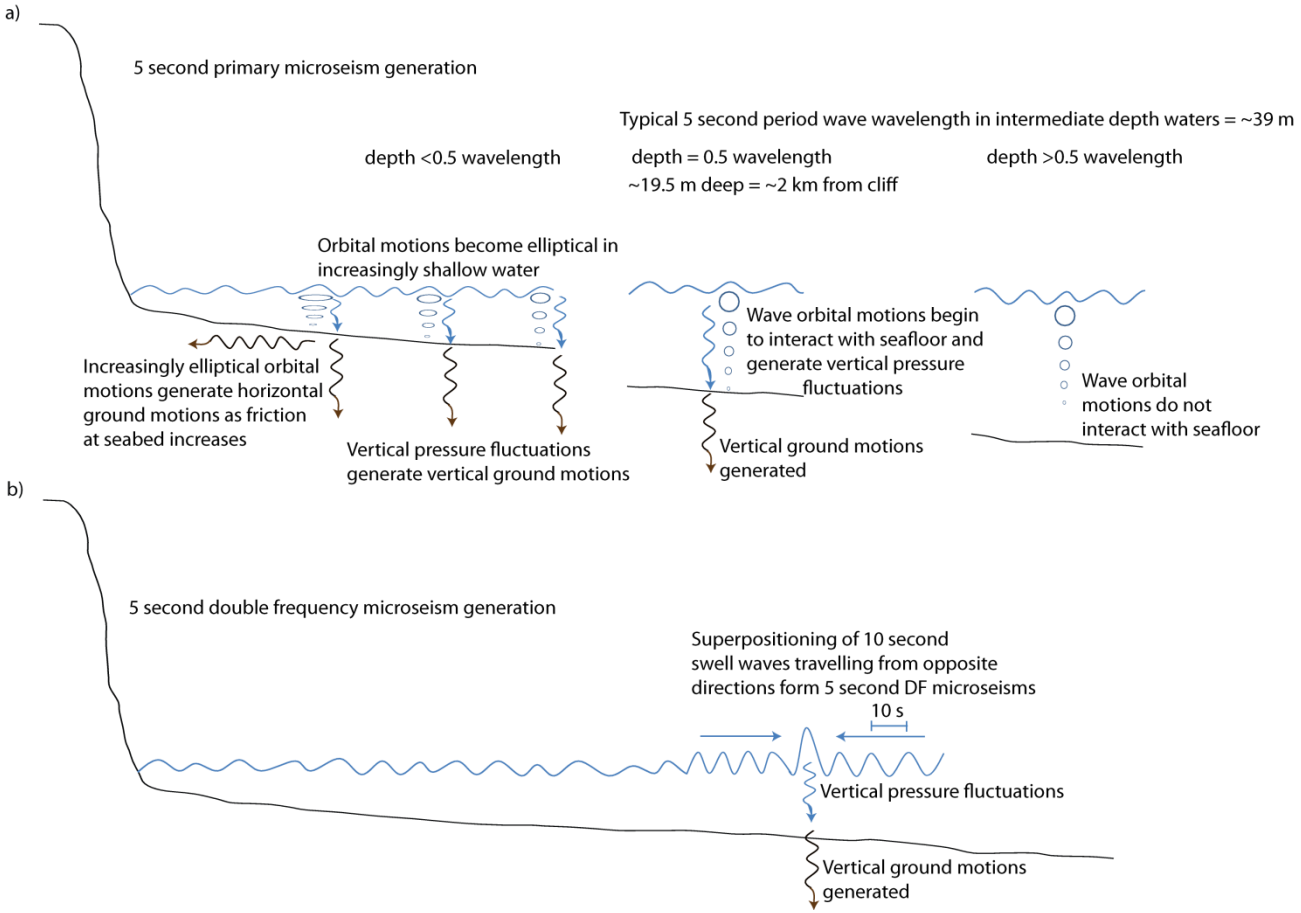

Figure 6.10: Mechanisms of energy transfer to the cliff potentially generating the 5 s MS frequency. 5 s microseisms can be generated by two different mechanisms: a) primary microseisms are generated as the orbital motions beneath waves come into contact with the seafloor; b) double frequency (DF) microseisms are generated as waves of the same period superpose. DF microseisms can be generated in any depths, so this frequency could be generated in the nearshore or offshore. The pressure fluctuations generated by both mechanisms produce ground motions that are dominant in the vertical direction.

6.2.4.3 The microseism (MS) frequency band: 10 s period signal

The 10 s signal has been selected as it corresponds to the primary microseism noise peak in the global noise models (e.g. Peterson, 1993), representing swell waves generated offshore. This signal can be compared against the 5 s signal to better distinguish the roles of primary and DF microseisms within the microseism (MS) frequency band. In the spectrograms, higher power at the 10 s period (0.1 Hz) is linked with the higher power in the MS and LP frequency bands. The 10 s signal power is typically the lowest of these ranges. The regression analyses will test the hypothesis that the 10 s signal is generated at the coast by the primary microseism mechanism generated by incoming swell waves of the same period.

In the PQLX plots (Figure 3.3) it is evident that at 10 s the seismometer reaches the noise floor. This means that at times the power of the instrument noise is greater than that of the 10 s MS signal, and so the two are indistinguishable. The seismometer is therefore not capable of recording the lower powers at this period and so not all of the signal power may be accurately represented. This partly explains the low R^2 values of this signal in the regression models (Figure 6.11). This signal, as with the other MS signals, demonstrates a strong seasonality, with greater power recorded during the winter, which matches the seasonal characteristics of the environmental variables (Chapters 4 and 5). The noise floor therefore has a greater effect on the data recorded during the summer when the power of this signal period is lower due to calm weather and marine conditions. This means that the environmental variables' significance in the regression models are best represented during the more energetic winter conditions.

The regression results suggest that stormy offshore conditions that generate swell waves are more important in generating signal power than conditions within the 1000 m extent of nearshore examined (Figure 6.11). This suggests that the signal represents primary microseisms generated beyond the nearshore by swell waves. In Peterson's (1993) seismic noise model, the DF microseism peak (around 5 s) is approximately 20 dB greater in power than that of the primary microseism peak (at around 10 s). The 10 s signal power at this study site is on average 14 dB lower than the 5 s signal, which may indicate that these are the primary microseisms generating the 5 s DF microseisms. The significance of wave heights, set-up and tide residuals within the nearshore however do indicate that 10 s primary microseisms within this zone also contribute to this signal (Figure 6.11b).

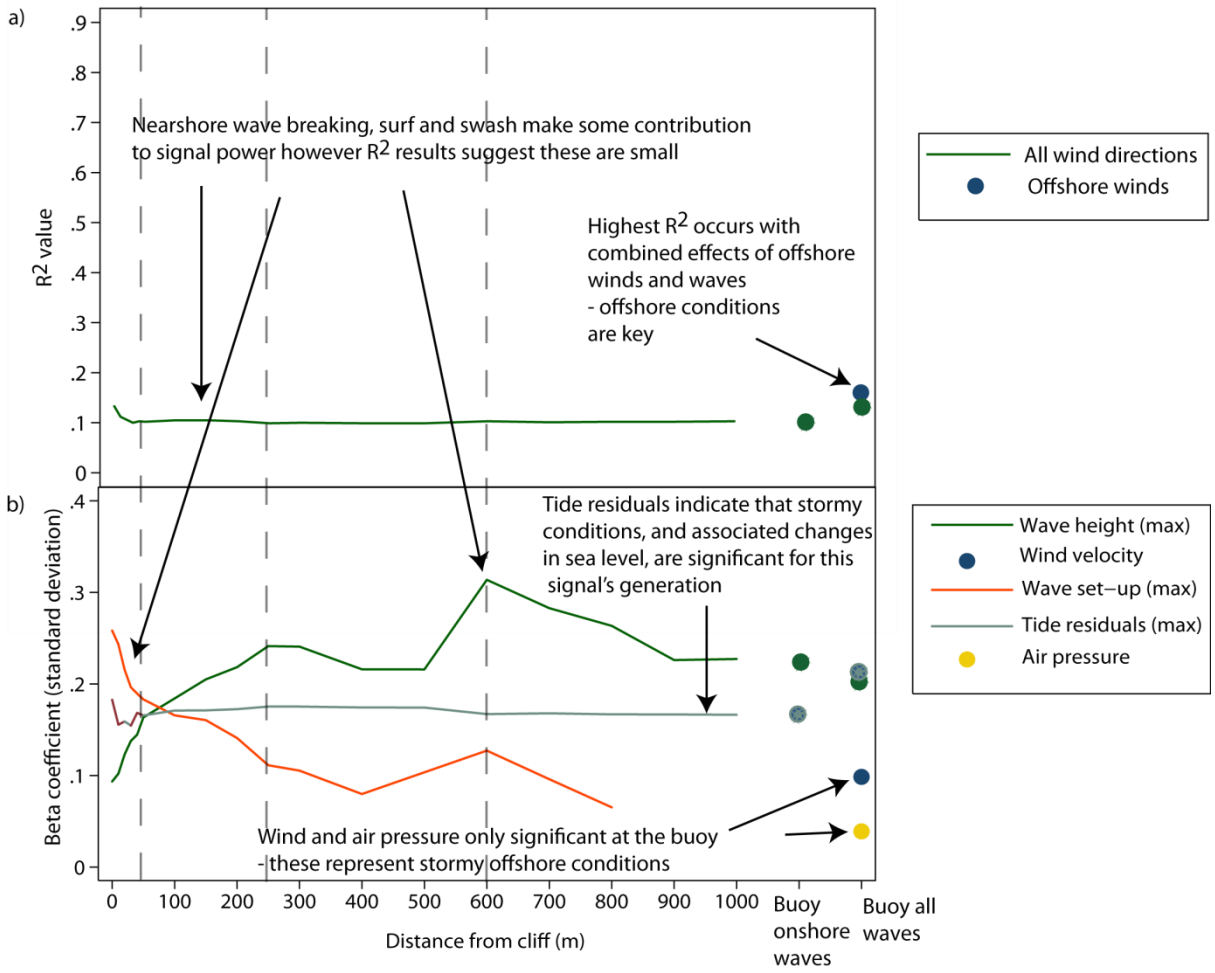

Figure 6.11: The best fit multiple regression model outputs of the 10 s (MS) signal: a) R^2 values (To test the effect of wind direction onshore winds, offshore winds and winds from all directions were tested in the multiple regression models.) Onshore winds are insignificant to the generation of the signal; b) Beta coefficients. Dashed lines represent significant changes in seabed slope which affect the wave height and set-up contributions. At periods of 10 seconds the seismometer noise floor is reached so some of the seismic signal is obscured. This may partly explain the low R^2 values. The low R^2 values may also indicate that the signal is poorly explained by the locally monitored environmental conditions and that there are other variables, not used here, that contribute to the signal power such as wind and wave conditions further offshore in the North Sea. Dots represent the conditions at the offshore wave buoy.

It is likely that the 10 s signal does not represent DF microseisms. Because DF microseism periods are half the period of the waves that generate them, 10 s DF microseisms will be produced by 20 s waves. The fetch of the North Atlantic is incapable of generating waves of 20 s period, even during severe winter storms (Webb, 1998) and DF microseisms that travel as surface waves generated in much deeper waters in mid-oceans are believed to attenuate before

reaching land (Bromirski et al., 2005; Bromirski, 2009). Therefore 10 s DF microseisms generated further away in larger oceans will not be detected at this coastal seismometer. The results suggest that the signal represents primary microseisms generated beyond the nearshore by swell waves and thus supports the hypothesis. The average wavelength of 10 s waves at the site is approximately 154 m and therefore start to interact with the seafloor at approximately 77 m depth (Figure 6.12).

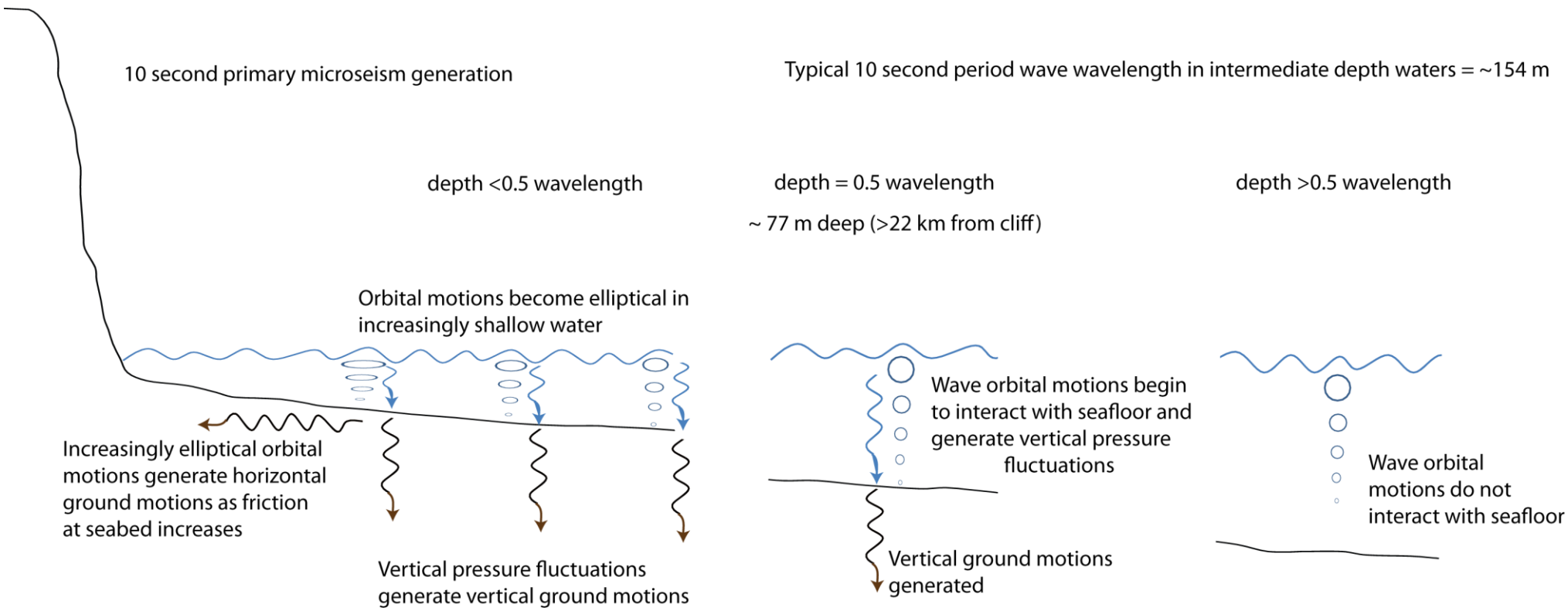

Figure 6.12: Mechanisms of energy transfer to the cliff potentially generating the 10 s MS frequency. 10 second microseisms are generated by the primary microseism mechanism - vertical pressure fluctuations are generated as the orbital motions beneath waves come into contact with the seafloor. The pressure fluctuations produce ground motions that are dominant in the vertical direction however as the depth decreases the orbital motions become more horizontal producing horizontal ground motions.

6.2.4.4 The microseism (MS) frequency band: 15 s period

The 15 s signal was selected to further explore the energy transfer from and signal associated with swell waves at the study site. Swell waves of 15 s period are generated offshore by winds that have travelled over long fetches. In the spectrograms, the 15 s signal powers appear to be more closely associated with the LP frequency band than with the MS frequency band. Waves of 15 s periods are recorded at the buoy; however only 1% of the 30-minute maximum wave periods are 15 s or longer. The signal power is typically lower at 15 s than at the longer periods.

The noise floor is lower in the E horizontal component than in the Z vertical component (Figure 3.3). The signal power of wave periods longer than 10 s is higher in the horizontal components than the vertical component. This means that although the noise floor of the seismometer appears to affect all wave periods longer than 10 seconds, much less of the 15 s low power elements of the signal are lost when explored in the E component. The hypothesis to be tested is that the 15 s MS signal is generated by swell waves via the primary microseism mechanism as the waves enter shallow water.

The R^2 values and significance of the environmental variables suggests that the signal is generated by stormy marine conditions across the nearshore (Figure 6.13). The significance of wave heights and the swell wave period indicate the signal is generated by microseism mechanisms. The longest period DF microseisms are cited as being 10 s, generated by the superposition of 20 s waves generated in the largest oceans (Webb, 1998). 15 s DF microseisms therefore do not occur, and this means that the 15 s signal must represent primary microseisms generated by swell waves in the shallow waters of the North Sea.

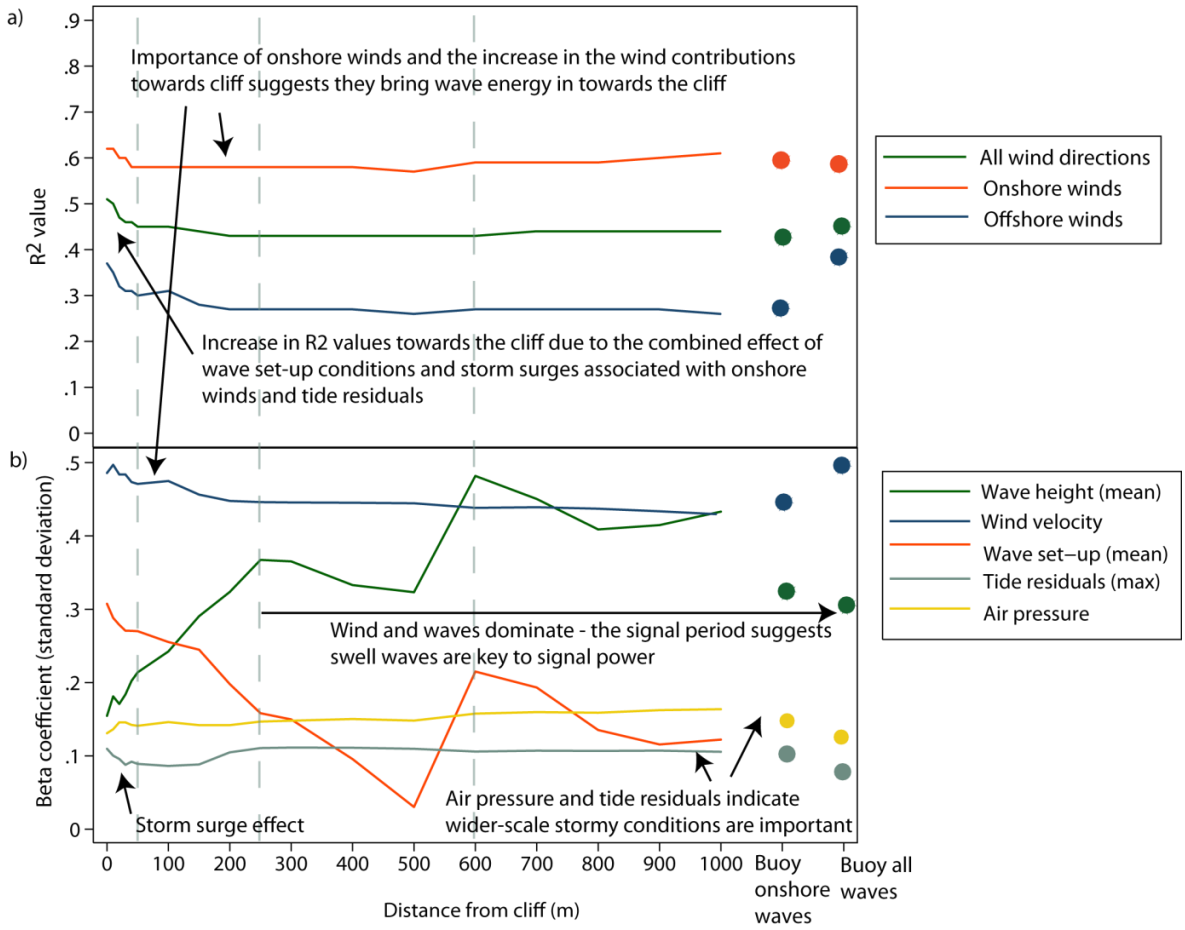

Figure 6.13: The best fit multiple regression model outputs of the 15 s (MS) signal: a) R^2 values (To test the effect of wind direction onshore winds, offshore winds and winds from all directions were tested in the multiple regression models); b) Beta coefficients. Dashed lines represent significant changes in seabed slope which affect the wave height and set-up contributions. Dots represent the conditions at the offshore wave buoy.

The significance of tide residuals and air pressure to the signal's generation indicate that wide-reaching storm conditions are important here. Swell is generated by distant storms and is therefore not necessarily related to the winds at the coast. However, the highest R^2 values are generated by the multiple regression models including onshore winds, showing that they are important to the generation of storm surges and bringing swell waves in towards the coast. The average wavelength of 15 s waves at the site is 307 m and therefore 15 s primary microseisms can start to be generated in depths of approximately 154 m (Figure 6.14), the shallow depth of the North Sea means that these microseisms can therefore be generated across the majority of the North Sea basin.

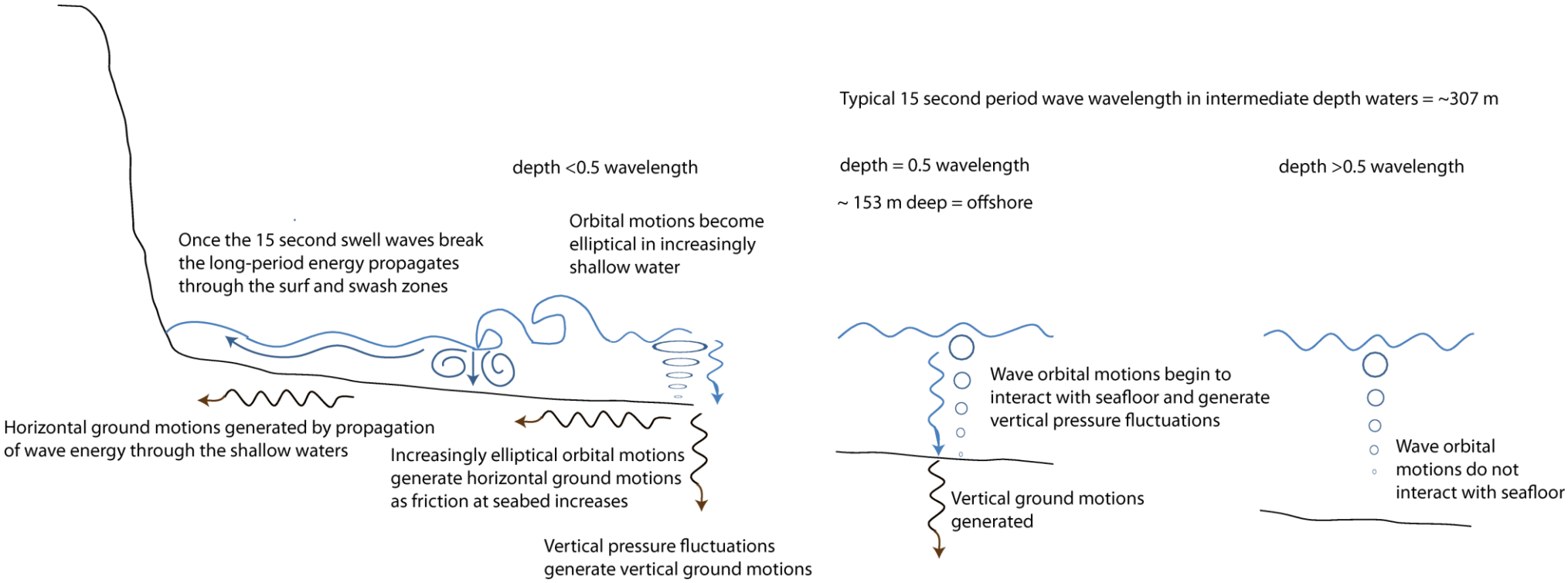

Figure 6.14: Mechanisms of energy transfer to the cliff potentially generating the 15 s MS frequency. 15 second microseisms are generated by the primary microseism mechanism - vertical pressure fluctuations are generated as the orbital motions beneath waves come into contact with the seafloor. The pressure fluctuations produce ground motions that are dominant in the vertical direction however as the depth decreases the orbital motions become more horizontal producing horizontal ground motions. The increase in R^2 and wave and set-up contributions across the nearshore suggest once 15 second waves have broken, their energy propagates through the shallow water through the surf and swash zones.

These results demonstrate that stormy conditions can result in longer period cliff ground motions as well as high frequency ringing of the cliff. The increase of the R^2 values near the cliff demonstrate that longer period energy of swell waves brought into the coast can propagate through the shallow intertidal zones. The focussing of long-period energy in shallow surf and swash zones has been identified by a number of studies (e.g. Guza and Thornton, 1982; Holman and Sallenger, 1985). In fact, the highest R^2 values occur at the cliff, demonstrating that increased energy delivery occurs at the cliff. The beta coefficients show this is due to the combined effect of storm surges and wave set-up. The results therefore support the hypothesis.

6.2.5 The long-period (LP) frequency band: 70 s period signal

The 70 s LP signal was selected to explore the long-period signals at the site as it has some of the highest powers of this period range. The LP frequency band is more powerful in the horizontal directions and power typically increases in parallel with the MS frequency band. Tidal signals also sometimes feature within the LP signals suggesting this energy can be focussed within the shallow waters. Infragravity ocean waves occupy the period range 30 - 300 s and have been observed to occupy a significant amount of energy in the surf zone, and are increasingly energetic in storms (Masselink and Hughes, 2003). The hypothesis to be tested by the regression analyses is that the 70 s LP signal is generated by ocean infragravity waves in shallow water.

The R^2 values of the best fit regression models show that the environmental conditions within the intertidal zone contribute more to this signal than they do seawards of the low tide mark (Figure 6.15). This fits well with findings of numerous studies which have identified infragravity wave energy to feature strongly within surf and swash zones (e.g. Guza and Thornton, 1982; Holman and Sallenger, 1985) which at this site will commonly feature within the wide intertidal zone.

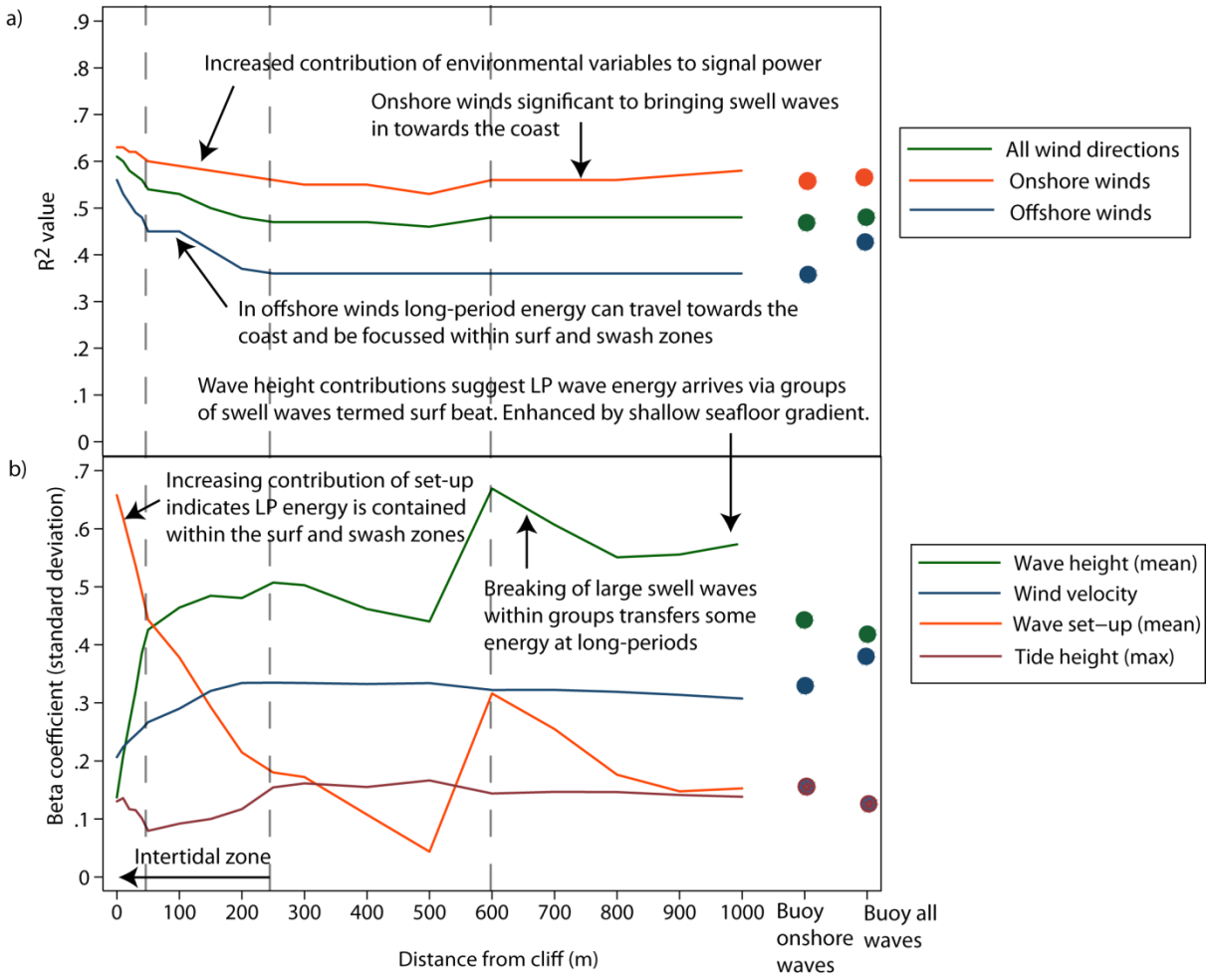

Figure 6.15: The best fit multiple regression model outputs of the 70 s (LP) signal: a) R^2 values (To test the effect of wind direction onshore winds, offshore winds and winds from all directions were tested in the multiple regression models); b) Beta coefficients. Dashed lines represent significant changes in seabed slope which affect the wave height and set-up contributions. Dots represent the conditions at the offshore wave buoy.

Long-period energy is believed to be brought into the coast via the 'surf beat' effect of incoming groupings of swell waves that result in long period increases and decreases in the mean sea level (e.g. Munk, 1949; Tucker, 1950). The long-period energy of groups of swell waves continues to travel through the surf zone after the swell wave groups have broken (Davidson-Arnott, 2010), which may help to explain the propagation of this energy through the intertidal zone where the surf and swash zones will typically occur. A strong tidal signal could sometimes be seen in the spectrograms in Chapter 4, which suggests that tides may effectively trap long-period energy at the coast, a phenomenon also observed by Okihiro and Guza (1995).

The dominant contribution of wave heights to this signal (Figure 6.15b) can be explained as long period energy has been found to increase with incoming wave heights (Guza and Thornton, 1982; Holman and Sallenger, 1985). The power of long-period signals within swash zones is therefore higher during stormy conditions when larger waves arrive at the coast. This can be seen in the spectrograms when signal powers within the longer periods increase during stormy conditions of higher wind velocities and larger waves (e.g. Figure 4.7).

Increases in the contributions from set-up to signal power (Figure 6.15b) also indicate that long-period energy is focussed within the surf and swash zones, as set-up occurs post-breaking. The coast-normal width of surf and swash zones also increases and they become more energetic during stormy conditions as larger waves result in greater set-ups. This increases the still water-level elevation, moving the waterline closer to the cliff. Tide height is therefore important in determining where and when the long period energy is distributed in terms of the location of the waterline and potential width of the swash zone. Higher tides mean it can extend over more of the wide gently sloping foreshore and also determine its proximity to the cliff (Figure 6.16). The results suggest the hypothesis is correct.

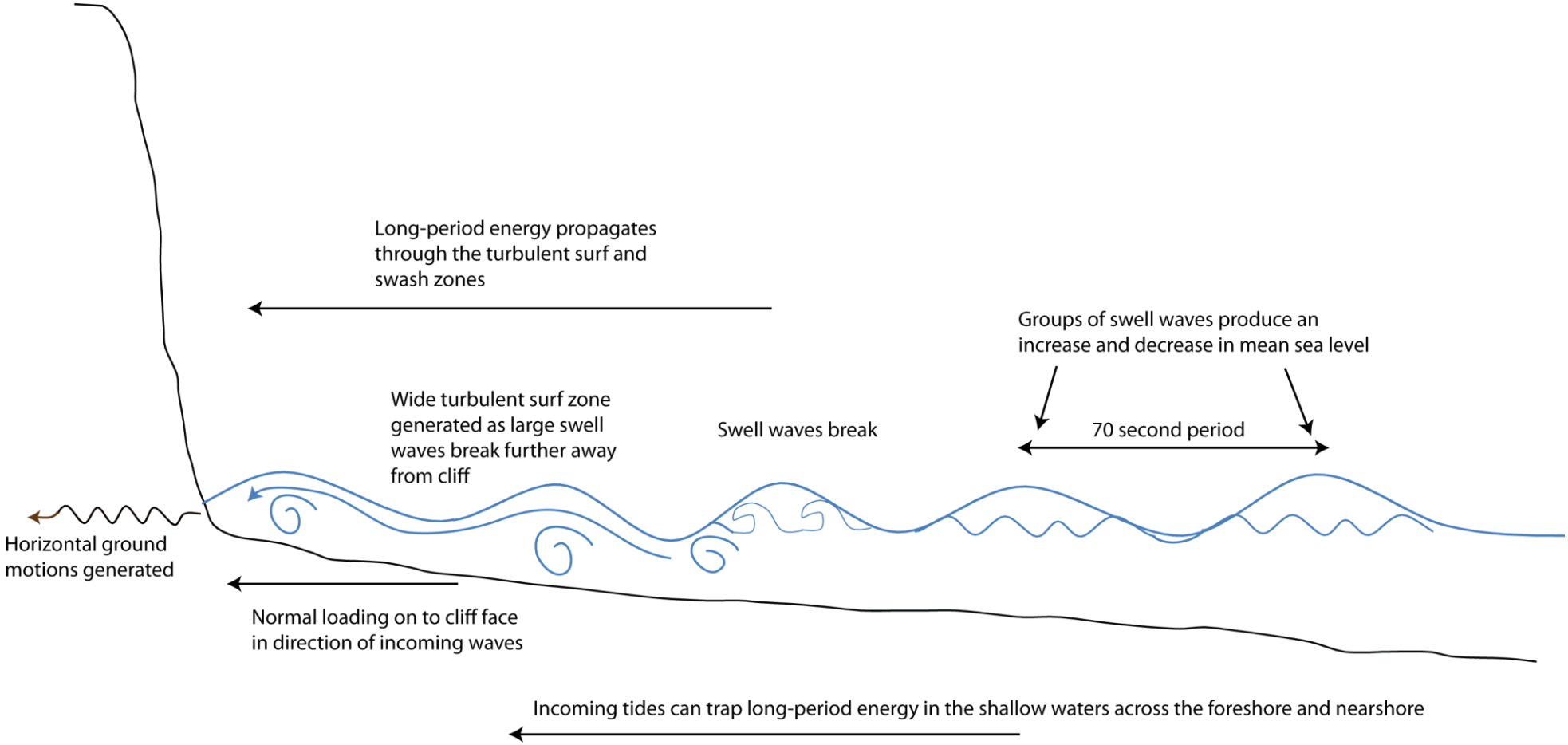

Figure 6.16: Mechanisms of energy transfer to the cliff potentially generating the 70 s LP frequency. Groups of swell waves arriving at the coast cause increases and decreases in mean sea level, producing long-period waves. This LP energy propagates through the shallow surf and swash zones once the swell waves have broken.

6.3 Relative contributions to energy delivery

So far the seismic signals have been explored via their relative power, which provides a measure of the relative rate at which energy is transferred to the cliff from the environmental forces that generate these signals. The relative contributions of the different seismic signals, and therefore the environmental forces / conditions they represent, to the energy recorded by the cliff top seismometer have also been examined (Figure 6.17). The values presented are the statistics of the hourly average energy over the monitoring period in micro-joules, calculated from the hourly power spectral density estimates.

The relative energy of the seven different signals provides interesting, and somewhat surprising, results. The two components Z and E have again been examined because the signals are dominant in different directions

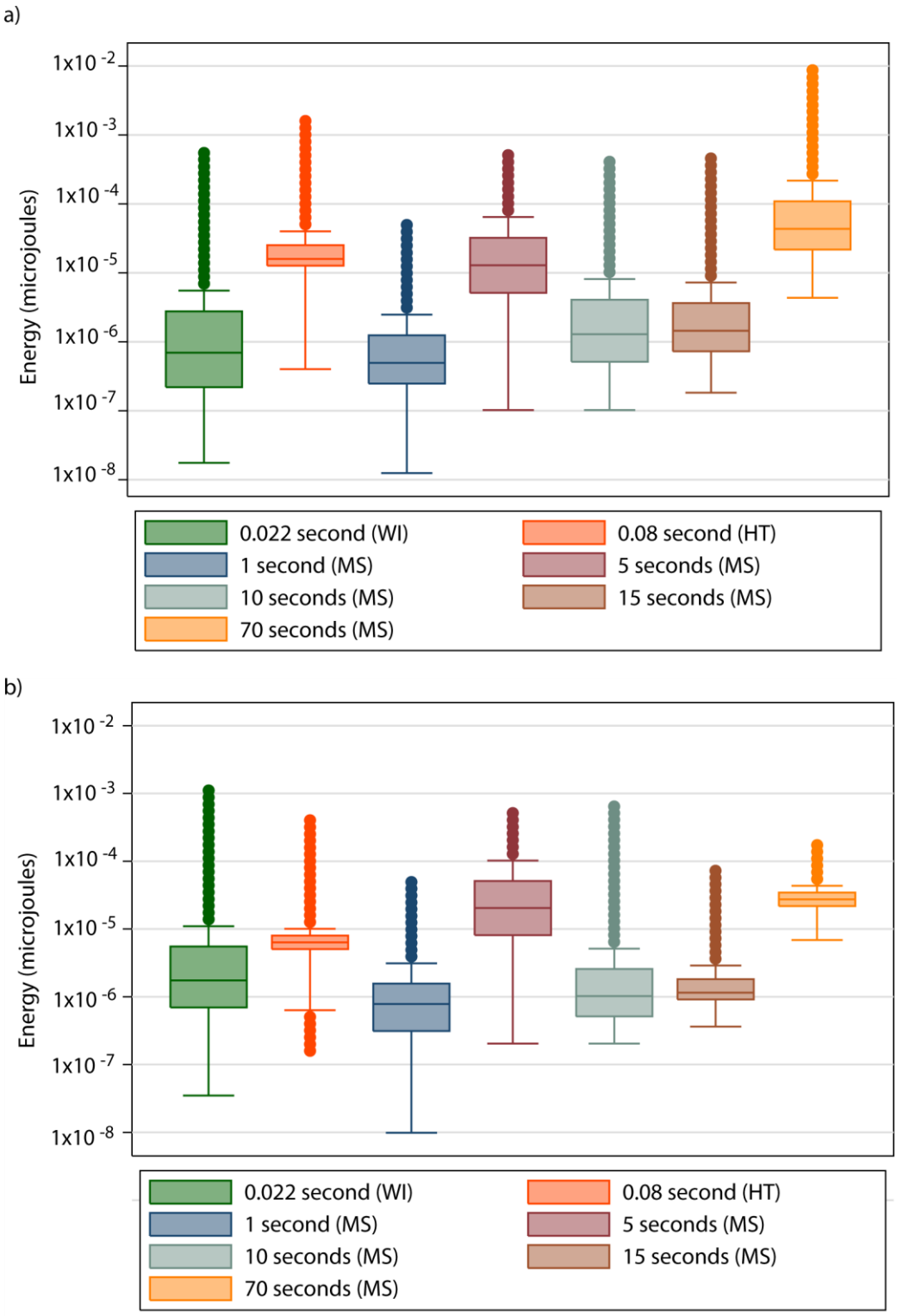

Figure 6.17: Relative energy transferred to the cliff from the different frequencies as recorded by the cliff top seismometer for the: a) East-west horizontal component; b) Z vertical component. Statistics denoted by the box plots are: Box = inter-quartile range (IQR); central horizontal line = median; tails and horizontal lines = upper and lower adjacent values (defined as 1.5 * IQR); dots = outside extreme values.

These results are surprising as they show that the HT and WI frequencies, which have the highest power in the spectrograms, do not in sum actually transfer the greatest amounts of energy to the cliff. The findings regarding the HT signal are the most significant as wave impacts against cliffs are commonly acknowledged to be the greatest source of energy delivery to coastal cliffs and to be the most important environmental driver of cliff change (e.g. Sunamura, 1992; Trenhaile, 2000). Clearly, if we assume microseismic energy to relate to erosive potential or efficacy, this is problematic. These results however show that greater energy is transferred to the cliff by infragravity wave energy within shallow waters at the coast, and also, in the vertical direction, by some microseisms near the coast (Figure 6.17). Fundamentally, this raises the question as to whether energy delivered by the LP and MS frequency bands, is an effective erosive agent.

The MS and LP signals are both generated by swell waves, which are able to transfer energy over a large area. The results in Section 6.2 show that the wave processes represented by the 15 s MS and the LP signal can also deliver energy across the nearshore and, during high tides, directly to the cliff. During storms the mechanisms generating these signals can bring in large amounts of energy and storm surges focus this at the coast.

The 5 s MS signal transfers more energy than the 10 and 15 s MS signals, which may be explained by the instrument noise-floor being reached at these longer periods, and so some of the lower amplitudes of these periods are being lost. Conversely, the higher energy of the 5 s MS signal may indicate that this signal largely represents DF microseisms, which have higher amplitudes than primary microseisms.

Identification of the high levels of energy transferred to the cliff from waves moving and breaking away from the cliff face is hugely important, as this demonstrates that the largest source of microseismic energy transferred to the cliff is not recognised by most rocky coast geomorphology studies. This means that these environmental forces are not considered within studies and therefore are not monitored or modelled to test their effects on foreshore and / or cliff erosion.

The high relative energy transfer from the 5 s MS signals suggests that wave mechanisms that generate these signals occur closer to the cliff than the regression models indicate. This indicates that the environmental datasets used in the regression may poorly represent these wave conditions. The assessment of energy delivery shows that the microseisms do deliver energy to the cliff and suggest microseisms are generated in the nearshore more frequently than was indicated by the regression models. This may help to explain why regional-scale

environmental datasets traditionally do not correlate that well with cliff change data, because they poorly represent conditions near to the cliff.

The HT signal typically has a high rate of energy transfer to the cliff (power). However, the LP and MS 5 s signals are believed to transfer greater amounts of energy because of the spatial extent and temporal duration during which they deliver energy. The HT signal interacts with a small area of the lower cliff face, which varies with the tide, compared to 1,000s of m^2 that the MS and LP signals act across. The LP signal power was identified in Section 6.2 above to be particularly important over the intertidal zone, which is considerably larger than the area of cliff face inundated by high tides. The 5 s MS signal generated by the DF microseism mechanism can potentially operate over the largest area as it can be generated in deeper offshore waters. In addition the HT signal is limited temporally and only transfers energy during high tides when sufficient ratios of wave height to tide depths occur. As identified earlier, the sea only lies at the cliff face 30% of the time (accounting for waves and set-up heights). The MS and LP conditions however occur more frequently. The MS signals are not limited by tides and therefore can transfer energy any time suitable wave conditions are available to generate them. The LP signals can also be generated at any time appropriate conditions occur, however the highest power of this signal occurs during tidal signals, indicating greater energy transfer or efficiency of energy transfer, occurs over the foreshore during high tides.

The constant transfer of energy from the sea across a large area, represented by the MS and LP signals, results in dynamic loading of the cliff, demonstrated by the ground motions monitored. This cyclic loading of the nearshore, and beyond, has potential for deteriorating rock strength via micro-fracturing, potentially preparing the rock for failure. This may partially help to explain poor correlations found by other studies between regional-scale environmental conditions and rockfalls if some of the important variables were not being tested (e.g. Rosser et al., 2007; Lim et al., 2010a). Whether these wave mechanisms have an effect on cliff erosion at the site will be tested in the next chapter, but clearly this effect may be more apparent in locations which lend themselves to the generation of MS seismic frequencies.

There is low energy transfer from wind (WI signal) (Figure 6.17). Although the wind delivers energy over a greater area of the cliff face and top than the waves at the bottom, waves during high tides, represented by the HT signal, deliver more energy than the wind. Compared to the seismic source areas of the MS and LP signals, the area affected by the WI signal is low. The spectrograms also show wind to transfer energy in short, intermittent bursts whereas once swell waves have been generated they will continue to travel and transfer energy until they are completely dissipated at the coast. These results demonstrate that significantly greater energy

is delivered to the cliff from marine sources than from wind sources, and that marine sources are likely to be the dominant forcing mechanisms acting on coastal cliffs.

Despite the 1 s MS signal being best explained by the regression models, this frequency actually transfers the least energy to the cliff. This suggests that the signal largely represents short period, locally generated DF microseisms across the nearshore, as the waves are generally small and therefore transfer low levels of energy to the cliff.

The differences between the relative energy transferred by the different processes in the Z and E directions (Figure 6.17) suggests that the resulting ground motions would be highly diverse, producing complex stress paths, with potential to iteratively degrade the rock strength.

6.4 Summary

The results of the regression analyses have indicated that the four ground motion frequency bands each represent a range of processes, generated by specific combinations of environmental variables. The results have demonstrated that energy is transferred to the cliff from marine and atmospheric processes not just directly at the cliff but from sources distributed across the foreshore, nearshore and further offshore (Figure 6.18). The energy transferred to the cliff from each of these processes and mechanisms may have the potential to contribute to erosion of the cliff either through direct loading or from iterative generation of stress. These findings are highly important for the exploration of coastal cliff erosion as they demonstrate the potential limitations of models that focus on wave energy delivery to the cliff toe alone; the system is clearly more complex. In order to improve understanding of the environmental controls of cliff behaviour, studies must look at the whole range of environmental forces acting on cliffs from a wide variety of processes and consider their interactions with the cliff material. This will be addressed in the next chapter.

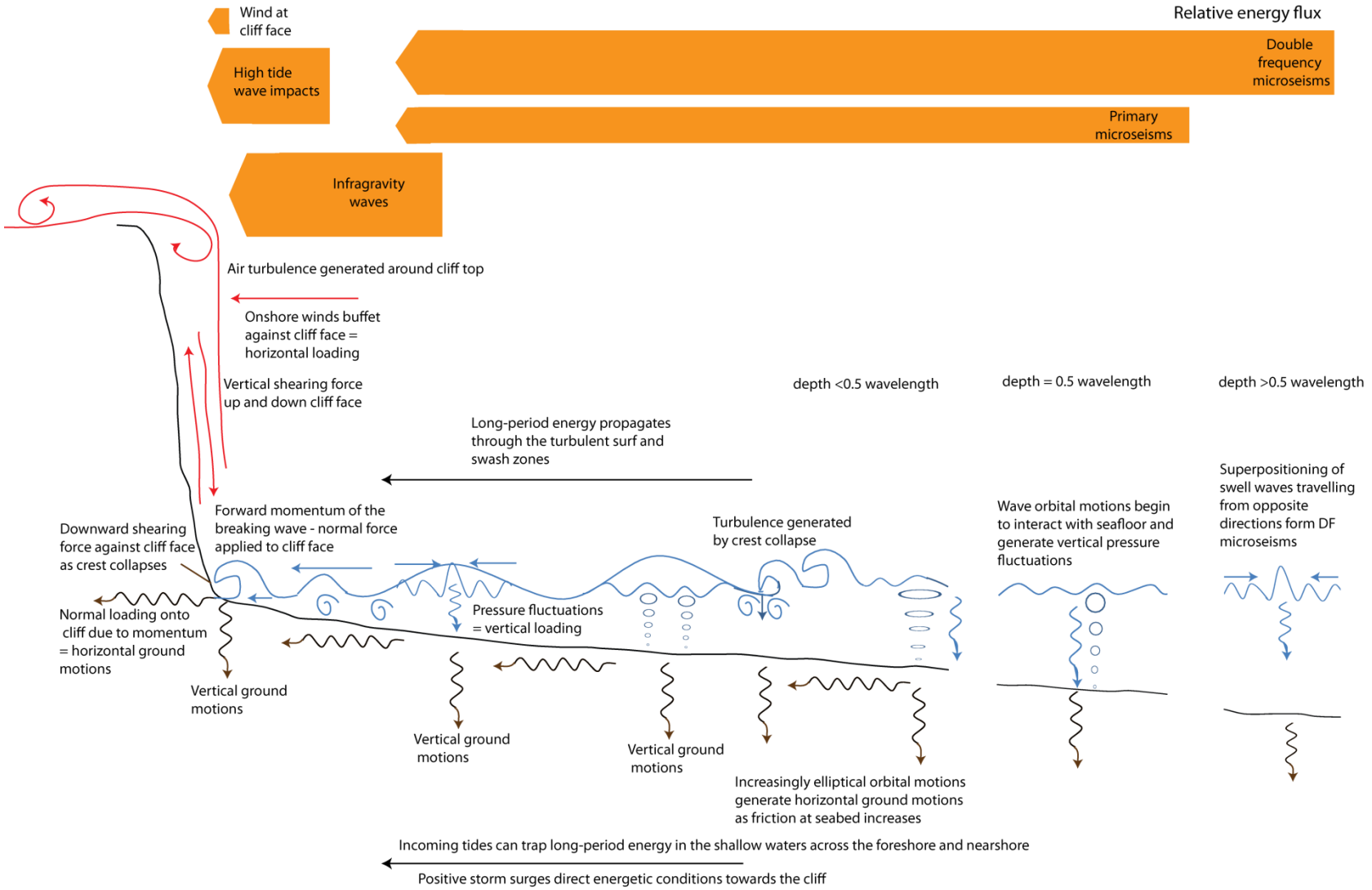

Figure 6.18: Summary of the processes and mechanisms that transfer energy to the cliff, represented by the four microseismic frequency bands. The width of the orange arrows indicate the relative amounts of energy (μ J) transferred by the different processes to the cliff.

The variety of processes and mechanisms found to transfer energy to the cliff, the combinations of environmental variables that drive them and the wide area over which these processes operate, highlights the diversity and complexity of controls of cliff erosion. To explore interactions between these processes and the cliff and the environmental controls of observed cliff erosion, relationships between the rockfall data and ground motion frequencies and regional-scale datasets will be tested in Chapter 7.

By exploring the power and energy of the different frequencies of ground motion, different ways in which the processes can potentially affect the cliff have been identified. Signal power has been shown to represent well how such processes transfer energy to the cliff, indicating characteristics of the mechanisms that transfer energy and generate the different microseismic ground motions. The energy provides an indication of the relative energy available to drive the different processes, which will now be considered in Chapter 7.

Chapter 7: Observed coastal cliff erosion and environmental controls

The aims of this chapter are to characterise change on the cliff during the two-year monitoring period and to identify the environmental controls (both preparatory and triggers) of the observed erosion using the environmental and microseismic datasets collated.

The previous chapter demonstrates that microseismic ground motions represent the energy transferred by marine and atmospheric conditions to the cliff. By using microseismic data as a proxy for the environmental conditions this data may provide a means of better understanding the marine and atmospheric controls of coastal cliff change. Thus, the energy delivery to the cliffs may relate to the levels of erosion experienced at the coast.

7.1 Observed rockfall characteristics

The cliff was scanned using a terrestrial laser scanner (TLS) approximately every month during the two-year monitoring period from July 2008 – June 2010. This produced 21 epochs of cliff change data. The total area of the monitored section of cliff was 4,840 m^2. This section has been split into two zones that are exposed to different sets of environmental conditions, to explore the controls on rockfall activity and their characteristics (Figure 7.1). The 'inundation zone' (369.6 m^2) is the lower 5 m of the cliff (which extends from 1.6 mOD to 6.6 mOD), and is exposed to marine conditions during high tides, and non-marine conditions during low tides. The 'non-inundated zone' (4,470.4 m^2), which is the remainder of the cliff above the inundation zone, is not exposed to marine conditions, but instead experiences subaerial processes, including fluctuating wind speeds and directions; temperatures and moisture levels, determined by the local weather. The height of the inundation zone was estimated by adding the maximum tide, modelled wave and set-up heights at the cliff and by adding the max wave height to account for wave run-up and splash. These heights were used because no equations were available to calculate wave run-up and splash heights on vertical faces.

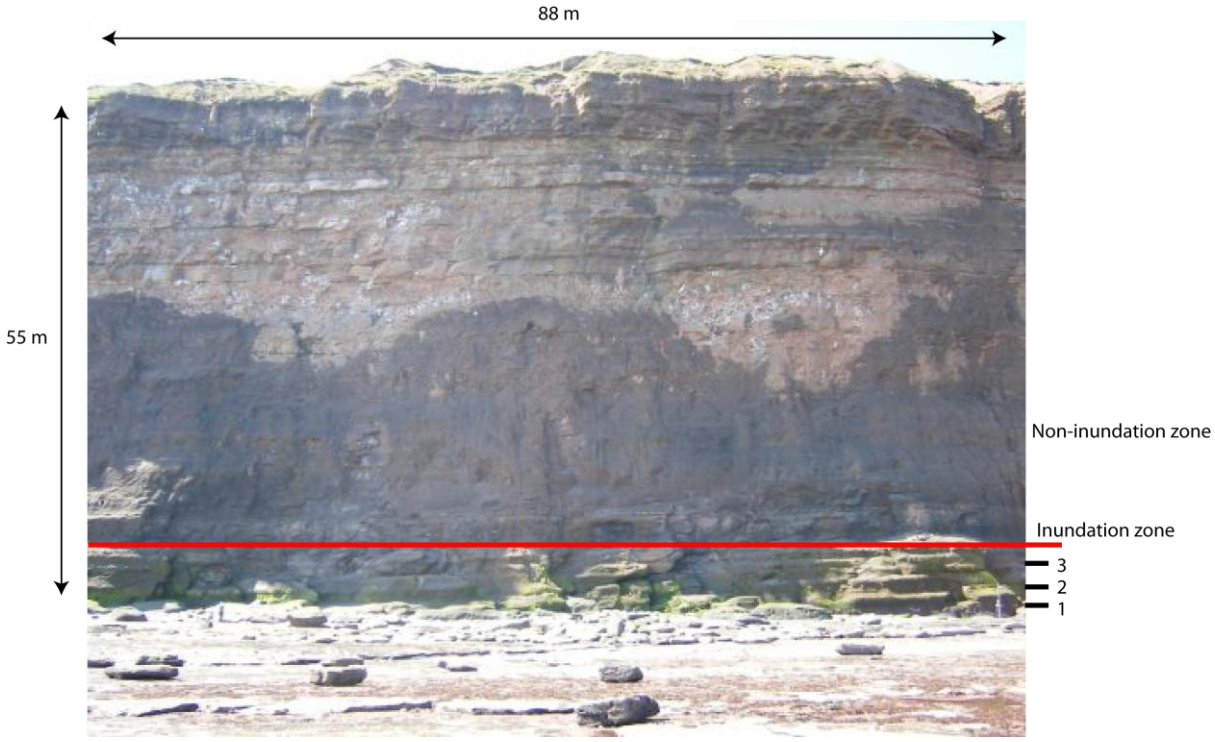

Figure 7.1: The monitored cliff section. The red line marks the upper limit of the inundation zone. 1 = cliff toe (1.6 mOD), 2 = max tide height (1.67 m above cliff toe), 3 = combined max tide, wave and set-up height (2.9 m above cliff toe). The cause of the water mark on the face is uncertain, but it does not represent inundation by the sea. This lower section of the cliff protrudes beyond the upper section and so the water mark may reflect where water has washed over the cliff top, or groundwater seepage.

7.1.1 Distribution of erosion across the cliff face

During the two-year monitoring period there were 31,987 rockfalls (above the threshold volume of 0.00156 m^3) identified from the whole cliff face, resulting in a total volume change of 235.62 m^3 (Table 7.1). This is equivalent to a retreat rate of 0.024 m yr^{-1}, which is half the rate estimated from comparisons of cliff toe and top locations with historical maps (c. 0.05 m yr^{-1}; Agar, 1960). The inundation and non-inundation zones have very different rates of retreat (0.12 m yr^{-1} and 0.02 m yr^{-1} respectively - Table 7.1), with the inundation zone having the highest rate despite having a lower total rockfall volume than the non-inundation zone, indicating more activity per m^2 than the non-inundation zone above. The inundation zone's mean rockfall volume is also larger than that of the non-inundation zone, as is its standard deviation, indicating larger and more variably sized rockfalls are sourced from within this zone (Table 7.1). The variability of retreat rates up the cliff profile, as identified by the high resolution TLS

monitoring, highlights the complexity that lies within mean cliff retreat rates obtained from historical maps, often used in management decision making, such as the Shoreline Management Plans for England and Wales.

Lim et al. (2010a) measured a retreat rate of 0.009 m yr^{-1} from monitoring at the same site using the same technique over the period September 2003 – April 2005. The differences between the two datasets, and the scatter of the data seen in Section 7.1.2, indicate high variability in rockfall activity over time, and that much longer monitoring periods are required to fully characterise cliff behaviour.

Table 7.1: Rockfall statistics for the different sections of the cliff over the two-year monitoring period of July 2008 – June 2010.

Section of cliff	**Number of rockfalls**	**Total volume (m^3)**	**Mean volume (m^3)**	**Standard deviation (m^3)**	**Maximum volume (m^3)**	**Minimum volume (m^3)**	**Annual retreat rate (m yr^{-1})**
Whole cliff face	31,987	235.621	0.0180	0.163	12.732	0.00156	0.0243
Inundation zone	5,736	79.535	0.0409	0.249	8.139	0.00156	0.1076
Non-inundation zone	26,621	159.131	0.0128	0.130	12.732	0.00156	0.0178

The images of change over the monitoring periods enable examination of the spatial and temporal distribution of rockfall characteristics, and it is clear that change occurs across the whole cliff face throughout the monitoring period (Figure 7.2).

a)

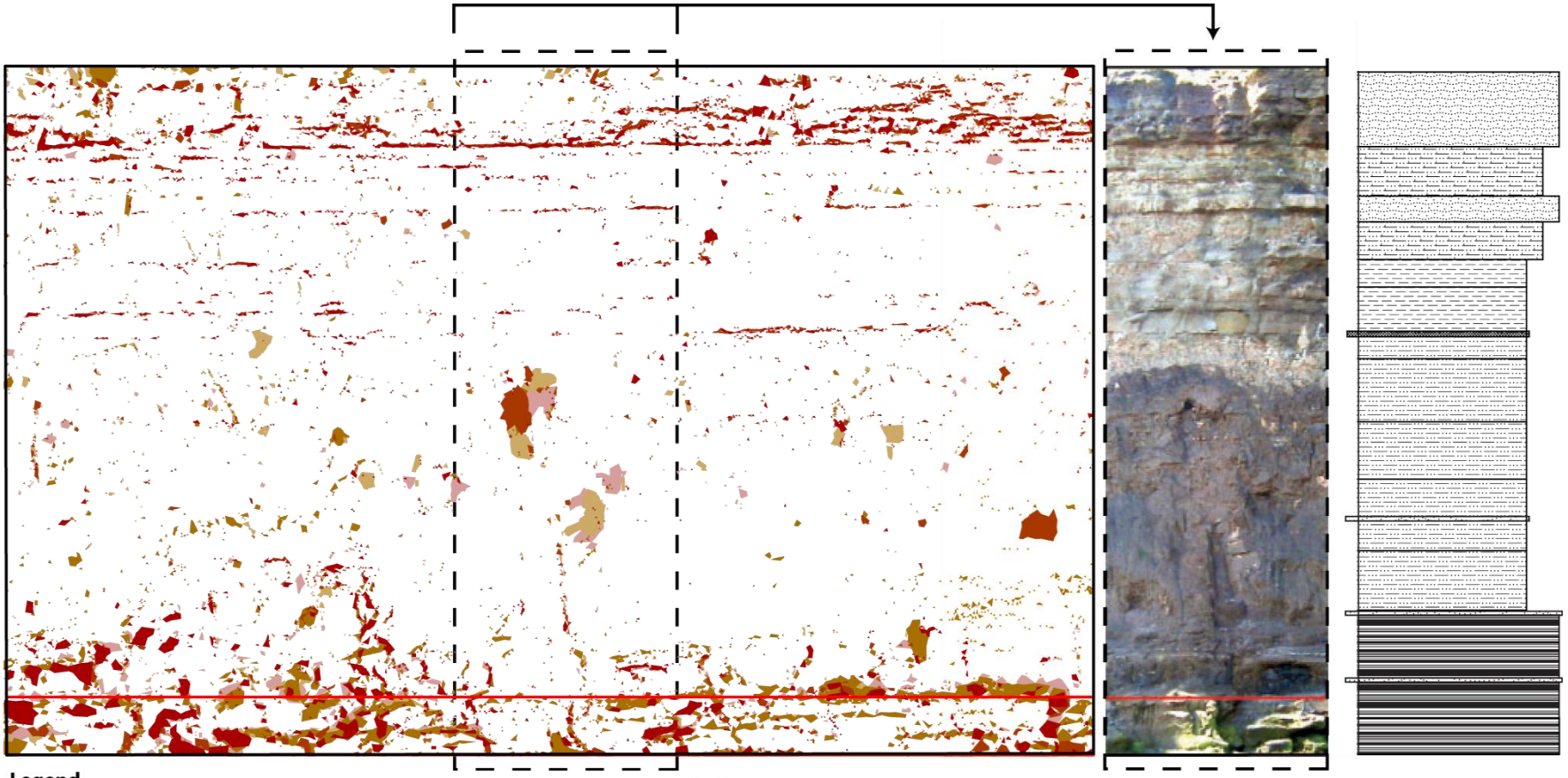
Legend
12 Dec - 14 Jan 2009
13 Nov - 11 Dec 2008
16 Oct - 12 Nov 2008
02 Sep - 15 Oct 2008
21 Jul - 01 Sep 2008
Wave impact zone
Hard, ferruginous sandstone
Siltstone
Silty shale
Thin red ironstone
Grey bituminous shale
Dark grey mudstone
Scale 1 cm : 4.2 m
10 m

b)

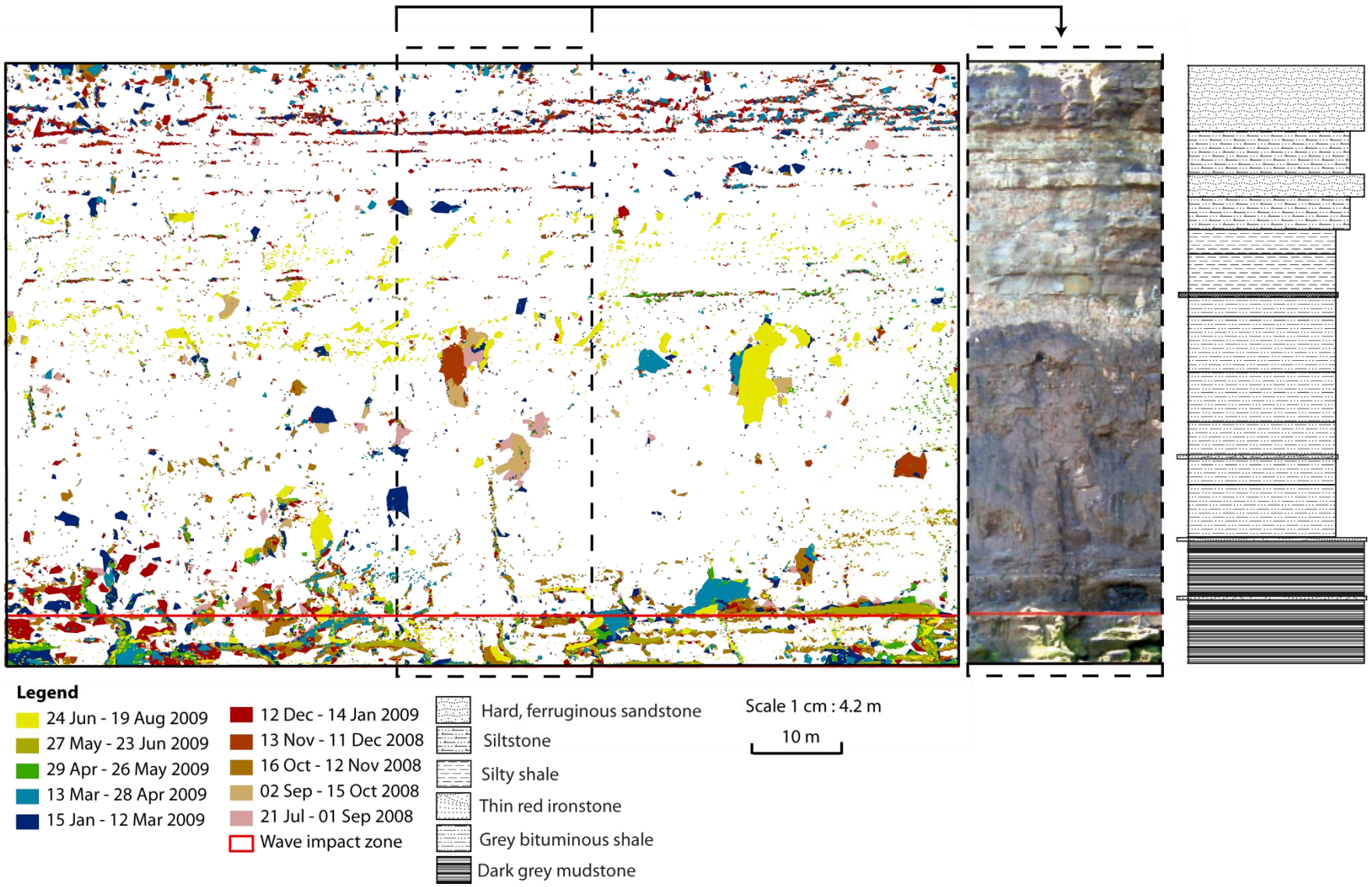
Legend
24 Jun - 19 Aug 2009
27 May - 23 Jun 2009
29 Apr - 26 May 2009
13 Mar - 28 Apr 2009
15 Jan - 12 Mar 2009
12 Dec - 14 Jan 2009
13 Nov - 11 Dec 2008
16 Oct - 12 Nov 2008
02 Sep - 15 Oct 2008
21 Jul - 01 Sep 2008
Wave impact zone
Hard, ferruginous sandstone
Siltstone
Silty shale
Thin red ironstone
Grey bituminous shale
Dark grey mudstone
Scale 1 cm : 4.2 m
10 m

c)

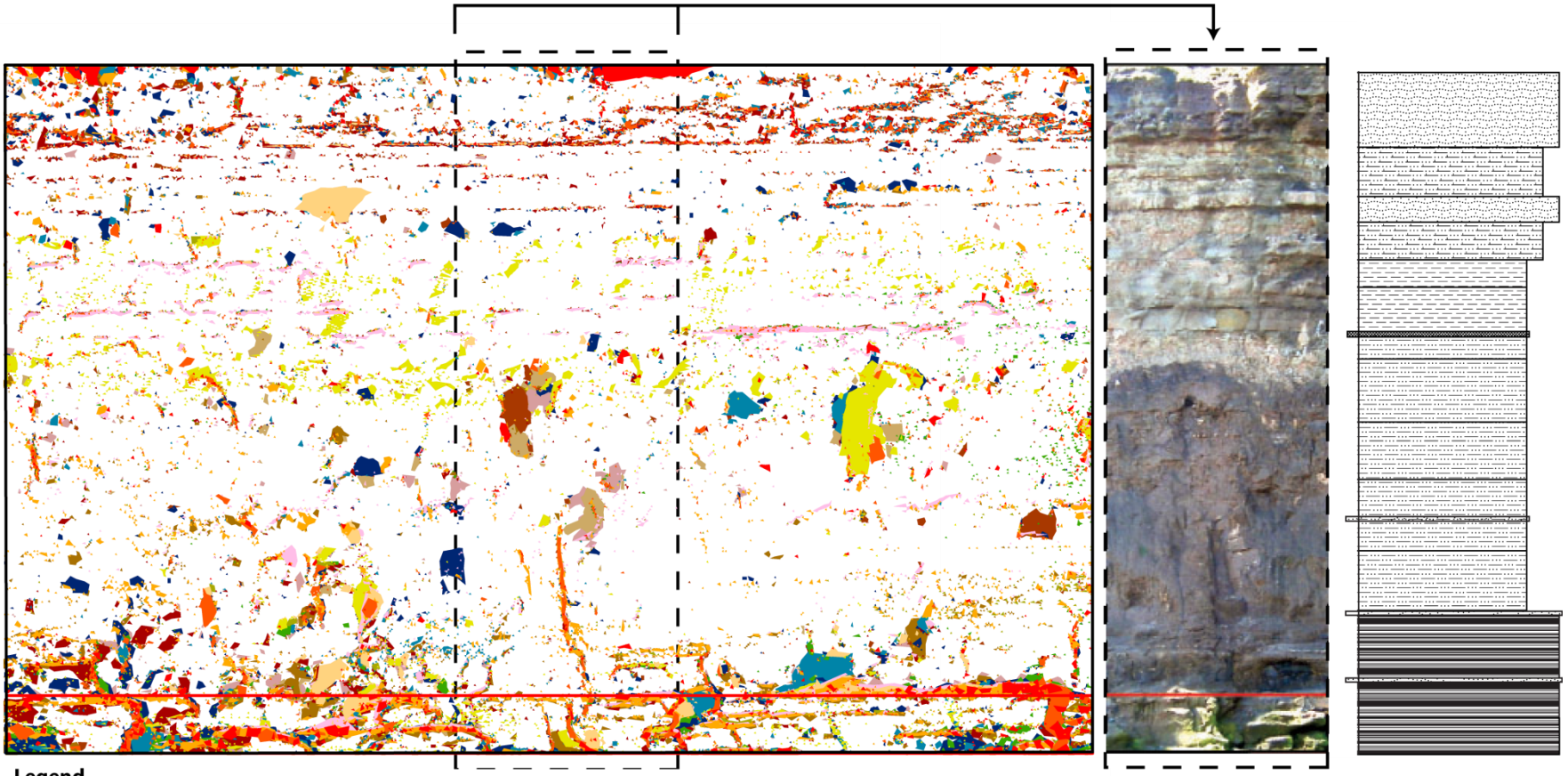
Legend
03 Dec - 03 Jan 2010
17 Nov - 02 Dec 2009
20 Oct - 16 Nov 2009
17 Sep - 19 Oct 2009
20 Aug - 16 Sep 2009
24 Jun - 19 Aug 2009
27 May - 23 Jun 2009
29 Apr - 26 May 2009
13 Mar - 28 Apr 2009
15 Jan - 12 Mar 2009
12 Dec - 14 Jan 2009
13 Nov - 11 Dec 2008
16 Oct - 12 Nov 2008
02 Sep - 15 Oct 2008
21 Jul - 01 Sep 2008
Wave impact zone
Hard, ferruginous sandstone
Siltstone
Silty shale
Thin red ironstone
Grey bituminous shale
Dark grey mudstone
Scale 1 cm : 4.2 m
10 m

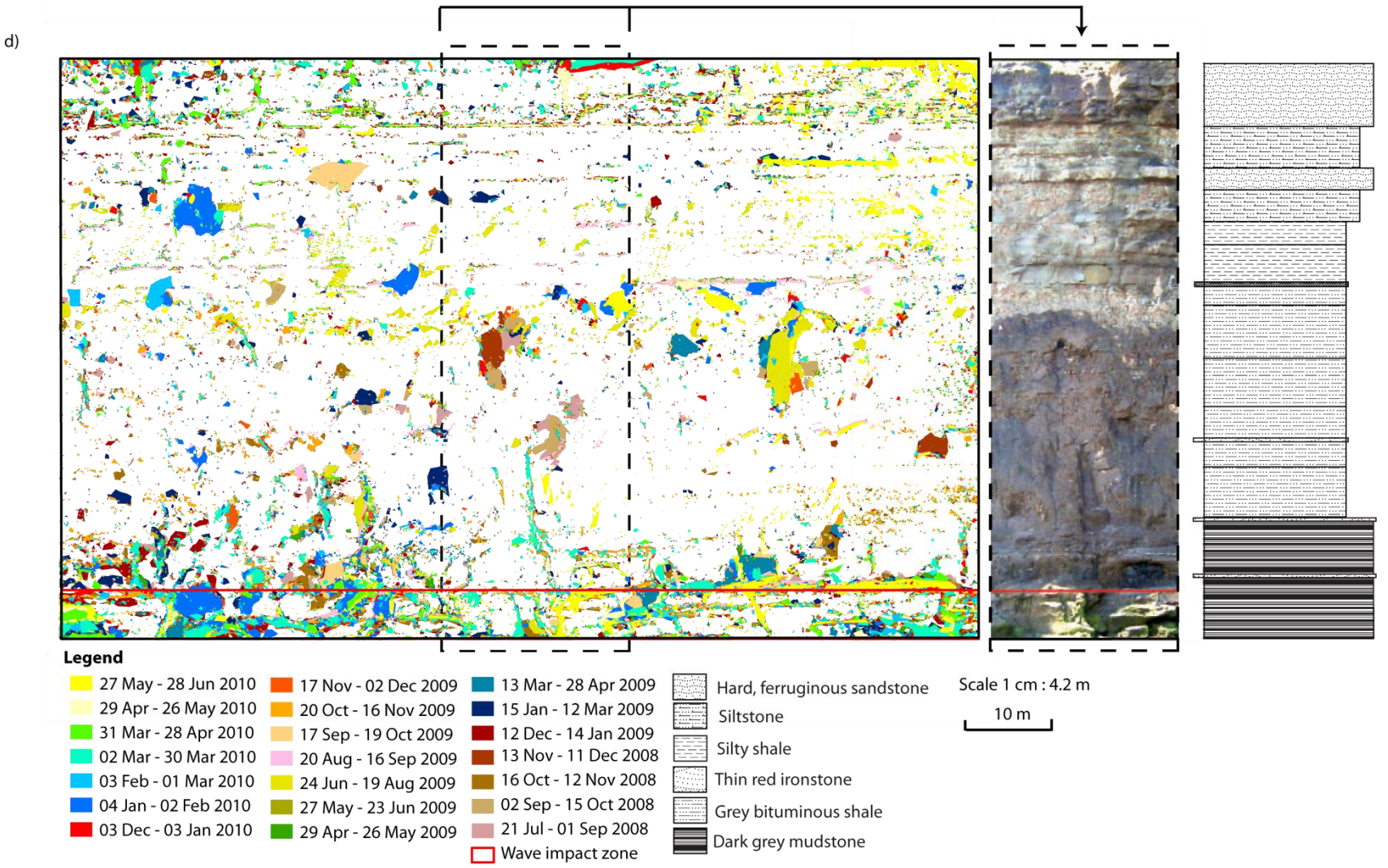

Figure 7.2: Erosion across the cliff face through the two-year monitoring period: a) July 2008 – January 2009; b) July 2008 – August 2009; c) July 2009 – January 2010; d) Erosion over the whole monitoring period July 2008 – July 2010. The area of each rockfall is shown, colour coded by the period of detachment. The red line delimits the inundation and non-inundation zones. N.B. For each monitoring period it is assumed that each area of change represents one individual rockfall as super-imposed failures during a monitoring period can not be identified.

There is a strong geological control on the rockfall characteristics, also observed by other studies at the same location (e.g. Rosser et al., 2007 and Lim et al., 2010a). Rockfalls occur along bedding planes and joints, particularly in the siltstones and sandstones, removing convex protrusions, notably in the mudstone and shale. The rockfall characteristics vary by rock type. Small rockfall volumes occur along joints and bedding planes in the top layers of sandstone and siltstone suggesting that, despite the large, angular, blocky structure of these layers, the occurrence and geometry of failures sourced from them are heavily controlled by joints and that these layers are relatively stable. High amounts of change occur in the mudstone which makes up the lower 20 m of the cliff (Figure 3.17). The lowest 5 m of the mudstone is directly inundated by the sea, and makes up the inundation zone. A greater number of rockfall volumes > 0.1 m^3 also occurs within the mudstone above the inundation zone. There are fewer joints in the mudstone, and those that occur are more widely spaced than those in the sandstone and siltstone above, which means that individual rockfall geometries are less controlled by jointing and that larger rockfalls can occur. In the field the surface of the mudstone is smooth, indicating abrasive action by sediment laden seawater. Thin platelets of the mudstone also flake off, however both this and the erosion due to abrasion aren't evident in the TLS change data because their dimensions are below instrument precision. The shale is friable, producing a steady stream of small rock fragments, but again these are too small to be detected by the TLS. The shale produces a wide range of rockfall volumes; in fact the largest failure occurred in the shale layers between June and August 2009 (Figure 7.2b).

Examining the time series of change (Figure 7.2) it is apparent that where the greatest change occurs on the cliff there is commonly a clustering of rockfalls that occur around the same location over a number of months. Note for example the failures that gradually occur in the very centre of the scan area (Figure 7.2). Change sometimes occurs repeatedly within a previous failure scar in successive months, and smaller changes often occur around the edges of earlier larger failures. This phenomenon appears more commonly in the shale and mudstone layers. However, the largest sandstone failure (which occurred in September - October 2009) was not preceded by any change, and only three or four months later did any other change occur around this failure. This supports the previous observation regarding the geological controls on rockfall characteristics and the variations that occur between the rock types. This pattern of behaviour in the shale and mudstone may indicate stress release that over time propagates through the local material, generating 'hot spots' of failure. This was also observed by Hapke and Richmond (2002) and Young et al. (2011a). These observations may also represent the loosening of material around one failure, which is then gradually removed by various environmental triggers or progressive fracturing. The exact temporal pattern of this behaviour,

which might provide clues regarding the causal mechanisms, is however obscured by the monitoring resolution used. Rosser et al. (2007) identified similar patterns of failure behaviour in a previous dataset from the same coastal area, in the form of precursory behaviour before a larger failure. In this dataset increases in failure occurrence in an area are apparent, which results in a large amount of change focussed within that area, rather than occurring as one large failure. However, the largest failures that affect this cliff may not have occurred during the relatively short monitoring period of this study. This is discussed further in Section 7.1.4 below.

Although there is significant change in the lower section of the cliff, there is no notch at the toe, commonly cited to be a key feature of cliff erosion (Sunamura, 1992). The cliff toe actually protrudes in most of this section of cliff, with some sections in line with the rest of the cliff above (Figure 7.3). Although there are some concave features within the mudstone, the surface of which is smooth, there are a number of similar features lying at distinct heights within the mudstone, but even here they do not form a single distinctive notch. As erosion of the toe is evident from the rockfall data for the inundation zone, the absence of a notch may reflect geological controls on the cliff response to toe erosion. It is possible that if the rock structure is unable to withstand undercutting then a notch will not develop as any erosion of the toe will relatively quickly de-buttress and propagate up the cliff profile. Given the relative weakness of the shales above the mudstone, this may well explain the absence of notching and cantilever collapse at the site.

Change occurs throughout the cliff profile, with large failures occurring in the layers well above the reach of the sea, in contrast to the traditional notch and cantilever collapse model of cliff evolution. The change in geology up the cliff profile makes isolating the geological and environmental controls on rockfall characteristics complex. In Section 7.2 below the environmental controls are tested by regressing rockfall characteristics with environmental and microseismic ground motion conditions.

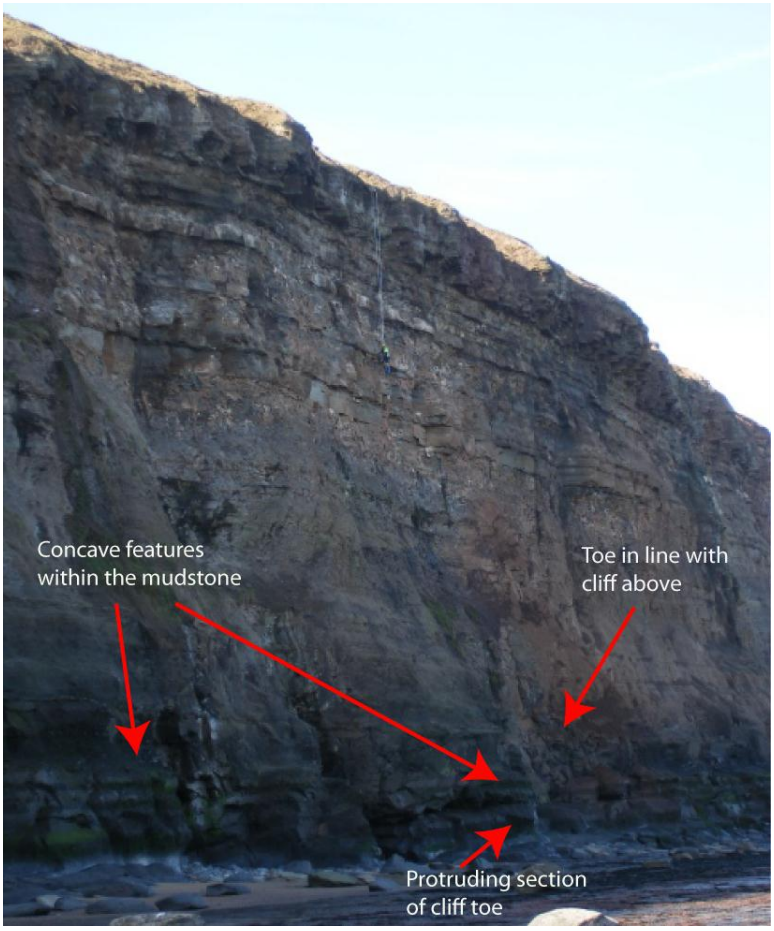

Figure 7.3: Morphological features within the mudstone toe.

7.1.2 Rockfall characteristics over time

The largest total volumes of rockfall occurred in the winter months (Figure 7.4a) when both subaerial and marine conditions were more energetic. The overall trend shows seasonality but the data is noisy, with erosion rates varying significantly between survey epochs. Despite covering a much smaller area (369.6 m^2 compared to the non-inundation zone 4,470.4 m^2) the total volume of change in the inundation zone is often similar to that of the non-inundation zone above, and sometimes greater (e.g. November 2008).

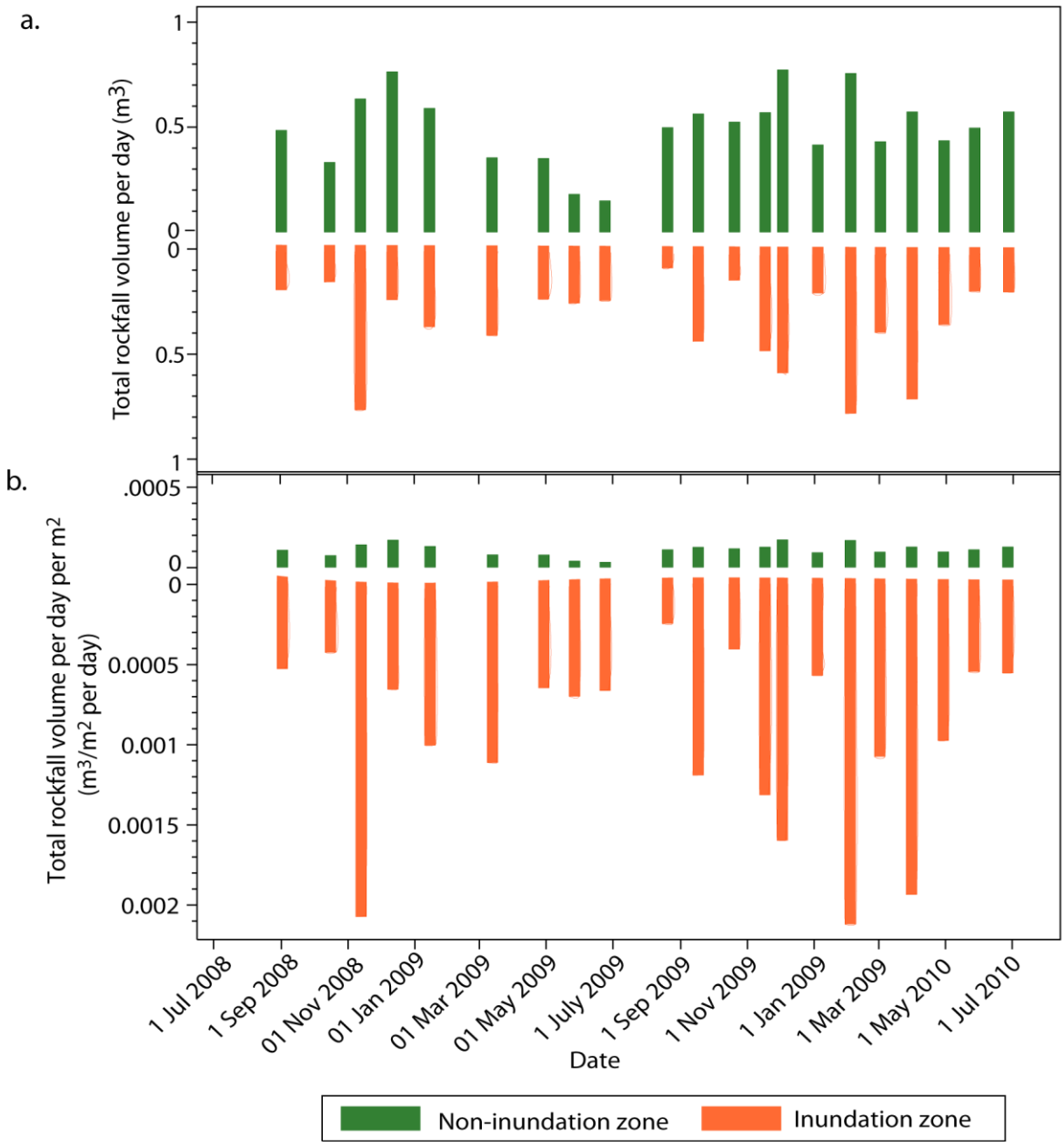

Figure 7.4: Total rockfall volumes for each monitoring epoch for the inundation and non-inundation zones: a) Daily rockfall volumes; b) Daily erosion rates (volume per m^2 per day).

The total volume of cliff face change activity per day per m^2 is on average 0.000856 m^3 (approximately nine times) higher in the inundation zone than in the non-inundation zone above it (Figure 7.4b). As discussed in Section 7.1.1 the variation in geology between the two zones has some control over the differences observed. The role of the different environmental conditions in the two zones in determining rockfall is tested in Section 7.2.

The highest mean, maximum and standard deviation of the rockfalls typically occurred in the winter months, although the data is noisy (Figure 7.5). A notable exception is the largest failure which actually occurred in the non-inundation zone between June and August 2009, resulting in

a higher standard deviation during that period (Figure 7.5). The ground motion data during the summer of 2009 (Figure 4.6) show storms occurred during July, which may have triggered this large failure.

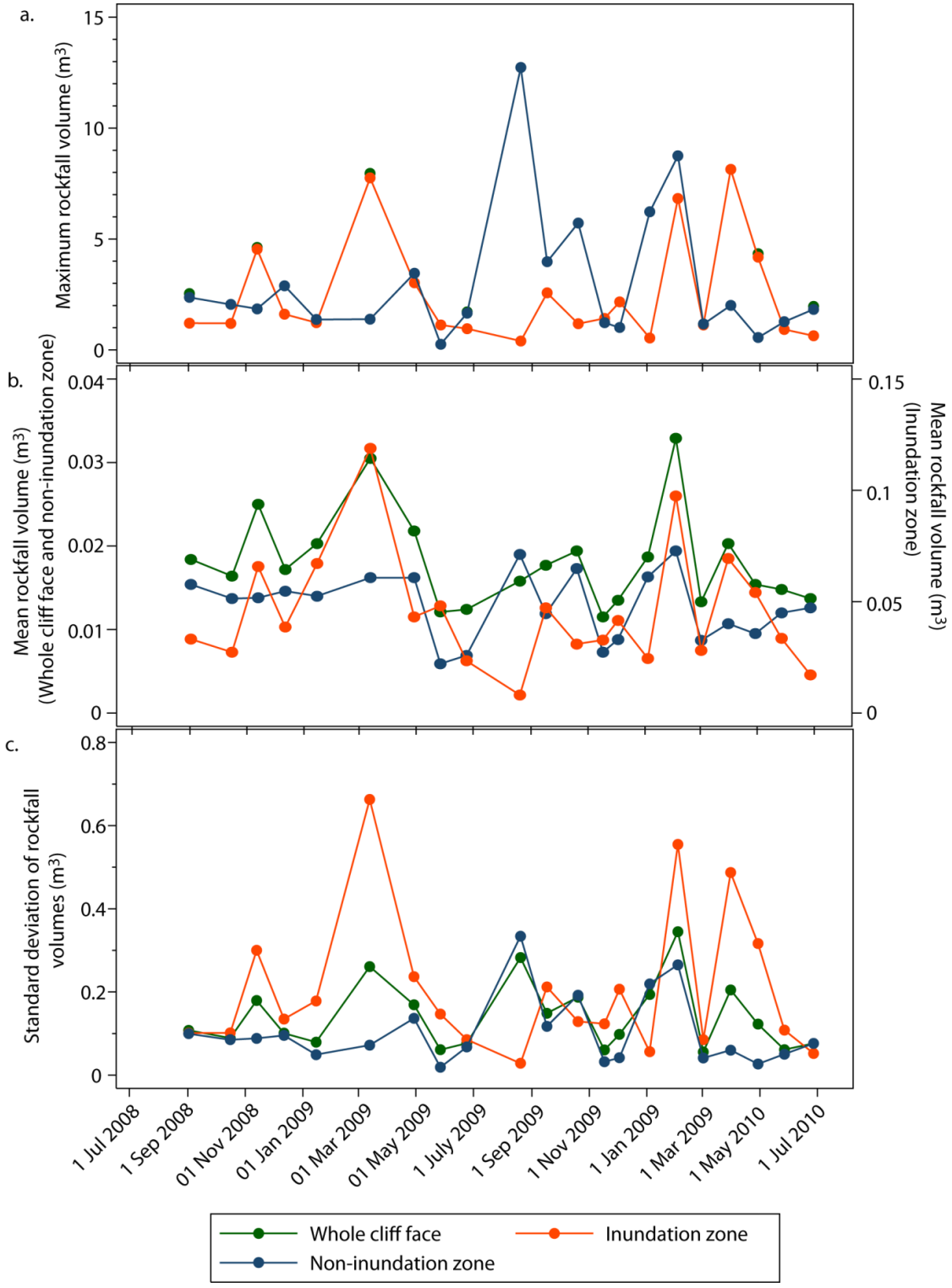

Figure 7.5: Rockfall statistics per monitoring period. a) Maximum rockfall volume; b) mean rockfall volume; c) standard deviation of rockfall volume.

Mean rockfall volumes are larger in the inundation zone than the non-inundation zone throughout the monitoring period. It is evident that not only greater volumes of change occur in the inundation zone per m^2 but also that rockfall sizes are typically larger. The peaks in mean rockfall volume typically coincide with the peaks in maximum and standard deviation of rockfall volume. This suggests that peaks in mean rockfall volumes are due to the occurrence of individual large failures captured in each monitoring epoch.

The temporal patterns in rockfall characteristics (Figure 7.5) suggest that environmental conditions do prepare or loosen cliff material, which sometimes results in rockfall failures, with increased volumes and larger rockfalls occurring during more stormy months, when tide residuals (storm surges), wave heights and therefore wave set-up heights are higher. The ground motion data in Chapter 4 demonstrates that during these conditions energy is transferred to the cliff at a higher rate (Figure 4.7), resulting in greater potential for erosion via hydraulic processes, abrasive and wetting processes. Whether this results in an identifiable increase in erosion rates, and if this can be related to specific rockfall characteristics will be tested in Section 7.2 below.

7.1.3 Rockfall magnitude-frequency distribution of the whole cliff

To explore the rockfall size characteristics sourced from across the whole cliff in detail, and to identify how the frequency of cliff change relates to the magnitude of change, the relationship between rockfall magnitudes and frequencies of the dataset have been examined (Figure 7.6). First the logarithms of rockfall volumes from the entire monitoring period were calculated (31,987 observed rockfalls), and a kernel density estimate (using a kernel half width of 0.0004 m^3) was used to calculate frequency density at log-spaced rockfall volume intervals. This method is described fully in Barlow et al. (2012). The resulting relationship between rockfall frequency and magnitude is exponential, represented by a power law with scaling coefficient (*b*-value) of 2.172. The *b*-value is the slope of the relationship, indicating the relative frequency of the different rockfall volumes, with higher *b*-values indicating a greater contribution in net volume from smaller rockfalls.

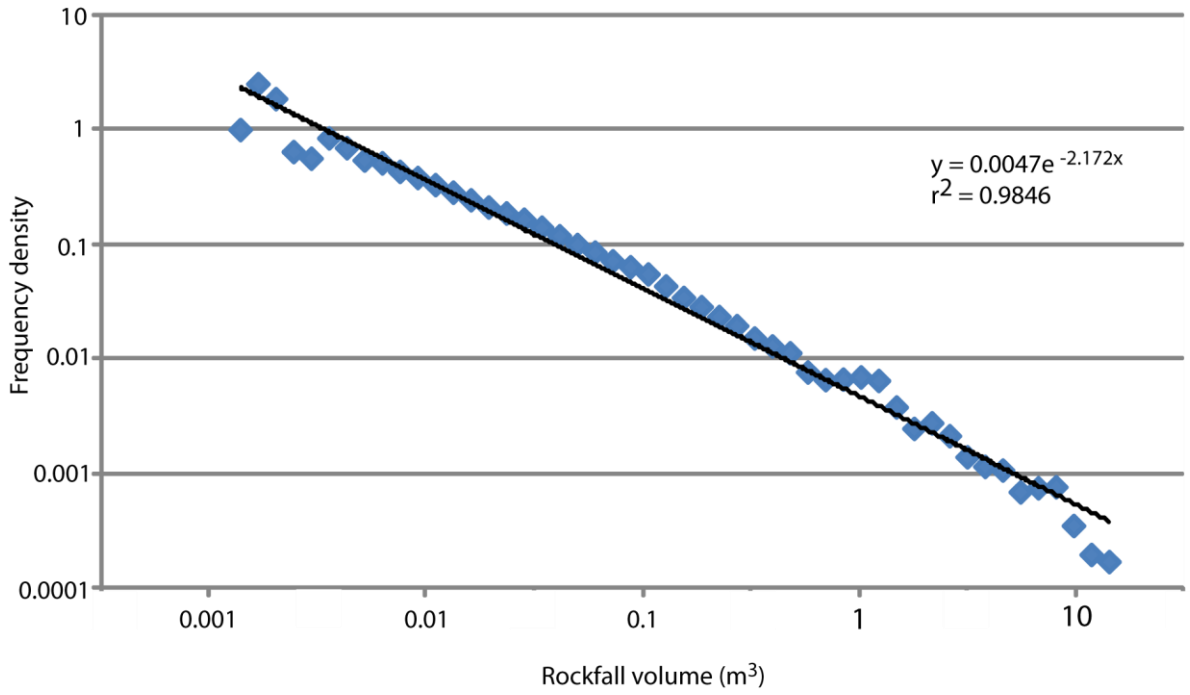

Figure 7.6: Magnitude-frequency relationship for rockfalls from across the whole cliff face during the two year monitoring period (July 2008 – July 2010).

The *b*-value of 2.172 is high compared to other coastal cliff rockfall volume datasets, which have also included similar rockfall volumes (e.g. Marques, 2008; Lim et al., 2010a), due to the occurrence of larger rockfalls at the sites where these other datasets were collected. The largest failure recorded here was only 12.73 m^3, but to determine whether even larger rockfalls do occur at this site a much longer monitoring period, or a more detailed study of the cliff structure and potential maximum rockfall size, is needed. The relatively limited temporal duration of the dataset means there is likely insufficient data to identify the full magnitude-frequency distribution of rockfall volumes. It is therefore necessary to rely upon observations from other studies to extrapolate the likely behaviour.

The absence of a rollover in this dataset at the smaller volumes, which commonly features in other mass movement inventories (e.g Stark and Hovius, 2001; Guthrie and Evans, 2004), suggests that this effect is caused by under-representation of the smallest rockfalls due to the spatial resolution of monitoring. The high-resolution of the TLS technique used in this study means that the small rockfall volumes, down to the limit imposed by the surface grid resolution (determined by the TLS point spacing), can be accurately identified. The imposed size threshold means that all rockfalls within this range are included, and these results show the power-law magnitude-frequency relationship to continue throughout the smallest rockfalls detected, with a high r^2 of 0.99 ($p < 0.001$). This observation is also made by Young et al. (2011a) commenting on Lim et al.'s (2010a) dataset, that was collected across a wider area of the same stretch of

coastline as this study, using the same monitoring technique. To fully test whether the rollover is a feature of monitoring resolution relative to rockfall sizes, even higher-resolution monitoring would be required.

7.1.4 Spatial variations of rockfall volumes

Across the whole cliff face, 80% of the rockfalls that occurred had volumes < 0.01 m^3 and only 2% are > 1 m^3 (Figure 7.7). Despite their high frequency, rockfalls of volumes < 0.01 m^3 only result in 15% of the total cliff change volume. Rockfalls of volume between 0.1 and 10 m^3 are responsible for 60% of the total volume of change, and so do the greatest amount of work modifying the cliff.

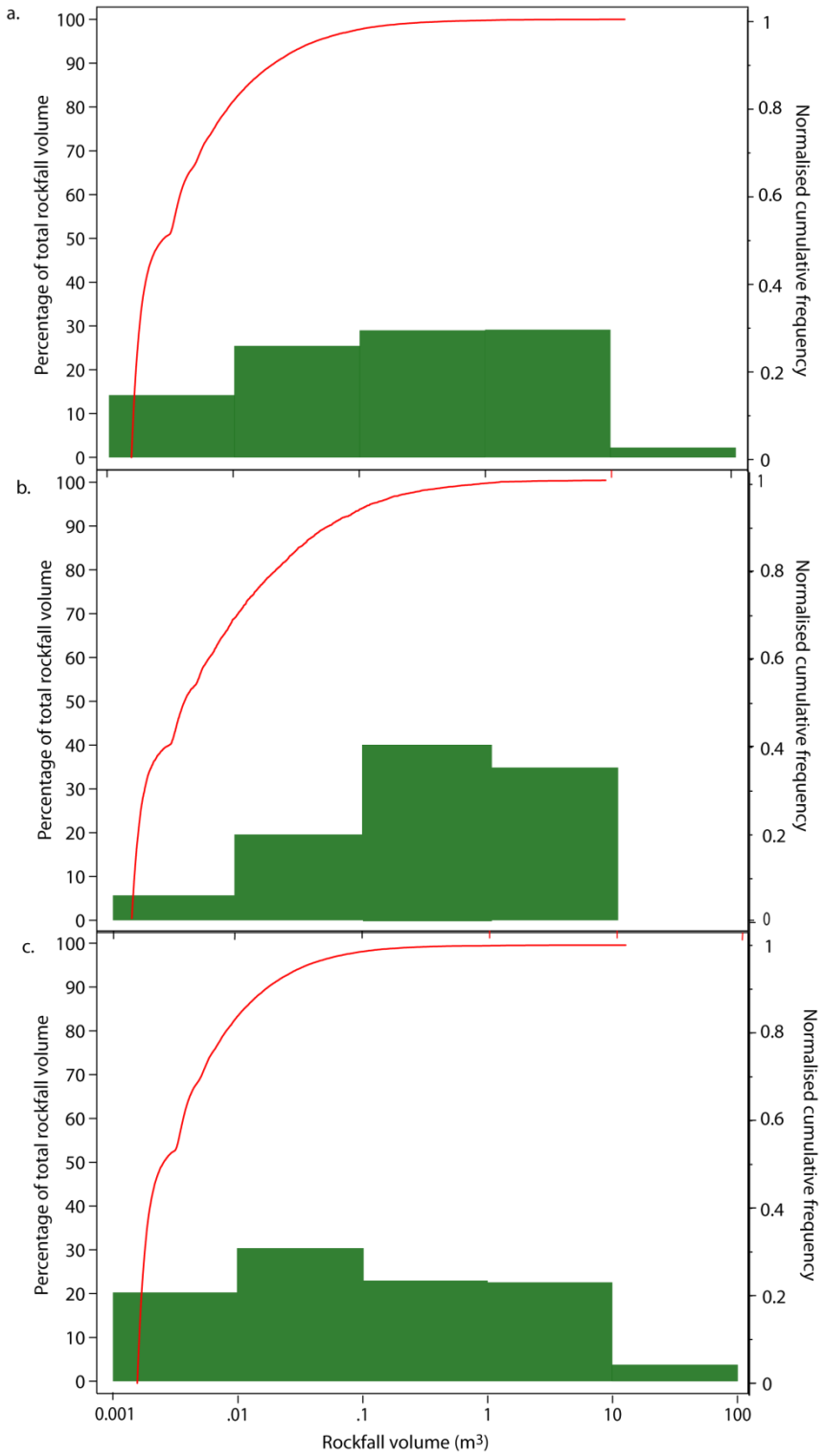

Figure 7.7: Cumulative frequency and percentage of total rockfall volume contributions for: a) Whole cliff face; b) Inundation zone; and c) Non-inundation zone. The step in each of the cumulative frequency curves occurs at the volume corresponding to two pixels on the surface grid. The step features at the same level in all graphs indicating an error caused by the processing techniques used rather than being a natural phenomenon.

The magnitude-frequency distribution of rockfalls in the two zones varied, with larger rockfalls occurring more frequently in the inundation zone (Figure 7.7b & c). In the non-inundation zone approximately 82% of the rockfalls (Figure 7.7c) had volumes < 0.01 m^3, whereas in the inundation zone they make up approx 68% of the number of rockfalls (Figure 7.7b). In the inundation zone rockfalls of volumes between 0.1 - 1 m^3 make up 40% of the total volume of cliff face change. Rockfalls of 1 - 10 m^3, which only make up 2% of the rockfall frequency, resulted in approximately 35% of the volume of cliff change. In the non-inundation zone smaller rockfalls make up a greater percentage of the failures and contribute more to the total volume of change (Figure 7.7c). Rockfall volumes of 0.1 - 1 m^3 make up approximately 23% of the change volume in the non-inundation zone, 1 - 10 m^3 approximately 23% of the change volume, and rockfalls > 10 m^3 contribute to about 3% of the total change volume.

The differences between the magnitude-frequency distributions in these zones are probably due to differences in both geological and environmental conditions. In the inundation zone larger rockfalls are likely to have been more frequent due to the massive nature of the mudstone, and was driven by direct attack by waves. In the non-inundation zone the more friable shale, which is vulnerable to a wider suite of weathering processes, is more likely to result in a higher frequency of smaller failures, as observed.

Despite occurring much less frequently, larger failures are by far the most geomorphically effective. On an individual basis, the majority of rockfalls that occur do not significantly alter the cliff form. Instead, cliff change typically occurs gradually, via frequent small failures (< 0.01 m^3) across the cliff face, with occasional larger failures which rapidly alter one section of the cliff, but which do not instantly result in the large-scale failure of surrounding material. In the short-term, rockfall effects appear to remain localised to specific areas of the cliff face at any one time. Coastal cliff change is commonly assumed to be episodic, driven by the stochastic nature of extreme energetic environmental conditions as triggers (Hapke and Richmond, 2002; Hall et al., 2008). Change at the study site is not episodic in one sense, as it is evidently frequent with typically > 1,000 rockfalls occurring per month. However, most rockfalls are small (< 0.01 m^3) and individually do not result in large morphological changes to the cliff face. Larger events (> 1 m^3), which account for most of the volumetric change in form, are rare and therefore in this sense significant change of the cliff form is episodic. Whether these episodic larger failures at the site are caused by environmental conditions and therefore limited by their occurrence is explored in Section 7.2.

7.1.5 Temporal variations of rockfall volumes

To examine the temporal variations in the contributions to net volume from the different rockfall sizes, the relationships between rockfall magnitude and frequency were calculated for each of the monitoring epochs using least squares regression analysis. The power law exponents *b* and *a* obtained using least squares regression indicate the relative contributions of small and large rockfalls to total cliff change. The *b*-value indicates the relative frequency of the rockfall volumes of various sizes, with higher values showing a greater contribution from smaller rockfalls. The *a*-value represents the y-intercept, which is the frequency value when the y-axis crosses the x-axis at 0, however because the volumes were treated as log(volume), x = 0 actually represents volumes of 1 m^3. The *a*-values therefore represent the frequency of rockfalls of 1 m^3. They provide a more specific indicator of the frequency of larger volumes within each monitoring epoch.

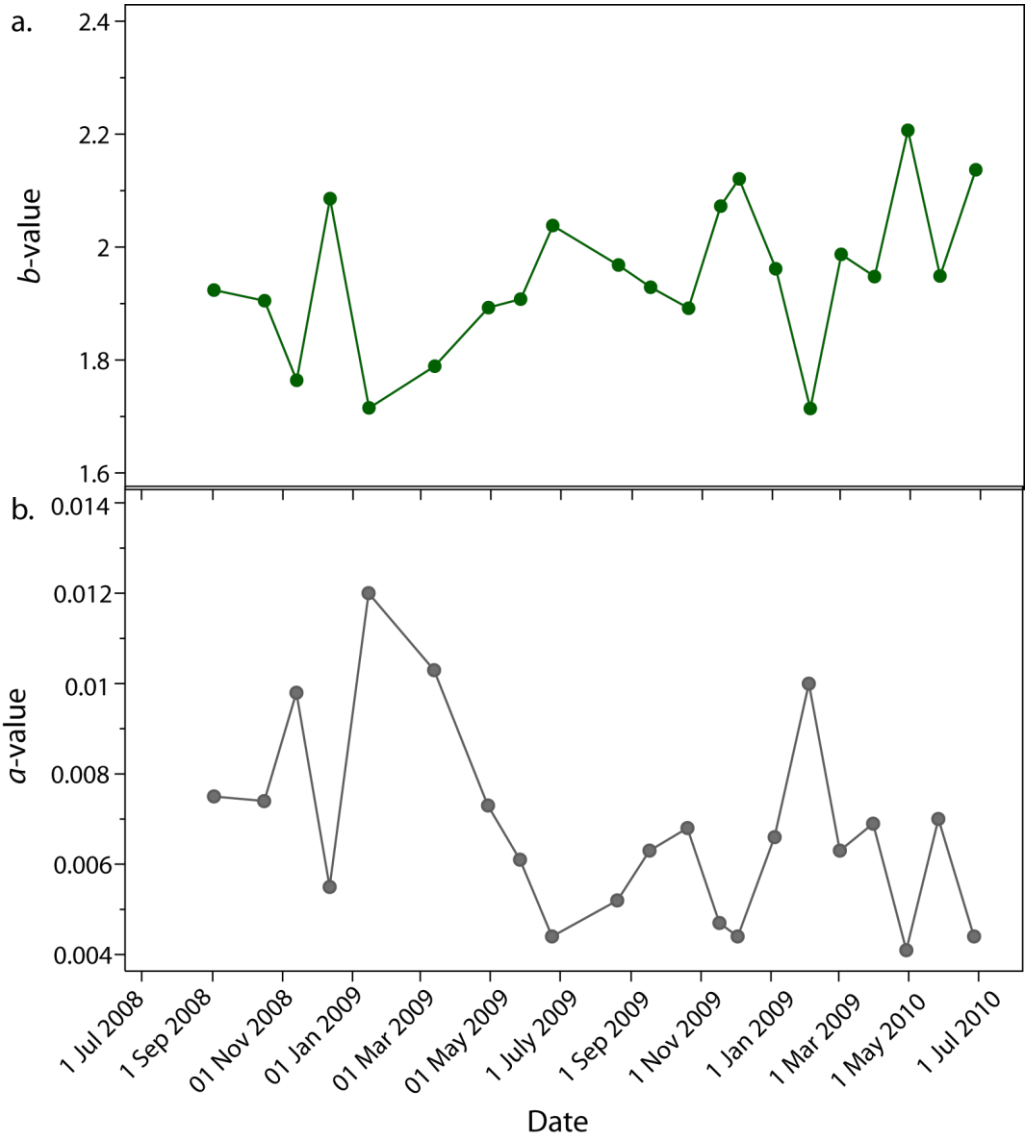

Figure 7.8: Magnitude-frequency power law *a*- and *b*-values over time.

The *b*-values varied throughout the two-year monitoring period, ranging from 1.66 – 2.24, with high values occurring in both winter and summer months, indicating greater contributions from smaller rockfalls during these times. The lowest *b*-values, which indicate increased frequency of larger rockfalls, occurred in winter months. The apparently seasonal variations in *b*-values over time suggest there are environmental controls on the frequency of different sized rockfalls. This is tested further in Section 7.2 below, and is discussed more widely in Barlow et al. (2012).

The *a*-values indicate the frequency of the larger rockfalls of volume = 1 m^3, which also vary over time, with the highest values occurring during the winter months. This suggests that during winter months more aggressive, stormier, more energetic conditions result in a more frequent occurrence of larger rockfalls (~1 m^3).

7.2 Observed environmental controls on rockfalls

The rockfall characteristics identified in Section 7.1 indicate that there are environmental controls upon rockfall activity, which also appear to determine the size of failures that occur. Regression analysis has been used to test these environmental controls upon rockfalls. Improving understanding of these controls will enable a better estimation of the timing of failures, and the conditions under which coastal cliff erosion may increase, either at present, or into the future.

In the previous chapter, specific seismic frequency bands were found to represent relative energy transferred to the cliff from a range of environmental sources. By implication, the seismic data therefore provides a more accurate picture of the atmospheric and marine conditions specifically at the cliff, than is possible to be obtained from regional-scale environmental monitoring and shoreward extrapolation of these datasets. Both the microseismic ground motion data and the environmental time series have been correlated using least squares regression against the monthly rockfall data to examine the role of environmental conditions as controls of rockfalls, and to test whether microseismics can be used to better identify and characterise these controls.

The following questions have guided the regression analyses. These questions consider specific interactions between environmental variables and the cliff, where energy transfer has been identified and therefore these are variables that may have a potential control on erosion:

1. Does increased wind velocity (represented by the WI seismic frequency band) result in the accelerated removal of material from the cliff face?

2. Do energetic sea conditions at the cliff toe during high tides (represented by the HT seismic frequency band) result in preferential removal of cliff material from the inundation zone as compared to the non-inundation zone?
3. Does long-period infragravity wave energy transferred to the foreshore and cliff face (represented by the LP seismic frequency band) have a demonstrable control on the rate of short-term cliff erosion?
4. Does wave energy transferred to the nearshore, but not directly to the cliff toe (represented by the MS seismic frequency band), have a control on cliff erosion?
5. Does wave energy transferred to the seabed away from the cliff and foreshore (represented by the MS seismic frequency band) hold any control on the nature of cliff erosion?

7.2.1 Data considerations

Despite the high resolution of the seismic and environmental datasets, all the data variables used in the regressions have been re-sampled to the resolution of the coarsest dataset, i.e. to the monitoring interval of the rockfall data. Five of the seismic signals analysed in the previous chapter, believed to best represent the energetic environmental conditions identified at the study site, were used in the regression. These were: 0.022 s wind (WI) signal; 0.08 s high tide (HT) signal; 1 s microseism (MS) signal; 5 s microseism (MS) signal; and 70 s long-period (LP) signal. The total signal power and total energy per monitoring period of these five seismic frequencies were derived, in addition to the total ground motion velocity per monitoring period of the E (cliff normal) and Z components.

The environmental variables tested were those which in the previous chapter were shown to generate readily identifiable seismic signals. These were tide, wave and wave set-up heights; tide residuals; wind velocities and air pressure. The mean and max of each variable per monitoring period were calculated. The combinations of environmental variables identified in the previous chapter as drivers of the different seismic signals were also regressed against the rockfall characteristics using multiple linear regression.

Various derivatives of the datasets have been used to represent the ground motion, environmental and rockfall variables. The total power, energy and velocity of the ground motion frequencies was considered to be the most suitable derivative as it represents the sum of forcing from each group of environmental processes that they represent, and therefore the potential geomorphic work exerted on the cliff. The mean values of the environmental and

rockfall datasets smooth out the effects of high-energy events, but do however provide a measure of the seasonality of the variables. The maximums highlight the extreme events that for the environmental variables may represent increased geomorphic efficacy, and for the rockfall dataset will represent large failures in response to environmental or material controls. The standard deviation of the rockfalls were included to reflect the variability of the rockfall volumes per month which may indicate response to varying controlling conditions, and total number and volume of rockfalls were used to represent the cumulative response to forcing across the full range of size distributions.

The total, mean, maximum and standard deviation of the rockfall volumes and the number of rockfalls in the inundation zone and the non-inundation zone, and the total rockfall volumes of each of the five class sizes (class 1 = < 0.01 m^3, class 2 = 0.01 < 0.1 m^3, class 3 = 0.1 < 1 m^3, class 4 = 1 < 10 m^3, class 5 = > 10 m^3) were regressed against the ground motion and environmental data, and their derivatives.

The majority of regression models provided statistically insignificant relationships between the seismic or environmental variables and the rockfall characteristics. Only the statistically significant relationships are focussed upon. The following variables produced no statistically significant relationships in either zone:

- The total ground motion velocity for either the E and Z components;
- Multiple regression models using combinations of environmental variables;
- The numbers of rockfalls captured per monitoring period.

7.2.2 Environmental controls on rockfalls in the inundation zone

There were no statistically significant results from the regression models between any of the seismic signals' power and rockfall variables within the inundation zone. The WI, HT and 5 s MS seismic signal energy however did produce a statistically significant result (Table 7.2). Of the environmental conditions regressed against the rockfall characteristics, the marine conditions at the cliff face produced statistically significant results – the tide, wave, set-up heights, tide residuals and variables of combined tide, wave and set-up heights (Table 7.3). Of these, the most significant are the wave heights at the cliff, the combined height of tides, waves and set-up, and the tide residuals. These represent energetic, stormy marine conditions at the cliff toe and the results suggest they are capable of removing material from the cliff face in the inundation zone.

Table 7.2: Statistically significant r^2 values of the regression analyses between the seismic signals' energy values and inundation zone rockfall characteristics. Statistically significant r^2 values are highlighted in **bold**. The stars beside the r^2 values indicate their level of significance at the following p values: *=0.05 **=0.01 ***=0.001.

Rockfall volumes	0.022 s (WI) seismic signal energy	0.08 s (HT) seismic signal energy	5 s (MS) seismic signal energy
Mean volume	**0.362****	0.059	**0.360****
Standard deviation of volume	0.166	0.134	**0.245***
Max volume	0.085	0.17	0.163
Total volume	0.163	0.152	**0.296***
Class 1 volume	0.136	0.055	0.056
Class 2 volume	0.001	0.008	0.085
Class 3 volume	**0.188***	0.001	0.159
Class 4 volume	0.126	**0.226***	**0.241***
Class 5 volume			

Table 7.3: Statistically significant r^2 values of the regression analyses between the environmental variables and inundation zone rockfall characteristics. There were no statistically significant relationships between the seismic signals' powers and the inundation zone rockfall characteristics. Statistically significant r^2 values are highlighted in **bold**. The stars beside the r^2 values indicate their level of significance at the following p values: *=0.05 **=0.01 ***=0.001.

Rockfall volumes	Tide height above toe max	Combined tide, wave, set-up height mean	Combined tide, wave, set-up height max	Wave height at 1000 m mean	Wave height at cliff mean	Wave height at cliff max	Set-up at cliff mean	Wind velocity max	Offshore wind velocity max	Tide residuals max	Air pressure max
Mean volume	0.165	0.16	0.115	0.113	**0.203***	0.122	0.089	**0.293***	**0.301***	**0.497*****	0.001
Standard deviation of volume	0.081	**0.204***	0.12	0.09	**0.227***	0.103	0.077	**0.195***	**0.206***	**0.346****	0
Max volume	0.067	**0.269***	0.154	0.108	**0.291***	0.127	0.1	0.125	0.136	**0.322****	0
Total volume	0.182	**0.341****	**0.198***	**0.202***	**0.443****	**0.198***	**0.221***	**0.209***	**0.201***	**0.536*****	0.016
Class 1 volume	0.029	0	0	0.014	0	0	0	0.131	0.148	0.096	0.044
Class 2 volume	0.01	0.163	0.093	0.138	0.183	0.059	0.181	0.001	0.003	0.069	**0.193***
Class 3 volume	**0.208***	0.054	0.071	0.103	0.14	0.105	0.134	0.141	0.133	**0.371****	0.002
Class 4 volume	0.11	**0.310***	0.152	0.138	**0.357****	0.142	0.132	**0.191***	**0.198***	**0.396****	0.004
Class 5 volume											

Each of the environmental and microseismic ground motion variables used in this study may be considered to provide a measure of a specific environmental condition e.g. wind velocity or wave height, or may be a proxy for related processes e.g. wind buffeting or wave breaking. The fact that a variable correlates well with a rockfall characteristic means that either the specific environmental variable is a significant control of that rockfall characteristic, or the variable is a good proxy for the driving processes. For example, the WI seismic signal's energy correlation with mean rockfall volume suggests that either the wind velocity, or the processes that wind drives e.g. wind buffeting, loading and shaking of the cliff face, have a control on mean rockfall volume. However, because of the range of processes that different environmental conditions can generate, and the multiple regression correlations between a range of complimenting environmental variables and each of the four distinct seismic frequency bands (WI, HT, MS and LP) (see Chapter 6), it is assumed in this study that each of the frequency bands acts a proxy for a range of processes generated by certain combinations of environmental variables.

From the environmental variables, the highest r^2 values, which also have the highest significance level, result from the maximum tidal residuals, which are a good indicator of stormy marine conditions representing elevated sea levels and storm energy directed towards the coast. The tidal residuals have the highest significance and r^2 values of the inundation zone models. Significant relationships extend across the different derivatives of rockfall characteristics, and also with the class 3 (0.1 - 1 m^3) and 4 (1 - 10 m^3) rockfall volumes. These are the largest rockfalls, which in Section 7.1.3 were identified to account for most of the geomorphic change that occurs in the inundation zone. Stormy marine conditions at the toe therefore are capable of removing large blocks of rock from this zone, contributing significantly to geomorphic change.

The maximum wind velocities from all directions, and specifically offshore directions, as well as air pressure fluctuations, also produce some statistically significant r^2 values in the correlation analysis. However their effect is more likely to be via their influence on wave conditions and sea level, or as a general descriptor of background environmental state, rather than their direct interaction with the lowest 5 m of the cliff.

The significant relationships between the energy of the WI, HT and 5 s MS seismic signals, which represent wind and wave conditions at the cliff face and widespread wave conditions respectively, also suggest that it is stormy conditions both at the cliff face and more widely that are important in controlling the occurrence of rockfalls in the inundation zone. The correlations produced by the microseismic energy but not the microseismic power of these specific frequency bands indicate that in the inundation zone the energy provides a better measure of

the amount of energy available to drive marine erosive processes. The seismic signal power is believed to better represent the resulting shaking, swaying or loading of the cliff generated by these processes.

The inundation zone is subject to the combined effect of the ground motions that result from foreshore wave conditions and direct wave impacts, but also to erosive hydraulic and mechanical processes. Rockfall characteristics in this zone, the absence of significant relationships between the seismic signal power and rockfall variables, and the significance of the seismic signal energy and stormy marine conditions, together suggest that cliff material in the inundation zone is largely removed via marine processes such as quarrying rather than by the resulting ground motions. The energy available to drive, and the occurrence of, processes of block removal appear to be more geomorphically effective than the ground motions despite being caused by the very same sea conditions. The wide joint spacing and strength of the mudstone in this zone play a significant part in defining the size of blocks that can be removed. If the shale, siltstone or sandstone formed the base of the cliff, the rockfall geometry would likely be very different; an observation made by Lim et al. (2010a) across sites with different cliff toe lithology.

These results demonstrate the importance of using local marine conditions at the cliff rather than relying upon regional-scale datasets, such as distal tide gauge and wave buoy data. As identified, the two datasets have very different success in explaining rockfall occurrence. Both tide gauge and wave buoy data produced no significant relationships with the rockfall characteristics alone. Environmental data from regional-scale monitoring are commonly used when exploring coastal erosion rates, fundamentally driven by rockfall, as they are readily available. Despite this, such data has failed to show significant relationships between rockfall and environmental datasets in this study, echoing the findings of others (Rosser et al., 2007; Lim et al., 2010a). Fundamentally, the only data often available may generate a misleading explanation of the processes in action, and so may not be as valuable as its availability implies. The cliff marine variables used here have been modelled from the tide gauge and wave buoy data, and have shown to represent actual conditions well, and encouragingly have been successful in identifying significant relationships between environmental variables and rockfall characteristics.

Considering the questions that guided the regression analyses, the results of the regressions have shown that erosive marine processes at the cliff face during stormy marine conditions, and wider spread, energetic, stormy conditions are significant in driving erosion of the inundation zone.

7.2.3 Environmental controls on rockfalls in the non-inundation zone

Statistically significant relationships occur between the total seismic signal power and rockfall characteristics within the non-inundation zone (Table 7.4). The signal power for each of five seismic frequency bands show statistically-significant relationships with mean and total rockfall volumes, and there is little variation in the r^2 values between different frequency bands. The energy of the HT and 1 s MS seismic signals also correlated against the rockfall characteristics (Table 7.5).

Marine conditions at the cliff toe also have statistically-significant relationships with the rockfall characteristics from the non-inundation zone above. Tide, wave and set-up heights, and particularly the variable that combines all three, have significant linear relationships with all the rockfall statistics and some of the highest r^2 values (Table 7.4). This zone is believed to be above the direct reach of the sea therefore the significance of energy from the HT signal and marine variables suggest that: a) the inundation zone may extend further up the cliff than estimated; b) the effect of marine energy transfer to the cliff extends beyond the zone it is directly transferred to.

There are also some statistically-significant relationships between the marine variables at the cliff and the larger rockfall size classes (3 (0.1 – 1 m^3) and 4 (1 - 10 m^3)), which do not correlate with the microseismic signals. The highest r^2 values for these rockfall size classes occur with the combined tide, wave and set-up height at the cliff. This suggests again that the direct influence of the sea extends further up the cliff than identified by the estimated limit of the inundation zone.

Although the modelled wave and set-up conditions at the cliff have proved to better estimate sea conditions at the site than the regional datasets, results indicate that actual wave conditions and water levels monitored at the cliff are needed to be able to more accurately identify the zone exposed to marine erosive processes, and subsequently the relationships between sea conditions and rockfall characteristics.

The HT seismic signal energy better represents marine processes at the cliff toe than the 1 s MS signal energy because of the relatively high energy values of the HT signal (see Chapter 6). The correlations between the 1 s MS signal energy and rockfall characteristics in the non-inundation zone suggest that this frequency may be close to the resonant frequency of the cliff in response to wave conditions and processes at the cliff toe and across the foreshore. Notably, the resonant frequency will remain the same irrespective of the driving frequency.

Table 7.4: Statistically significant r^2 values of the regression analyses between the seismic signals' power and non-inundation zone rockfall characteristics and also environmental variables and non-inundation zone rockfall characteristics. Statistically significant r^2 values are highlighted in **bold**. The stars beside the r^2 values indicate their level of significance at the following p values: *=0.05 **=0.01 ***=0.001.

Rockfall volumes	0.022 s (WI) seismic signal power	0.08 s (HT) seismic signal power	1 s (MS) seismic signal power	5 s (MS) seismic signal power	70 s (LP) seismic signal power	Tide height above toe mean	Combined tide, wave, set-up height mean	Combined tide, wave, set-up height max	Wave height at 1000 m max	Wave height at cliff mean	Wave height at cliff max	Set-up at cliff mean	Set-up at cliff max	Onshore wind velocity max
Mean volume	**0.348****	**0.349****	**0.329****	**0.340****	**0.350****	0.174	**0.457****	**0.254***	**0.212***	**0.331****	**0.248***	0.113	0.184	**0.226***
Standard deviation of volume	**0.203***	0.176	0.179	**0.218***	**0.190***	0.076	**0.277***	0.104	0.062	0.159	0.134	0.093	0.025	0.132
Max volume	**0.189***	0.159	0.164	**0.206***	0.172	0.058	**0.204***	0.075	0.041	0.119	0.116	0.07	0.008	0.088
Total volume	**0.274***	**0.268***	**0.252***	**0.260***	**0.267***	0.149	**0.307***	0.146	0.147	**0.283***	0.177	0.097	0.119	0.102
Class 1 volume	0.001	0.002	0.003	0.006	0.003	0.06	0.014	0.003	0	0.045	0.003	0.03	0.001	0.003
Class 2 volume	0.015	0.022	0.015	0.007	0.016	0.039	0.025	0.053	0.052	0.063	0.039	0.021	0.077	0.008
Class 3 volume	0.157	0.183	0.161	0.143	0.164	0.007	0.094	0.036	**0.226***	0.075	0.05	0.037	**0.237***	0.024
Class 4 volume	0.024	0.024	0.02	0.022	0.026	**0.309***	**0.516*****	**0.214***	0.08	**0.399****	0.196	**0.200***	0.065	0.175
Class 5 volume	0.310	0.26	0.288	0.343	0.285	0.009	0	0.001	0	0.001	0.005	0.018	0.008	0

Table 7.5: Statistically significant r^2 values of the regression analyses between the seismic signals' energy and non-inundation zone rockfall characteristics. Statistically significant r^2 values are highlighted in **bold**. The stars beside the r^2 values indicate their level of significance at the following p values: *=0.05 **=0.01 ***=0.001.

Rockfall volumes	0.08 s (HT) seismic signal energy	1 s (MS) seismic signal energy
Mean volume	**0.399****	**0.227***
Standard deviation of volume	**0.579*****	**0.236***
Max volume	**0.557*****	**0.196***
Total volume	**0.274***	0.12
Class 1 volume	0.001	0.001
Class 2 volume	0.004	0.001
Class 3 volume	0.004	0.013
Class 4 volume	**0.436****	**0.344****
Class 5 volume	0.099	0.001

Onshore wind velocities have a statistically-significant relationship with mean rockfall volumes, suggesting that winds blowing directly onto the cliff face are potentially capable of removing loose rock from it. The statistically-significant relationship between the WI seismic signal and rockfalls also suggests that the high-power, high-frequency shaking that results from wind turbulence at the cliff surface is capable of detaching loose material. The WI signal produces more statistically significant relationships with the various rockfall characteristics than the wind velocity, which has only a statistically-significant relationship with mean rockfall volumes. This suggests that the WI signal better represents the interaction between the wind and the cliff than the wind velocity data, which is actually recorded 3 km from the study site and is notably inland. This may also indicate that the WI signal to some extent, also represents wider stormy conditions via wind effects on wave characteristics and sea levels.

This mechanism of rock removal is most likely to occur with very small volumes of rock below that detectable by the point spacing of the TLS data. These results suggest that wind buffeting around the cliff also has the potential to remove larger blocks (i.e. those with volumes above the minimum volume of 0.00156 m^3). This may possibly be due to the knock-on or cascading effects of small failures on surrounding material. For example, the triggering of failure of small fragments of rock can result in the dislodging of surrounding rock due to unloading or de-buttressing effects. This is particularly likely for highly weathered sections of the cliff face, and has been commonly observed to occur in the shales at the site. The magnitude of the failure trigger therefore may not be expected to directly relate to the resulting failure magnitude. However the results of these linear regressions do indicate that increases in environmental forcing are linked to increases in rockfall volumes, believed to be due to greater energy transfer, loading and more effective erosive processes, and therefore increased potential degradation of the rock strength and exceedance of critical strain thresholds. This observed behaviour may arise from either larger forcing resulting in larger failures, or larger forcing resulting in greater numbers of smaller failures. The lack of a statistically-significant relationship between the onshore wind velocity and the WI seismic signal power and the rockfall size classes means it remains impossible to identify the sizes of rockfalls to which these conditions lead.

Interestingly, the power of the seismic signals that are generated by wave conditions across the nearshore and further out to sea (the 1 s MS and 5 s MS signals) and also the long-period 70 s LP signal, also have statistically-significant relationships with the rockfall variables. The frequencies of these signals represent much longer period ground motion than the WI and HT signals, and therefore do not represent high frequency shaking of the cliff. Rather, these longer period signals represent stormy marine and atmospheric conditions in the local coastal basin. Their

power relationships with the rockfall occurrence suggest that these wider-scale stormy conditions can generate rockfalls in addition to the direct wave impacts and winds against the cliff face. However the actual variables of the wave conditions away from the cliff, air pressure and tide residuals have not produced statistically-significant relationships with the rockfall data. This suggests the microseismic ground motions provide a better proxy of wide-scale stormy conditions, or the geomorphic effect of these. The statistically-significant relationships between seismic signal power and rockfall in the non-inundation zone suggests that above the direct reach of the sea, atmospheric and marine conditions drive erosion in part via dynamic loading, causing shaking and swaying of the cliff represented by the ground motion signal powers, which can potentially have a preparatory effect on the rock as well as triggering failures. These results demonstrate that the seismic signals also represent wider-scale environmental conditions well, and are useful in monitoring and identifying the environmental conditions that lead to rockfall.

Regression analysis in the non-inundation zone has addressed questions 1, and 3 – 5, identifying that wind turbulence around the cliff can trigger rockfalls, and that wider-scale stormy conditions also coincide with increased rockfall activity. Both of these factors are better identified by the microseismic time series than by the environmental variables themselves.

All of the statistically significant r^2 values produced by the regression analyses remain < 0.6, which may be more widely regarded as low. These are likely to be explained by the very low temporal resolution of the rockfall data used – the seismic and environmental datasets collected at 100 Hz and 1 minute - 1 hour resolutions had to be reduced to one value (total / mean / max) per 4 - 8 week rockfall monitoring period. It is anticipated that by monitoring the rockfall activity at much higher temporal resolutions the strength of these relationships would be improved. Considering the relative speed with which the cliffs as a landform change and evolve to achieve any form of regression that derives a statistically significant result is encouraging.

7.2.4 Environmental controls on the whole cliff rockfall magnitude-frequency distribution

To test the effect of environmental conditions on the rockfall size distribution, the magnitude-frequency *b* and *a* coefficients for the monitoring periods have been regressed against the total seismic signal power and energy, and mean and max environmental conditions during each monitoring epoch.

There were no statistically-significant relationships between the seismic signal powers and the *a* and *b* coefficients. However the WI signal energy produced significant correlations with the *a* and *b* values, indicating that as energy increases so does the relative number of large rockfalls (positive correlation) but the number of small rockfalls decreases (negative correlation). The 5 s MS signal energy produced significant positive correlations with the *a*-values and therefore the relative occurrence of larger rockfalls (Table 7.6). The tide and wave heights; the combined tide, wave and set-up height variable; and tide residuals have statistically-significant relationships with both the *a* and *b* values (Table 7.7). The coefficients of each of the regression models show that as these water levels at the cliff increase, there is a corresponding decrease in *b*-values, and an increase in *a*-values, which means an increase in the frequency of large rockfalls. These results indicate that *a* and *b*-values are potentially varying in a co-linear manner, and that the same controls are determining simultaneous increases in *a*-values with decreases in *b*-values.

Table 7.6: Statistically significant r^2 values of the regression analyses between the seismic signals' energy and the magnitude-frequency power law *a*- and *b*-values. Statistically significant r^2 values are highlighted in **bold**. The stars beside the r^2 values indicate their level of significance at the following p values: *=0.05 **=0.01 ***=0.001. The regression model coefficients indicate the *b*-values had negative correlations with the seismic variables and the *a*-values had positive correlations with the seismic variables.

	0.022 second (WI) seismic signal energy	5 seconds (MS) seismic signal energy
b-value	**0.313****	0.111
a-value	**0.482*****	**0.245***

Table 7.7: Statistically significant r^2 values of the regression analyses between the environmental variables and the magnitude-frequency power law *a*- and *b*-values. Statistically significant r^2 values are highlighted in **bold**. The stars beside the r^2 values indicate their level of significance at the following p values: *=0.05 **=0.01 ***=0.001. The regression model coefficients indicate the *b*-values had negative correlations with the environmental variables and the *a*-values had positive correlation with the environmental variables.

	Tide height above toe mean	Tide height above toe max	Combined tide, wave, set-up height mean	Combined tide, wave, set-up height max	Wave height cliff mean	Wave height cliff max	Tide residuals max
b-value	**0.201***	**0.400****	**0.225***	**0.212***	**0.326****	**0.316****	**0.439****
a-value	0.161	**0.468*****	**0.237***	**0.255***	**0.336****	**0.322****	**0.558*****

These results tentatively imply that as marine conditions at the cliff and wider scale conditions become more energetic so larger rockfalls occur, and therefore that more geomorphic work is done.

7.3 Summary

The results of the monitored rockfall data show that cliff change occurs across the cliff face, with no concave notch at the toe being created, sustained or preserved. Rockfall characteristics are found to be strongly influenced by cliff face geology. Whilst small rockfalls are the most frequent, in volume terms they make a relatively small contribution to the total geomorphic work done to the cliff during the monitoring period. Conversely, the majority of geomorphic work in rockfall volume terms is done by large, infrequent failures.

Linear regressions between regional-scale environmental variables, specific microseismic frequency bands and rockfall characteristics have shown that environmental conditions do control cliff erosion, and notably influence the occurrence of larger failures. In the inundation zone, erosion occurs as a result of stormy marine conditions at the cliff face and stormy conditions more widely. In the non-inundation zone rockfalls may relate to: wind turbulence around the cliff; the high power, high frequency shaking driven by energy transferred from stormy marine conditions at the cliff toe; and due to dynamic loading by local coastal stormy marine and atmospheric conditions.

Both the microseismic and environmental datasets have allowed identification of the environmental conditions that promote rockfall occurrence. In the inundation zone, the marine variables best represent the wave characteristics at the cliff toe that drive the erosive processes, and therefore in turn the geomorphic effectiveness of these processes. Microseismic variables provide a better measure of the wider stormy conditions that influence erosion in the inundation zone. Higher up the cliff in the non-inundation zone, the microseismic variables best represent environmental drivers of erosion such as local marine and atmospheric stormy conditions.

The energy and power of the microseismic frequency bands thus represent the different ways in which environmental forces and processes, that generate cliff microseismic ground motions, control cliff erosion. Measures of microseismic energy and power are useful in exploring the mechanisms of environmental controls on cliff change.

Chapter 8: Discussion - Developments in understanding of hard rock coastal cliff erosion and the environmental controls

The aim of this thesis has been to improve understanding of the environmental controls of coastal cliff erosion by exploring cliff microseismic ground motions. The results presented in the previous chapters demonstrate that in addition to the processes widely considered to act on coastal cliffs, such as those associated with wave impacts at the cliff toe, other local environmental processes generate significant ground motions and therefore have the potential to alter the cliff. These include wind buffeting, wave pressure fluctuations and long-period energy in the surf and swash zones. The microseismic data has been shown to be useful in providing a measure of the relative forcing of different groups of processes acting on cliffs, using a common measure, that are associated with various environmental conditions. Each distinct frequency band of microseismic motion that has been identified acts as a proxy for a range of processes driven by different environmental conditions.

In addition, statistically-significant correlations exist between the frequency bands of microseismic ground motions and rockfalls from the cliff. This suggests that it is not just the processes acting directly at the cliff face, but processes acting across the foreshore, nearshore and offshore, and also the ground motions that these generate, that control cliff erosion, both in the short-term and in the medium- to long-term. The potential controls of these processes on cliff erosion are considered in the discussion below. The geomorphic efficacy of the environmental processes represented by the different frequency bands of microseismic ground motions, and indeed the ground motions themselves, are examined in the final section.

8. 1 The nature and role of environmental controls on cliff erosion

Cliff erosion and coastline retreat result from the combined effects of a range of processes that act across a range of spatial and temporal scales. Prior to failure, progressive mechanisms act to weaken and degrade the cliff rock mass, for example by weathering the materials and thus increasing susceptibility to detachment (e.g. Moon and de Lange, 2010). The initiation of failure is complex, involving both undetectable changes that cause the system to cross a critical threshold and direct triggers such as seismic excitation or large wave impacts. Within the inundated zone of the cliff toe, these processes are further complicated by the presence of elevated hydraulic pressures, drag, abrasion and turbulence resulting from fluid flow with entrained sediment and air. Fundamentally, across the whole cliff, these processes to a greater

or lesser extent interact, act in sequence or act as a catalyst to each other, so that differentiating the direct impact of one process on observed changes to cliff morphology remains challenging. This is confounded when real-time monitoring of these processes and their effects remains effectively impossible. In the context of microseismicity, not all erosion processes may generate a seismic signal distinguishable at the scales monitored here. Thus, the analysis presented assumes that this abundance of processes can be distilled into broad groups, represented primarily by discrete microseismic frequency bands, which in turn can be attributed to specific environmental forcing mechanisms. To identify the relative significance of the different groups of processes, microseismic signals need to be explored both as the amount of energy, and the rate of energy (power), transferred to the cliff.

8.2 Using microseismics to measure marine and atmospheric conditions at coastal cliffs

Despite recent developments in techniques to monitor and quantify cliff change, and to accurately identify rockfall distributions and characteristics, the environmental controls on cliff change remain poorly understood. A key limitation has been the lack of capability to accurately quantify environmental conditions at the cliff, which can then be correlated against rockfall data. Previous hard rock cliff studies that have collected high resolution rockfall data have compared these datasets with regional-scale datasets of wave, tide, wind, rain and temperature (e.g. Rosser et al., 2007; Lim et al., 2010a). However, these approaches have yielded only poor correlations between the environmental and rockfall datasets (e.g. Rosser et al., 2007; Lim et al., 2010a). This observation also applies to this study, where very few significant correlations between regional-scale datasets and the high-resolution rockfall data have been found. Such relatively poor relationships can be attributed to:

1. The insensitivity of regional-scale environmental data to the actual conditions at the cliff; and/or
2. The low temporal frequency of the monthly TLS monitoring relative to the timescale of environmental variability, which results in the necessity to aggregate environmental conditions to single monthly derivatives.

Conditions at the cliff have been observed to differ dramatically from the regional-scale monitoring data due to the potentially significant modification of environmental conditions over short distances or short timescales around the cliff, demonstrated by the wave model results. This arises primarily as a function of changing physical conditions close to the coast, such as water depth, steep coastline topography, land cover and / or coastal morphology. It is the

marine and atmospheric conditions that interact with cliff lithology that need to be quantified in order to be able to examine environmental influences on cliff change behaviour.

In recent years there has been growing use of microseismic data to identify and examine the locations, magnitudes and variability of storms and waves, in both current day and historically from archives (e.g. Tillotson and Komar, 1997; Aster et al., 2008; Bromirski, 2009). The cliff microseismic ground motion data collected in this study has been shown to represent environmental conditions experienced at the cliff, which has enabled an examination of the marine and wider environmental forces in action. A number of characteristic ground motion frequency bands have been isolated that have been attributed to different environmental conditions in the vicinity of the cliff, their relative forcing and their temporal characteristics. These signals have been used to quantify the net relative contribution from the various environmental sources known to act upon the coast, and to test their relative efficacy and significance in driving cliff change behaviour.

Critically, the microseismic data demonstrate that there are a range of environmental forces acting on the cliff that generate microseismic motions in addition to waves impacting upon the cliff toe. The results of this study show that energy is transferred to the cliff from marine and atmospheric conditions that occur directly at the cliff face, but also from sources further afield, including travelling waves and / or breaking waves across the nearshore and foreshore, with seismic sources identifiable over 1,000 m from the cliff toe. Although other studies that have collected cliff top microseismic data to examine marine energy delivery (Adams et al., 2002; Adams et al., 2005; Young et al., 2011b) have also identified and examined wave and tide signals in monitored ground motions, generated in the waters surrounding the cliff, these studies have not explored the full range of environmental forces acting on the cliff, nor have they tested their effect on cliff change behaviour.

Previous studies by Adams et al. (2002) and (2005) primarily examined the data in the time domain as time series of the power of the whole cliff motion (Adams et al., 2002) and velocity or displacement (Adams et al., 2005) and during high tides identified increased energy transfer and dominant ground motion periods to match those of incoming wave periods, however they observed poor links between ground motion and wave periods during low tides. The results of this study have however shown exploration of the cliff seismic data (as velocity) in the time domain to be limited in the extent to which it can explore the range of environmental forces that result in cliff ground motion. As demonstrated by the time series of velocity examined in Chapter 4, where peaks in the minute or hourly maximum occurred only during the high power, high frequency HT and WI frequency band events. These HT events correspond to the wave

impacts during high tides observed by Adams et al. (2005) and Young et al. (2011b). Energy transferred from the MS and LP frequency bands were not evident in the velocity data of this study yet exploration of these frequency bands showed the widespread marine sources that generate these motions actually transfer the greatest amounts of energy to the cliff.

By exploring the frequency spectrum of the cliff's ground motions this study has been able to identify and explore a much wider range of environmental forces. The results of this study correspond well to the findings of Young et al. (2011b) who also examined a number of specific cliff motion frequencies and monitored cliff toe water levels. They observed displacement amplitudes of the long-period and primary microseism frequencies to correspond with cliff toe water levels at the same frequencies, the power of which decreased at low tides. Young et al. (2011b) also found that during low tides however, the primary microseism power at the cliff top seismometer was similar to that at an inland seismometer, evidence that this microseism signal was also generated by distal sources, as was the double-frequency microseism signal during both high and low tides, supporting the findings of this study. The largest ground motion displacements observed by Young et al. (2011b) were at the long-period infragravity frequency which supports the observations of the LP signal of this study which was found to transfer the greatest amount of energy to the cliff. The results of this study and Young et al. (2011b) demonstrate the vast amount of information regarding environmental forcing on coastal cliffs, and the distribution of sources, that can be obtained by exploring different frequencies across the ground motion spectrum.

It has not been possible to compare the relative motions of the different cliffs of these studies because each study has presented a different feature of the microseismic data e.g. Adams et al. (2002) presented the power of the whole cliff motion – not individual frequencies, Adams et al. (2005) presented displacement and velocity of the whole cliff motion, Lim et al. (2011) used the number or rate of seismic impacts and Young et al. (2011b) examined displacements and power spectra of a range of frequencies. The results of this study, and those of Young et al. (2011b), have shown that to fully identify and quantify all sources it is necessary to explore the frequency spectrum of the data. This study has also demonstrated frequency power and energy to provide different insights into energy transfer to the cliff, and that both are valuable in considering the relative effects of the environmental forces the ground motions represent. In addition, to fully compare ground motions of different cliffs, longer datasets are necessary, such as the two-year dataset of this study, in order to obtain a representative quantification of the cliff ground motion behaviour, accounting for seasonal variations.

Both environmental forcing at the cliff face and the more distal and dispersed sources have been found in this study to broadly relate to rockfall activity. Lim et al. (2011) previously did not find statistically significant relationships between the number of seismic impacts with concurrent rockfall activity, however found relationships between seismic impacts and rockfall activity of the following month. This may represent a cumulative build up and preparatory effect of microseismic impacts on the cliff rock, resulting in delayed cliff responses to environmental forcing. The application of a broadband seismometer by this study has enabled a more detailed examination of the microseismic cliff ground motions than the geophone used by Lim et al. (2011), and has identified relationships over the same monitoring period between rockfalls and cliff motions that represent different environmental forces. These findings have major implications for the way we think about the interactions between coastal cliffs and the environmental conditions that surround and shape them, and hence on the environmental controls on cliff change. The spatial distribution of the marine and atmospheric sources of seismic energy, and the resultant rockfalls that are triggered, provide insights into the mechanisms and processes that control cliff erosion.

8.3 Environmental conditions at coastal cliffs and their controls on cliff erosion

The movement of tides and waves across the near- and foreshore result in dynamic loading of the cliff, observed here and in other cliff microseismic studies (e.g. Adams et al., 2005 and Young et al., 2011b). Adams et al. (2005) and Young et al. (2011b) both observed cliffs to sway downwards and seawards during wave approach and run-up and the reverse during wave backwash away from the cliff. Young et al. (2011b) identified the cliff mass displacement caused by wave loading, to vary with tide heights. This dynamic loading has the potential to decrease rock strength via damage accumulation, which may facilitate cliff failure (Sunamura, 1992; Adams et al., 2005; Brain et al., 2010). Failure may then either be caused by a process directly resulting in detachment, or a process that acts as a catalyst for other mechanisms. In addition to this potential for preparation of the cliff for failure, correlations between longer period microseismic signals and rockfall occurrences across the upper, non-inundated section of the cliff face demonstrate that there may also be a more immediate response to the longer period ground motions generated by waves. However, as yet the stresses and strain generated by wave loading have not been tested, and whether they are of sufficient magnitudes to degrade rock strength is currently unknown.

Wave conditions experienced at the coast, beyond those directly at the cliff toe, are not generally considered in coastal cliff erosion models (e.g. Walkden and Hall, 2005; Young et al., 2009b), and hence have not previously been considered as a potential driver of cliff change. The identification of the potential importance of marine conditions away from the cliff toe is hugely significant as this analysis provides some explanation of the role of environmental conditions that influence cliff change in the upper non-inundated parts of the cliff. Erosion of the upper cliff is typically attributed to either: a) subaerial processes, as it is beyond the inundation limit of waves (Emery and Kuhn, 1982; Sallenger et al., 2002); or b) to cantilever failure of overhanging material above an eroded cliff toe (e.g. Young and Ashford, 2008). However, the findings here demonstrate that marine controls potentially extend beyond the cliff toe and should be considered as drivers of rockfalls in the upper non-inundated cliff sections, in addition to subaerial processes.

Wave energy in the near-coastal zone is known to decrease towards the waterline as decreasing water depths result in wave shoaling (Thornton and Guza, 1983; Battjes and Stive, 1985). In general, only energy that remains within the wave field transferred to the cliff is considered to have the potential to directly cause erosion, either via hydraulic and mechanical processes that occur as waves impact against the cliff (Anderson et al., 1999; Stephenson and Kirk, 2000a; Trenhaile, 2000). Energy transferred to the seabed / foreshore is not usually considered to have the potential to affect the cliff. Because sites with wide foreshores or beaches have a relatively large area over which waves can dissipate energy to the seafloor, less energy in the wave field reaches the cliff compared to sites with shorter, steeper foreshores and thus there is less potential for direct erosion of the cliffs (Stephenson and Kirk, 2000a; Trenhaile, 2000; Ruggiero et al., 2001). The results of this study show that the dissipation of waves as they shoal transfers significant energy to the seabed, which in turn generates microseisms that reach the cliff. For the first time, this signal has been related to rockfall activity above the inundated zone of the cliff. It is therefore not only the energy delivered directly to the cliff by wave impacts that is important for cliff erosion, but also wave energy dissipation conditions across both the foreshore, and also further afield offshore. A large foreshore has conventionally been considered a defensive feature that acts to reduce energy transfer to the cliff, lowering erosion rates, yet here it is shown that at least some of this energy can be transferred landward to the cliff itself. This data also shows a clear differentiation between the nature of the energy transfer by these two mechanisms to the cliff; this raises the question as to whether a given quantity of energy delivered iteratively over a relatively long period over a distributed area, such as the foreshore, is as geomorphologically effective as the same quantity of energy delivered over a shorter, tidally modulated time period across a concentrated zone, such as the cliff toe. It is

evident from these findings that if microseisms are a factor in driving cliff erosion, we firstly need to understand if this form of energy transfer is geomorphologically significant. If so, there needs to be a change in the ways in which wave energy in the nearshore and foreshore is considered in cliff erosion models, and indeed to coastal structures more widely.

Currently wave energy dissipated at the seabed appears not to be considered to be transferred to the cliff. However, wave energy that is transferred to the seafloor throughout shallow waters is coupled to the seabed, travels to the coast and provides sufficient energy to generate cliff ground motions, and at this site leads to increases in the rate of rockfalls. Rather than purely being a buffer of wave energy, foreshore extent and geometry may in certain circumstances provide a considerable microseismic source. Moreover, energy dissipation in the foreshore, and transfer as microseismic ground motion, may add a further mechanism to foreshore downwearing.

This variety of wave processes may help to explain observed variations in rates of erosion across foreshores (e.g. Stephenson and Kirk, 1998; Inkpen et al., 2010; Stephenson et al., 2010). Whilst foreshore downwearing is often attributed to increased variability in subaerial conditions and processes (e.g. Stephenson and Kirk, 1998; Stephenson and Kirk, 2000b; Inkpen et al., 2010), block removal from vertical steps (backwearing) on foreshores is more likely to be due to wave erosion (e.g. Trenhaile and Kanyaya, 2007; Dornbusch and Robinson, 2011). The exploration of microseisms generated across foreshores with corresponding platform erosion may be useful to explore the role of marine processes in driving both spatially variable foreshore downwearing and backwearing of steps. However, foreshore erosion rates are typically low (Dornbusch and Robinson, 2011) and short-term swelling and shrinking in some rock types (Stephenson and Kirk, 1998) may make exploring such relationships between them difficult.

In addition to the wide-scale marine conditions, the microseismic signals reported here represent energetic conditions at the cliff face during high tides with large waves and high winds. Although wave impacts at the cliff face are the most commonly cited driver of cliff erosion (Sunamura, 1977; Sunamura, 1982; Benumof et al., 2000; Budetta et al., 2000; Ruggiero et al., 2001; Walkden and Hall, 2005), wind energy delivery and excitation and the resultant erosion of cliff material is not commonly included in cliff erosion models, nor has it been identified by other cliff microseismic studies as a forcing mechanism acting on the cliff. The microseismic ground motions show that wave and wind loading at the cliff face manifest as high-power, high-frequency shaking. Correlations between the frequency band attributed to wind velocity (3.33 Hz – 50 Hz) with the rockfall data in the upper part of the cliff suggest that in addition to erosion via the cliff shaking, wind may also trigger rockfall via generating shear and

lift across the rock surface as a result of turbulence at the cliff, removing loose or damaged material at the cliff surface.

Interestingly, the microseismic signal that represents wave impacts (1.67 Hz – 50 Hz) during high tides does not correlate with the rockfall data within the inundation zone. Instead marine conditions modelled from the wave buoy and tide gauge data to represent sea conditions at the cliff toe proved to better represent wave impact processes. These sea heights at the cliff face produced positive correlations with both the net rockfall rate and the occurrence of larger rockfalls, indicating that increases in wave and set-up heights during high tides accelerates the erosion process. It is likely that these modelled wave variables more accurately represent the variability in wave and tide heights and their relative magnitudes, and therefore the erosive efficacy of the hydraulic and mechanical processes of quarrying and abrasion. Studies of cliffs cut in material with lower uniaxial compressive strength, such as those on the Californian coast, that have adjusted far-field wave and tide datasets to represent actual conditions at the cliff have found correlations with cliff failure and erosion (e.g. Collins and Sitar, 2008; Young et al., 2009b). The results presented here demonstrate that offshore to onshore modelling of wave conditions sufficiently represents conditions at the cliff to be useful to identify relationships between the sea conditions and erosion. Direct removal of material by waves can therefore be observed in hard rock cliffs as well as soft rock cliffs, where the erosion is more immediately observable.

Sunamura's (1977; 1992) function of cliff erosion (Equation 2.1) is widely employed to explain that the magnitude of cliff erosion is determined by the relative magnitudes of the assailing force of waves versus the resistance provided by the cliff material. Although various methods have been used to measure rock resistance (commonly compressive strength), quantifying the assailing force of waves has remained challenging. The microseismic data provides a method of quantifying the assailing force of waves that can be compared to other environmental forces. Microseismic data, and in particular the ability to discretize the data into frequencies attributable to specific processes, provides a potentially valuable method of describing individual processes, in addition to comparing and contrasting the net influence of all environmental forces. This technique has also demonstrated that Sunamura's (1992) model provides a simplified view of the factors eroding the cliff, and indicates that commonly used static measures of cliff material strength conceal any form of incremental deterioration in resistance to erosion. Whilst Sunamura (1992) demonstrates the importance of interactions between geology and environmental forces as a catalyst on the effectiveness of erosion processes, Sunamura's (1977; 1992) model is based on these interactions only at the cliff toe.

The results of this study however demonstrate that a range of conditions across the whole cliff, and also the foreshore and nearshore, need to be considered. Therefore Sunamura's (1977; 1992) model (Equation 2.1) is incomplete. The cliff's erosion rate can be much better accounted for by the combined effects of marine and atmospheric conditions more widely, the dynamic strength of cliff material and how these vary over time represented by Equation 8.1 below:

Equation 8.1: $$x = f(F_{HT}, F_{MS}, F_{LP}, F_{WI}, F_{RD}, t)$$

Where:

x = erosion across whole of cliff;

F_{HT} = power of wave impacts at cliff face/foreshore;

F_{MS} = power of microseisms generated across nearshore and beyond;

F_{LP} = power of infragravity waves across nearshore and beyond;

F_{WI} = power of winds at the cliff face;

F_{RD} = dynamic strength of cliff material;

t = time

8.4 Relative contributions to energy transferred to the cliff

Studies of coastal cliff erosion often assess the energy that is delivered to the cliff toe directly from waves (e.g. Benumof et al., 2000; Ruggiero et al., 2001). Comparison of the net energy recorded for each of the seismic frequency bands, which are attributed here to the different environmental conditions, shows that similar amounts of net energy are transferred to the cliff from the nearshore and foreshore as is transferred by waves directly impacting upon the cliff face. Energy is transferred to the seabed over a wide area, forming a distributed seismic source, which regardless of tide height occurs at almost all times. In contrast, the cliff face surface at the inundated toe is relatively small, and the period over which this transfer occurs is tidally modulated, occurring only during high tides. The implication is that the short-term rate of energy transfer to the cliff face must be higher than that to the seabed; this is also suggested by the microseismic frequency powers (see for example Figure 4.1 and the short duration, high power HT signal compared to the long duration, lower power LP signal).

The power and energy of the four frequency bands of microseismic ground motions have been found to represent different characteristics of the energy transfer to the cliff from marine and atmospheric conditions and to have varying effects on the cliff. In the regression analysis with the rockfall data in the non-inundation zone (which occupies the largest area of the cliff face), the net energy of each seismic frequency band provided fewer significant correlations with measures or derivatives of rockfall activity, than did the corresponding frequency band power. Whereas in the inundation zone, frequency band power provided no correlations with the rockfall data yet energy of the frequency bands which represent stormy conditions produced statistically significant correlations. The results suggest that the amount of energy represents the energy available to drive marine erosive processes and the potential to degrade rock mass strength. Whereas power better represents the ground motion characteristics and relative force of impacts against the cliff which trigger rockfalls.

8.5 The nature of cliff change behaviour

In this study rockfall activity has been observed to be distributed across the entire cliff face, with limited evidence of concave notch forms or development at the cliff toe, matching observations of hard rock cliff behaviour in previous studies (e.g. Rosser et al., 2007; Lim et al., 2010a). It is notable that the data collected in this study is restricted to changes > 0.1 m of failure depth, such that discriminating between the cumulative effects of processes such as abrasion, which result in minimal cliff-normal change, from those instantaneous processes such as rockfall, which generate discrete blocks of change, remains impossible. Furthermore, this analysis remains restricted by monthly resurveys of the cliff face, which has inevitable implications for the temporal resolution of the data generated. The observed distribution of change across the whole cliff face suggests that environmental (marine and subaerial) and material properties across the cliff control the nature of rockfall activity, and the foci of these processes need not necessarily be concentrated entirely at the cliff toe.

The majority of failures recorded from the cliff face are small (80% < 0.01 m^3), but these only account for a small percentage (15%) of the total volume of material eroded. Despite occurring much less frequently, larger failures are by far the most effective in eroding the cliff face. The infrequency of large failures has most likely led to the perception that cliff change is episodic (e.g. Hall et al., 2008), however the results of this study, and the other high resolution cliff face studies that precede it (e.g. Rosser et al., 2007; Lim et al., 2010a), demonstrate cliff change across the whole cliff face to be an on-going process. Typically > 1,000 rockfalls per month have

been observed from this cliff over an area of 4,840 m^2, although most of these are small and individually do not significantly change the cliff form, or erode the coast.

The occurrence of large failures and a preceding increase in activity of rockfalls, over space and time, has been observed by a number of studies, both coastal and terrestrial (e.g. Eberhardt et al., 2004; Rosser et al., 2007; Stock et al., 2012), and has been attributed to material-controlled progressive brittle failure, the timing of which is not necessarily influenced by prevailing environmental conditions at the point of failure (Main, 2000; Petley et al., 2005). During progressive failure, rock is increasingly weakened by stress redistribution and strain accumulation until a critical strain threshold is exceeded. In this mode of failure the progression to failure is controlled by the acceleration of crack and fracture development and strain localisation within the material to form a rupture (Main, 2000). Along the stretch of coastline this study site sits within, Rosser et al. (2007) observed patterns of increases in rockfall activity and rockfall volumes preceding larger failures (> 0.157 m^3 up to > 100 m^3), suggesting a progressive mode of failure. The clustering of failures over time and space observed by this study may reflect the precursory behaviour observed by Rosser et al. (2007); however this pattern of behaviour did not culminate in the scale of larger failures observed by the other study (e.g. > 12.73 m^3).

The absence of larger failures from the site may reflect a number of controls over rockfall volumes. The physical characteristics of a slope (e.g. rock structure, slope height and rock strength) can limit the sizes of failure that occur (Barlow et al., 2012). At this site, the results of this study and others (Rosser et al., 2007; Lim et al., 2010a) have identified structure to be a particularly important control on rockfall magnitudes. The absence of large failures may also suggest that the full magnitude-frequency distribution has not been identified over the relatively short two-year monitoring period, and that to fully capture the distribution a longer monitoring period is necessary to cover the return periods of larger failures (> 12.73 m^3). Although the other studies covered similar lengths of time, they both included a more extensive section of coastline, with increased chance of capturing this final stage of a potentially larger failure.

Although the power law relationship found for the magnitude-frequency distribution had a high r^2 value of 0.99 ($p < 0.001$), the absence of larger failures may mean that this relationship does not hold for higher volume rockfalls at the site. A number of landslide studies have demonstrated that the power law relationships can be limited to the mid-range of the dataset (e.g. Stark and Hovius, 2001; Brardinoni and Church, 2004; Guthrie and Evans, 2004). This has been attributed to resolution limits of monitoring technique and the resulting inability to

capture extreme sizes of rockfalls (Stark and Hovius, 2001), or due to physical controls that can limit the sizes that occur, such as slope and material characteristics (Brardinoni and Church, 2004; Guthrie and Evans, 2004; Barlow et al., 2012). The ability of TLS to accurately monitor all rockfalls up to the resolution set by the point or grid spacing chosen however means that spatially the technique is capable of capturing the majority of the magnitude-frequency distribution of rockfalls at the site, also noted by Lim et al. (2010a) and Young et al. (2011a). Ultimately, at the small end of this distribution, without a significant increase in spatial resolution of TLS and with it a significant increase in the volume of data generated, the finest rockfalls (< 0.00156 m^3), are not captured. The absence of much larger failures from this dataset suggests that the temporal resolution of the monitoring technique is as important as its spatial resolution in obtaining a full and accurate magnitude-frequency distribution.

Although the regression analysis between the microseismic signals and rockfalls showed positive and statistically-significant correlations, the highest r^2 value was 0.58 ($p < 0.001$). The results show that although the environmental conditions represented by the microseismic signals do influence rockfall activity, there are other influences, or purely noise in the data, that need to be considered. It is anticipated that the low r^2 values were partially due to the low temporal resolution of the data used in the regression models (limited to the 4 - 8 week intervals between TLS scans), which necessitated degrading or aggregating the relatively high-resolution microseismic data to a single derivative at 4 - 8 week intervals. The temporal clustering behaviour observed suggests that some of the rockfalls were triggered by the progressive failure mechanism, and that this superimposition and highly concentrated period of activity in the immediate period prior to final failure, may not have been captured adequately in this experimental design.

Traditionally, cliff change has been recorded as an annual rate of retreat, calculated from long-term change in position of one selected feature of the cliff, typically either the cliff top or toe which is used to derive the erosion of the whole cliff face (e.g. Agar, 1960; Bray and Hooke, 1997; Budetta et al., 2000; Andriani and Walsh, 2007). The variability in retreat rates between the inundated and non-inundated zones of this study, and also variability between rates of the different rock types observed by Rosser et al. (2007) and Lim et al. (2010a), highlight the inappropriateness of a single retreat rate to represent a cliff or coastline behaviour. In addition to locally variable retreat rates across the cliff face with varying environmental and geological conditions, retreat rates obtained across different monitoring periods have also varied. For example this study derived very different rates as compared to a previous study at the same site, e.g. 0.0243 m yr^{-1} compared to 0.009 m yr^{-1} of Lim et al. (2010a). These two studies used

approximately the same technique, so variation in rates demonstrates considerable temporal variability, in addition to the spatial patterns observed. By implication, long-term monitoring at high frequency is needed to obtain an increasingly accurate and precise representation of coastal erosion, and to unpick the relative contribution of the various processes and mechanisms which drive this change.

8.6 The relative influence of geological and environmental controls

The temporal and spatial distributions of rockfalls obtained by this and other studies that have monitored cliff face, rather than planform, change have demonstrated that rockfall geometry and patterns and rates of failure are controlled by the combination and interaction of geology and environmental processes. The structural characteristics of the individual lithological units and their combination determine the characteristics of rockfalls. The strong geological influence on rockfall characteristics makes it difficult to isolate geological from environmental controls on cliff behaviour within this study.

The rockfall characteristics within the inundation zone, compared to the non-inundation zone, suggest a higher rate of erosion and on average larger blocks are removed by hydraulic and mechanical erosive processes driven by wave impacts at the cliff face. Correlations between the rockfalls in the non-inundation zone and modelled marine conditions suggest that either the inundation zone itself, or the direct effects of marine inundation, extend higher up the cliff. Without across site comparison, it remains difficult to differentiate this observation from the lithological dominance of the mudstone that occupies the lower 20 m of the cliff. The previous studies at the site identified the mudstone to have one of the highest rates of change of the layers within the cliff (Rosser et al., 2007; Lim et al., 2010a), demonstrating that the mudstone may in part explain the higher rate of erosion of the inundation zone. The correlations between the marine conditions and rockfall rate suggest that wave processes also partly control the rockfall characteristics in the lower parts of the cliff. The strong geological control makes it impossible to identify the relative contributions of different environmental forces on rockfall activity when only looking at a single site with one lithological structure. Undertaking a wider scale study over a much larger geographical area covering varying rock types, would enable testing of the different rock types to the full range of environmental conditions and exploration of each rock type's response. A relatively consistent physiographic setting, including foreshore geometry, local bathymetry, atmospheric and wave climates would be required. In addition laser scanning the cliffs at an increased frequency would help to constrain responses within different rock type to specific environmental forces.

8.7 Cliff erosion models

The data generated in this thesis allows accurate quantification of cliff change and environmental drivers, and has generated results that challenge the assumptions of many established models of coastal cliff erosion. Both datasets, and the correlations between them, demonstrate that environmental conditions across a wide area influence the occurrence of cliff rockfalls across the whole cliff face.

The results presented demonstrate two fundamental problems with the present common conceptualisation of coastal cliff erosion. First, the widely-used coastal erosion models that consider tidally-modulated wave energy delivery and erosion of the cliff toe (e.g. Sunamura, 1977; Carr and Graff, 1981; Trenhaile and Layzell, 1981) have been shown, at least in this instance, to be overly simplified. Energy delivery has been shown here to occur throughout the tidal cycle, and it is evident that a comparable net flux of energy from non-wave impact forces is generated by mechanisms not considered in erosion models. Fundamentally, the question arises as to whether this constant delivery of energy is effective as an erosive agent. Second, the assumption that the rate of concave notch development at the cliff toe directly drives coastline retreat, via a process of cantilever collapse of the cliff rock mass, is also contrary to observations made from this monitoring data.

The absence of notches at the study site implies that toe erosion either: a) has insufficient capacity to cut a notch arising from the balance between rock strength and marine forcing; b) only forms notches which are rarely persistent, and so are not preserved and so are not a common coastal feature; or, c) cuts the cliff toe, but the cliff rock mass structure does not have sufficient integrity to support a visible notch structure, and so collapses or develops upslope in a different mechanism. The results of this study suggest that the notch model of erosion has received insufficient analysis, most probably due to a lack of field evidence or validation of notch formation. Notching does however provide a clear explanation for widely observed cliff behaviour, particularly when the ability to quantify and test this model has been impossible due to a lack of suitable monitoring techniques. The importance of notches and cantilever failure is therefore likely to be over-emphasised. In the absence, until recently, of methods to quantify cliff-wide behaviour and environmental conditions at the cliff itself, the notch model has continued to be used widely to explain erosion, and as the basis of cliff erosion models (e.g. Sunamura, 1977; Budetta et al., 2000; Walkden and Hall, 2005). The results of this study indicate that a wide range of processes operate at coastal cliffs resulting in a more complex distribution of erosion.

Within models that are based on toe erosion, the vertical extent at risk from direct erosion by wave impacts is determined by a calculation of tidal inundation duration. Using this approach, the wave energy delivery, which is deemed to approximate erosion, is derived for all elevations through the tidal range, as a function of cumulative time for which the tide is at or above any given level (Trenhaile and Layzell, 1981; Carr and Graff, 1982). By adding modelled wave and set-up heights to the tide height to produce an inundation model for the whole foreshore and cliff face, this study derives a significantly different distribution of energy by time and elevation to that derived from the tidal cycle alone. Positive correlations between the combined influences upon sea level and the rockfall data show that the tidal duration model does not represent the distribution of erosion driven by wave impacts. In addition, the correlations between the microseismic signals that represent wave conditions across the near and foreshore and the rockfall data in the upper cliff section imply that waves delivering energy to the cliff can trigger rockfalls way above the inundated zone across the whole cliff face. Fundamentally, the results show that tidal inundation duration models do not provide an accurate representation of energy transfer as a method of understanding cliff erosion.

The findings of this study indicate that the cliff toe dominated model of coastal erosion, and the use of tidal inundation duration, represent an oversimplified consideration of cliff behaviour. On coasts with sufficiently aggressive marine conditions paired with weak cliff lithologies, the overriding dominance of toe erosion may act to mask the observations made here on relatively hard cliffs, yet it is likely that, to a greater or lesser extent, similar processes to those which have been observed here must act in the majority of coastal cliff systems. A full understanding of coastal erosion can only be obtained from monitoring the whole cliff face, implying that focus should be broadened beyond purely a toe erosion based assessment of processes acting to drive cliff erosion.

To explore further the range of processes identified by this study to be acting on coastal cliffs and the cliff response, the following monitoring set-up is recommended:

- TLS monitoring of cliff erosion. The highest temporal resolution used so far is monthly, monitoring the cliffs at a higher temporal resolution e.g. fortnightly, would reduce the superimposition of rockfalls over time. Using a lower point spacing e.g. < = 0.05 m, would enable smaller rockfall volumes to be quantified.
- Monitoring of wave conditions across the foreshore and at the cliff toe using pressure sensors would provide a more accurate representation of wave transformation across shallow waters than produced by the model. A sampling rate of 2 Hz is suggested to capture the full spectrum of ocean waves.

- Filming or time series photography of the lower section of the cliff during high tides would enable clarification of the actual extent of the inundation zone and the reach of splash up the cliff face. Currently no quantification of this has been made, which has resulted in highly varied estimates of the height of the inundation zone.
- Monitoring of wind conditions at the cliff top would be desirable. In this study a station 3 km away has been used; it is anticipated wind conditions vary across that distance, as suggested by Lim et al. (2010b). In addition offshore wind conditions, sometimes monitored at wave buoys, would be interesting to compare with the cliff top values to see how well they represent the wave-generating wind conditions. Higher resolution sampling, at around 1 - 5 minutes would provide a more accurate representation of conditions than the hourly resolution provided by the Met Office.
- A cliff top, broadband, three component seismometer should be used to monitor microseismic ground motions. This study has demonstrated that one seismometer is sufficient to explore the range of microseismic ground motions affecting a coastal cliff. A less noisy seismometer which is sensitive to lower periods ~200 s, would produce a more accurate representation of the long-period wave frequency band. Combined with the wave pressure sensors this would provide more information on this largest source of net energy transferred to the cliff. A sampling rate of 100 Hz would enable capture of the high frequency impact signals generated at the cliff face.

8.8 A new conceptual model of hard rock coastal cliff erosion

The results of this study have demonstrated that there are a range of marine and atmospheric forces acting upon coastal cliffs. Whilst much can or could be learned from studies of terrestrial rock slopes, it is clear that coastal slopes present their own set of challenges for study. The influence of each of the different forces on the cliff varies both up the cliff profile (and potentially along the coast, although this was not studied here), as does the cliff geology. Each of these factors determines at any given location the geometry, frequency and timing of erosion.

The combination of the microseismic and TLS rockfall datasets provides insight into cliff erosion and the relative role of a range of marine and atmospheric processes. The quantification of a wide range of environmental forces, a measure of their relative efficacy, and the detail in rockfall characteristics, provides the opportunity to examine the environmental and material controls on cliff behaviour in more detail. A new framework of the mechanisms and processes controlling the observed cliff behaviour is presented below, which is based on observations of

the relative importance of environmental and geological controls on both rockfall activity and rockfall characteristics (Figure 8.1). This model builds on those that have already moved beyond an emphasis on the cliff toe (e.g. Adams et al., 2005; Rosser et al., 2007). The model adds in elements that have been identified from the findings of this study to consider the diversity of mechanisms and processes controlling cliff erosion.

1. The microseismic ground motions demonstrate that environmental conditions at the coast result in dynamic loading of the cliff, also observed by Adams et al. (2005) and Young et al. (2011b) (Figure 8.1). This loading occurs across a wide range of frequencies, which correspond to those of the environmental conditions acting on the cliff and foreshore. This loading results in ground motions in different directions, both in the horizontal plane and also vertically. Dynamic loading of rock is known in some systems to result in the gradual deterioration of rock strength (Sunamura, 1992; Main, 2000). The loading by marine and environmental forces near and at the cliff is anticipated to generate, albeit it small, stresses within the cliff rock, which over time may result in the formation and development of micro-fractures, as proposed by Adams et al. (2005). With repeated loading these micro-fractures may propagate through the intact rock, gradually decreasing the bulk rock mass strength. The cyclical loading effects of marine and atmospheric forces near and at the cliff therefore have the potential to weaken the cliff material and increase its vulnerability to failure (Sunamura, 1992; Adams et al., 2005; Brain et al., 2010). The spatial distribution of the intensity of this process may reflect the attenuation of seismic energy through the cliff, which may in turn be reflected in the rockfall distribution. This study has been at a necessarily insufficient duration and resolution to obtain data to assess this process, but this is clearly an area for future research.
2. Weathering and marine processes close to or directly at the cliff face can deteriorate the rock surface by accelerating micro-fracture growth via a number of mechanisms (Figure 8.1): Temperature and moisture fluctuations result in expansion and contraction of the rock generating stress and strain (Stephenson and Kirk, 2000b); freeze-thaw results in the expansion and contraction of water within the rock opening and exploiting cracks (Matsuoka, 2008); the growth of marine derived salt crystals can again exploit cracks (Dupperet et al., 2005); the compression of air and water into voids under impacts by the sea forces cracks to grow, may create new cracks or may have sufficient force to detach blocks of rock along other discontinuities such as joints, and result in rock damage and strength deterioration (Sunamura, 1992).
3. In addition to representing the environmental dynamic loading of the cliff, the microseismic signal detected by the cliff top seismometer may represent another mechanism capable of

damaging the cliff rock mass and therefore enhancing the rock preparation for failure. As seismic waves travel through rock they generate stresses. Due to the imperfect elastic nature of the material, energy is attenuated to the surrounding rock, known as anelastic damping (Stacey et al., 1975; Lowrie, 1997). This has the potential to generate strain and therefore damage accumulation within the coastal rocks through which the microseismic waves travel (Figure 8.1).

4. Points 1 – 3 above represent relatively long-term iterative processes which act to weaken the cliff, increasing susceptibility to erosion. The positive correlations between the microseismic data and rockfalls from the upper parts of the cliff suggest that there may also be a more immediate effect on the timing and magnitude of rockfalls. It is anticipated that the ground motions can also directly trigger the removal of close-to-failure or highly fractured, loose, rock (Figure 8.1). This appears to extend across the full spectrum of ground motions observed, not just the high-frequency shaking caused by waves and wind impacts against the cliff directly, but also from the longer period swaying caused by waves traversing across the near- and foreshore.
5. Weathering and marine processes at the cliff face also physically detach cliff material via wind shear, hydraulic pressures (which drive quarrying), air compression in cracks, mechanical abrasion aided by entrained sediments and detachment via mechanical weathering processes of freeze thaw, wetting and drying, temperature stress and salt crystal growth (Figure 8.1). The relative importance of weathering versus marine processes is unclear; the rockfall distribution across the two zones monitored here show that the very different environmental conditions in these zones combine to act as effective triggers of rockfall activity. The near-vertical profile of the cliff suggests that erosion rates of the inundation and non-inundation cliff sections equate over time, implying that the marine and weathering processes are effectively equivalent. What is not clear from this dataset is how the processes in the two zones interact and underpin the connectivity between the erosion of the cliff toe and the retreat of the cliff top.
6. Stress re-distribution post-failure results in the extension of micro-fracturing and the area of rock that is damaged, extending the area of cliff face vulnerable to failure (Figure 8.1). Stress re-distribution and resulting crack propagation has been observed to result in a long-term series of failures extending outwards from an initial failure zone by Stock et al. (2012). This has also been attributed to causing patterns of precursory failure observed in coastal cliffs (Rosser et al., 2007). Moreover, failures triggered by environmental forcing can remove supports for over-lying material, the stress re-distribution from which can result in an upwards propagation of failure (Krautblatter and Dikau, 2007; Young and Ashford, 2008).

7. Strain accumulates within the cliff rock mass due to stresses generated by the range of environmental forces (Sunamura, 1992; Selby, 1993), and the re-distribution of stresses as a result of continuing failure (Stock et al., 2012). Eventually strain within the rock will reach a critical threshold, beyond which the rate of failure development is driven by the progressive brittle failure of the tertiary stage of brittle rock deformation (Figure 8.1) (Petley et al., 2005). Progressive failure is dominated by the rate of fracturing of the rock and is believed to result in increased precursory rockfalls in the build up to a larger-scale failure (Rosser et al., 2007; Styles et al., 2011). Progressive failure may well be a hidden cause of failures that appear to occur without a direct environmental trigger.

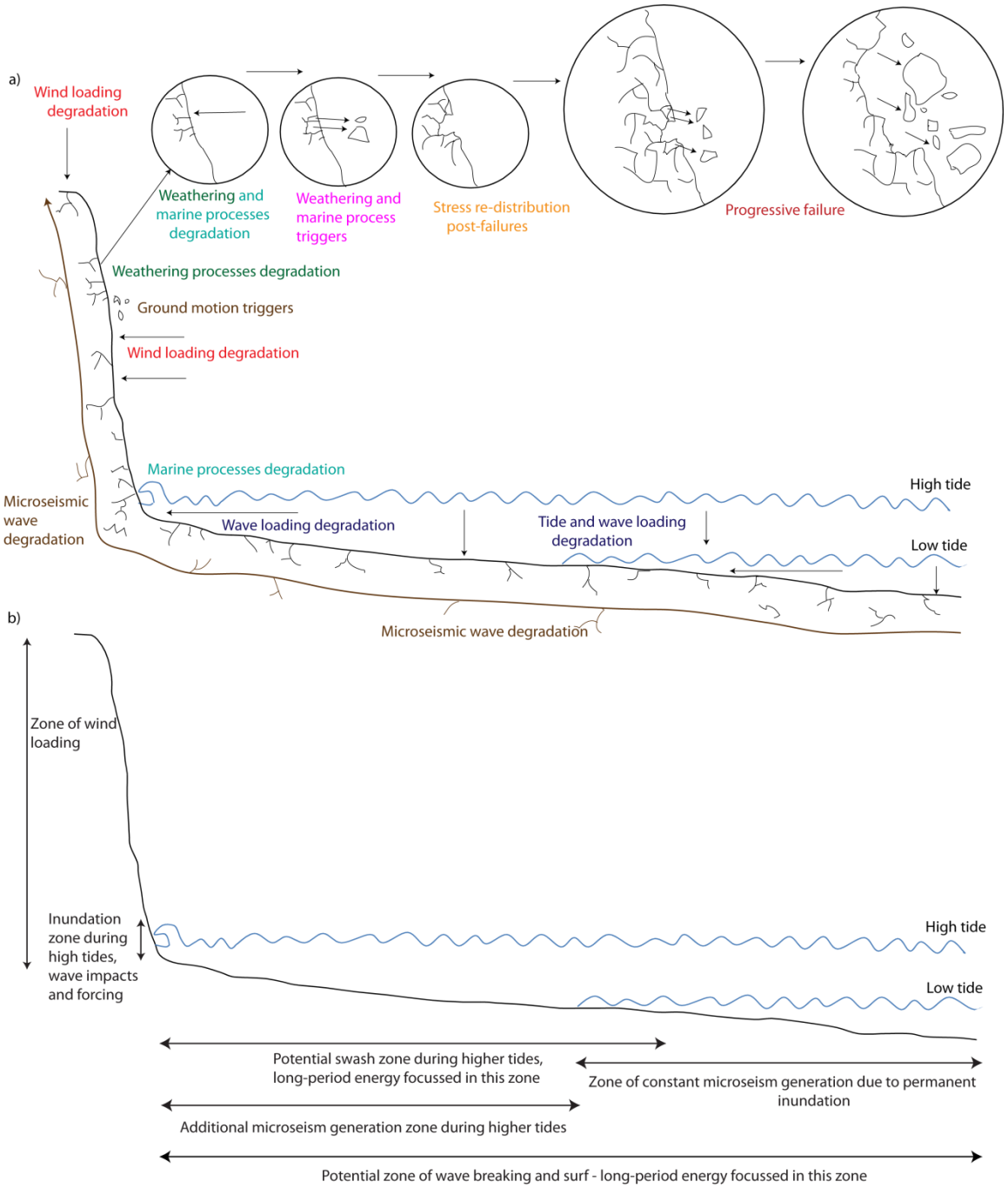

Figure 8.1: Mechanisms and processes driving cliff failure (not to scale). a) Environmental forcing on the cliff and across the nearshore generates stresses within the rock which result in strain build-up via micro-fractures which decrease rock strength and lead to failure. Environmental forces that damage the rock are: Dynamic loading of the cliff and foreshore by tides and waves; Weathering and marine processes; Microseismic waves. Rockfalls are triggered by: Ground motions caused by environmental forcing; Weathering and marine processes. Following failures stress re-distribution extends the damaged area of rock. Once a critical threshold of strain is exceeded, strain accumulation accelerates until failure occurs. b) Zones where different environmental processes operate.

The model illustrates mechanisms that both prepare the rock for failure and that trigger failure i.e. determine the rockfall timing; environmental conditions contribute to rockfall activity via both mechanisms (Figure 8.1). Mechanisms can be material-controlled by the deformation characteristics of the rock (mass), or environment-controlled. The influence of the different mechanisms can extend across the whole cliff face (e.g. subaerial weathering and wind loading), or can vary up the cliff profile (e.g. marine processes) (Figure 8.1 and Table 8.1). The different mechanisms also operate over various timescales (Table 8.1). Ultimately, the effectiveness and relative importance of the different mechanisms and processes within the model will depend on the combinations of geology and environmental conditions and the nature of their interactions.

Table 8.1: Characteristics of the mechanisms and processes controlling cliff change behaviour.

Mechanism/process	**Control (environmental/ material)**	**Preparation for/Trigger of failure**	**Location where effective**	**Timescale operates over**
1. Dynamic loading of cliff, nearshore and foreshore by environmental forces	Environmental	Damage/ preparation	Whole cliff	Same periods as ground motions of the different sources, also seasonally controlled
2. Weathering and marine processes	Environmental	Damage/ preparation	Weathering – greater influence in upper cliff Marine – influences lower cliff	At frequency of environmental events e.g. semi-diurnal/ diurnal/ seasonal variations
3. Microseismic waves	Environmental	Damage/ preparation	Whole cliff	Same periods as ground motions of the different sources, also seasonally controlled
4. Cliff ground motions	Environmental	Trigger	Upper section of cliff	Same periods as ground motions of the different sources, also seasonally controlled
5. Weathering and marine processes	Environmental	Trigger	Weathering – greater influence in upper cliff Marine – influences lower cliff	At frequency of environmental events e.g. semi-diurnal/ diurnal/ seasonal variations
6. Stress re-distribution	Material	Damage/ preparation	Whole cliff	Sporadic with failures
7. Progressive failure	Material	Damage, Trigger	Whole cliff	Gradual, unknown temporal controls, accelerates as closer to failure, return period of larger failures >2 years

Chapter 9: Conclusion

9.1 Conclusions

The conclusions of this study are presented in the context of the five research objectives, set out at the start of the thesis.

- To quantify environmental forces acting on a coastal rock cliff, using microseismic ground motions.

A two-year dataset of coastal cliff microseismic ground motions has been collected using a cliff top broadband seismometer. Four different frequency bands of ground motions have been identified (Figure 4.1), which each represent forcing from specific marine and atmospheric conditions, and the associated processes that they drive. Wave impacts at the cliff toe during high tides (Figure 6.5), and winds interacting with the cliff face (Figure 6.3) generate high-power, high-frequency cliff shaking or ringing. Longer period ground motion was attributed to ocean waves of gravity (Figures 6.9 and 6.11) and infragravity (Figure 6.15) wave periodicities, across the offshore, nearshore and foreshore.

Microseismic monitoring is able to quantify the relative forcing from the different sources and the results demonstrate that greater energy is transferred to the cliff from infragravity waves across the foreshore than from wave impacts at the cliff toe although the amount from both sources is relatively similar (Figure 6.17). Although wave impacts at the cliff toe are commonly cited as the most important driver of cliff erosion, until now a method to test this assumption has not been available. If significant as a geomorphic agent, infragavity waves hold significant potential for degrading cliff material, which may act as a catalyst on the rate of cliff erosion. However, the high concentrated rate and net energy transfer by wave impacts makes wave impacts potentially more erosively effective, as either a driver of rockfalls or in iteratively degrading cliff material strength. The measurement of this relative forcing has allowed the distinction of the relative timing, duration and magnitude of these processes, which are commonly debated, but have not until now been assessed in rocky coast geomorphology.

- To quantify cliff erosion using high-resolution terrestrial laser scanning.

The results produced by the monitoring of cliff change using terrestrial laser scanning (TLS) build upon the findings of previous studies at the site that have applied similar techniques (e.g. Rosser et al., 2007; Lim et al., 2010a). The rockfall volume dataset demonstrates that erosion across the observed range of rockfall magnitudes is sourced from across the entire cliff face (Figure 7.2). Although the majority of rockfalls are small (< 0.01 m^3) (Figure 7.7), the larger, less

frequent failures (> 0.1 m^3) do the most geomorphic work. There is an absence of toe notching and resultant cantilever failure of the cliff rock mass at the site, which together with the near-vertical profile, suggests erosion at the toe propagates quickly vertically due to the re-distribution of stresses as and when material is removed. The clustering of rockfalls over time and space (Figure 7.2) suggests progressive failure may play an important role in the failure and release of rockfalls. Together with the apparent rock-type dependence of rockfall geometry, results indicate a strong geological control on cliff erosion (Figure 7.2). The observed nature and distribution of rockfall indicates that controls on erosion are invariably far more complex than is perhaps implied by the more conventional models of cliff erosion; particularly those focused on erosion of the cliff toe alone.

- To examine the control of marine and atmospheric conditions and processes on rockfall activity.

Regression analyses between the frequency and characteristics of the monitored rockfalls and the energy and power of ground motion frequencies has provided insight into the dominant environmental controls driving coastal cliff erosion (Tables 7.2 – 7.5). Again these findings support the observation that the nature of cliff erosion is far more diverse than suggested by traditional models. Relationships between the power of each of the monitored ground motion frequency bands and rockfall activity through the monitoring period demonstrate that in addition to wind and wave conditions directly at the cliff face, marine conditions across the foreshore, nearshore and offshore appear to bear some control on the nature of cliff erosion (Table 7.4). The wind and wave cliff conditions represent erosive processes acting directly on the cliff face and therefore potentially represent processes triggering failure. Wave conditions distal to the cliff are indicative of the iterative dynamic loading effect driven by long-period ground motion, and the degrading effect on rock strength, contributing over time to weakening and failure preparation. In addition, the correlations with rockfall occurrences suggest that ground motion generated by the longer period wave conditions upon the foreshore and at a distance, and higher frequency impacts of waves and winds at the cliff face, can themselves directly trigger rockfalls (Table 7.4).

This study also modelled regional-scale tide and wave datasets to estimate conditions across the nearshore, foreshore and at the cliff face to better constrain the marine conditions around the cliff. Whilst offshore wave transformations accounting for local bathymetry and beach / foreshore characteristics have been used for softer rock cliffs (e.g. Benumof et al., 2000; Ruggiero et al., 2001), wave transformation modelling has not previously been used in hard rock cliff erosion studies. These modelled datasets have provided improved understanding of the

marine conditions at the site and variations over time and space and have shown the unadjusted regional-scale datasets used by Rosser et al. (2007) and Lim et al. (2010a) to poorly represent conditions near the cliff. The modelled marine datasets were found to better relate to the observed rockfall data than the unadjusted regional-scale datasets (Tables 7.3 and 7.4), and therefore were able to provide some explanations of the marine conditions that control cliff erosion.

The modelled marine conditions indicate that tidal inundation models do not accurately represent where wave energy, and therefore where wave erosion, is focussed on the cliff face through the duration of the tidal cycle (Figures 5.20 and 5.21). This has significant implications, as tidal inundation models often form the basis of cliff erosion models, the geometry of which define the cantilever collapse and cliff retreat rate. The vertical distribution and temporal inundation up the cliff face were greatly altered once the modelled wave and set-up heights were added to the monitored tide conditions (Figure 5.21).

Rock cliffs respond immediately to wave impacts and do not react to environmental forcing / erosive processes as slowly as traditionally perceived. One of the preconceptions which appears to have diminished the number of studies of hard rock cliffs has been the assumption that rates of change are imperceptibly slow, and essentially stochastic. However in this study, strong relationships between modelled marine conditions at the cliff toe and rockfall occurrence within the inundated zone (Table 7.3) demonstrate that hard rock cliffs can respond directly to apparently short term variations in environmental conditions, as is evident for soft rock cliffs where response to stormy marine conditions is more immediate. In addition these relationships demonstrate that hard rock cliffs bear the imprint of these erosion processes in their geometry. From the relationships observed, and in particular with the high number of small rockfalls observed to occur each month from across the whole cliff face (Figure 7.2), it is apparent that hard rock cliffs change much more frequently than previously believed, albeit at small scales.

- To establish the viability of using microseismic ground motions as a proxy for environmental conditions and processes acting on coastal rock cliffs, and to explore controls on cliff erosion.

The results of this study demonstrate that microseismic motion of coastal cliffs provides a measure of marine and atmospheric forcing at the coast. Critically this study has illustrated the wide range of sources that drive this motion. As the different frequency bands of ground motion are effectively proxy measurements of the various environmental conditions, obtaining this form of data overcomes the problems of monitoring these conditions in dynamic and often

inaccessible coastal cliff environments. Combined with high-resolution TLS monitoring of erosion, the microseismic ground motion data has provided insight into timing, magnitude and frequency of the environmental controls of cliff erosion. The ability to quantify processes over an extensive area has also identified previously unconsidered potential controls on erosion, that have not been articulated in previous studies using regional-scale environmental monitoring datasets alone. These results demonstrate that the combination of high-resolution monitoring techniques holds potential for further exploration of environmental and material controls of coastal cliff erosion.

Exploration of the ground motion frequency power and energy indicate both of these metrics represent different characteristics of the environmental conditions that generate ground motion. Power best characterises environmental processes represented by the specific frequency bands, providing several significant correlations with rockfall character and occurrence (Table 7.4). This finding suggests that the rate of energy transfer, as a measure of ground motion, is more significant in determining the timing of rockfall failure. Net energy however is believed to be more representative of the preparatory effects of ground motions on the rock, as a descriptor of the amount of energy available to drive erosive processes and the potential to degrade rock strength. Exploring both the ground motion frequency power and energy has provided further insight into how the processes they represent interact with cliff material, and therefore the mechanisms of energy transfer to the foreshore and cliff rock. This has enabled consideration of the likely failure mechanisms and highlights the necessity to explore different measures of cliff ground motion.

- To develop a new conceptual model of the environmental processes and failure mechanisms that control coastal cliff erosion.

The results of this study, obtained by the high-resolution monitoring of cliff microseismic ground motion, rockfall and modelled nearshore and cliff face marine conditions, indicate that the current dominant conceptual model of the environmental controls of cliff erosion and cliff response is over-simplified, based on the following key findings:

1) A range of marine and atmospheric conditions across a wide area are important controls of cliff erosion, not just wave impacts at the cliff toe (Tables 7.2 – 7.5), and these controls can contribute via both preparation for, and triggering of, failure;

2) Rockfalls are distributed across the whole cliff face and failure mechanisms are more diverse and complex than toe notching and cantiliever collapse of the rock mass, which were not observed at the site (Figure 7.2);

3) Tidal duration models which are commonly used to define and delimit the inundation zone at the toe of the cliff were found to be inaccurate, with modelled sea conditions combining tides, waves and set-up heights producing a very different inundation duration (Figure 5.21). Further, this revised dataset correlates more strongly with rockfall occurring in the inundation zone (Table 7.3).

From the results produced by monitored and modelled datasets of this study a new conceptual model of the environmental processes and failure mechanisms that control coastal cliff erosion has been produced (Figure 8.1). The model identifies that processes driven by wave impacts and wind forcing at the cliff face, primary and double frequency microseisms across the nearshore and offshore, and long-period infragravity waves in the nearshore and particularly across the foreshore, transfer energy to the cliff that over varying temporal scales result in erosion of the cliff. Within the model, the loading effects of these processes on the cliff are anticipated to produce stresses and micro-fracturing of the cliff rock mass, degrading its rock strength and preparing the rock for failure. Wind and wave processes at the cliff face are capable of directly triggering failures, in addition the ground motions themselves may trigger the removal of highly fractured or weathered loose material. The model also considers progressive failure of the cliff due to stress re-distribution and strain accumulation, with final failures controlled by the acceleration of the final stage of brittle failure once critical strain thresholds have been exceeded. The processes represented by the different ground motion frequency bands are anticipated to have varying degrees of geomorphic effectiveness, however these need to be tested.

9.2 Recommendations for further research

Long-period ground motion that represents swell and infragravity waves have proven to transfer significant amounts of energy to the cliff, even during low tides when the cliff face is dry. It is recommended that these frequency bands are examined further, critically by using seismometers with a frequency response that extends to these longer periods to allow quantification of the full signal power spectrum. This research indicates that a maximum frequency roll off at 200 Hz would be best suited for this application.

TLS has again been demonstrated an invaluable technique in monitoring change across steep, high and unstable rock cliffs. More frequent (fortnightly) TLS monitoring intervals, using a higher-resolution point spacing, will enable further examination of the rockfall characteristics, providing data of smaller scales of rockfalls and a more accurate estimation of failure timings

and sequencing. An enhanced level of detail may also permit the differentiation of various process mechanisms, via for example identification of abrasion, removal of platelets or block detachment, based upon the morphology of change. Both environmental and geological controls on cliff erosion have been observed in this study, and separating their influences has proven challenging. It is recommended as a result that further monitoring across a wider stretch of coastline is undertaken, which should incorporate cliff sections of varying geology, and ideally exposure to the variety of environmental conditions, as a function of climate or variable wave conditions. Continuing to build up the long-term erosion dataset will allow further tests of the magnitude-frequency relationship of rockfalls, which has proven valuable in forecasting erosion rates by accounting for events of all possible scales, and particularly to characterise the likelihood of the distribution of large failures, which are commonly those which are hardest to manage and mitigate.

Monitoring cliff change at a higher temporal and spatial resolution, combined with continuous microseismic monitoring, will enable more detailed examination of the direct environmental controls on cliff erosion. More effectively aligning the derivatives of the microseismic data to a higher monitoring frequency with laser scanning will help to distil the more immediate cliff response to local variations in environmental conditions and resulting processes. Usefully, data of the type generated in this thesis, and the variability contained within has the potential to be used to appraise the potential long-term response of the coast to future variations in sea level and / or storminess.

In this study the modelled marine conditions provided an estimation of the conditions at the cliff toe and the elevation of the cliff face directly inundated and hence exposed to marine processes. However, the accuracy of the height of the modelled inundation zone derived in this study is questioned by the correlations obtained between cliff toe marine conditions and rockfall occurrence in the non-inundation zone above. To consider this zone more carefully and to gain further understanding of the direct interactions between the sea and cliff face, wave and water level conditions need to be monitored directly at the toe. The combination of these types of data, and microseismic monitoring, would provide an insightful monitoring network for further examining the interactions between environmental conditions and cliff erosion.

Traditionally, energy is assumed to be dissipated across foreshores as waves shoal, break and form surf and swash. The results of this study imply that energy released from waves as they dissipate across the foreshore is not lost, but is at least in part transferred through the foreshore rock platform and beyond. As a result, in terms of driving microseismic ground motions, the foreshore is a highly important source of energy which then transfers to the cliff.

Wave energy has been widely studied in its role in downwearing foreshore rock platforms, and it is highly likely that insight into the spatial variability of foreshore downwearing may be gained from an assessment of the spatial distribution of energy and intensity of coastal microseismic ground motions to better understand the marine controls of foreshore erosion. The positioning of a seismometer would depend on how much of the foreshore is inundated, but in examples such as the study site where the foreshore is completely inundated at high tides, it is anticipated that combined with monitoring of wave conditions across the foreshore, a cliff top microseismic dataset would be suitable.

The microseismic data has demonstrated the significance of the dynamic loading of coastal cliffs by the sea and other forces, and that it potentially plays an important role both as a trigger of rockfall but also, it is anticipated, as a potential source of cliff rock degradation. This however can only be speculated from this study, and it is evident that significant work is now needed to test the role of environmental loading of coastal cliffs in damaging and accelerating the preparation of rock material for failure, and therefore to further understanding of the mechanisms controlling rockfalls.

The microseismic data demonstrates that loading of the cliff by environmental forces, largely the sea, results in both horizontal and vertical ground motions. The direction of loading and resulting ground motions will result in varying stress paths within the rock. The observed simultaneous loading by numerous sources, in different directions, suggests that stress paths within the rock have the potential to be highly complex. The actual nature of the resulting stress paths, the strain implications and potential damage of this are unknown and lab testing of this observed simultaneous multi-directional loading is needed to examine the rock strength implications. In addition the removal of material from the cliff face acts as an unloading mechanism with the potential to change horizontal stresses in the cliff, with stress magnitudes varying depending on rate and magnitudes of failures (Brain et al., 2010), and depending on where the failure occurs relative to a point of interest. Significant work exploring the dynamic loading and effects on stress path and strain accumulation is needed to be able to unravel these effects of environmental forces acting on the cliff.

Appendix 1a: Probability plots of PSD for seismometer 2 for the period 14/05/10 – 05/06/10, for components: a) E (horizontal E-W); b) N (horizontal N-S); c) Z (vertical). Grey lines denote Peterson's (1993) high and low noise models. The dashed black line denotes mean probability.

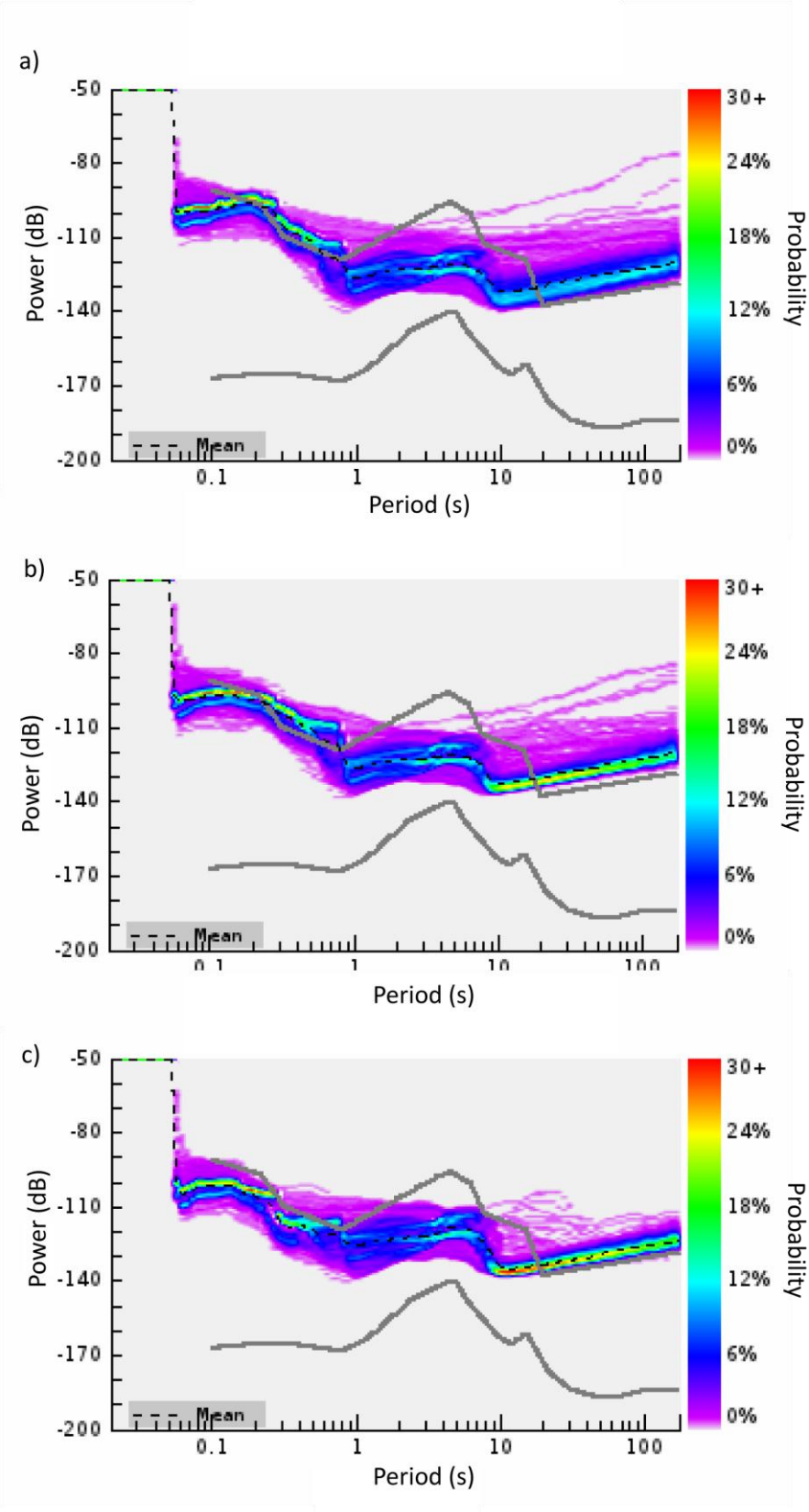

Appendix 1b: Probability plots of PSD for seismometer 3 for the period 14/05/10 – 05/06/10, for components: a) E (horizontal E-W); b) N (horizontal N-S); c) Z (vertical). Grey lines denote Peterson's (1993) high and low noise models. The dashed black line denotes mean probability.

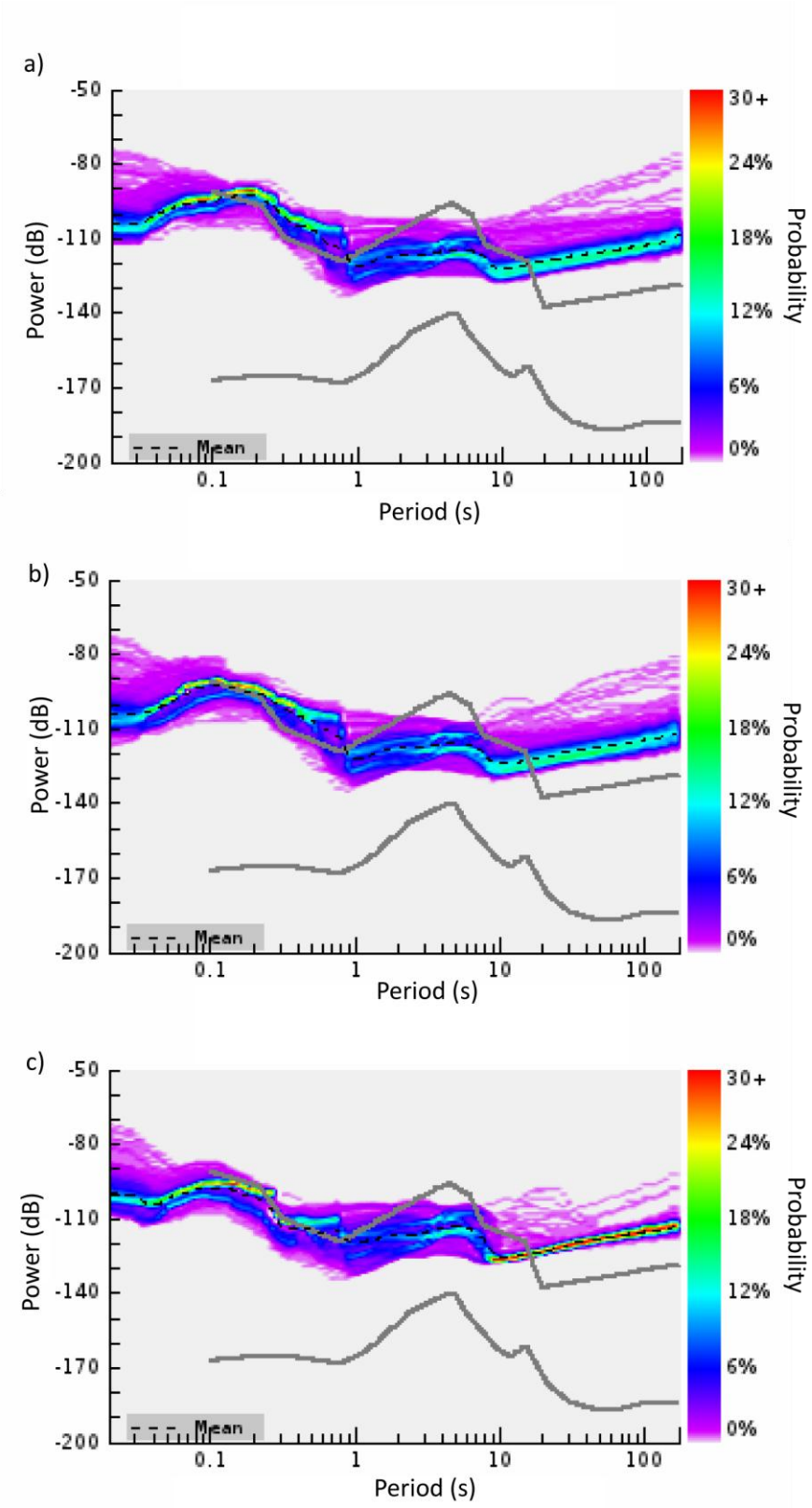

Appendix 1c: Probability plots of PSD for seismometer 4 for the period 14/05/10 – 05/06/10, for components: a) E (horizontal E-W); b) N (horizontal N-S); c) Z (vertical). Grey lines denote Peterson's (1993) high and low noise models. The dashed black line denotes mean probability.

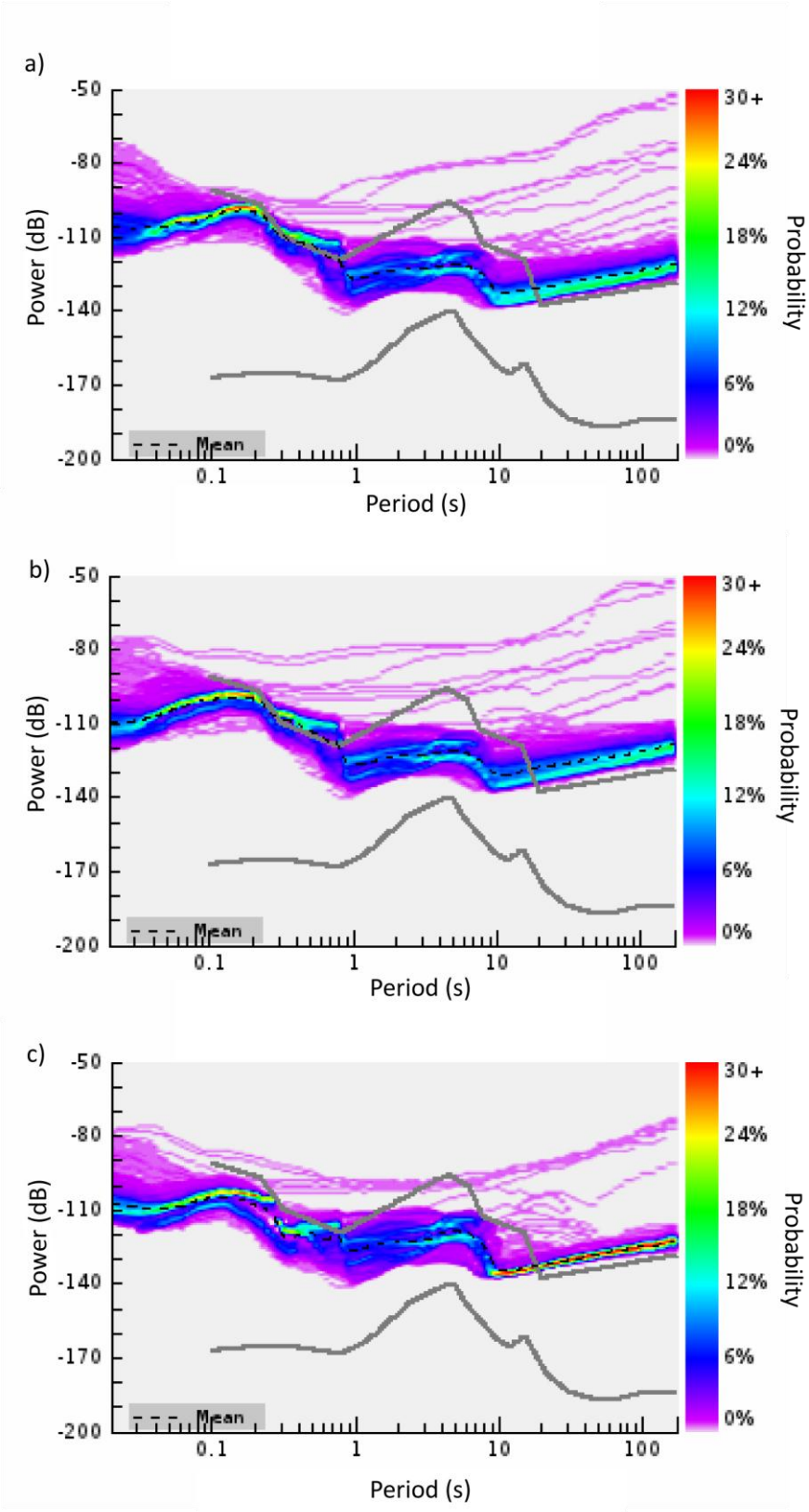

Appendix 1d: Probability plots of PSD for seismometer 5 for the period 14/05/10 – 05/06/10, for components: a) E (horizontal E-W); b) N (horizontal N-S); c) Z (vertical). Grey lines denote Peterson's (1993) high and low noise models. The dashed black line denotes mean probability.

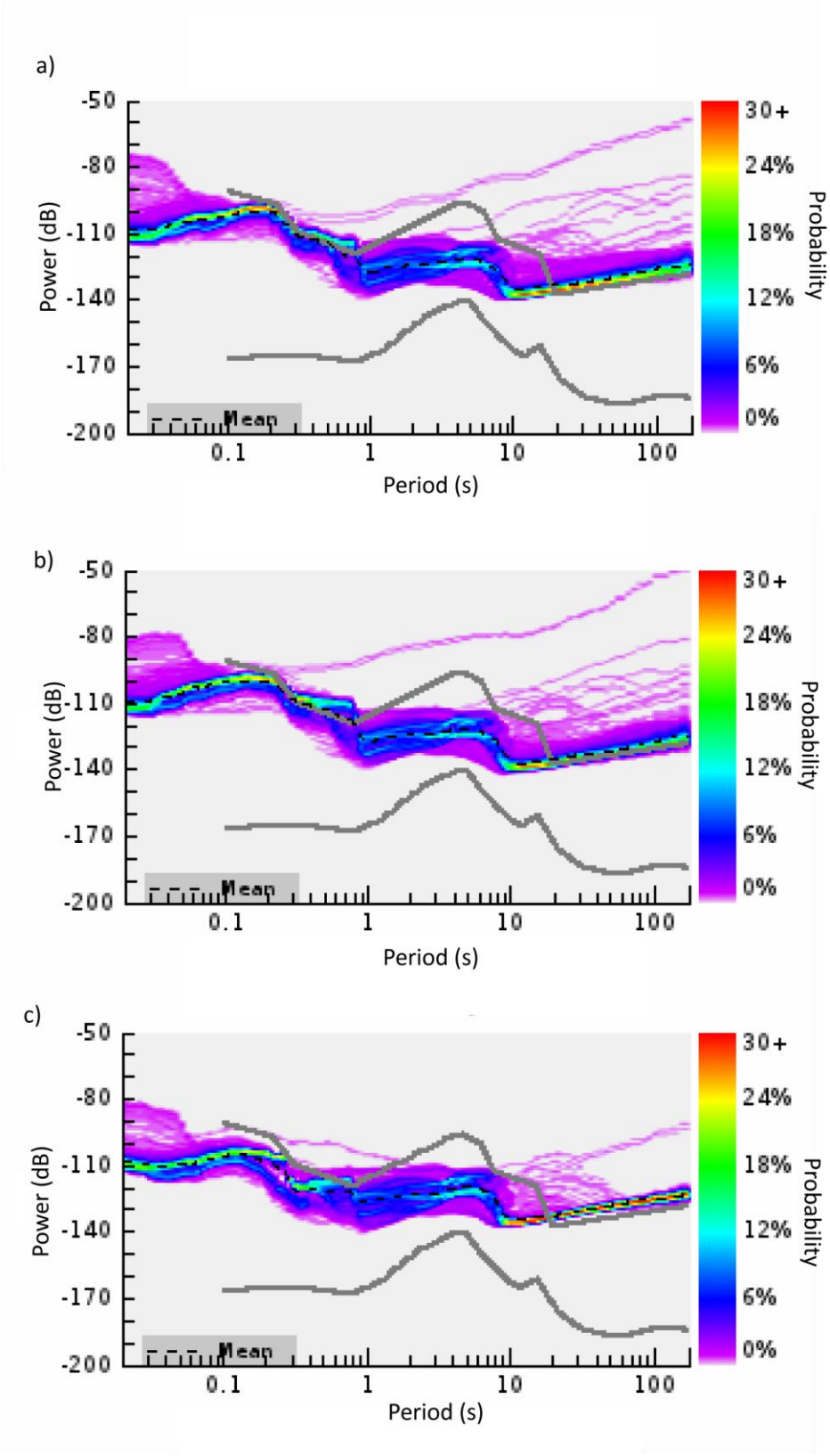

Appendix 2: Guralp script to read raw .gcf files into Matlab

```
function [samples,streamID,sps,ist] = readgcffile(filename, streamID)
% ReadGCFFile
%
%   [SAMPLES,STREAMID,SPS,IST] = READGCFFILE(filename, streamID)
%
%   Reads in the specified GCF formatted file, and returns:
%     Samples - an array of all samples in file
%     Stream ID (string up to 6 characters)
%     SPS - sample rate of data in SAMPLES
%     IST - start time of data, as serial date number
%
%   example:
%   [samples,streamID,sps,ist]=readgcffile('test.gcf');
%   streams=readgcffile('test.gcf','list');
%   [samples,streamID,sps,ist]=readgcffile('test.gcf','TESTZ2');
%
%   M. McGowan, Guralp Systems Ltd.
%   2004/09/23 M. McGowan (support@guralp.com)
%     Added support for multiple streams in a GCF file, where the user can
%     specify which stream ID they want to extract. See 'streamID' input
%     parameter. This is optional - if ommited, it will use the first
%     streamID it finds. Note that it IS case-sensitive - all IDs should
be
%     uppercase. If StreamID is a cell array of strings, this function
will
%     return array structures containing data for all streams specified.
%     [SAMPLES,STREAMID,SPS,IST] = READGCFFILE(FILENAME, 'list')
%     Specifying 'list' for the streamID will return a cell array of
strings,
%     one string for each streamID found in the file. This can be used to
%     iterate through each streamID in the file to read all the data
contained
%     in the file. For an example, see the 'plot' option.
%     READGCFFILE(FILENAME, 'plot')
%     The 'plot' option is an example of reading all streams in a file and
%     displaying them.
%
%     If the specified stream is a status stream, 'samples' will return an
%     array of numbers which can be converted into text using
%     char(samples').
%
%     Modified code to cope with gaps, overlaps and out-of-sequence data.
%     Uses the first block timestamp as a reference, so will not return
any
%     data in the file that has a timestamp older than the first
%     block in file.
%     In the case of an overlap, the data found further through the file
will
%     overwrite the data read earlier.
%     Where a gap exists, it will be padded with sample values of NaN.
%
%   2008/11/13 M.McGowan (support@guralp.com)
%     Updated plotfile routine - only plots data streams (sps>0), and
plots
%     aligned for time
%
%   2008/11/28 M.McGowan (support@guralp.com)
%     Updated readgcfblock for sample rates >250
```

```
%     2009/03/05 M.McGowan (support@guralp.com)
%     Fixed bug picking up streamID from first block. Was preventing code
%     from reading a GCF file without a Stream ID being specified


% initialise output variables to 'invalid'. Can't leave them non-existing,
% as that doesn't compile properly in 6.x.
sps=-1;
ist=-1;
wstreamID=-1;
expectedtime=-1;

if (nargin>1) && iscell(streamID),
  for i = 1:length(streamID),

[samples{i},streamID{i},sps(i),ist(i)]=readgcffile(filename,streamID{i});
  end
  return
end

if (nargin>1) && strcmp(streamID,'plot'),
  plotfile(filename);
  return
end

fid = fopen(filename,'r','ieee-be');
if fid==-1,
    [p,n,e]=fileparts(filename);
    if ~strcmpi(e,'.gcf'),
        fname2 = [filename,'.gcf'];
        fid = fopen(fname2,'r','ieee-be');
    end
end
if fid==-1,
    error(['Unable to open file "',filename,'"']);
    return;
end

if (nargin>1) && strcmp(streamID,'list'),
  samples=getstreamidlist(fid);
  fclose(fid);
  return
end

if nargin>1,
  wstreamID = base2dec(streamID,36); % faster to compare numbers than
strings, so use a 'working' streamID
end
% to read the file, first create the array to handle the entire file's
samples,
% then read in block by block, copying into the array in the correct
place.
% This is MUCH faster than adding on to the end of an array each block.
sampcount=samplesinfile(fid);
%samples=NaN*ones(sampcount,1);
samples=repmat(NaN,sampcount,1); % faster than the above, according to
docs for repmat
sampcount=1;
```

```
onesec = datenum(0,0,0,0,0,1);
onemsec = onesec/1000;

while ~feof(fid)
  if wstreamID < 0, % no stream ID has been pre-specified, so use the
first one we find
    [blksamples,blksysID,blkstreamID,blksps,blkist] = readgcfblock(fid);
    wstreamID = blkstreamID;
  else
    [blksamples,blksysID,blkstreamID,blksps,blkist] =
readgcfblock(fid,wstreamID);
  end
  if sps < 0,
    sps = blksps;
  end
  if ist < 0,
    ist = blkist;
  end
  if (sps>0) && (~isempty(blksamples)),
    if expectedtime>=0,
      if expectedtime+onemsec < blkist,
        disp(['Warning: Gap in ',dec2base(blkstreamID,36),', Expected
',datestr(expectedtime,31),', found ',datestr(blkist,31)]);
      end
      if blkist+onemsec < expectedtime,
        disp(['Warning: Overlap in ',dec2base(blkstreamID,36),', Expected
',datestr(expectedtime,31),', found ',datestr(blkist,31)]);
      end
    end
    secs = length(blksamples)/sps;
    expectedtime = blkist + secs*onesec;
  end
  % Copy the samples into the pre-prepared array
  if blksps>0,
    ofs = round((blkist-ist)*blksps/onesec);
  else
    ofs = sampcount;
  end
  endofs = ofs + length(blksamples);
  while endofs > length(samples), %if array not big enough, expand until
it is
    samples = [samples;NaN*ones(length(samples),1)];
  end

  if ofs>=0,
    samples(ofs+1:endofs)=blksamples;
    sampcount = max([sampcount,endofs]);
  else
    disp(['Warning: discarding data from',dec2base(blkstreamID,36),' as it
is before the start of file. FileStart=',datestr(ist,31),'
BlockStart=',datestr(blkist,31)]);
  end
end
fclose(fid);
samples=samples(1:sampcount);     % trim samples array to actual length
streamID = dec2base(wstreamID,36); % convert numerical streamID back to a
string
```

```
function [samps,sysID,streamID,sps,ist] = readgcfblock(fid,nstrid)
samps=[];
sps=0;
ist=0;
sysID = fread(fid,1,'uint32');
streamID = fread(fid,1,'uint32');
if nargin>1, % if we have specified a particular ID, keep searching until
we find it
  while ~feof(fid) && (nstrid ~= streamID),
    fseek(fid,1016,'cof');
    sysID = fread(fid,1,'uint32');
    streamID = fread(fid,1,'uint32');
  end
end
if feof(fid)
  return
end

date = fread(fid,1,'ubit15');
time = fread(fid,1,'ubit17');
reserved = fread(fid,1,'uint8');
sps = decodesps(fread(fid,1,'uint8'));
frac = fread(fid,1,'ubit4');
compressioncode = fread(fid,1,'ubit4');
numrecords = fread(fid,1,'uint8');

% Convert GCF coded time to Matlab coded time
hours = floor(time / 3600);
mins = rem(time,3600);
ist = datenum(1989,11,17, hours, floor(mins / 60), rem(mins,60) ) + date;
% add in the fractional second offset (if any)
if sps>0,
  if sps==400, step=50; else step=250; end;
  diff=frac*step/sps; % fractions of a second
  ist=ist+ diff/86400;
end

if (sps ~= 0),
   fic = fread(fid,1,'int32');
   switch compressioncode
   case 1,
      diffs = fread(fid,numrecords,'int32');
   case 2,
      diffs = fread(fid,numrecords*2,'int16');
   case 4,
      diffs = fread(fid,numrecords*4,'int8');
   end
   ric = fread(fid,1,'int32',1000-numrecords*4);
   diffs(1) = fic;
   samps = cumsum(diffs);
else
   samps =
char(fread(fid,numrecords*4,[num2str(numrecords*4),'*uchar=>uchar'],1008-
numrecords*4)');
end


function samps = samplesinfile(fid)
fseek(fid,14,'bof');
```

```
% Read number-of-records and compression-code of every block into an array
nr = fread(fid,'uint16',1022);
% Separate number-of-records and compression-code from the 16 bit value
read
cc = bitshift(nr,-8);
nr = bitand(nr,255);
% sum up the number of samples in each block
samps=sum(cc.*nr);
frewind(fid);

  function list = getstreamidlist(fid)
fseek(fid,4,'bof');
list=fread(fid,'uint32',1020);
list=dec2base(list,36);
list=unique(cellstr(list));

 function plotfile(fname)
% EXAMPLE SCRIPT TO READ AND PLOT ALL STREAMS IN A GCF FILE
list=readgcffile(fname,'list');
for i = 1:length(list),
  [samples{i},id{i},sps(i),Tstart(i)]=readgcffile(fname,list{i});
  Tend(i)=Tstart(i);
  if sps(i)>0,
    Tend(i)=Tstart(i) + (length(samples{i})/sps(i))/86400;
  end
end
Tmin=datevec(min(Tstart));
Tmax=datevec(max(Tend));
Tdiff=etime(Tmax,Tmin);
datachans=find(sps>0);
numchans=length(datachans);
for i = 1:numchans,
  subplot(numchans,1,i);
  Soffset=etime(datevec(Tstart(datachans(i))),Tmin);

plot((Soffset:1/sps(datachans(i)):Soffset+(length(samples{datachans(i)})-
1)/sps(datachans(i))),samples{datachans(i)});
  ylabel(id(datachans(i)));
  ax=axis;
  axis([0 Tdiff ax(3) ax(4)]);
end

 function [outsps]=decodesps(insps)
switch insps
  case 157,  outsps=0.1;
  case 161,  outsps=0.125;
  case 162,  outsps=0.2;
  case 164,  outsps=0.25;
  case 167,  outsps=0.5;
  case 171,  outsps=400;
  case 174,  outsps=500;
  case 176,  outsps=1000;
  case 179,  outsps=2000;
  case 181,  outsps=4000;
  otherwise outsps=insps;
end
```

Appendix 3: Matlab script to read multiple raw hour-long .gcf files from one folder into Matlab, create time variables and export as .txt files

```
% Script to read in hour-long .gcf files and prep them as .txt files for
% stata script.
filenames=ls('*.gcf');  % Generate a list of all files in current
directory
numfiles = size(filenames); % Variable of how many files in 'filenames'
list.
indir='G:\to_copy\6047e'; % In directory - used below.
outdir='G:\to_copy\6047e'; % Out directory - used below.

for fileid=1:numfiles(1); % For every file of folder id 1-n.
    infile=(filenames(fileid,:)); % Creates a variable 'infile' which is
the current filename being used, specified by the file number 'fileid'
    [samples,streamID,sps,ist]=readgcffile(infile); % Function to read in
the hour-long .gcf file as specified by infile.
    time1=0:1/sps:(length(samples)-1)/sps; % Create time variable.
    time2=time1/86400+ist;
    time=reshape(time2,length(samples),1);
    clear ist sps streamID time1 time2
    outvar=[time samples]; % Combine time and samples into a 2 column
matrix.
    cd (outdir) % Go to out directory.
    fid=fopen([infile(1:14),'.txt'],'wt'); % Create a .txt file combining
time and samples variables as 2 columns.
    % Use the infile specified above as the new .txt filename including
    % only digits 1-14 so .gcf ending is removed.
    fprintf(fid,'%16.9f, %6.0f \r\n',outvar'); % Transpose outvar so will
export as 2 columns, format output text columns.
    fclose(fid)

    cd(indir) % Return to in directory and then loops through rest of .gcf
files in directory.


end
```

Appendix 4: Stata script to read in multiple 24-hour files (at 100 Hz) from one folder, convert to velocity, calculate minute and hourly statistics and reduce data resolution

```
cd H:\6084z2_full_days
! dir *.txt /a-d /b >H:\filelists\filelist.txt, replace

file open myfile using H:\filelists\filelist.txt, read
file read myfile line

while r(eof)==0 {
        // read in .txt files created in Matlab
insheet using `line', double
        rename v1 time
        format time %16.9f
        gen double date1=time-715876
        format date1 %16.9f
        format date1 %td
        gen double date=cofd(date1)
        format date %tc
        rename v2 amp
        format amp %6.0f
        save `line'.dta,

        // Adjust amp for mean and create all positive amps
        su amp
        gen mean_amp = r(mean)
        gen adjusted_amp = amp - (sqrt(mean_amp^2))
        // +/- depending on whether mean is negative/positive
        su adjusted_amp
        gen pos_amp =  sqrt(adjusted_amp^2)
        drop mean_amp amp adjusted_amp

        // Convert amplitude counts to velocity - change digitising factor and
        // sensitivity for each instrument and their different components.
        gen velocity=((pos_amp*0.983)/1000000)/2380
        drop pos_amp

        // calculate minute and hourly statistics of velocity and reduce data resolution to
        hours/minutes
        sort date
        gen doy = doy(dofc(date))
        generate hours = hh(date)
        gen double new_doy = doy * 10000000
        gen double new_hour = hours * 10000
        generate minutes = mm(date)
        gen double all_minutes = new_doy+new_hour+minutes
        egen tag_all_minutes = tag(all_minutes)
        gen cumu_minute_tag = sum(tag_all_minutes)

        gen double all_hours = new_doy+new_hour
        egen tag_all_hours = tag(all_hours)
        gen cumu_hour_tag = sum(tag_all_hours)

        drop new_doy new_hour all_hours
```

```
sort cumu_hour_tag
by cumu_hour_tag: egen hour_mean = mean(velocity)
by cumu_hour_tag: egen hour_max = max(velocity)

sort  cumu_minute_tag
by cumu_minute_tag: egen minute_max = max( velocity)
by cumu_minute_tag: egen minute_mean = mean( velocity)

sort date
save `line'.dta, replace

drop if tag_all_minutes !=1
drop velocity hours minutes all_minutes tag_all_minutes time
save `line'_2.dta, replace

drop _all
file read myfile line
}
```

Appendix 5a: Command to extract power spectral density estimates from PQLX

For hourly estimates:

exPSDhour *PQLX server name project code instrument code* -- HH*component start date (YYYY-MM-DD) end date (YYYY-MM-DD)* 00:00 24:00 |grep ":00:00" > *file location to output to*

For 30-minute estimates:

exPSDhour *PQLX server name project code instrument code* -- HH*component start date (YYYY-MM-DD) end date (YYYY-MM-DD)* 00:00 24:00 > *file location to output to*

Appendix 5b: Matlab code to create spectrograms

```
load power.txt % load in signal power and period vectors
load periods_100hz.txt

days=[134:0.041666666:156.95836]; % generate x axis of Julian day
numbers at hourly intervals
cnt=1 % Generates a counter starting at 1

for x=1:552  % x is the day variable - the second number needs to be
the no. of time intervals (i.e. the no. of hours).
    for y=1:106   % y is the frequency variable – are 106 frequencies
in the 100 Hz data
        matrix(y,x)=blb09_z_power(cnt);  % creates matrix of power
values
        cnt=cnt+1;
    end
end

surface(days,periods_100hz,matrix,'EdgeColor','none'), colorbar
% generate 'surface' image
title ('14/05/10 - 05/06/10 BLB12 E errors replaced','FontSize',14)
xlabel ('Day','FontSize',14)
ylabel ('Period (seconds)','FontSize',14)
axis ([134 157 .02 179])
% log the y axis
```

Appendix 6: Details of the wave transformation model, based on that of Battjes and Stive (1985).

There are two types of input into the model: those that were calculated across the entire time- and space-frame i.e. values were provided for each location in the profile (see Figure 3.15) at each time-step; and those that were just given initial values for each time-step at the offshore location (at 1000 m from coast). Depth was calculated at each location for each time-step based on the sea-bed bathymetry at a height in mOD, and the tide height. Wave group celerity (Cg) was calculated according to Airy linear wave theory (Equation A6.10 – A6.14) and accounted for changes in depth via the resulting change in wavelength (L). Wave number (k) was also calculated according to linear wave theory and this also varied with depth due to its dependence on wavelength (L) (Equation A6.1). The peak wave period for each time-step was obtained from the wave buoy data and was constant throughout the depth profile for each time-step. A distance of 1000 m from the coast was used as the start point for the wave transformations as at this location, according to linear wave theory, the depths were still considered to be 'deep water' when compared to the wavelength. Therefore at this location, wave conditions were very similar to those at the buoy as the deep water meant no interaction between the seabed and waves had yet occurred. The spacing intervals of calculations in the profile were decreased approaching the intertidal zone where more significant changes in wave characteristic occurred so more accurate model outputs for these areas could be attained (Figure 3.15).

$$k = \frac{2\pi}{L} \qquad \text{(Equation A6.1)}$$

Where: L = wavelength (calculated using Hunt's (1979) adaptation of the dispersion equation)

Initial values of the wave height at 1000 m from the coast were obtained via shoaling the offshore significant wave heights measured at the wave buoy to 1000 m via standard Airy linear equation (Equation A6.2). This was then converted to the root mean square wave height (H_{rms}) (as this was the wave height value required by the model – a standard requirement of most wave transformation models (e.g. Battjes and Jansen, 1978; Thornton and Guza, 1983; Battjes and Groenendijk, 2000) using the widely accepted conversion of $H_{rms}=1.42H_s$, where H_s is the significant wave height (Goda, 2000). The initial H_{rms} values at 1000 m from the coast were provided as initial wave height values in the model.

$$H_2 = \left(\frac{C_1 n_1}{C_2 n_2}\right)^{0.5} H_1 \qquad \text{(Equation A6.2)}$$

Where C_1 = wave celerity at buoy (see Equation A6.11 – A6.13 to calculate$C$.)

C_2 = wave celerity at 1000 m

n_1 = n at buoy (see Equation A6.14 to calculate n)

n_2 = n at 1000 m

The model uses two coefficients (α and γ) that determine the level of energy dissipation in a breaking wave (α) and the fraction of breaking waves (γ via its inclusion in the calculation of breaking wave height H_m (Equation A6.3)) (Battjes and Stive, 1985). Battjes and Stive (1985)

obtained optimum values of the two coefficients by comparing their modeled results with lab and field results. The field site conditions of the Dutch coast that were used by Battjes and Stive (1985) are similar to the input wave and depth conditions used in this study. They found α to be constant=1 and γ to vary with offshore wave steepness (H_{rms}/L_o where H_{rms} is root mean square wave height and L is wave length). Both coefficients feed into the calculation of energy dissipation (D), α directly and γ via its effect on the breaking wave height (H_m). The height at which waves break is determined by offshore wave steepness (included in γ), local water depth and wave number (Equation A6.3).

$$H_m = 0.88k^{-1}\tanh(\gamma kd/0.88) \qquad \text{(Equation A6.3)}$$

Where k is the wavenumber, γ is the breaker height coefficient (see Equation A6.4 below) and d is the water depth below the still tide water level.

Wave breaking is in part affected by the seabed slope and wave steepness (the ratio of wave height to wave length). In their comparisons of model results with the lab and field data, Battjes and Stive (1985) found breaker height not to be affected by seabed slope or the iribarren number (surf similarity parameter, which is a measure of ratio of the seabed slope to wave steepness) but found it to be affected by offshore wave steepness ($s_o = \mathrm{H_{rms}/L_o}$). They produced the breaker height coefficient γ (Equation A6.4) used to predict breaking wave heights (Equation A6.3 above).

$$\gamma = 0.5 + 0.4\tanh(33s_o) \qquad \text{(Equation A6.4)}$$

The model calculates energy dissipation based on the fraction of waves (Q) that are breaking. Key to this is identifying the height at which waves will break in the local water conditions (H_m see Equation A6.3 above) which is used as a cutoff to identify the proportion of breaking waves in the cumulative probability (Rayleigh) distribution of wave heights. The fraction of breaking waves (Q) is calculated iteratively (see Equation A6.5) based on the ratio of the root mean square wave height (H_{rms}) to the breaking wave height (H_m). When H_{rms}>=H_m the water depth is approaching 0 and Q is equal to 1, such that the majority of waves are broken. When H_{rms}>=H_m it has been set to equal H_m so the wave energy decreases once the majority of waves have broken.

$$\frac{1-Q}{-lnQ} = \left(\frac{H_{rms}}{H_m}\right)^2 \qquad \text{(Equation A6.5)}$$

The adaptation of Battjes and Stive's (1985) model used here to estimate wave heights at the field site from 1000 m into the coast was created in Matlab. The Matlab command *fzero* has been used to iteratively calculate the value of Q at each step by finding the value of Q which solves Equation A6.6. The *fzero* command searches within the interval limits of Q = 0 - 10 which satisfy the requirements of the *fzero* command (Matlab, 2011).

$$\frac{1-Q}{-lnQ} - \left(\frac{H_{rms}}{H_m}\right)^2 = 0 \qquad \text{(Equation A6.6)}$$

The variables and coefficients above are used to calculate the rate of energy dissipation (per unit of horizontal area) (D) that occurs as waves are breaking (Equation A6.7).

$$D = \frac{1}{4}\,\alpha Q f \rho g {H_m}^2 \qquad \text{(Equation A6.7)}$$

Where f is the peak frequency of the waves (obtained from the wave buoy data), ρ is the density of sea water (1,030 kg m^{-3}) and g is gravitational acceleration (9.81 m s^{-2}). D is used in the integration of the energy flux (P) (rate of energy density transfer per unit horizontal area) through the depth profile (Equation A6.8) as it accounts for energy dissipation due to the fraction of waves that are breaking as they progress towards the coast through increasingly shallower waters. Once waves begin to break, the rate of energy dissipation (D) will increase towards the point at which all waves have broken/are breaking. In the model energy flux (P) is integrated from 1000 m to the water's edge and varies according to the rate of energy dissipation (D).

$$Px = ECn = ECg \qquad \text{(Equation A6.8)}$$

Where E is the wave energy density (Equation A6.9) and Cg (Cn) is the wave group celerity (speed) (Equations A6.10 – A6.14) which is the speed at which the energy density is transported.

$$E = \frac{1}{8}\rho g H^2 \qquad \text{(Equation A6.9)}$$

$$Cg = Cn \qquad \text{(Equation A6.10)}$$

According to Airy linear theory different equations are used to calculate wave celerity in different water depths, determined by the ratio of water depth (d) to offshore wavelength (L_o).

Intermediate water depth ($0.25>d/L_o>0.05$) $C = \frac{L}{T}$ (Equation A6.11)

Deep water ($d/L_o>0.5$) $C_{o=\frac{gT}{2\pi}}$ (Equation A6.12)

Shallow water ($d/L_o=<0.05$) $C_{s=\sqrt{gd}}$ (Equation A6.13)

$$n = \frac{1}{2}\left[1 + \frac{2kd}{\sinh(2kd)}\right] \qquad \text{(Equation A6.14)}$$

Wave group celerity is used to calculate wave energy flux because waves travel over long distances in groups. In deep water n≈0.5 so according to Equation A6.14 the wave group travels half as fast as individual deep water waves, whereas in shallow water n≈1 so the wave group travels at the same speed as individual waves (Masselink, 2005).

The energy flux (P) is integrated over the depth profile (Equation A6.15) for each location (x), accounting for the energy dissipation due to wave breaking that occurs between x and the previous location (x-1) (Battjes and Stive, 1985).

$$\frac{\delta Px}{\delta x} + D = 0 \qquad \text{(Equation A6.15)}$$

This was solved using Equation A6.16.

$$P_x = \delta x_x\,(-D_x) + P_{x-1} \qquad \text{(Equation A6.16)}$$

From the energy flux (Equation A6.16) the predicted H_{rms} is calculated (Equation A6.17)

$$H_{rms\,x} = \sqrt{\frac{P_x 8}{\rho g C g_x}} \qquad \text{(Equation A6.17)}$$

Changes in the mean water level occur as waves break, called set-up and set-down, caused by the momentum flux (S_{xx}) (Equation A6.18) of waves on sloping beaches / foreshores (Komar, 1998). This wave set-up and set-down is calculated by the model at each location (x) along the depth profile via integration of the momentum flux. As waves approach a sloping beach / foreshore and are preparing to break there is a shoreward increase in momentum which exerts stresses (called radiation stresses) that act in a number of directions (Davidson-Arnott, 2010). It is the shoreward radiation stress (S_{xx}) that represents the shoreward momentum flux which increases as the wave height increases towards the breakpoint (Davidson-Arnott, 2010). Wave set-up and set-down is a response to the changes in momentum flux as the wave approaches and passes the breakpoint and is caused as a pressure gradient or force is generated that balances the momentum flux S_{xx} (Komar, 1998). As the wave height increases and reaches the breakpoint there is an increase in momentum flux (S_{xx}) and a corresponding decrease in mean water level, i.e. set-down (Komar, 1998). Once the wave has broken the momentum flux (S_{xx}) decreases and there is a corresponding increase in mean water level, i.e. set-up (Komar, 1998).

$$S_{xx} = \left(\frac{1}{2} + \frac{2kh}{\sinh 2kh}\right) E \qquad \text{(Equation A6.18)}$$

The energy density in Equation A6.9 is calculated from the energy flux (Equation A6.16). The water depth (h) used in Equation A6.18 is the sum of the depth at still tide level (d) at location x plus the wave set-up height (η) calculated at the previous location (x-1). Initial values of wave set-up at 1000 m from the coast were calculated using Equation A6.19.

$$\eta = \frac{kH^2}{8\sinh(2kd)} \qquad \text{(Equation A6.19)}$$

The wave set-up (η) that occurs across the rest of the profile is then calculated via the integration of the momentum balance (Equation A6.20).

$$\frac{\delta S_{xx}}{\delta x} + \rho g(d+\eta)\frac{\delta \eta}{\delta x} = 0 \qquad \text{(Equation A6.20)}$$

This is solved using Equation A6.21.

$$\eta_x = \left(-\frac{\delta S_{xx}}{\delta x}\right)\left(\frac{1}{\rho g(d_x+\eta_{x-1})}\right)\delta x + \eta_{x-1} \qquad \text{(Equation A6.21)}$$

The model loops through the depth integrating both the energy flux and momentum flux to produce the key outputs, the rms wave height (H_{rms}), wave set-up (η), energy flux (P) and energy flux dissipation (D) at each location within the profile (red dots in Figure 3.15). Once the waves break i.e. H_{rms}=H_m then the predicted wave height (H_{rms}) is set to = H_m for the rest of the depth profile up to the water's edge. This simulates real-world surf zones where broken waves travel through the surf zone and dissipate energy to the foreshore via bed friction and turbulence, resulting in decreasing wave height (Komar, 1998). From the breakpoint energy dissipation can no longer be calculated using Equation A6.7 and instead the breaking wave height (H_m) is used to calculate the wave energy density using Equation A6.9, and energy flux is calculated using Equation A6.8 as the group celerity (Cg) is already known.

Appendix 7: Matlab script for wave transformation model

```
load time.txt
load location.txt
load depth.txt
load cg.txt
load kp.txt
load y.txt
load frequency.txt
load hr.txt

m=length(time);

n=length(location); % Number of observation values of variable xx

qq=depth*0.0; % Creates vector Q = 0s
px=depth*0.0; % Creates vector Px (energy flux)= 0s
dd=depth*0.0; % Creates vector D (energy dissipation)= 0s
nn=depth*0.0; % Creates vector of setup = 0s
ee=depth*0.0;
sxx=depth*0.0;
dsdx=depth*0.0;
hh=depth*0.0;
hm=depth*0.0;


rho=1030.0; % Density of sea water
gg=9.81; % Gravitational acceleration


for l=1:m; %Calculates wave setup(nn) at 1st location (1000m)
    for k=1
        nn(l,k)=-
((kp(l,k)*(hr(l,k)^2))/(8*(sinh(2*kp(l,k)*depth(l,k)))));
    end;
end

for l=1:m; %Calculates mean water depth which includes depth below SWL
and setup (nn)
    for k=1
        hh(l,k)=depth(l,k)+nn(l,k);
    end;
end


for l=1:m;

    for k=1:n;
    hm(l,k)=0.88*(kp(l,k)^-1.0)*tanh(y(l)*kp(l,k)*depth(l,k)/0.88);
    end;

end
for l=1:m;
    for k=1
        ee(l,k)=1.0/8.0*rho*gg*(hr(l,k)^2.0);
        px(l,k)=ee(l,k)*cg(l,k);
    end;
end

for l=1:m;
    for k=1
```

```
sxx(l,k)=(1/2+((2*kp(l,k)*depth(l,k))/(sinh(2*kp(l,k)*depth(l,k)))))*ee
(l,k);
        % Use depth or hh in here? hh.....
    end
end

q=0.0;
qq(1,1)=q;

  for l=1:m;
     q=0.0;

    for k=2:n;

      if (hr(l,1)~=0)

        if (isnan(hm(l,k))==0)%) %((q<1) &&

    for count=1:3;
        count

        if ((count==1) && (hr(l,k-1)<hm(l,k)))

            h1=(hm(l,k-1)+hm(l,k))/2.0;
            h2=hr(l,k-1); % Used to calc Q

            ff=@(q)(1-q)/(-log(q))-(h2/h1)^2.0;
            qq2=fzero(ff,[0.0 10.0]);
            qq(l,k)=qq2;

            dx(l,k)=location(k)-location(k-1); % Change in x is x2-x1
            dd(l,k)=1.0/4.0*1*qq2*frequency(l)*rho*gg*(hm(l,k)^2);

            px(l,k)=dx(l,k)*(-dd(l,k))+px(l,k-1); % Calculates Energy
flux at current x location
            hr(l,k)=sqrt(px(l,k)*8.0/(rho*gg*cg(l,k))); % Calculates
Hrms at current x location
            q=qq2;

            ee(l,k)=px(l,k)/cg(l,k);
            sxx(l,k)=(1/2+((2*kp(l,k)*(depth(l,k)+nn(l,k-
1)))/(sinh(2*kp(l,k)*(depth(l,k)+nn(l,k-1))))))*ee(l,k);
            dsdx(l,k)=(sxx(l,k)-sxx(l,k-1))/dx(l,k);
            nn(l,k)=(-dsdx(l,k))*(1/(rho*gg*(depth(l,k)+nn(l,k-
1))))*dx(l,k)+nn(l,k-1);
            hh(l,k)=depth(l,k)+nn(l,k);

         elseif ((count==2) && (hr(l,k)<hm(l,k)))
            h1=(hm(l,k-1)+hm(l,k))/2.0;
            h2=(hr(l,k-1)+hr(l,k))/2.0;

         elseif ((count==3) && (hr(l,k)<hm(l,k)))
            h1=(hm(l,k-1)+hm(l,k))/2.0;
            h2=(hr(l,k-1)+hr(l,k))/2.0;

         elseif ((count==1)&& (hr(l,k-1)>=hm(l,k-1)))
            h1=hm(l,k)
            h2=hm(l,k)

            ff=@(q)(1-q)/(-log(q))-(h2/h1)^2.0;
            qq2=fzero(ff,[0.0 10.0]);
```

```
            qq(l,k)=qq2;

            dx(l,k)=location(k)-location(k-1); % Change in x is x2-x1
            %dd(l,k)=1.0/4.0*1*qq2*frequency(l)*rho*gg*(hm(l,k)^2);

            %px(l,k)=dx(l,k)*(-dd(l,k))+px(l,k-1); % Calculates Energy
flux at current x location
            hr(l,k)=hm(l,k); % Calculates Hrms at current x location
            q=qq2;

            %ee(l,k)=px(l,k)/cg(l,k);
            ee(l,k)=1.0/8.0*rho*gg*(hr(l,k)^2.0);
            px(l,k)=ee(l,k)*cg(l,k);
            sxx(l,k)=(1/2+((2*kp(l,k)*(depth(l,k)+nn(l,k-
1)))/(sinh(2*kp(l,k)*(depth(l,k)+nn(l,k-1))))))*ee(l,k);
            dsdx(l,k)=(sxx(l,k)-sxx(l,k-1))/dx(l,k);
            nn(l,k)=(-dsdx(l,k))*(1/(rho*gg*(depth(l,k)+nn(l,k-
1))))*dx(l,k)+nn(l,k-1);
            hh(l,k)=depth(l,k)+nn(l,k);

         elseif ((count==1)&& (hr(l,k-1)>=hm(l,k)))
            h1=hm(l,k)
            h2=hm(l,k)

            ff=@(q)(1-q)/(-log(q))-(h2/h1)^2.0;
            qq2=fzero(ff,[0.0 10.0]);
            qq(l,k)=qq2;

            dx(l,k)=location(k)-location(k-1); % Change in x is x2-x1
            %dd(l,k)=1.0/4.0*1*qq2*frequency(l)*rho*gg*(hm(l,k)^2);

            %px(l,k)=dx(l,k)*(-dd(l,k))+px(l,k-1); % Calculates Energy
flux at current x location
            hr(l,k)=hm(l,k); % Calculates Hrms at current x location
            q=qq2;

           % ee(l,k)=px(l,k)/cg(l,k);
            ee(l,k)=1.0/8.0*rho*gg*(hr(l,k)^2.0);
            px(l,k)=ee(l,k)*cg(l,k);
            sxx(l,k)=(1/2+((2*kp(l,k)*(depth(l,k)+nn(l,k-
1)))/(sinh(2*kp(l,k)*(depth(l,k)+nn(l,k-1))))))*ee(l,k);
            dsdx(l,k)=(sxx(l,k)-sxx(l,k-1))/dx(l,k);
            nn(l,k)=(-dsdx(l,k))*(1/(rho*gg*(depth(l,k)+nn(l,k-
1))))*dx(l,k)+nn(l,k-1);
            hh(l,k)=depth(l,k)+nn(l,k);

           %elseif ((count~=1) && (hr(l,k-1)>=hm(l,k)))
           % h1=hm(l,k)
            %h2=hm(l,k)

            %ff=@(q)(1-q)/(-log(q))-(h2/h1)^2.0;
           % qq2=fzero(ff,[0.0 10.0]);
           % qq(l,k)=qq2;

           % dx(l,k)=location(k)-location(k-1); % Change in x is x2-x1
           % dd(l,k)=1.0/4.0*1*qq2*frequency(l)*rho*gg*(hm(l,k)^2);

           % px(l,k)=dx(l,k)*(-dd(l,k))+px(l,k-1); % Calculates Energy
flux at current x location
           % hr(l,k)=hm(l,k); % Calculates Hrms at current x location
           % q=qq2;
```

```
            %ee(l,k)=px(l,k)/cg(l,k);
            %sxx(l,k)=(1/2+((2*kp(l,k)*(depth(l,k)+nn(l,k-
1)))/(sinh(2*kp(l,k)*(depth(l,k)+nn(l,k-1))))))*ee(l,k);
            %dsdx(l,k)=(sxx(l,k)-sxx(l,k-1))/dx(l,k);
            %nn(l,k)=(-dsdx(l,k))*(1/(rho*gg*(depth(l,k)+nn(l,k-
1))))*dx(l,
            %k)+nn(l,k-1);
            %hh(l,k)=depth(l,k)+nn(l,k);

         elseif ((count==2) && (hr(l,k)>=hm(l,k)))
            h1=hm(l,k)
            h2=hm(l,k)

            ff=@(q)(1-q)/(-log(q))-(h2/h1)^2.0;
            qq2=fzero(ff,[0.0 10.0]);
            qq(l,k)=qq2;

            dx(l,k)=location(k)-location(k-1); % Change in x is x2-x1
            %dd(l,k)=1.0/4.0*1*qq2*frequency(l)*rho*gg*(hm(l,k)^2);

            %px(l,k)=dx(l,k)*(-dd(l,k))+px(l,k-1); % Calculates Energy
flux at current x location
            hr(l,k)=hm(l,k); % Calculates Hrms at current x location
            q=qq2;

            %ee(l,k)=px(l,k)/cg(l,k);
            ee(l,k)=1.0/8.0*rho*gg*(hr(l,k)^2.0);
            px(l,k)=ee(l,k)*cg(l,k);
            sxx(l,k)=(1/2+((2*kp(l,k)*(depth(l,k)+nn(l,k-
1)))/(sinh(2*kp(l,k)*(depth(l,k)+nn(l,k-1))))))*ee(l,k);
            dsdx(l,k)=(sxx(l,k)-sxx(l,k-1))/dx(l,k);
            nn(l,k)=(-dsdx(l,k))*(1/(rho*gg*(depth(l,k)+nn(l,k-
1))))*dx(l,k)+nn(l,k-1);
            hh(l,k)=depth(l,k)+nn(l,k);

         elseif ((count==3) && (hr(l,k)>=hm(l,k)))
            h1=hm(l,k)
            h2=hm(l,k)

            ff=@(q)(1-q)/(-log(q))-(h2/h1)^2.0;
            qq2=fzero(ff,[0.0 10.0]);
            qq(l,k)=qq2;

            dx(l,k)=location(k)-location(k-1); % Change in x is x2-x1
            %dd(l,k)=1.0/4.0*1*qq2*frequency(l)*rho*gg*(hm(l,k)^2);

            %px(l,k)=dx(l,k)*(-dd(l,k))+px(l,k-1); % Calculates Energy
flux at current x location
            hr(l,k)=hm(l,k); % Calculates Hrms at current x location
            q=qq2;

           % ee(l,k)=px(l,k)/cg(l,k);
            ee(l,k)=1.0/8.0*rho*gg*(hr(l,k)^2.0);
            px(l,k)=ee(l,k)*cg(l,k);
            sxx(l,k)=(1/2+((2*kp(l,k)*(depth(l,k)+nn(l,k-
1)))/(sinh(2*kp(l,k)*(depth(l,k)+nn(l,k-1))))))*ee(l,k);
            dsdx(l,k)=(sxx(l,k)-sxx(l,k-1))/dx(l,k);
            nn(l,k)=(-dsdx(l,k))*(1/(rho*gg*(depth(l,k)+nn(l,k-
1))))*dx(l,k)+nn(l,k-1);
            hh(l,k)=depth(l,k)+nn(l,k);
```

```
      end
  end

      end
    end
end


end;


%save ('hr_outputs.txt','hr', '-ascii')
%save ('qq_outputs.txt','qq', '-ascii')
%save ('px_outputs.txt','px', '-ascii')
%save ('dd_outputs.txt','dd', '-ascii')
%save ('hm_outputs.txt','hm', '-ascii')
%save ('nn_outputs.txt','nn', '-ascii')
%save ('sxx_outputs.txt','sxx', '-ascii')
```

References

ADAMS, P. N., ANDERSON, R. S. & REVENAUGH, J. (2002) Microseismic measurement of wave-energy delivery to a rocky coast. *Geology,* 30**,** 895-898.

ADAMS, P. N., STORLAZZI, C. D. & ANDERSON, R. S. (2005) Nearshore wave-induced cyclical flexing of sea cliffs. *Journal of Geophysical Research-Earth Surface,* 110.

AGAR, R. (1960) Post-glacial erosion of the North Yorkshire coast from the Tees estuary to Ravenscar. *Proceedings of the Yorkshire Geological Society,* 32**,** 409-428.

AMITRANO, D. (2006) Rupture by damage accumulation in rocks. *International Journal of Fracture,* 139**,** 369-381.

AMITRANO, D., GRASSO, J. R. & SENFAUTE, G. (2005) Seismic precursory patterns before a cliff collapse and critical point phenomena. *Geophysical Research Letters,* 32.

ANDERSON, R. S. (1998) Near-surface thermal profiles in alpine bedrock: Implications for the frost weathering of rock. *Arctic and Alpine Research,* 30**,** 362-372.

ANDERSON, R. S., DENSMORE, A. L. & ELLIS, M. A. (1999) The generation and degradation of marine terraces. *Basin Research,* 11**,** 7-19.

ANDRIANI, G. F. & WALSH, N. (2007) Rocky coast geomorphology and erosional processes: A case study along the Murgia coastline South of Bari, Apulia - SE Italy. *Geomorphology,* 87**,** 224-238.

ASHTON, A. D., WALKDEN, M. J. A. & DICKSON, M. E. (2011) Equilibrium responses of cliffed coasts to changes in the rate of sea level rise. *Marine Geology,* 284**,** 217-229.

ASTER, R. C., MCNAMARA, D. E. & BROMIRSKI, P. D. (2008) Multidecadal climate-induced variability in microseisms. *Seismological Research Letters,* 79**,** 194-202.

BARLOW, J., LIM, M., ROSSER, N., PETLEY, D., BRAIN, M., GEER, M. & NORMAN, E. (2012) Modeling cliff erosion using negative power law scaling of rockfalls. *Geomorphology,* 139 - 140**,** 416 - 424.

BATTJES, J. A. & STIVE, M. J. F. (1985) Calibration and verification of a dissipation model for random breaking waves. *Journal of Geophysical Research-Oceans,* 90**,** 9159-9167.

BENUMOF, B. T., STORLAZZI, C. D., SEYMOUR, R. J. & GRIGGS, G. B. (2000) The relationship between incident wave energy and seacliff erosion rates: San Diego County, California. *Journal of Coastal Research,* 16**,** 1162-1178.

BERNATCHEZ, P. & DUBOIS, J.-M. M. (2008) Seasonal quantification of coastal processes and cliff erosion on fine sediment shorelines in a cold temperate climate, north shore of the St. Lawrence maritime estuary, Quebec. *Journal of Coastal Research,* 24**,** 169-180.

BERNATCHEZ, P., JOLIVET, Y. & CORRIVEAU, M. (2011) Development of an automated method for continuous detection and quantification of cliff erosion events. *Earth Surface Processes and Landforms,* 36**,** 347-362.

BORMANN, P. (ed.) (2009) *New manual of seismological observatory practise (NMSOP-1),* Potsdam: IASPEI, GFZ German research centre for geosciences.

BRAIN, M., ROSSER, N., PETLEY, D., LIM, M., BARLOW, J. & NORMAN, E. (2010) Dynamic rock strength in coastal rock cliffs. *In:* WILLIAMS, A. L., PINCHES, G. M., CHIN, C. Y., MCMORRAN, T. J. & MASSEY, C. I., (eds.) *Geologically Active*. Auckland, New Zealand, CRC Press.

BRARDINONI, F. & CHURCH, M. (2004) Representing the landslide magnitude-frequency relation: Capilano River Basin, British Columbia. *Earth Surface Processes and Landforms,* 29**,** 115-124.

BRAY, M. J. & HOOKE, J. M. (1997) Prediction of soft-cliff retreat with accelerating sea-level rise. *Journal of Coastal Research,* 13**,** 453-467.

BROMIRSKI, P. D. (2001) Vibrations from the "Perfect Storm". *Geochemistry Geophysics Geosystems,* 2**,** art. no.-2000GC000119.

BROMIRSKI, P. D. (2009) Earth Vibrations. *Science,* 324**,** 1026-1027.

BROMIRSKI, P. D., DUENNEBIER, F. K. & STEPHEN, R. A. (2005) Mid-ocean microseisms. *Geochemistry Geophysics Geosystems,* 6.

BUCKLEY, S. J., HOWELL, J. A., ENGE, H. D. & KURZ, T. H. (2008) Terrestrial laser scanning in geology: data acquisition, processing and accuracy considerations. *Journal of the Geological Society,* 165**,** 625-638.

BUDETTA, P., GALIETTA, G. & SANTO, A. (2000) A methodology for the study of the relation between coastal cliff erosion and the mechanical strength of soils and rock masses. *Engineering Geology,* 56**,** 243-256.

BUNGUM, H., MYKKELTVEIT, S. & KVAERNA, T. (1985) Seismic noise in Fennoscandia, with emphasis on high-frequencies. *Bulletin of the Seismological Society of America,* 75**,** 1489-1513.

BURT, J. E., BARBER, G. M. & RIGBY, D. L. (2009) *Elementary statistics for geographers,* New York, The Guilford Press.

CARR, A. P. & GRAFF, J. (1982) The tidal immersion factor and short platform development - discussion. *Transactions of the Institute of British Geographers,* 7**,** 240-245.

CESSARO, R. K. (1994) Sources of primary and secondary microseisms. *Bulletin of the Seismological Society of America,* 84**,** 142 - 148.

COELINGH, J. P., VAN WIJK, A. J. M. & HOLTSLAG, A. A. M. (1998) Analysis of wind speed observations on the North Sea coast. *Journal of Wind Engineering and Industrial Aerodynamics,* 73**,** 125-144.

COLLINS, B. D. & SITAR, N. (2008) Processes of coastal bluff erosion in weakly lithified sands, Pacifica, California, USA. *Geomorphology,* 97**,** 483-501.

CROWELL, M., LEATHERMAN, S. P. & BUCKLEY, M. K. (1991) Historical shoreline change - error analysis and mapping accuracy. *Journal of Coastal Research,* 7**,** 839-852.

DASGUPTA, R. (2011) Whither shore platforms? *Progress in Physical Geography,* 35**,** 183-209.

DAVIDSON-ARNOTT, R. (2010) *Introduction to coastal processes and geomorphology,* Cambridge, Cambridge University Press.

DAVIES, J. L. (1980) *Geographical variation in coastal development,* London, Longman.

DEFRA (2002) *Soft cliffs: Prediction of recession rates and erosion control techniques*, DEFRA.

DEWEZ, T., CHAMBLAS, G., STARK, C., LASSEUR, E. & VANDROMME, R. (in press) Multi-temporal laser scanning surveys of Mesnil-Val coastal chalk cliff, Normandy (France): point-cloud processing, rockfall inventory and quantification of probabilistic rockfall hazard. *Earth Surface Processes and Landforms*.

DICKSON, M. E., KENNEDY, D. M. & WOODROFFE, C. D. (2004) The influence of rock resistance on coastal morphology around Lord Howe Island, Southwest Pacific. *Earth Surface Processes and Landforms,* 29**,** 931-931.

DORNBUSCH, U., ROBINSON, D. A., MOSES, C. A. & WILLIAMS, R. B. G. (2008) Temporal and spatial variations of chalk cliff retreat in East Sussex, 1873 to 2001. *Marine Geology,* 249**,** 271-282.

DORNBUSCH, U. & ROBINSON, D. A. (2011) Block removal and step backwearing as erosion processes on rock shore platforms: a preliminary case study of the chalk shore platforms of south-east England. *Earth Surface Processes and Landforms,* 36**,** 661-671.

DUPERRET, A., GENTER, A., MORTIMORE, R. N., DELACOURT, B. & DE POMERAI, M. R. (2002) Coastal rock cliff erosion by collapse at Puys, France: The role of impervious marl seams within chalk of NW Europe. *Journal of Coastal Research,* 18**,** 52-61.

DUPERRET, A., TAIBI, S., MORTIMORE, R. N. & DAIGNEAULT, M. (2005) Effect of groundwater and sea weathering cycles on the strength of chalk rock from unstable coastal cliffs of NW France. *Engineering Geology,* 78**,** 321-343.

DUSSAUGE-PEISSER, C., HELMSTETTER, A., GRASSO, J. R., HANTZ, D., DESVARREUX, P., JEANNIN, M. & GIRAUD, A. (2002) Probabilistic approach to rock fall hazard assessment: Potential of historical data analysis. *Natural Hazards and Earth System Sciences,* 2**,** 15-26.

EBERHARDT, E., STEAD, D. & COGGAN, J. S. (2004) Numerical analysis of initiation and progressive failure in natural rock slopes - the 1991 Randa rockslide. *International Journal of Rock Mechanics and Mining Sciences,* 41**,** 69-87.

EMERY, K. O. & KUHN, G. G. (1982) Sea cliffs - their processes, profiles, and classification. *Geological Society of America Bulletin,* 93**,** 644-654.

FRAYSSINES, M. & HANTZ, D. (2006) Failure mechanisms and triggering factors in calcareous cliffs of the Subalpine Ranges (French Alps). *Engineering Geology,* 86**,** 256-270.

FRIEDRICH, A., KRUGER, F. & KLINGE, K. (1998) Ocean-generated microseismic noise located with the Grafenberg array. *Journal of Seismology,* 2**,** 47-64.

GIVEN, H. K. (1990) Variations in broad-band seismic noise at IRIS/IDA stations in the USSR with implications for event detection. *Bulletin of the Seismological Society of America,* 80**,** 2072-2088.

GREENWOOD, R. O. & ORFORD, J. D. (2008) Temporal patterns and processes of retreat of drumlin coastal cliffs - Strangford Lough, Northern Ireland. *Geomorphology,* 94**,** 153-169.

GUNZBURGER, Y. & MERRIEN-SOUKATCHOFF, V. (2011) Near-surface temperatures and heat balance of bare outcrops exposed to solar radiation. *Earth Surface Processes and Landforms,* 36**,** 1577-1589.

GURROLA, H., MINSTER, J. B., GIVEN, H., VERNON, F., BERGER, J. & ASTER, R. (1990) Analysis of high-frequency seismic noise in the western United-States and eastern Kazakhstan. *Bulletin of the Seismological Society of America,* 80**,** 951-970.

GUTHRIE, R. H. & EVANS, S. G. (2004) Analysis of landslide frequencies and characteristics in a natural system, Coastal British Columbia. *Earth Surface Processes and Landforms,* 29**,** 1321-1339.

GUZA, R. T. & THORNTON, E. B. (1982) Swash oscillations on a natural beach. *Journal of Geophysical Research-Oceans and Atmospheres,* 87**,** 483-491.

HALL, A. M., HANSOM, J. D. & JARVIS, J. (2008) Patterns and rates of erosion produced by high energy wave processes on hard rock headlands: The Grind of the Navir, Shetland, Scotland. *Marine Geology,* 248**,** 28-46.

HAMPTON, M. A., GRIGGS, G. B., EDIL, T. B., GUY, D. E., KELLEY, J. T., KOMAR, P. D., MICKELSN, D. M. & SHIPMAN, H. M. (2004) Introduction. *In:* HAMPTON, M. A. & GRIGGS, G. B. (eds.) *Formation, Evolution, and Stabilty of Coastal Cliffs - Status and Trends.* U.S. Geological Survey.

HAPKE, C. & RICHMOND, B. (2002) The impact of climatic and seismic events on the short-term evolution of seacliffs based on 3-D mapping: northern Monterey Bay, California. *Marine Geology,* 187**,** 259-278.

HASSELMANN, K. (1963) A statistical analysis of the generation of microseisms. *Reviews of Geophysics,* 1**,** 177-210.

HAUBRICH, R. A., MUNK, W. H. & SNODGRASS, F. E. (1963) Comparative spectra of microseisms and swell. *Bulletin of the Seismological Society of America,* 53**,** 27-37.

HEDLIN, M. A. H. & ORCUTT, J. A. (1989) A comparative study of island, seafloor, and subseafloor ambient noise-levels. *Bulletin of the Seismological Society of America,* 79**,** 172-179.

HODGE, R., BRASINGTON, J. & RICHARDS, K. (2009) In situ characterization of grain-scale fluvial morphology using Terrestrial Laser Scanning. *Earth Surface Processes and Landforms,* 34**,** 954-968.

HOLMAN, R. A. (1983) Edge waves and the configuration of the shoreline. *In:* KOMAR, P. D. (ed.) *Handbook of coastal processes and erosion.* CRC Press.

HOLMAN, R. A. & SALLENGER, A. H. (1985) Setup and swash on a natural beach. *Journal of Geophysical Research-Oceans,* 90**,** 945-953.

HUNT, J. N. (1979) Direct solution of wave dispersion-equation. *Journal of the Waterway Port Coastal and Ocean Division-Asce,* 105**,** 457-459.

HUTHNANCE, J. M. (1991) Physical oceanography of the North Sea. *Ocean and Shoreline Management,* 16**,** 199-231.

INKPEN, R. J., STEPHENSON, W. J., KIRK, R. M., HEMMINGSEN, M. A. & HEMMINGSEN, S. A. (2010) Analysis of relationships between micro-topography and short- and long-term erosion rates on shore platforms at Kaikoura Peninsula, South Island, New Zealand. *Geomorphology,* 121**,** 266-273.

KIBBLEWHITE, A. C. & EWANS, K. C. (1985) Wave-wave interactions, microseisms, and infrasonic ambient noise in the ocean. *Journal of the Acoustical Society of America,* 78**,** 981-994.

KOMAR, P. D. (1998) *Beach processes and sedimentation,* Upper Saddle River, N.J., Prentice Hall.

KRAUTBLATTER, M. & DIKAU, R. (2007) Towards a uniform concept for the comparison and extrapolation of rockwall retreat and rockfall supply. *Geografiska Annaler Series a-Physical Geography,* 89A**,** 21-40.

KRAUTBLATTER, M. & MOSER, M. (2009) A nonlinear model coupling rockfall and rainfall intensity based on a four year measurement in a high Alpine rock wall (Reintal, German Alps). *Natural Hazards and Earth System Sciences,* 9**,** 1425-1432.

KRAUTBLATTER, M., VERLEYSDONK, S., FLORES-OROZCO, A. & KEMNA, A. (2010) Temperature-calibrated imaging of seasonal changes in permafrost rock walls by quantitative electrical resistivity tomography (Zugspitze, German/Austrian Alps). *Journal of Geophysical Research-Earth Surface,* 115.

LAY, T. & WALLACE, T. C. (1995) *Modern global seismology,* San Diego; London, Academic Press.

LEE, E. M. (2008) Coastal cliff behaviour: Observations on the relationship between beach levels and recession rates. *Geomorphology,* 101**,** 558-571.

LIM, M. (2006) Coastal cliff evolution with reference to Staithes, North Yorkshire. Ph.D. Thesis, University of Durham, Durham, 378 pp.

LIM, M., PETLEY, D. N., ROSSER, N. J., ALLISON, R. J., LONG, A. J. & PYBUS, D. (2005) Combined digital photogrammetry and time-of-flight laser scanning for monitoring cliff evolution. *Photogrammetric Record,* 20**,** 109-+.

LIM, M., MILLS, J. & ROSSER, N. (2009) Laser scanning surveying of linear features: considerations and applications. *In:* HERITAGE, G. & LARGE, A. (eds.) *Laser scanning for the environmental sciences.* Wiley Blackwell.

LIM, M., ROSSER, N. J., ALLISON, R. J. & PETLEY, D. N. (2010a) Erosional processes in the hard rock coastal cliffs at Staithes, North Yorkshire. *Geomorphology,* 114**,** 12-21.

LIM, M., ROSSER, N., PETLEY, D., NORMAN, E., BARLOW, J. & BRAIN, M. (2010b) Characterising coastal cliff erosional environments: Microclimate-rock interactions. *In:* WILLIAMS, A. L., PINCHES, G. M., CHIN, C. Y., MCMORRAN, T. J. & MASSEY, C. I., (eds.) *Geologically Active*. Auckland, New Zealand, CRC Press.

LIM, M., ROSSER, N. J., PETLEY, D. N. & KEEN, M. (2011) Quantifying the Controls and Influence of Tide and Wave Impacts on Coastal Rock Cliff Erosion. *Journal of Coastal Research,* 27**,** 46-56.

LIMBER, P. W. & MURRAY, A. B. (2011) Beach and sea-cliff dynamics as a driver of long-term rocky coastline evolution and stability. *Geology,* 39**,** 1147-1150.

LONGUET-HIGGINS, M. S. (1950) A theory of the origin of microseisms. *Philosophical Transactions of the Royal Society of London. Series A, Mathematical and Physical,* 243**,** 1-35.

LOWE, J. A., HOWARD, T., PARDEENS, A., TINKER, J., JENKINS, G., RIDLEY, J., LEAKE, J., HOLT, J., WAKELINE, S., WOLF, J., HORBURGH, K., REEDER, T., MILNE, G., BRADLEY, S. & DYE, S. (2009) *UK Climate Projections science report: Marine and coastal projections*, DEFRA.

LOWRIE, W. (1997) *Fundamentals of geophysics,* Cambridge ; New York, NY, USA, Cambridge University Press.

MAIN, I. G. (2000) A damage mechanics model for power-law creep and earthquake aftershock and foreshock sequences. *Geophysical Journal International,* 142**,** 151-161.

MALAMUD, B. D., TURCOTTE, D. L., GUZZETTI, F. & REICHENBACH, P. (2004) Landslide inventories and their statistical properties. *Earth Surface Processes and Landforms,* 29**,** 687-711.

MARQUES, F. (2008) Magnitude-frequency of sea cliff instabilities. *Natural Hazards and Earth System Sciences,* 8**,** 1161-1171.

MASSELINK, G. (2005) Waves. *In:* SCHWARTZ, M. L. (ed.) *Encyclopedia of coastal science.* Dordrecht, Springer.

MASSELINK, G. & HUGHES, M. (2003) *Introduction to coastal processes and geomorphology,* London, Hodder Education.

MATSUOKA, N. (2008) Frost weathering and rockwall erosion in the southeastern Swiss Alps: Long-term (1994-2006) observations. *Geomorphology,* 99**,** 353-368.

MATSUOKA, N., MORIWAKI, K. & HIRAKAWA, K. (1996) Field experiments on physical weathering and wind erosion in an Antarctic cold desert. *Earth Surface Processes and Landforms,* 21**,** 687-699.

MAVKO, G., MUKERJI, T. & DVORKIN, J. (1998) *The rock physics handbook: tools for seismic analysis in porous media,* Cambridge, Cambridge University Press.

MCCREERY, C. S., DUENNEBIER, F. K. & SUTTON, G. H. (1993) Correlation of deep ocean noise (0.4-30 Hz) with wind, and the Holu spectrum - a worldwide constant. *Journal of the Acoustical Society of America,* 93**,** 2639-2648.

MCNAMARA, D. E. & BULAND, R. P. (2004) Ambient noise levels in the continental United States. *Bulletin of the Seismological Society of America,* 94**,** 1517-1527.

MET OFFICE. (2011) Met Office surface data users guide [Online]. Accessed 1st November 2011, from www.badc.nerc.ac.uk/data/ukmo-midas/ukmo_guide.html#5.5

MOON, V. G. & DE LANGE, W. P. (2010) Controls on coastal cliff erosion in Waitemata Group rocks, Auckland. *In:* WILLIAMS, A. L., PINCHES, G. M., CHIN, C. Y., MCMORRAN, T. J. & MASSEY, C. I., eds. Geologically Active, 2010 Auckland, New Zealand. CRC Press.

MOORE, L. J. (2000) Shoreline mapping techniques. *Journal of Coastal Research,* 16**,** 111-124.

MUNK, W. H. (1949) The solitary wave theory and its application to surf problems. *Annals of the New York Academy of Sciences,* 51**,** 376-401.

MURPHY, J., SEXTON, D., JENKINS, G., BOORMAN, P., BOOTH, B., BROWN, K., CLARK, R., COLLINS, M., HARRIS, G. & KENDON, L. (2009) *Climate change projections*, DEFRA.

NAYLOR, L. A., STEPHENSON, W. J. & TRENHAILE, A. S. (2010) Rock coast geomorphology: Recent advances and future research directions. *Geomorphology,* 114**,** 3-11.

OKIHIRO, M. & GUZA, R. T. (1995) Infragravity energy modulation by tides. *Journal of Geophysical Research-Oceans,* 100**,** 16143-16148.

O'REILLY, W. C. & GUZA, R. T. (1993) A comparison of 2 spectral wave models in the southern California Bight. *Coastal Engineering,* 19**,** 263-282.

OSPAR (2000) Quality status report 2000. London, OSPAR.

PETERSON, J. (1993) Observations and modeling of seismic background noise. *U.S. Geological Survey technical report 93-322.*

PETLEY, D. N. (2004) The evolution of slope failures: Mechanisms of rupture propagation. *Natural Hazards and Earth System Sciences,* 4**,** 147-152.

PETLEY, D. N., HIGUCHI, T., PETLEY, D. J., BULMER, M. H. & CAREY, J. (2005) Development of progressive landslide failure in cohesive materials. *Geology,* 33**,** 201-204.

PORTER, N. J., TRENHAILE, A. S., PRESTANSKI, K. & KANYAYA, J. I. (2010) Patterns of surface downwearing on shore platforms in eastern Canada. *Earth Surface Processes and Landforms,* 35**,** 1793-1810.

PROUDMAN OCEANOGRAPHIC LABORATORY. (2011) About the UK network [Online]. Accessed 1st November 2011, from www.pol.ac.uk/ntslf/tgi/

QUINN, J. D., ROSSER, N. J., MURPHY, W. & LAWRENCE, J. A. (2010) Identifying the behavioural characteristics of clay cliffs using intensive monitoring and geotechnical numerical modelling. *Geomorphology,* 120**,** 107-122.

RAWSON, P. F., WRIGHT, J. K. & GREENSMITH, J. T. (1992) *The Yorkshire coast,* London, Geologists' Association.

ROBINSON, L. A. (1977) Marine erosive processes at cliff foot. *Marine Geology,* 23**,** 257-271.

ROSSER, N. J., PETLEY, D. N., LIM, M., DUNNING, S. A. & ALLISON, R. J. (2005) Terrestrial laser scanning for monitoring the process of hard rock coastal cliff erosion. *Quarterly Journal of Engineering Geology and Hydrogeology,* 38**,** 363-375.

ROSSER, N., LIM, M., PETLEY, D., DUNNING, S. & ALLISON, R. (2007) Patterns of precursory rockfall prior to slope failure. *Journal of Geophysical Research-Earth Surface,* 112.

RUGGIERO, P., KOMAR, P. D., MCDOUGAL, W. G., MARRA, J. J. & BEACH, R. A. (2001) Wave runup, extreme water levels and the erosion of properties backing beaches. *Journal of Coastal Research,* 17**,** 407-419.

SALLENGER, A. H., KRABILL, W., BROCK, J., SWIFT, R., MANIZADE, S. & STOCKDON, H. (2002) Sea-cliff erosion as a function of beach changes and extreme wave runup during the 1997-1998 El Nino. *Marine Geology,* 187**,** 279-297.

SASS, O. (2005) Rock moisture measurements: techniques, results, and implications for weathering. *Earth Surface Processes and Landforms,* 30**,** 359-374.

SCHÜRCH, P., DENSMORE, A. L., ROSSER, N., LIM, M. & MCARDELL, B. W. (2011) Detection of surface change in complex topography using terrestrial laser scanning: application to the Illgraben debris-flow channel. *Earth Surface Processes and Landforms,* 36**,** 1847 - 1859.

SEIS-UK. (2005) CMG-6TD specification [Online]. Accessed 13th November 2011, from www.le.ac.uk/seis-uk/equipment6t.htm

SELBY, M. J. (1980) A rock-mass strength classification for geomorphic purposes: With tests from Antarctica and New Zealand. *Zeitschrift für Geomorphologie,* 24**,** 31-51.

SELBY, M. J. (1993) *Hillslope materials and processes,* Oxford, Oxford University Press.

SENFAUTE, G., DUPERRET, A. & LAWRENCE, J. A. (2009) Micro-seismic precursory cracks prior to rock-fall on coastal chalk cliffs: a case study at Mesnil-Val, Normandie, NW France. *Natural Hazards and Earth System Sciences,* 9**,** 1625-1641.

SMITHSON, P., ADDISON, K., ATKINSON, K. & BRIGGS, D. (2002) *Fundamentals of the physical environment,* London, Routledge.

STACEY, F. D., GLADWIN, M. T., MCKAVANAGH, B., LINDE, A. T. & HASTIE, L. M. (1975) Anelastic damping of acoustic and seismic pulses. *Surveys in geophysics,* 2**,** 133-151.

STARK, C. P. & HOVIUS, N. (2001) The characterization of landslide size distributions. *Geophysical Research Letters,* 28**,** 1091-1094.

STEIN, S. & WYSESSION, M. (2003) *An introduction to seismology, earthquakes, and earth structure,* Malden, Mass; Oxford, Blackwell.

STEPHENSON, W. J. (2000) Shore platforms: a neglected coastal feature? *Progress in Physical Geography,* 24**,** 311-327.

STEPHENSON, W. J. & KIRK, R. M. (1998) Rates and patterns of erosion on shore platforms, Kaikoura, South Island, New Zealand. *Earth Surface Processes and Landforms,* 23**,** 1071-1085.

STEPHENSON, W. J. & KIRK, R. M. (2000a) Development of shore platforms on Kaikoura Peninsula, South Island, New Zealand - Part one: The role of waves. *Geomorphology,* 32**,** 21-41.

STEPHENSON, W. J. & KIRK, R. M. (2000b) Development of shore platforms on Kaikoura Peninsula, South Island, New Zealand - II: The role of subaerial weathering. *Geomorphology,* 32**,** 43-56.

STEPHENSON, W. J., KIRK, R. M., HEMMINGSEN, S. A. & HEMMINGSEN, M. A. (2010) Decadal scale micro erosion rates on shore platforms. *Geomorphology,* 114**,** 22-29.

STIVE, M. J. F. (1984) Energy dissipation in waves breaking on gentle slopes. *Coastal Engineering,* 8**,** 99-127.

STOCK, G., MARTEL, S., COLLINS, B. & HARP, E. (2012) Progressive failure of sheeted rock slopes: The 2009 - 2010 Rhombus Wall rock falls in Yosemite Valley, California, USA. *Earth Surface Processes and Landforms,* 37**,** 546 - 561.

STURZENEGGER, M., YAN, M., STEAD, D. & ELMO, D. (2007) Application and limitations of ground-based laser scanning in rock slope characterization. *In:* EBERHARDT, E., STEAD, D. & MORRISON, T., (eds.) *Rock mechanics: Meeting society's challenges and demands* Vancouver, Canada, Taylor and Francis.

STYLES, T. D., COGGAN, J. S. & PINE, R. J. (2011) Back analysis of the Joss Bay Chalk Cliff Failure using numerical modelling. *Engineering Geology,* 120**,** 81-90.

SUMMERFIELD, M. A. (1991) *Global geomorphology : an introduction to the study of landforms,* Harlow, Longman.

SUNAMURA, T. (1975) Laboratory study of wave-cut platform formation. *Journal of Geology,* 83**,** 389-397.

SUNAMURA, T. (1976) Feedback relationship in wave erosion of laboratory rocky coast. *Journal of Geology,* 84**,** 427-437.

SUNAMURA, T. (1977) Relationship between wave-induced cliff erosion and erosive force of waves. *Journal of Geology,* 85**,** 613-618.

SUNAMURA, T. (1982) A predictive model for wave-induced cliff erosion, with application to Pacific coasts of Japan. *Journal of Geology,* 90**,** 167-178.

SUNAMURA, T. (1992) *Geomorphology of rocky coasts,* Chichester; New York, J. Wiley.

SUNAMURA, T. (2005) Cliffs, lithology versus erosion rates. *In:* SCHWARTZ, M. L. (ed.) *Encyclopedia of coastal science.* Dordrecht, Springer.

TEIXEIRA, S. B. (2006) Slope mass movements on rocky sea-cliffs: A power-law distributed natural hazard on the Barlavento Coast, Algarve, Portugal. *Continental Shelf Research,* 26**,** 1077-1091.

THORNTON, E. B. & GUZA, R. T. (1983) Transformation of wave height distribution. *Journal of Geophysical Research-Oceans and Atmospheres,* 88**,** 5925-5938.

TILLOTSON, K. & KOMAR, P. D. (1997) The wave climate of the Pacific Northwest (Oregon and Washington): A comparison of data sources. *Journal of Coastal Research,* 13**,** 440-452.

TRENHAILE, A. S. (1987) *The geomorphology of rock coasts,* Oxford, Clarendon Press.

TRENHAILE, A. S. (2000) Modeling the development of wave-cut shore platforms. *Marine Geology,* 166**,** 163-178.

TRENHAILE, A. S. (2001) Modelling the Quaternary evolution of shore platforms and erosional continental shelves. *Earth Surface Processes and Landforms,* 26**,** 1103-1128.

TRENHAILE, A. S. (2002) Rock coasts, with particular emphasis on shore platforms. *Geomorphology,* 48**,** 7-22.

TRENHAILE, A. S. & LAYZELL, M. G. J. (1981) Shore platform morphology and the tidal duration factor. *Transactions of the Institute of British Geographers,* 6**,** 82-102.

TRENHAILE, A. S. & KANYAYA, J. I. (2007) The role of wave erosion on sloping and horizontal shore platforms in macro- and mesotidal environments. *Journal of Coastal Research,* 23**,** 298-309.

TUCKER, M. J. (1950) Surfbeats: Sea waves of 1 to 5 minutes period. *Proceedings of the Royal Society of London,* 202**,** 565-573.

VAN DER WESTHUYSEN, A. J. (2010) Modeling of depth-induced wave breaking under finite depth wave growth conditions. *Journal of Geophysical Research-Oceans,* 115.

WAKELIN, S. L., WOODWORTH, P. L., FLATHER, R. A. & WILLIAMS, J. A. (2003) Sea-level dependence on the NAO over the NW European Continental Shelf. *Geophysical Research Letters,* 30.

WALKDEN, M. & DICKSON, M. (2008) Equilibrium erosion of soft rock shores with a shallow or absent beach under increased sea level rise. *Marine Geology,* 251**,** 75-84.

WALKDEN, M. J. A. & HALL, J. W. (2005) A predictive Mesoscale model of the erosion and profile development of soft rock shores. *Coastal Engineering,* 52**,** 535-563.

WEBB, S. C. (1998) Broadband seismology and noise under the ocean. *Reviews of Geophysics,* 36**,** 105-142.

WIECZOREK, G. F. & JAGER, S. (1996) Triggering mechanisms and depositional rates of postglacial slope-movement processes in the Yosemite valley, California. *Geomorphology,* 15**,** 17-31.

WITHERS, M. M., ASTER, R. C., YOUNG, C. J. & CHAEL, E. P. (1996) High-frequency analysis of seismic background noise as a function of wind speed and shallow depth. *Bulletin of the Seismological Society of America,* 86**,** 1507-1515.

YOUNG, A. P. & ASHFORD, S. A. (2008) Instability investigation of cantilevered seacliffs. *Earth Surface Processes and Landforms,* 33**,** 1661-1677.

YOUNG, A. P., FLICK, R. E., GUTIERREZ, R. & GUZA, R. T. (2009a) Comparison of short-term seacliff retreat measurement methods in Del Mar, California. *Geomorphology,* 112**,** 318-323.

YOUNG, A. P., GUZA, R. T., FLICK, R. E., O'REILLY, W. C. & GUTIERREZ, R. (2009b) Rain, waves, and short-term evolution of composite seacliffs in southern California. *Marine Geology,* 267**,** 1-7.

YOUNG, A. P., GUZA, R. T., O'REILLY, W. C., FLICK, R. E. & GUTIERREZ, R. (2011a) Short-term retreat statistics of a slowly eroding coastal cliff. *Natural Hazards and Earth System Sciences,* 11**,** 205-217.

YOUNG, A. P., ADAMS, P. N., O'REILLY, W. C., FLICK, R. E. & GUZA, R. T. (2011b) Coastal cliff ground motions from local ocean swell and infragravity waves in southern California. *Journal of Geophysical Research-Oceans,* 116.

YOUNG, C. J., CHAEL, E. P., WITHERS, M. M. & ASTER, R. C. (1996) A comparison of the high-frequency (>1 Hz) surface and subsurface noise environment at three sites in the United States. *Bulletin of the Seismological Society of America,* 86**,** 1516-1528.